The In Silico Limb: Data-based Spatio-temporal Modelling of Vertebrate Limb Organogenesis

Inauguraldissertation

zur Erlangung der Würde eines Doktors der Philosophie

vorgelegt der

Philosophisch-Naturwissenschaftlichen Fakultät

der Universität Basel

von

Erkan Ünal

aus Acıpayam, der Türkei

Basel, 2015

Genehmigt von der Philosophisch-Naturwissenschaftlichen Fakultät
auf Antrag von
Prof. Dr. Rolf Zeller (Fakultätsverantwortlicher)
Prof. Dr. Dagmar Iber (Dissertationsleiterin)
Prof. Dr. Savas Tay (Korreferent)

Basel, den 21. April 2015

Prof. Dr. Jörg Schibler
Dekan

1. Table of Contents

2. ABSTRACT

With the advantages of characterized signaling centers, known regulatory networks and characterized mutants, vertebrate limb bud is a paradigm to study organogenesis. Classical and molecular experiments have identified major key components and have provided snap shot information about the underlying regulatory processes. The mechanisms that control the size and shape of the limb bud have to some extent remained elusive and quantitative data is missing. To that end, I have acquired high quality quantitative data from defined stages of mouse and chicken limb bud development. In addition, my research aimed to gain an integrative understanding of the limb bud development utilizing an *in silico* modeling approach. This was done by using real geometries and the gene expression domains of particular genes.

For generating a quantitative dataset of mouse and chicken forelimb and wing bud growth, I have combined limb bud specific reporter expression, FACS analysis and 3-D imaging. We find that the growth and proliferation rates decline over time in a way that a biphasic growth behavior is observed. After the initial expansion, a distinct second phase starts around the stages when the hand plates are formed. Even though Sox9 positive cells have a lower proliferation rate, we show that the increasing conversion of Sox9 negative cells into Sox9 positive chondrogenic progenitors alone cannot be responsible for the observed lowering in growth rates. This is due to the fact that the fraction of Sox9 positive cells remains constant at the time when the growth rate drops and the proliferation rates decrease in both Sox9 positive and negative populations. I propose that the decrease of growth and

proliferation rates over time is independent of the known limb patterning mechanism.

For generation of the *in silico* limb bud model simulations, I first collected a 4-D gene expression data set in mouse limb buds by combining RNA in situ hybridization with Optical Projection Tomography (OPT) analysis between embryonic day 9 (E9) and E12.5. Using these high-resolution image data sets, I extracted limb bud geometries to allow solving reaction-diffusion equations on these scaffolds. Our *in silico* model simulations show the spatio-temporal kinetics of the molecular interactions that control initiation, propagation and termination of mouse limb bud development. Moreover, our model simulations are able to explain behaviors of various mouse limb bud mutants, which alter the levels and spatio-temporal kinetics of gene expression.

Based on predictions from the OPT analysis and the *in silico* simulations, I have also evidence of an additional pathway that appears to regulate *Gremlin1* expression during limb bud development. Firstly, using Prx-Cre mediated mesenchymal inactivation of the WNT pathway effector β-Catenin and specific inhibitors of the WNT pathway, I have shown that WNT pathway activity is required for the characteristic distal-anterior expansion of *Grem1* expression during progression of limb bud development E10.75 onwards. Using Hoxa13-Cre inactivation of the WNT pathway inactivation, I have shown that WNT signalling is also needed for characteristic *Gremlin1* expression during hand plate development.

3. INTRODUCTION

3.1 A brief introduction into vertebrate limb bud development

The vertebrate limb bud is a prime model system to investigate the genetic and cellular responses that govern vertebrate organogenesis (Zeller et. al., 2009). The fore- and hind limb buds emerge at defined positions perpendicular to the primary axis. Within three days a bulge of undifferentiated cells gives rise to an extremely complex structure, which has a defined asymmetrical arrangement of its skeletal elements.

The limb bud is patterned along its three axes: proximo-distal (PD), antero-posterior (AP) and dorso-ventral (DV) axis by distinct genetic mechanisms (Figure 1-A). The PD axis consists of three main skeletal domains: stylopod (humerus or femur) is the most proximal part, followed by zeugopod (radius, ulna/tibia/fibula) and the distalmost autopod (carpals, fingers/tarsals/toes) (Figure 1-A). The AP axis is established as ulna to radius and thumb to pinky. The DV axis of the limb differentiates the dorsal limb (knuckles, nails) and the ventral limb (pads, soles).

About six decades ago, experimental manipulation of chicken limb buds has led to the discovery of the two main signaling centers in limb buds: the apical ectodermal ridge (AER) and the zone of polarizing activity (ZPA). These are the main regulators of the outgrowth and patterning of the PD and the AP axis as they secrete molecules that instruct the proliferation and fate of the progenitors that form the skeletal elements. For the DV axis, dorsal and ventral ectoderm is responsible for the pattern formation (Loomis et. al., 1996).

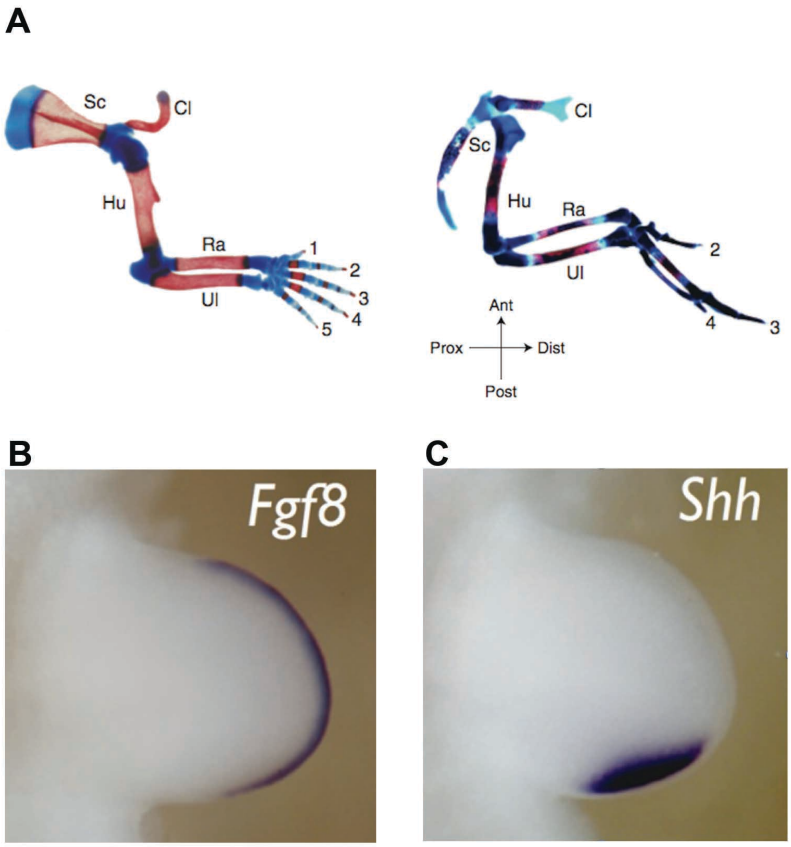

Figure 1. Vertebrate Limb bud as model system for studying organogenesis

(A) Skeletal preparation of a mouse limb at birth (left) and a chicken limb at day 15 of embryonic development (right). Bones and cartilages are stained with alizarin red and alcian blue respectively. Limb consists of Scapula (Sc), humers (Hu), radius (Ra) and ulna (ul). Digit identities are indicated with numbers. The basic bauplan is conserved among the vertebrate limbs, the orientation of proximo-distal, (prox-dist) and antero-posterior (ant-post) is indicated by the arrows (right, bottom). Visualization of signaling centers AER by *Fgf8* **(B)** and ZPA by *Shh* **(C)** in situ hybridization. (Adapted from Benazet and Zeller, 2009)

Limb bud development has attracted the attention of modelers very early on. Ede and Law addressed the expansion of limb bud cell populations in their model (Ede and Law, 1969). In different models, they compared the impact of the homogenous cell division, cell division with a gradient, and cell division with a gradient plus distalward movement of cells. By combining the first and third model they could simulate the paddle like elongated shape of the late limb bud. By altering the outgrowth and division parameters, they

simulated the *Talpid*[3] limbs, which show polydactyl by implementing higher cell division rates (Ede and Law, 1969).

3.2 Limb bud patterning

The grafting experiments and molecular and developmental genetics shed light on the key morphogens, receptors and transcription factors and what regulate vertebrate limb bud growth and patterning. Several key concepts and models were formulated to explain and understand limb bud morphogenesis, especially for each axis of the limb bud.

3.2.1 Proximo-distal (PD) axis patterning

The PD axis is mainly regulated by factors produced by the AER (Figure 1-B). Saunders observed that removal of the AER led to truncation of distal limb bud development. Removal of the AER at later stages led to the loss of more distal elements (Saunders, 1948). These observations led to the formulation of the progress-zone (PZ) model by Wolpert and colleagues (Summerbell , et. al., 1973). The progress zone was defined as the mesenchymal region underlying the AER. According to this model, cells are kept in an undifferentiated state by signals from the AER and their positional character is defined by the time they have spent in the PZ (Figure 2-A). Once cells leave the PZ, they are no longer under the influence of the AER and their identity is determined. Thus, this model suggests that PD patterning is regulated in a temporal- spatial manner. A recent study defines these factors from the AER as FGF and ectodermal WNT signals, which activate targets synergistically and keep the distal-mesenchymal cells in an undifferentiated state (ten Berge et.al., 2009).

The key signals expressed and secreted by the AER are fibroblast growth factor (*Fgf*) family members. This was discovered as the implantation of a FGF4 soaked bead rescues outgrowth and patterning following AER removal in chicken wing buds (Niswander et. al., 1993). The FGF family is composed of 18 ligands and four transmembrane tyrosine kinase receptors. FGFs bind to their receptors with the help of heparane sulfate proteogylcanes (HSPG). Ligand induced dimerization leads to the activation of an intracellular kinase domain. MAPK signaling pathways are predominantly activated upon FGF-receptor (FGFR) activation to regulate proliferation, survival, migration and differentiation (Corson et. al., 2003 , Turner and Grose , 2010). Four *Fgf* ligands are expressed by the AER: *Fgf4*, *Fgf8*, *Fgf9* and *Fgf17* (Sun et. al., 2002). *Fgf8* is the earliest activated gene and is the one required for the limb bud patterning since limbs lacking *Fgf4*, *Fgf9* and *Fgf17* develop normally (Mariani et. al., 2008). *Fgf10* is expressed in the limb bud mesenchyme and involved in the induction of *Fgf8* expression in early limb bud development (Ohuchi et. al., 1997). Embryos lacking *Fgf10* do not develop limbs and limb bud outgrowth is arrested at a very early stage (Min et. al., 1998 , Sekine et. al., 1999). *Fgf8* also up-regulates the *Fgf10* expression. Thus, the positive feedback is crucial for the limb bud initiation and outgrowth (Ohuchi et. al., 2000).

Dudley and colleagues formulated the early specification model by studying chicken limbs. They found that the loss of distal elements is rather due to cell death upon the removal of the AER (Dudley et. al., 2002). Using cell labeling and fate mapping experiments, they concluded that the limb bud

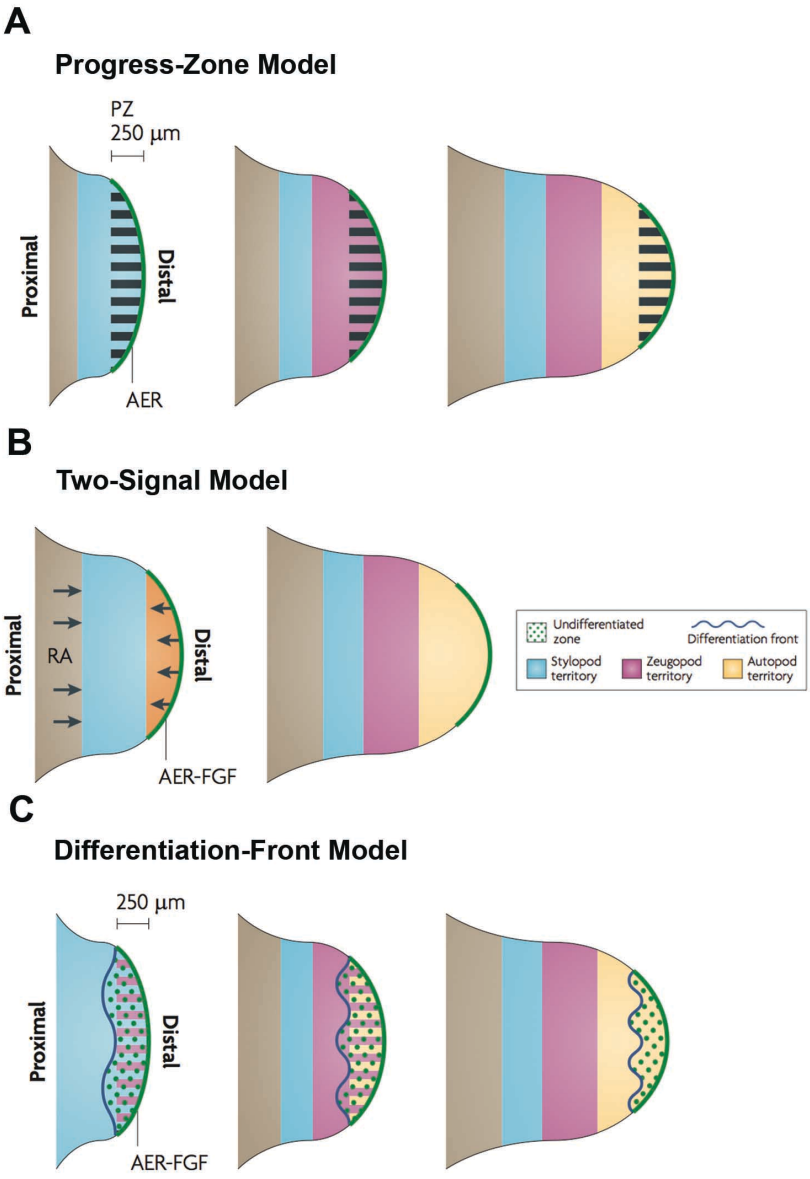

Figure 2. Models to explain PD axis outgrowth and patterning

(A) Progress-Zone Model: the cells in the distal are kept undifferentiated by the signals derived from the AER. The identity of the cells is determined according to the time they spend in the PZ and as the cells leave the progress zone their identities are determined. **(B)** Two-Signal Model: The PD identity is predominantly determined by two signals, the flank derived signal RA gives the proximal identity, whereas FGFs derived from the AER specify more distal identities. **(C)** Differentiation-Front Model: The distal limb bud mesenchyme is kept by the AER signal in undifferentiated state. As the cells leave the differentiation front, the combination of genes determine the fate of the cells. (Adapted from Zeller et. al., 2009)

cell fates are determined at a relatively early stage and that the compartments expand by proliferation. However, no specific markers that support this model have so far been identified.

The experiments performed by Mercader and colleagues have led to the two-signal model. According to this model two opposing signals, retinoic acid (RA) from the flank mesenchyme and the FGFs from the AER pattern the PD axis of the limb (Mercader, et. al., 2000, Figure 2-B). RA is a proximalizing factor and controls proximal identities by regulating Meis1 and Meis2 genes. FGF signals from the AER promote the distalization of the limb bud and regulate the expression of *Hoxa13* and *Hoxa11*. In a spatial and temporal model using realistic limb bud domains and partial differential equations (PDE's), the RA and FGF pathways and their interactions were studied (Probst et. al., 2011). RA is needed for proximal limb bud elements (Mercader et. al., 2000), where FGF signals promote distal limb bud formation (Mariani et. al., 2008). AER-FGFs that are enhanced by SHH upregulate Cyp26b1, resulting in RA clearance from the distal limb bud compartment (Probst et. al., 2011). The PDE model predicted an additional interaction, where RA inhibits FGF signals at the proximal part, which was confirmed experimentally (Probst et. al., 2011). Additionally, RA binding to its receptors limits its diffusion and receptor saturation would enable RA to form a gradient to specify the PD axis (Probst et. al., 2011). Further studies using chicken limb bud manipulation support the RA gradient-based PD axis specification (Cooper et. al., 2011, Rosello- Diez et. al., 2011). Furthermore, in mouse limbs lacking *Fgf4, 9 and 17*, the *Meis1* gene expression is expanded (Mariani et. al., 2008). However, the functional relevance of RA is still a debated topic since the detection of the

RA levels that is present in the limb is not possible and the concentrations used in the experiments might induce teratogenic effects (Kawakami et. al., 2013). Recently, some experiments have challenged the effect of RA (Zhao, et. al., 2009, Cunningham et. al., 2011). Retinaldeyde dehydrogenese-2 and -3 (Raldh-2, -3) mutant mice are deficient for RA synthesis and die around E8.5. These mutant mice have normal limbs after RA supplement to the mother mice. This indicates that RA is necessary for the limb bud induction but not for the limb patterning (Zhao et. al., 2009).

Wolpert and Tabin formulated the differentiation front model in order to reconcile AER removal experiments with these molecular data. According to this model, the distal limb bud mesenchyme is kept in an undifferentiated state by AER-FGFs. When proximal mesenchymal cells leave the proliferative zone at the proximal border, which is called the differentiation front, they will be determined and activate *Sox9* expression. Cells leaving the undifferentiated proliferating zone will be committed according to transcriptional regulators expressed at the time they are no longer under the influence of AER-*Fgf* signals (Tabin and Wolpert, 2007, Figure 2-C). Various *Hox* transcription factors such as *Hoxb11* for the zeugopod and *Hoxa13* and *Hoxd13* for the autopod elements are key regulatory factors in these processes.

In summary, various models for PD axis development and patterning have been proposed. More integrative models are needed to understand the global behavior of the key signals that regulate the patterning along this axis.

3.2.2 The spatio-temporal control of antero-posterior (AP) axis

Saunders and Gasseling performed transplantation experiments of various regions of the limb bud mesenchyme in the chicken embryos. The transplantation of cells from the posterior mesenchyme to the anterior margin resulted in mirror image duplications (Saunders and Gasseling, 1968). Thus, AP axis patterning is coordinated by a mesenchymal group of cells located in the posterior of the limb bud, termed ZPA or polarizing region (Figure 1-C).

The french flag model was proposed by Wolpert and utilized to explain how digit identities are determined by a diffusible morphogen produced by the ZPA (Wolpert , 1969). This morphogen diffuses from its source and forms a gradient. This gradient instructs digit identities according to concentration thresholds. For example, the highest concentration induces the posterior-most digit 4 in chicken wing buds, an intermediate concentration will induce the digit 3 and the lowest concentration induces digit 2 (Figure 3-A). This was evident from grafting experiments: when the ZPA of the donor chick limb bud was transplanted to the anterior of the recipient limb bud, the result was a mirror image duplication, 4-3-2-2-3-4 for the chicken limb (Figure 3-B,C). In line with the model, smaller grafts resulted in partial duplications.

Around two decades later, SHH was discovered as key morphogen produced by the ZPA. This was shown by grafting experiments using chicken fibroblasts overexpressing SHH (Riddle et. al., 1993). SHH expressing cells induced mirror image duplications when grafted into anterior limb buds (Riddle et. al., 1993). Although SHH is the major regulator of the AP patterning, there exists a pre-patterning mechanism that is active in the early limb bud stage before the activation of *Shh.*

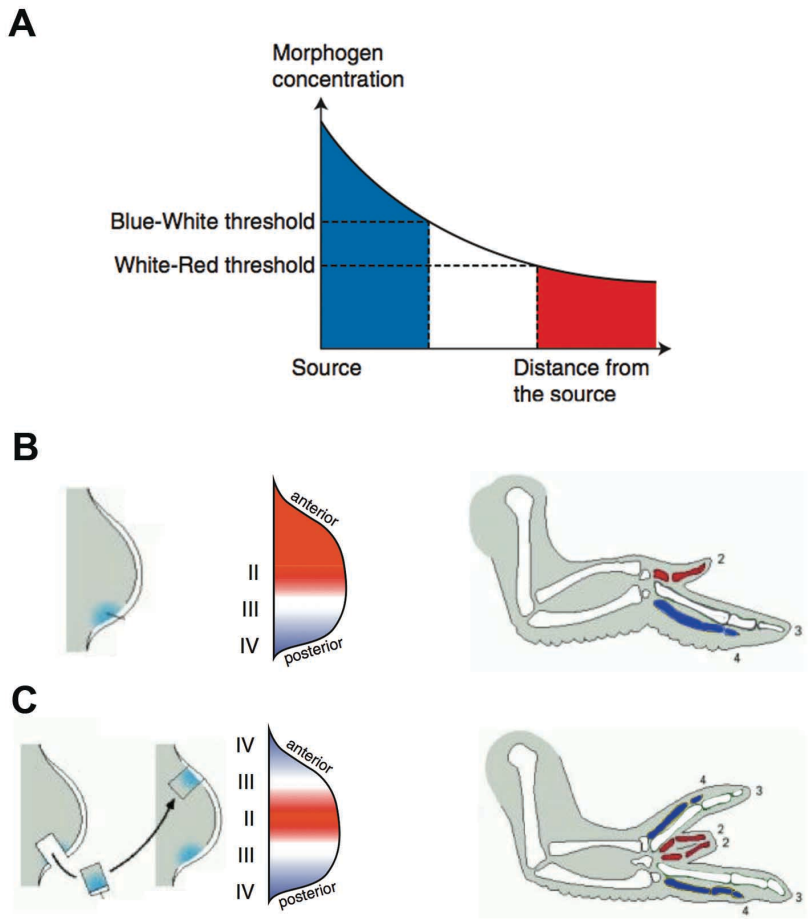

Figure 3. French flag model

(A, B) French flag model. Concentration gradient of the morphogen is formed from the source (ZPA) to the sink (anterior mesenchyme). Activity thresholds giving rise to digit identities are represented with blue, white (intermediate concentration) and red (low concentration) colors (left). The digit pattern is 2-3-4 (right). **(C)** The chicken engrafting experiments. Donor ZPA engrafted into the anterior mesenchyme of the host limb bud gives rise to mirror image duplications (left) generating a 4-3-2-2-3-4 digit pattern (right). (Adapted from Benazet and Zeller, 2012, Gilbert 10th edition and Iber and Zeller, 2012)

Upon the limb bud initiation *Gli3* and *Hand2* genes are activated in the anterior and posterior of the limb bud, respectively. In *Gli3* deficient limbs, *Hand2* expression extends to the anterior mesenchyme (teWelscher et. al., 2002a). In *Hand2* deficient limbs, *Gli3* expression is expanded to the posterior

part of the limb (teWelscher et. al., 2002a). Thus, these genes mutually antagonize each other (teWelscher et. al., 2002a, Figure 4-A). Limbs deficient for both *Hand2* and *Gli3* completely lack AP axis identities and are polydactylous (Galli et. al., 2010). Recently, a chip-seq analysis using limb buds that express endogenous HAND2 protein fused to 3xFLAG epitope identified genome-wide binding sites of this transcription factor. This analysis identified *Tbx3* as a key downstream effector of *Hand2* to restrict *Gli3* expression to the anterior of the limb bud mesenchyme (Osterwalder et. al., 2014).

In *Shh* deficient limb buds limb patterning is disrupted and only one zeugopodal element and one digit are formed (Chiang et. al., 1996, Figure 4-B). The proximal-most structures were patterned normally, suggesting *Shh* signaling does not regulate stylopod patterning (Chiang et. al., 1996). The loss of skeletal elements in the *Shh* deficient limb is caused by massive cell death in the limb bud mesenchyme (Zhu et. al., 2008). However, the removal of both *Shh* and its transcriptional mediator *Gli3* from the limb bud leads to polydactylous limbs similar to *Gli3 (Xt)* mutant limbs (teWelscher et. al., 2002b, Litingtung et. al., 2002). This suggests that the main role of SHH is to counteract the processing of GLI3 into GLI3-repressor (GLI3R), which blocks SHH targets transcriptionally in the posterior limb bud (Wang et. al., 2000, Figure 4-C). Additional studies revealed that AP axis patterning is a more dynamic and complex process. By activating the LacZ reporter using Shh-Cre-GFP mouse genetic fate mapping of the ZPA-descendant population (Shh descendants) was achieved (Harfe et. al., 2004). This analysis identified that in mouse limb buds, Shh descendants contribute to digit 5,4 and partially

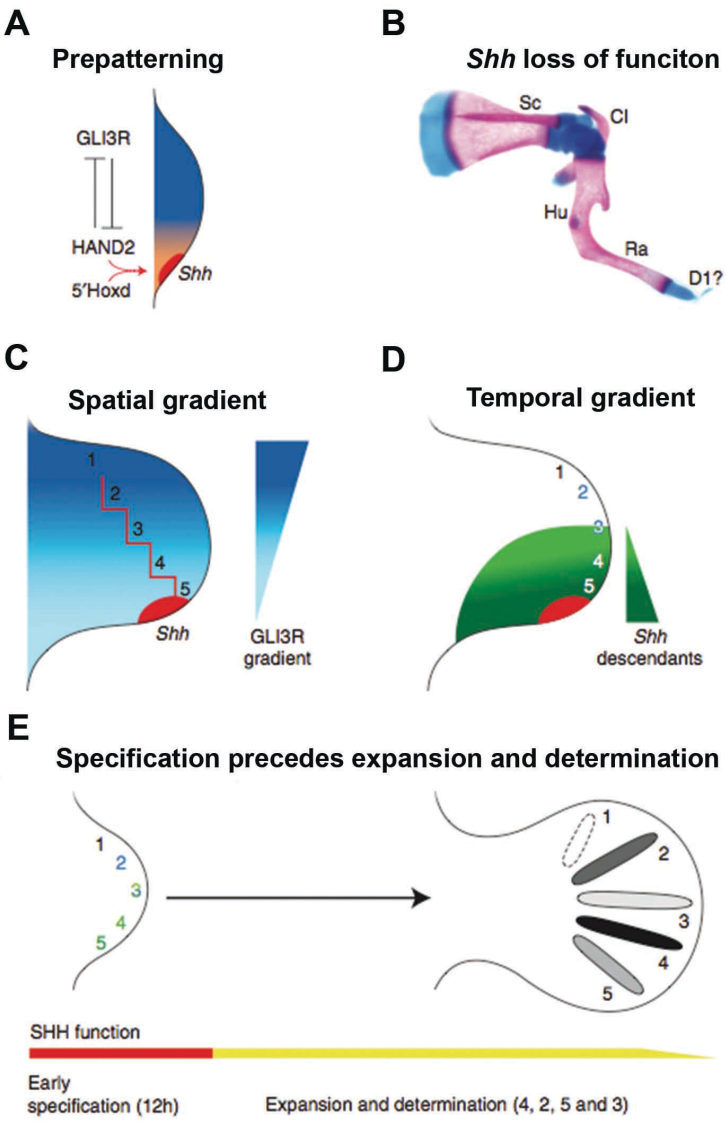

Figure 4. Patterning of the AP axis

(A) Pre-patterning of the AP axis upstream of *Shh* activity. HAND2 and GLI3 restrict and refine the boundaries of the counterpart to the posterior and anterior mesenchyme, respectively. HAND2 and 5' HOXD factors activate *Shh* expression. **(B)** Skeletal preparation of *Shh* mutant limb. Limb buds lacking *Shh* show massive malformation and possess only one zygopod element and one digit. Scapula (Sc), Clavicle (Cl), humerus (Hu), radius (Ra) and digit1 (D1) is formed **(C)** Spatial gradient model. Diffusion of SHH from the ZPA creates a GLI3R gradient across the limb bud mesenchyme by inhibiting processing of full length GLI3. Red lines indicate the activity and digit identity thresholds. **(D)** Temporal gradient model. *Shh* descendants contribute to digits 5, 4 and partially to digit 3. Digit 2 and parts of digit 3 are specified by long-range SHH signaling. Digit 1 is patterned independent of SHH signaling. **(E)** Genetic analysis by inactivating *Shh* at different developmental time points identify that patterning role of *Shh* is early and transient. Subsequently, *Shh* is required for proliferative expansion and determination of the specified digit identities. (Adapted from Benazet and Zeller, 2012)

to the digit 3 (Harfe et. al., 2004, Figure 4-D). The mesenchymal cells acquire a kinetic memory of the time and dose of exposure to SHH, which is ultimately interpreted to establish their AP identities in the limb bud.

The inactivation of a conditional *Shh* allele using Hoxb6-Cre ER^{T2} at different developmental time points showed that SHH plays a role in not only patterning but also for the survival and proliferative expansion of the limb bud mesenchymal progenitors (Zhu et. al., 2008). *Shh* has an early transient role in patterning to regulate digit identity and an extended growth promoting phase in which the digit precursors that form the digit primordial are generated (Zhu et. al., 2008, Figure 4-E).

In summary, AP axis patterning is regulated first by the pre-patterning mechanism involving *Hand2* and *Gli3* and then by SHH signaling in a spatially and temporally coordinated manner. The AP and PD patterning are controlled by strictly regulated, complex mechanisms.

3.2.3 The epithelial-mesenchymal SHH/GREM1/AER-FGF signaling feedback loop

Already the early experiments by Zwilling suggested that the two signaling centers might somehow be linked. ZPA grafts gave rise to digit duplications only if engrafted close to the AER (Zwilling et. al., 1956). After the identification of the genes produced in the AER and ZPA, it was found that AER-*Fgf* expression requires SHH signaling and in turn *Shh* expression depends on AER-FGF signaling (Laufer et. al., 1994, Niswander et. al., 1993). The secreted BMP antagonist GREMLIN1 (GREM1) was identified as a key mesenchymal component mediating these so-called epithelial-

mesenchymal (e-m) feedback loop (Zuniga et. al., 1999, Khokha et. al., 2003, Michos et. al., 2004). GREM1 is required to protect the AER-FGFs from BMP factors by antagonizing them and to establish the SHH/GREM1/AER-FGF e-m feedback signaling loop. In *Grem1* deficient limb buds, the e-m feedback loop is disrupted and the expansion and specification of distal limb bud elements are aberrant (Khoka et. al., 2003, Michos et. al., 2004). By combining mouse genetics and mathematical modeling, it was shown that the e-m feedback loop is initiated by BMP4 and than propagated by SHH through differential transcriptional activity (Benazet et. al., 2009, Figure 5). BMP4 is required for the establishment of the AER but is an inhibitor of the AER-FGFs. During the initial high BMP4 activity, BMP4 activates its antagonist *Grem1* in a fast feedback loop, which rapidly reduces the BMP activity thereby enabling the establishment of SHH/GREM1/AER-FGF feedback loop (Benazet. et. al., 2009, Figure 5). The termination of the system could be achieved by the expanding population of SHH descendants and the widening gap between *Shh* and *Grem1* expression domains (Scherz et. al., 2004). Additionally, a late negative feedback loop from AER-FGFs to *Grem1* terminates the SHH/GREM1/FGF feedback system (Verheyden and Sun, 2008). Thus, interconnected feedback loops define a self-regulatory signaling system that differentially impacts on *Grem1* expression (Benazet and Zeller, 2009).

Since the *Grem1* is the key regulator of the e-m feedback loop, the understanding of its expression is of major importance. *Grem1* expression is highly dynamic and regulated by several pathways. In early limb buds BMP4 activates *Grem1* expression in a fast feedback loop, whereas *Shh* enhances

Grem1 expression via the e-m feedback loop (Panman et. al., 2006, Benazet et. al., 2009). During the hand plate formation and digit ray condensations, GLI3 was shown to inhibit *Grem1* in the anterior parts of the limb, which results in limb bud mesenchymal progenitors to exit from the proliferative cell cycle phase and to initiate the differentiation (Lopez-Rios et. al., 2012). Furthermore the AER-FGF signaling inhibits *Grem1* in advanced limb buds, which results in termination of the e-m feedback signaling system (Verheyden and Sun, 2008). *HoxA* and *HoxD* genes were also shown to regulate the anterior expansion of the *Grem1* expression (Sheth et. al., 2014).

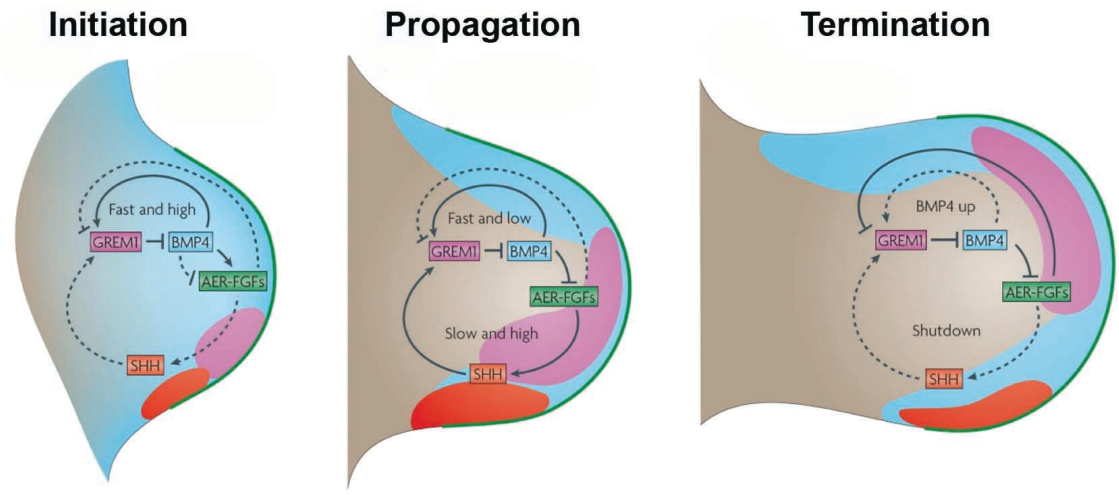

Figure 5. SHH/GREM1/AER-FGF feedback loop

The interlinked signaling feedback loops show self-regulatory properties. During the initiation phase, high *Bmp4* levels are required for the establishment of the AER and activation of *Grem1*. During the propagation phase BMPs inhibit the FGF signals and GREMLIN1 antagonizes the BMPs and protect the AER. FGF signals can regulate the PD outgrowth and *Shh* activation. In the termination phase, the *Shh* expressing domain is wide apart from *Grem1* and *AER-Fgf's* have an inhibitory effect on *Grem1* expression, which leads to termination of the e-m feedback loop. (Adapted from Zeller et. al., 2009)

Several cis-regulatory modules (CRM) have been identified that regulate the *Grem1* expression. A 70 kilobase (kb) CRM was discovered to be critical for the expression of *Grem1* in mouse limb buds (Zuniga et. al., 2004). This CRM is localized between exons 19-23 of the neighboring *Formin1 (Fmn1)* gene (Zuniga et. al., 2004). Within this 70 kb CRM, a highly conserved Gremlin regulatory sequence 1 (GRS1) leads to a comparable expression pattern to Grem1-LacZ (Zuniga et. al., 2012). A 438-bp Gli3-binding region that is located >100kb downstream of the *Grem1* locus can give rise to similar expression pattern to endogenous *Grem1 expression* (Vokes et.al., 2008). This CRM is called Gli responsive element 1 (GRE1). Transgenic mice expressing this element were shown to respond to *Shh* signaling (Li et. al., 2014). However, the removal of this element showed that it is not essential for the *Grem1* expression and suggested redundancy among the CRMs regulating *Grem1* in the limb bud (Li et. al., 2014).

3.2.4 Dorso-ventral (DV) limb axis patterning

The dorsal-ventral polarity of the limb bud is determined by the limb ectoderm. Classical analysis showed that rotation of the limb ectoderm with respect to the mesenchymal core results in a partial reversal of the DV axis (MacCabe et. al., 1974). One signal that appears important in specifying DV polarity is WNT7A. *Wnt7a* is expressed in the dorsal ectoderm in chicken and mouse limb buds (Parr et. al., 1995). Genetic inactivation of *Wnt7a* results in ventralized limbs, i.e bilateral sole pads, which show that *Wnt7a* induces dorsal mesenchymal identities (Parr et. al., 1995). *Engrailed-1* is expressed in the ventral part of the ectoderm and restricts the expression of *Wnt7a* to the

dorsal ectoderm (Loomis et. al.1998). *Engrailed-1* deficient limb buds lose DV polarity and develop secondary AERs and ectopic ventral digits (Loomis et. al., 1998).

The patterning of the limb bud along the three axes is strictly coupled with growth. Most key genes that regulate the patterning along the limb bud axes also regulate the limb bud proliferation and outgrowth in order to expand the mesenchymal cell pool to form functional digits in later stages. How this is accomplished in the limb bud is the subject of the following section.

3.4 Proliferation and outgrowth of the limb bud

Compared to the gene functions in patterning, the roles in controlling cell proliferation during the limb bud development is less understood. Initial analyses cell proliferation were performed using chick limbs by characterizing the mitotic index in sections by hematoxylin and eosin staining. The mitotic index was quantified to be 10 % in the early stage chicken limb buds and was shown to gradually drop during the patterning phase (Hornbuch and Wolpert, 1970). Cell density in the chicken limb buds was revealed to increase over the developmental stages and to correlate with the mitotic indexes (Summerbell and Wolpert, 1972). Fernandez-Teran and colleagues measured proliferation and apoptosis patterns in the chick and mouse limb buds by pH3 and TUNEL staining. Limb bud cells display a rather homogenous pattern of proliferation and very dynamic apoptosis patterns that are related to the formation of different skeletal elements of the stylopod, zeugopod and autopod (Fernandez -Teran and Ros, 2006).

Several signaling pathways that regulate the proliferation and outgrowth of limb buds have been identified. Ectodermal WNT signaling controls proliferation by regulating *N-myc* (tenBerge et. al., 2008). N-MYC is member of MYC family of proteins that mediate cell cycle entry (Trumpp et. al., 2001) and was shown to regulate the cell cycle in mouse limb buds (Ota et. al., 2007). Furthermore, WNT inhibits differentiation by blocking *Sox9* expression (tenBerge et. al., 2008). FGF8 produced by the AER has a synergistic effect on both functions of WNT signaling (tenBerge et. al., 2008). SHH signaling is coupled with growth to provide and digit specification (Towers et. al., 2009). Cyclopamine mediated inhibition of SHH signaling disrupts cell cycle and proliferative expansion of mesenchymal progenitors and results in the loss of posterior digit identities (Towers et. al., 2009).

Besides the progenitor proliferation of the cells, active and biased movements of mesenchymal cells are of great importance for normal limb bud outgrowth and patterning (Gros et. al., 2010). Fluorescent labeling of the early chicken limb buds allowed Vargesson and colleagues to produce fate maps of the limb bud mesenchyme and AER (Vargesson et. al., 1997). The fate maps showed that most of the wing skeleton arose from the posterior half of the wing bud and only the sub-apical mesenchyme gives rise to digits. Also the AER extends anteriorly, but not in concert with the mesenchyme, which indicated that mesenchymal cells might be actively moving or displaced.

Recently, combination of GFP electroporated chicken limb bud slices culture with live two-photon microscopy allowed the quantification of the velocity and cell division planes of the mesenchymal progenitors (Gros et. al., 2010, Figure 6-A). This analysis showed that distal cells have an increased

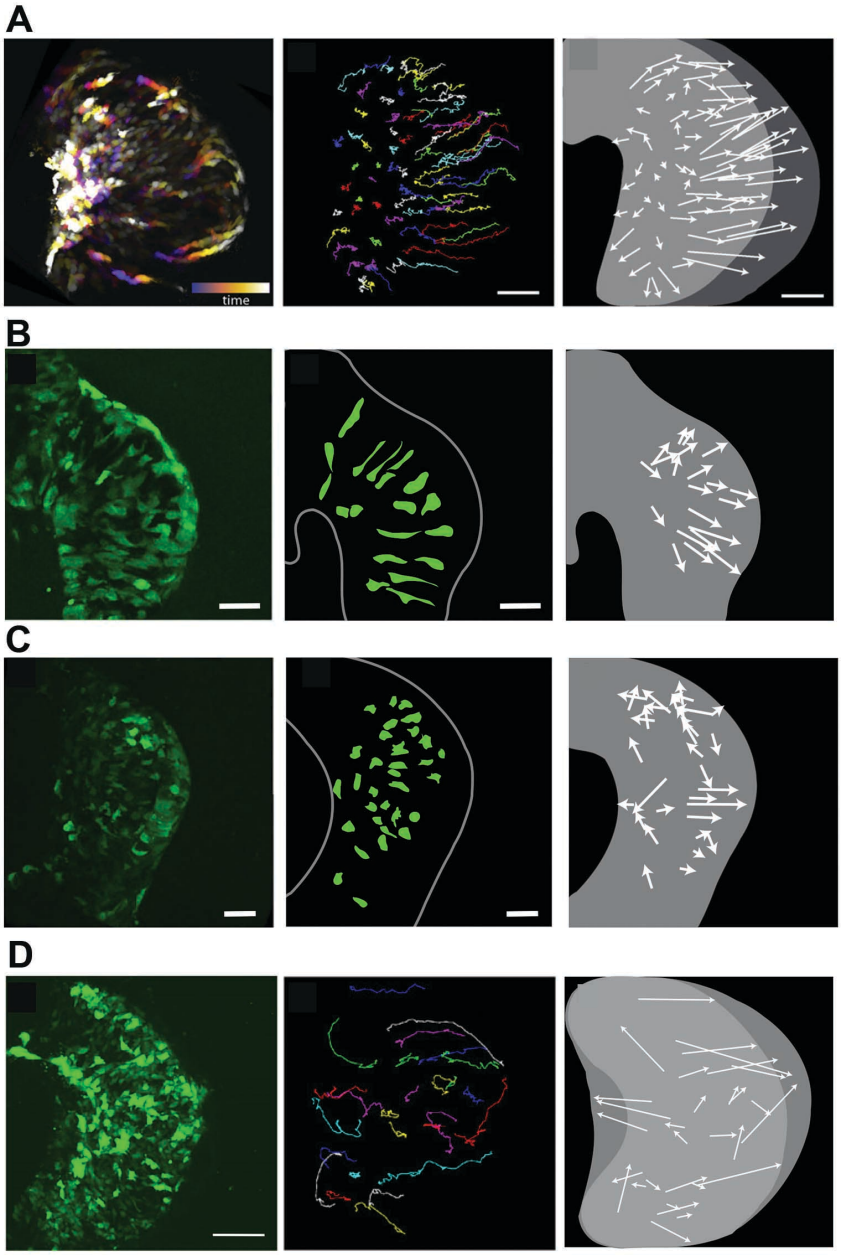

Figure 6. Live imaging of limb mesenchymal cell movements and proliferation

(A) Projection of 15 h time series view of cell movements of GFP electroporated chick embryo (left). Cell tracks of time-lapse experiment (middle). Schematic representing of cell movement and direction (right). **(B)** Transverse sections of WT; $XGFP^{+/-}$ and **(C)** $Wnt5a^{-/-}$; $XGFP^{+/-}$ mouse embryo displaying morphologies of GFP expressing cells (left) and schematics representing the cell shape (middle). Net cell movements measured from time-lapse experiments are shown with arrows (right). **(D)** Chick limb bud electroporated with MEK1 constitutively active construct to mimic FGF activity at higher levels. Cell tracks of time-lapse experiment (middle). Schematic representing of cell movement and direction (right). The cells have shown drastically increased distal ward movement. (Adapted from Gros et. al., 2010)

velocity (3.6 μm/h) compared to central (2 μm/h) and proximal cells (1.2 μm/h). The cells exhibit oriented cell division in the direction of the AER. In the mouse, similar velocity and cell behaviors were observed. Since WNT/planar cell polarity pathways have been shown to regulate both the oriented movement and cell division in developing embryos, this pathway is a candidate regulator of directed cell movement. *Wnt5a* is expressed with a proximal-to-distal bias in the mesenchyme and ectoderm of mouse and chicken limb buds and *Wnt5a* deficient mice show malformed skeletal elements with shortened limbs. Live imaging suggests that there is an around 40% decrease in velocity in Wnt5a deficient limb buds (3.6 μm/h) in comparison to WT controls (6 μm/h). In the chicken limb buds, grafting of *Wnt5a* expressing cells in the center of the limb bud induced a reversal of the cell movements. Thus, the WNT5A pathway controls both cell movement and orientation of the mesenchymal progenitors in the limb bud (Figure 6-B, C). Assessing the cell morphologies, Gros and colleagues define distal, central, dorsal and ventral cell orientation bias. Additionally, the effect of the FGF pathway was investigated since FGF-4 was suggested to be a chemo-attractant in limb buds (Li and Muneoka, 1999). A dominant-negative form of the FGF/ERK pathway signal transducer MEK1 and FGF inhibitor SU5402 were used to establish that FGF/ERK signaling promotes cell movement but not orientation of the cell division (Gros et. al., 2010, Figure 6-D).

By combining 3-D imaging and modeling, the hypothesis that “Isotropic cell proliferation with higher proliferation rates at the distal end can explain limb bud outgrowth” was challenged (Boehm et. al., 2010). Boehm and colleagues extracted the shapes of an E11 and E11.25 mouse and performed simulations

for the proliferation events for 6h. Double labeling experiments using IddU and BrdU were used to determine the cell cycle times in the neighboring sections (Figure 7-A). The cell proliferation rate measurements showed higher rates in the distal mesenchyme. However, using cell proliferation parameters, the simulated E11.25 limb was massively different from the real limb bud shape (Figure 7-B). Using parameter optimization with the initial and final shape, they could explore the growth dynamics and conclude that directional cell movement is needed for limb bud elongation (Figure 7-C). Thus, in agreement with Gros and colleagues, it was found that directional cell activities rather than a PD gradient of cell proliferation rates controls limb elongation (Boehm et. al., 2010).

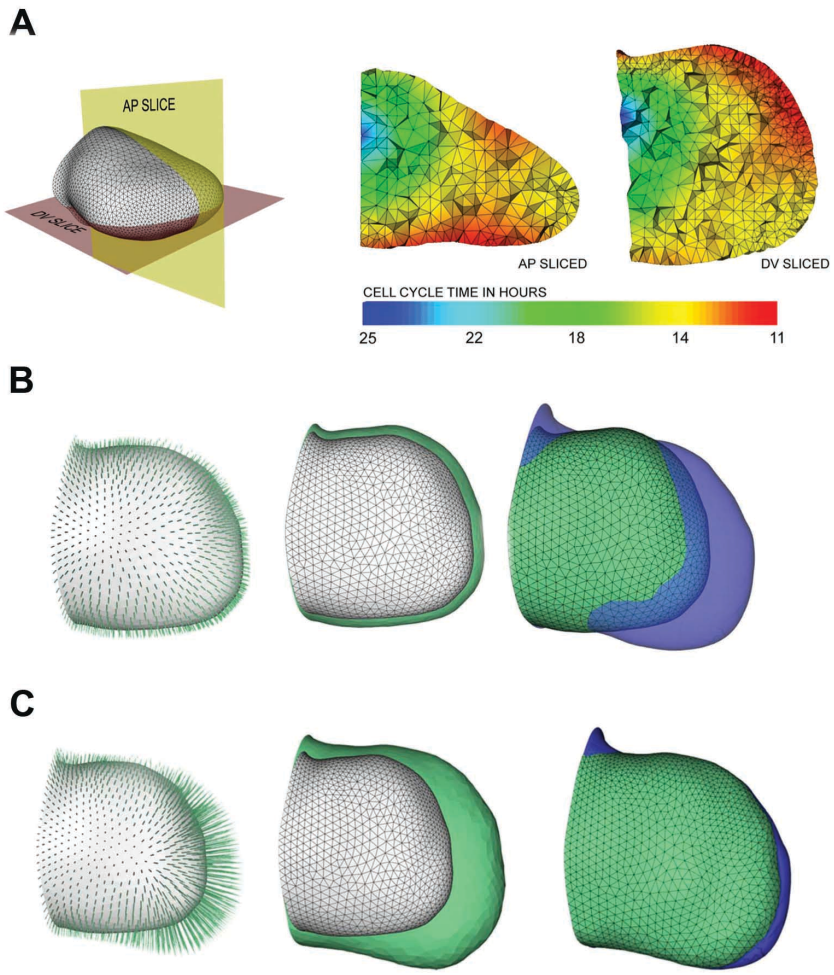

Figure 7. 3-D FEM model of limb bud proliferation

(A) Cell Cycle times measured from double-labeling experiments are implemented in a 3-D model. **(B)** The proliferation rates converted into a source term in a Navier-Stokes equation. By simulating the growth rate, the initial limb at E11.0 (gray) fails to give rise to the same growth pattern of the real E11.25 (blue) limb bud. Simulated shape is much smaller (green). **(C)** Parameter optimization suggests that directed cell behaviors (proliferation, migration) are needed for simulation of correct shape. Initial embryo at E11.0 (gray), simulated limb bud at E11.25 (green), real limb bud at E11.25 (blue). (Adapted from Boehm et. al., 2010)

3.5 Differentiation and formation of digit identities

Limb bud mesenchymal progenitors proliferate rapidly and are committed as either chondrocyte progenitors or other cell types. The committed progenitors from densely packed condensations and differentiate into chondrocytes (Akiyama et. al., 2002). The chondrocytes produce an extracellular matrix (ECM) that are cartilage specific and contains aggrecan and collagen type II. Combining live imaging with high density mesenchymal cell cultures, BMP signaling was shown as critical regulator for cell compaction during mesenchymal condensations, whereas *Sox9* is required for the maintenance of cell morphology to promote cartilage differentiation (Barna and Niswander, 2007). *Sox9* is the earliest marker that identifies the chondroprogenitors and differentiating chondrocytes (Ng et. al., 1997). The *Sox9* heterozygous mice die at postnatal day 20 (P20) with hypoplasia of all ossified skeletal elements. In embryonic limbs of *Sox9* heterozygous mice the mesenchymal condensations and precartilaginous mesenchyme show reduced alcian blue staining (Bi et. el., 2001). This result is consistent with human campomelic dysplasia disease caused by heterozygous mutations in the human *Sox9* gene (Akiyama et. al., 2004). Deletion of *Sox9* from limb bud mesenchyme leads to complete absence of limb cartilage and bone (Akiyama

et. al, 2002). The *Sox9* deficient limb buds showed an intact AER and normal paddle shape at E 11.5 suggesting *Sox9* is not needed for limb bud outgrowth. The transcription factor Runx2, which is required for osteoblast differentiation, is not detected in the mutant limbs, suggesting that *Sox9* is required for *Runx2* expression (Akiyama et. al., 2002). The limb buds that are deficient for *Sox9* show massive cell death, indicating that Sox9 is required for cell survival (Akiyama et. al., 2002).

Several major regulators of Sox9 expression in the limb were described (Hill et. al., 2005, Akiyama et. al., 2004, Benazet et. al., 2012). The WNT signaling mediated by *β-Catenin* is a major negative regulator of *Sox9* and *Sox9* represses *β-Catenin* mediated transcriptional activity (Hill et. al., 2005, Akiyama et. al., 2004). The WNT signals inhibit *Sox9* expression and confine it to the core of the limb bud (Akiyama, 2004, Hill, 2005). WNTs also regulate the delicate balance between the *Runx2* positive osteoblasts by limiting the *Sox9* positive chondroblasts (Hill et. al., 2005). Inactivation of both BMP receptors BMPR1a and BMPR1b results in loss *Sox9* expression (Yoon et. al., 2005). Thus, BMPs are required for chondrocyte proliferation, survival and differentiation (Yoon et. al., 2005).

How digit numbers and identities are determined remained a main question for several decades. The deletion of *Smad4*, an essential mediator of the TGF-β/BMP pathways from the limb bud mesenchyme leads to the loss of hand plate elements, where early Sox9 distribution remained similar (Benazet et. al., 2012). *Smad4* deficiency blocked the condensations of Sox9 positive progenitors. Thus *Smad4* is needed for the formation of digit ray primordia and chondrogenic differentiation (Benazet et. al., 2012).

Alan Turing proposed a system of two components, so called morphogens, which can interact with each other and diffuse through tissue. A homogenous system with noisy initial conditions may develop patterns or structures due to a diffusion driven instability (Turing , 1952, Figure 8-D).

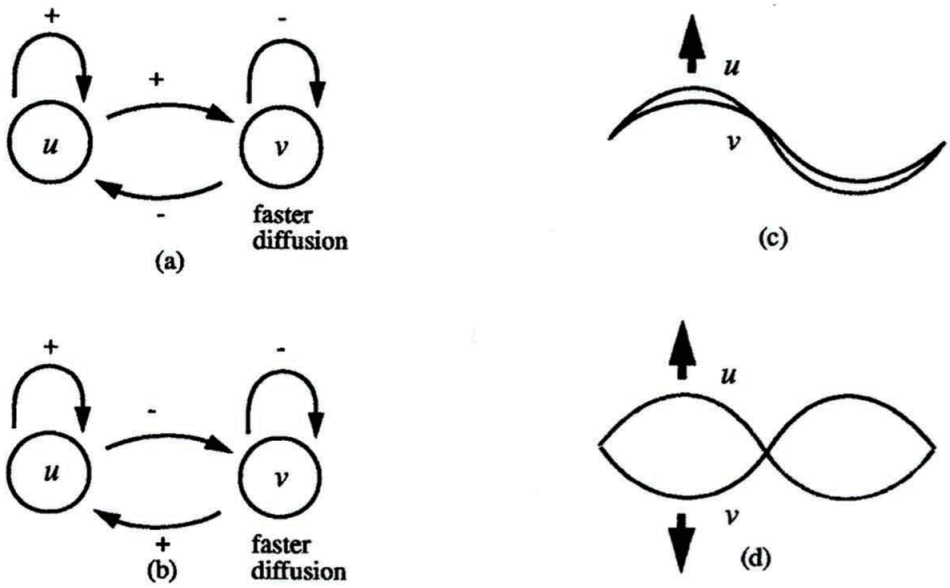

Figure 8. Turing pattern

Schematic illustrations of two different cases of Turing pattern. Self-activating u also activates also v, which in turn inhibits both (a). The resulting pattern is shown in (c). In the case of (b), self-activating u inhibits v but itself is activated by v. The resulting pattern is shown in (d). (Modified from Murray Mathematical Biology II.)

According to this model, networks of molecules with positive and negative feedback in production and consumption of the molecules and different diffusion rates leads to non-uniform pattern formation (Newman and Bhat, 2008). The Turing model is based on a reaction-diffusion (RD) system and many biological systems were suggested to be explicable with a Turing model, including the pigmentation of animal skin (Kondo and Asal, 1995),

feather germs (Prum and Williamson et. al, 2002), hair follicles (Sick et. al., 2006) and teeth (Salazar -Cuidad and Jernvall, 2002). Turing type models were repeatedly used to explain digit formation (Newman and Frisch, 1979, Sheth et. al., 2012, Badugu et. al., 2012, Raspopovic et. al., 2014). Newman and Frisch simulated digit patterning in chicken limbs (Newman and Frisch, 1979). The same group suggested TGF-ß2 to be the Turing molecule four decades later and performed simulations on growing limb bud domains (Hentschel et. al, 2004). By simulating a network consisting of BMP4 and BMP receptor as parts of a Schnakenberg-type Turing model, digit patterns of wild type and several mutants can be reproduced (Badugu et. al., 2012). These simulations were performed in realistic limb bud shapes that were extracted from 2-D limb bud images. FGFs were modulators of this core Turing model (Badugu et. al., 2012). The model was sensitive to the domain size and enlarged domains cause an increased digit number in concordance with the biological data. Sheth and collegues removed distal Hox genes (Hoxa13, Hoxd11-Hoxd13) from the *Gli3* mutant background, which caused more severe polydactyly (Sheth et. al., 2012). They proposed a Turing network of unknown components, where Hox and Fgf genes are modulators of the system (Sheth et. al., 2012). In Raspopovich et. al., a Turing network consisting of Bmp-Sox9-Wnt core elements was simulated in growing domains to explain digit formation. Inhibitors of BMP and WNT pathways were simulated and compared to the simulations (Raspopovich et. al., 2014).

Taking together, the gene regulatory networks governing limb bud morphogenesis are well studied and characterized extensively using mouse mutants at the morphogen, transcription factor and receptor level. Next step is

the integration of the available data at gene interaction and quantitative level to gain better understanding how limb bud patterning regulated. Systems biology approaches that combine molecular and genetic methods with mathematical modeling and imaging are therefore of great importance for the future experimental advances.

4. AIMS OF THE THESIS

The knowledge about the regulation of limb bud shape and size is sparse and quantitative data is missing to evaluate models and hypotheses. We sought to create quantitative data sets of limb bud development from E9 (22 S) to E12 (54 S), which covers developmental period for the initiation of limb bud outgrowth to digit formation. To reach this goal, I used inducible limb bud specific GFP expression in combination with FACS analysis to determine the number of mesenchymal cells. Subsequently, I performed an OPT analysis to determine the volume and length of all axes of mouse the limb buds. This quantitative analysis evidenced two phases of limb bud outgrowth. Next, I used BrdU assay for the characterization of the proliferation dynamics of the differentiating and non-differentiating cells at the stages adjacent to the two phases and evaluated the impact of the osteo-chondro progenitors for the proliferation regulation.

Limb bud development had been modeled intensely, but mostly using idealized static domains. However, the size of the limb bud changes almost an order of magnitude from its onset until the digit identities are outlined. Therefore, I created an *in silico* model and performed simulations in real geometries using selected gene expression domains as markers of signaling centers to gain an integrative understanding of limb bud development. This was only possible using an interdisciplinary approach that combines the experimental and genetics expertise from Prof. Zeller's group with the know-how of mathematical simulations from Prof. Iber's group. To create *in silico* geometries in real size and shape for the simulations, I established optical projection tomography (OPT) imaging in the laboratory and optimized image

acquisition and processing. This included reduction of noise, increasing zoom and resolution by single limb bud scanning with a rotation axis along the PD limb axis. We proceeded with geometry extraction and growth calculations to produce 2-D limb bud geometries with growth dynamics. Using these limb bud shapes, we simulated molecular network interactions that govern initiation, propagation and termination of limb bud development. The model can explain the gene expression alterations in a significant fraction of limb bud mutants. Based on the OPT analysis and modeling, I predicted the *Grem1* expression might be controlled by the WNT pathway. I verified this prediction using genetic analysis and inhibition of the WNT pathway in limb bud cultures.

5. MATERIALS AND METHODS

5.1 Mouse husbandry and experiments with mouse embryos

5.1.1 Ethics statement

The mouse experiments were approved by the legally required regional commission in strict accordance with Swiss law. All studies were classified as grade zero, implying minimal suffering of animals.

5.1.2 Mouse strains and embryo isolation

Wild type (WT) embryos for OPT analysis were collected by crossing C57BL/6 males with NMRI females. For cell-counting experiments Prx-Cre mice (Logan et. al., 2002) were crossed with βactin-GFP mice (Jägle et. al., 2007) to permit fluorescence-activated cell sorting (FACS) of limb bud mesenchymal cells. Prx-Cre mice was crossed with R26-LacZ (Soriano, 1999) for the OPT analysis. Conditional inactivation of the WNT pathway was achieved by crossing the Prx-Cre mice with β-Catenin$^{fl/fl}$ mice (Brault et. al., 2001). For embryo isolation, the pregnant females were sacrificed using CO_2 and the abdomen was sterilized using 70% EtOH. The uterine horns containing the embryos were dissected into ice-cold Phosphate Buffered Saline (PBS). Dissections were performed as rapid as possible and embryos were staged according to somite numbers. Embryos were fixed in 4% Paraformaldehyde (PFA, Sigma) overnight at 4 °C. Following this, the embryos were washed three times in PBS and dehydrated in a series of increasing methanol concentrations (25% to 100%) in PBS containing 1 % Tween-20 (PBT).

5.2 Egg incubation and chicken embryo isolation

Fertilized chicken eggs were bought from Animalco AG (Staufen, Switzerland). The eggs were incubated at 37 °C with 50 % humidity. The upper part was marked for the air bubble and the eggs were turned on a daily basis to avoid attachment of the embryo to the shell. The developmental stage of the embryos was monitored by opening a window on the shell. In case of a too early stage, the eggs were incubated longer. For isolation, the blood vessels were removed using surgical scissors and the embryo was lifted off in a spoon and placed in PBS until fixation. Embryos were fixed in 4% PFA (Sigma) overnight at 4 °C. Following this, the embryos were washed three times in PBS and dehydrated in a series of increasing methanol concentrations (25% to 100%) in PBS containing 1 % Tween-20 (PBT).

5.3 Histology techniques

5.3.1 Cryo-sectioning of limb buds

The embryos were fixed with 4% PFA on ice for 45 min and washed three times with PBS. A 10% sucrose gradient was performed overnight at 4°C. The next day, the embryos were incubated 20% and following 30% sucrose until they were equilibriated, i.e. sank in the solution. The limb buds were embedded in a 1:1 mix of 30% sucrose and optical cutting temperature compound (OCT, Tissue-Tek®) and stored at -80°C. The cryo-blocks were sectioned using a cryostat (Leica) at 7-15 µm. The slides with sections were stored at -80°C until use.

5.3.2 Immunofluorescence using limb bud sections

Slides were removed from the -80 °C freezer and dried at room temperature (RT) for 15 min. Following this, the slides were washed three times in PBS and permeabilized in 0.2% TritonX-100 in PBS at RT for 20 min and again washed in PBS three times. The slides were labeled using a thick-inked pen (Dakopen, Dako) and blocked using 1% BSA for 1 h at RT. The primary antibody diluted in the blocking solution was added to the slides and incubated at 4°C overnight. The slides were washed three times for 10 min in PBS and once with PBT for 5 min. The secondary antibody diluted in the 1 % BSA was added and incubated for 1 h at RT. Afterwards, the slides were washed three times with PBS at RT and stained with 5 µg/ml Hoechst 33342 in PBS for 10 min at RT. The slides were transferred to a glass tray and washed thoroughly using PBS three times for 5 min. After the last wash, the remaining PBS was removed and sections were covered using mowiol and a cover slip. After that they were kept for 2 h in the dark at RT. The slides were stored at 4°C in the dark for long-term storage.

5.4 Limb bud cultures

Embryos were carefully dissected in tissue culture grade PBS at RT and placed in a pre-equilibrated Limb Culture Medium (see below) until processing. ∆-Grids (EMBL Heidelberg) are placed in 24 well plates and 2 ml of LCM was pipetted on the grids without generating air bubbles. Hind limb buds and inner organs were removed from the embryos using sharp forceps. The trunks with forelimb buds were pinned on the grids using steel insect pins (FST, Heidelberg, Germany). Inhibitors were added at the desired

concentration and 1 ml of the medium was replaced in the 24-well plate. Following gentle pipetting to mix the medium with the inhibitor, the surplus medium was removed such that the trunk was just covered with medium. The trunks were incubated at 37°C and in 6 % CO_2. For grafts of beads or cell aggregates were inserted in limb buds following generation of a slit using tungsten needles. The exact position of each graft was recorded in the protocol book. The trunks with grafts were incubated as described above. Following incubation, the trunks were washed three times in PBS and fixed in 4 % PFA at 4°C overnight, then the limbs were washed three times in PBT and dehydrated (see 5.1.2, 5.2). The trunks were stored at -20°C until use.

Limb culture medium:

DMEM High Glucose (Gibco), 1 % L-glutamine (Gibco), 0.5% Penicilin-Streptomycin (Gibco), 1% non-essential amino acids (Gibco), 1% sodium pyruvate (Gibco), 1% D-glucose (45% Solution, Sigma), 0.1% L-ascorbic acid (200 mg/ml, freshly made and 0.22 µm-sterile filtered, Sigma), 1% lactic acid (20 mg/ml, freshly made and 0.22 µm-sterile filtered, Sigma), 0.1% D-biotin/Vitamin B12 (0.2 mg/ml D-Biotin and 40 µg/ml Vitamin B12 in DMEM, 0.22 µm-sterile filtered and stock solution kept at -20°C, Sigma), 0.1% PABA (2 mg/ml in PBS, 0.22 µm-sterile filtered and stock solution kept at -20°C, Sigma).

Inhibitors used:

Inhibitor	Concentration (μM)
IWP_2 (Tocris)	2
SU5402 (Santa Cruz)	10
LDN_2 (Sigma)	4

5.5 Determination of limb bud cell numbers using FACS and fluorescent beads

For cell counting experiments, the Prx-Cre$^{+/Cre}$; βactin$^{+/GFP}$ embryos were inspected under UV light using a FITC filter to identify embryos with green fluorescent limbs. The embryos were kept in cold PBS and, upon dissection, split to get individual limbs, also keeping flanking trunk parts. The limbs were dissociated in 1x Hanks' Balanced Salt Solution (HBSS) containing 1 mg/ml collagenase D (Roche) and 50μg/ml DNase I (Roche) at 37 °C in FACS tubes to avoid loss of cells (Figure 1-A). Limb buds were pipetted up and down every 10 min to prepare a single cell suspension. Biosphere tips (Sarstedt) were used to avoid attachment of cells to pipet tips. The total duration of the dissociation procedure was 20 min for early limb bud stages and 25-30 min for stages older than E11. Single cell suspensions were kept on ice until the next treatment step. Polystyrene fluorescent beads (TruCount^{TM}, BD Biosciences) were suspended in 1 ml PBS and counted for 1 min at the highest strength of the "Low" flow channel of the FACS Fortessa and was detectable in the green and red channels (BD Biosciences, Figure 1-B). The total bead count was between 2200 to 2300 (Figure 1-C). The TruCount^{TM} tubes contained 48809 beads. For an accurate cell number determination, the

flow of the beads and cells has to be constant (Figure 1-D,E). The counted volume was calculated using the following formula:

$$V_{count} = (\text{Bead Count} / 48809) \times 1000 \quad (1)$$

For each individual limb bud cells were counted for 1 min ($CellCount_{Raw}$) and the total number of cells (C_{Limb}) was calculated as following:

$$C_{Limb} = V_{count} = (CellCount_{Raw} / V_{Count}) \times 2000 \quad (2)$$

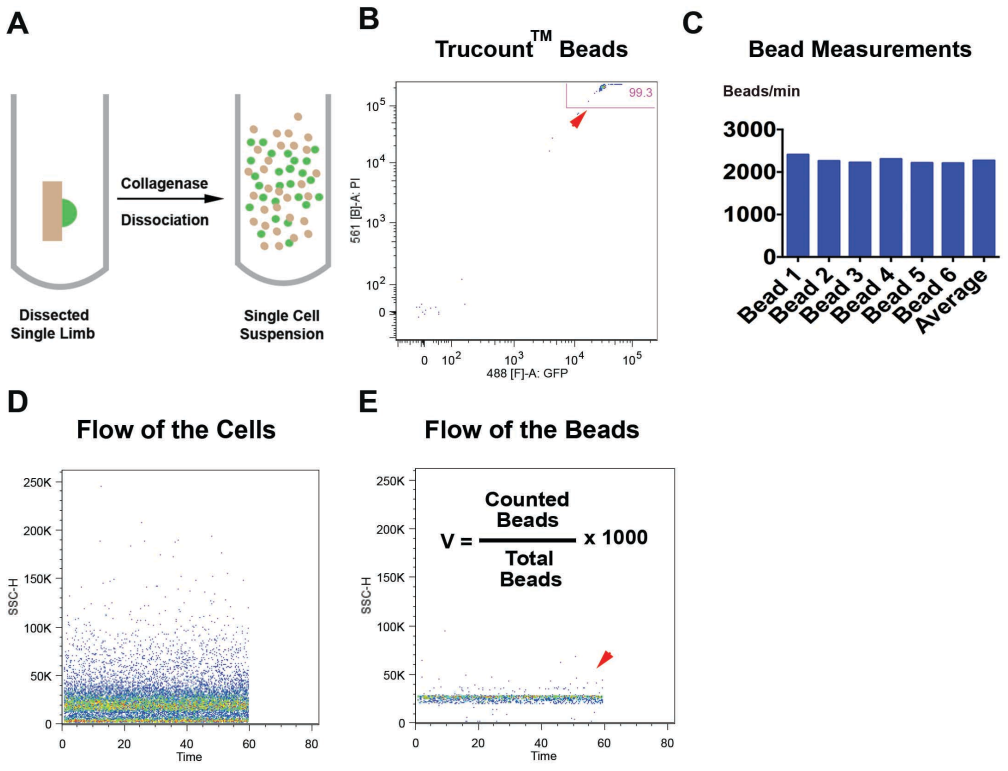

Figure 1. The method of quantification of limb bud mesenchymal cells

(A) Dissected single limb buds are dissociated mildly in a collagenase buffer directly in the FACS tubes to get a single cell suspension. **(B)** BD Trucount™ Beads suspended in 1 ml PBS fluoresce strongly (red arrowhead, top-left). (**C)** Six replicates of bead measurements and the average value are shown in the graph (bottom-right). The variation among each measurement is around 3 %. **(D)** Limb bud cells showed constant flow during the measurements. **(E)** The beads also show constant flow during 1 min measurement time (red arrow-head, top right panel) and are used to calibrate the counting volume with the formula indicated.

5.6 BrdU labeling of limb bud cells

1 mg of BrdU was injected into pregnant females 4h and 2h prior to embryo dissection. The embryos were dissected as described above and used either for FACS or IF analysis (see below).

5.6.1 Analysis of cell proliferation by FACS analysis using BrdU labeling

The forelimbs of the litters were dissected such as to encompass the Prx-Cre expression domain. Around 20 dissected forelimbs were pooled into a single FACS-tube for collagenase-dissociation into single cell suspension (See 5.5). Following dissociation, cells were centrifuged for 30 sec at 13000 rpm. The supernatant was removed and the cells were washed in 1 ml PBS. Next, the cells were suspended in 100 µl PBS and 1 µl Zombie (BD) solution was added to each tube. This staining was done in order to eliminate necrotic or late apoptotic cells that are not in the debris in the FACS plot. Cells were stained for 15 min at RT in the dark. BrdU staining for FACS analysis was performed using the APC BrdU Flow kit (BD-Pharmingen^{TM}) as follows: 1 ml Perm/Wash buffer was added to Zombie stained cells and centrifugation was done for 30 sec at 13000 rpm. Supernatant was removed and cells were re-suspended in 200 µl HBSS containing lineage antibody mixture (EpCAM, CD31, TER119, CD45, CD11b, Gr1b) coupled to avidin. Cells were stained for 15 min on ice to remove the blood and endothelial cells as follows: 1 ml HBSS was added and the cells were centrifuged. Then, the cells were stained in HBSS containing Biotin-491 for 5 min and the 1 ml HBSS wash was repeated. The cells were re-suspended in 200 µl fixation buffer (BD-

Pharmingen BrdU kit) and incubated for 20 min on ice, in the dark. Following this, the cells were washed in 1 ml PBS and later in 1 ml Perm/Wash buffer (BD-Pharmingen BrdU kit). The cells were re-suspended in 500 µl freezing medium (10% DMSO, 90% FBS) and stored at -80 °C for at least two days. On the day of analysis, the cells were removed from -80 °C, washed in 1 ml Perm/Wash buffer and centrifuged at 13000 rpm for 1 min. The supernatant was removed and the cells were re-fixed in 200 µl fixation buffer for 5 min. After washing the cells in 1 ml Perm/Wash buffer, they were washed in 1000 µl PBS and treated in 300 µg/ml DNase I at 37°C for 1 h (150 µl end volume). Next, the cells were washed in 1 ml Perm/Wash buffer and incubated in Perm/Wash buffer containing 1:50 anti-BrdU antibody for 20 min at RT. Following, the cells were washed in 1 ml Perm/wash buffer and stained with anti-GFP (1:1000, Lubio Biosciences) in 50 µl Perm/Wash buffer. After washing, the cells were stained with 7AAD for DNA content and analyzed using the BD^{TM} FACSAria III.

5.6.2 Immunofluorescence analysis of BrdU incorporation

The BrdU treated embryos were fixed in ice-cold 4% PFA on ice and washed three times in PBT. The embryos were embedded and sectioned as explained above in the histology section. The sections were washed three times in PBS for 5 min at RT upon removal from -80 °C. Then, the sections were permeabilized using 0.3% Tween-20 in PBS for 20 min at RT. Following this, DNA denaturation was performed by using 1 N HCl for 10 min at RT and 2 N HCl for 10 min at RT. The samples were incubated at 37 °C for 20 min and neutralized with 0.1 M pH 8.6 Borate Buffer for 15 min at RT. Next, the

sections were blocked using 10 % goat serum and 0.3 % Triton-100 in PBS for 1 h at RT. Following this, the sections were incubated with the primary antibody (rat anti mouse anti-BrdU antibody, 1:1000 in blocking buffer) overnight at 4°C. The samples were washed three times in PBS and incubated with the secondary antibody (goat anti rat Alexa-555) for 1 h at RT. Samples were washed three times in PBS and stained using DAPI for 5 min, washed three times in PBS and mounted using mowiol. Samples were kept at 4°C in the dark until imaging.

5.7 Nuclei counting

For z-stack confocal imaging, limb buds of mouse embryos at 10.5 with 34-36 somites were fixed in 4% PFA for 45 min on ice and whole mount stained using Hoechst at 40 µg/ml for 20 min at RT. The limb buds were sectioned using vibrotome (Leica) at 40 µm sections. The thick sections were embedded on depression slides using mowiol and imaged with a Leica SP5 Confocal microscope using 20X objective. 20 µm Z-stack images were recorded. The images were processed using IMARIS software and virtual cubes of 40x40x20 µm were cut. Using the 3-D slider, nuclei that were fully inside the cube were quantified for proximal, central and distal limb bud regions.

For the limb buds of mouse embryos at E 9 (18 somites), all nuclei were counted. The embryos were fixed as described above and embedded in 1:1 30% sucrose-OCT mixture. Next, 7 µm sections were cut and stained in 0.1 µg/ml Hoechst for 15 min. 20x images were done as described above and nuclei were counted using ImageJ.

5.8 Digoxigenin-labelled RNA riboprobe synthesis

The plasmid encoding the cDNA of interest was linearized and the antisense riboprobes were synthesized using the appropriate (T7, T3 or SP6) RNA polymerase with the DIG RNA labeling kit (Roche). The digoxigenin labeled riboprobes were precipitated with ethanol and linearized polyacrylamide as carrier and they were washed with ethanol. The SpeedVac dried riboprobes were resuspended in TE buffer (10 mM Tris HCl pH 7.4, 1 mM EDTA pH 8.0) and stored at -20°C.

5.9 Whole-mount in situ hybridization

For whole mount in situ hybridization experiments (WISH), embryos were rehydrated in stepwise MeOH/PBT suspensions (100% MeOH to 100 % PBT by 25 % steps). Next, the embryos were bleached in 6 % H_2O_2 for 15 min and washed in PBS. Following, the embryos were treated in 10 µg/ml Proteinase K (PK) for 15 min (25 min. for embryos older than E11.5). For the AER probes, PK treatment was performed for 5 min at 5 µg/ml concentration. The digestion reaction was stopped by replacing the PK solution with 10 µg/ml Glycine in PBS. Then, the embryos were washed three times with PBT and re-fixed for 20 min at 4 °C with 4 % PFA- 0.2 % gluteraldehyde solution. After fixation, embryos were washed three times in PBT. The embryos were incubated in prehybe solution (50% deionized formamide, 5xSSC pH 4.5, 2% BCI blocking powder (Roche), 0.1 % Tween-20, 0.5%CHAPS (Sigma), 50 µg/ml yeast RNA (Sigma R8759), 5mM EDTA, 50 µg/ml heparin (Sigma H5515)) at 70 °C for at least 2 h and then incubated in Probe mixture (10 µl antisense RNA diluted in 1 ml Prehybe) overnight at 70 °C. If the probe was

used for the first time, it was denaturated at 85 °C for 5 min and added to prewarmed prehybe solution at 70°C.

On the Day 2, the hybridization buffer containing the probe was replaced by prewarmed prehybridization buffer. This buffer was changed to 2xSSC (0.3M NaCl, 0.03M sodium citrate pH 4.5) gradually by a series of 25%, 50%, 75% with 5 min incubations at 70°C. The embryos were incubated with 20 µg/ml RNase A in 2xSSC, 0.1 % CHAPS for 45 min at 37°C. Next, the embryos were washed twice with maleic acid buffer (100 mM maleic acid disodium, 150 mM NaCl pH 7.5) for 10 min at RT and twice for 30 min at 70°C. Then, three washes in freshly prepared TBST (140 mM NaCl, 2.7 mM KCl, 25 mM Tris-HCl, 1% Tween 20), each for 5 min, were performed. This solution was replaced by blocking solution (10% lamb serum/TBST) for at least 1 h at RT. Following the blocking step, the embryos were incubated with blocking solution containing 1:5000 anti-digoxigenin-Fab-AP fragments (Roche) overnight at 4°C.

On Day 3, the embryos were washed at RT with TBST five times, for 1 h each, and washed with TBST overnight.

On Day 4, the embryos were washed with NTMT solution (100mM NaCl, 100mM Tris-HCl pH 9.5, 50 mM $MgCl_2$, 1% Tween-20) for 10 min three times at RT and incubated in BM-Purple solution at RT (Roche). The staining was monitored regularly to check the intensity and specificity of the signal. The staining reaction was stopped by replacing BM-Purple with PBT. The embryos were post-fixed with 4 % PFA. In case of Optical Projection Tomography (OPT) imaging, the developing solution was 175 µg/ml BCIP (Roche) and 20 µg/ml NBT (Roche).

Following WISH, embryos were washed for 48 h in PBT at 4°C. Limb buds were dissected from the embryos, keeping a small trunk part to help with handling and avoid damage.

5.10 Whole mount LacZ staining of embryos

Embryos were fixed in fixing solution (1% Formaldehyde, 0.2% Gluteraldehyde, 0.01% Sodium Deoxycolate, 0.02 % NP-40). After 30 min of fixation, the embryos were washed 3 times with PBS. After the last wash PBS was replaced by Staining Solution (1 mg/ml X-gal in dimethyl formamide, 0.25 mM $K_3Fe(CN_6)$, 0.25 mM $K_4Fe(CN_6)$, 0.01 mM NP-40, 0.4 mM $MgCl_2$, 1 % sodium deoxycolate in PBS). Embryos were incubated at 37 °C in a rotating incubator oven. Staining was monitored every hour, in case of weak staining, overnight staining was performed.

5.11 PCR

The following primers were used to genotype the indicated mouse lines:

	Forward	**Reverse**
Bactin-GFP	CATGAAGCAGCACGACTTCT	GCTTGTCGGCCATGATATAG
BetaCatenin	AAGGTAGAGTGATGA AAGTTGTT	CACCATGTCCTCTGTCTATTC
PrxCre	GGCTCTCTCCTTAGCTTCCC	CCTGGCGATCCCTGAACATGTCC
R26-LacZ	**Forward1:**	**Reverse1:**
	AATCCATCTTGTTCAATGGCCGATC	CCGGATTGATGGTAGTGGTC
	Forward2:	**Reverse2:**
	GGCTTAAAGGCTAACCTGATGTG	GGAGCGGGAGAAATGGATATG

5.12 3-D imaging using Optical Projection Tomography

The stained embryos using ISH or LacZ were washed in 50 ml PBS for three days prior to OPT imaging. Next, embryos were re-fixed in 4 % PFA for 1 h at 4°C and in 1 % gluteraldehyde overnight. Following extensive washes in PBT, the sample was transferred to 1 % low melting point agarose (Sigma) in deep 10 cm plastic dishes (Sterilin) with the least PBS possible. When limb bud were to image, single limb buds with small trunk parts were dissected for best orientation and image quality. The center of the dish was marked for the trimming procedure. The dish containing the sample was transferred onto a cooling plate and the sample was positioned using Pasteur pipets with closed ends to the center of the dish and mid-depth of the agarose. The sample was kept straight along the rotation axis that is chosen for imaging. After the agarose had solidified completely, the embedded limb bud was cut out as a cube of agarose using a razor blade, around 5x5x5 cm size. The cube was carefully dried using tissue paper and glued to the OPT magnets using cyanoacrylate glue (Patex). Then, the cube was trimmed to an octagonal prism, avoiding imperfections in the agarose and sharp egdes, and finally dehydrated in 100% technical grade MeOH overnight. The next day, the MeOH was replaced once more to completely remove the water from the agarose. The fully dehydrated samples were incubated overnight in 1:2 Benzyl alcohol- Benzyl Benzoate (BABB) solution. The samples were imaged using the OPT Bioptonics Scanner 3001. First, the sample was loaded onto the center of the magnet holder. Then, the Skyscanner software was used to adjust the rotation axis from each side of the sample. The sample was positioned in the middle of the viewing axis. The exposure time in the bright

field for colored stains was adjusted according to staining intensity and the background of the sample, in general between 20-60 milliseconds (ms). In the GFP channel (425/40nm, 475nmLP), the auto-fluorescence of the embryo was captured to reconstruct the 3-D limb bud anatomy. The exposure time was adjusted to the embryonic stage and staining and was between 400-1000 ms. Imaging was performed using a step size of 0.9 degrees that produces 400 images in each channel, at 1024x1024 resolution and at 3.1 μm voxel size. 3-D raw images were reconstructed using NRecon software that uses a filtered-back transformation into 16 bit TIFF format which enabled improved segmentation of the signal for image processing. Bioptonics viewer software was used for visualization, 3-D optical sectioning and taking snapshot images. The AMIRA software was used for the production of 3-D geometries, measurements and morphing of the different stages (see below).

5.13 Image processing and generation of *in silico* limb bud domains

Visualization and image processing of the OPT images was performed using the Amira 5.4. 3-D images in 16 bit TIFF format were loaded onto Amira as two channel images. The bright field channel was used to show the gene expression and the GFP channel was used to capture the anatomy of the limb by detection of the autofluorescence. Images were visualized using the VolRen module in VRT format. Images were segmented using AMIRA-segmentation tool. For each channel a new label field (material) was added to keep domain identities separate. The signal was segmented using the thresholding tool. High signal to noise ratio of OPT images allowed robust

identification and segmentation of gene expression domains. The segmented 3-D image was inspected using the 3D toggle for its quality. In case of incomplete domains, the 3-D brush tool was used to complete the domain. The segmented images with label fields were used for measurement and quantification. For volumetric measurements, the voxel count of each sample and channel was calculated using AMIRA-measurement tool. The voxel count in 3-D allowed calculation of the volumes of the samples.

Segmented images were aligned and registered for different genes to the correctly staged embryo using an arithmetic tool. To avoid a very dense mesh, the image was resampled by 1:3 in each dimension. Using the SurfaceGen module, the surface mesh was created from segmented images. The segmented data were smoothed three times with a sigma value of 0.3. To increase the quality of the mesh, i.e. the regularity of the triangles, the remesh module was used to reduce the mesh size by 80% at each step. This process was iterated up to seven times until the element size was around 20000 mesh elements. The surface was inspected for quality using the SurfaceView module. To create a 3-D volumetric domain from this surface mesh, the Tetragen module was used to create a volumetric mesh. For each subdomain, the desired number of tetrahedral elements was entered. This mesh was saved in I-DEAS universal data format. The data was opened using Gmesh software and saved as a Nastran Bulk data file. The resulting file extension was changed from UNV to DAT to make it compatible with the simulation software COMSOL Multiphysics. In COMSOL, a 3-D model was created and the mesh was imported under the Mesh module.

Different limb bud stages were aligned in 3-D using specific landmarks on the trunk and limb buds like the AER, the anterior-posterior limb bud-lateral mesenchyme borders or hand plate for the later stages. Using the SurfaceCut module, 2-D sections were extracted from the aligned 3-D image series. From 2-D sections, boundaries were created using the Intersect module and saved in ASCII format. Limb bud boundaries were processed in MATLAB 2013b to smooth and fine-tune the subdomains of the limb bud, which were then imported into COMSOL separately.

For the calculation of the displacement fields, a diffusion based method or registration point-to-point method was used (performed by Zahra Karimaddini, See Publication 4 in the Appendix). COMSOL Multiphysics 4.3b with the MATLAB Livelink™ function was utilizied to solve reaction diffusion equations and perform plotting and screening of the results of the simulations.

6. RESULTS

6.1 OPT imaging for a 3-D analysis of limb bud development

OPT imaging is a suitable method to obtain 3-D limb bud morphologies and to determine gene expression patterns in wild type (WT) and mutant mice (Sharpe et. al., 2002). I established the OPT method in the laboratory. By optimizing the sample preparation, imaging and visualization steps I was able to get high quality 3-D images for further quantitative analysis. For image analysis, a professional image processing software is required. I compared IMARIS, Amira, Drishti, Simpleware, Meshlab, Rhino and 3-D Slicer and decided to use Amira because it was performing best for performing measurements, 3-D domain creations, subdomain identifications for gene expression patterns and morphing of limb buds.

6.1.1 The basics of OPT imaging

Projection tomography allows collection of data that integrate the measured property along a linear projection traversing the entire specimen. These raw data sets are transformed using a filtered back-projection algorithm to recover the original structure of the specimen (Quintana and Sharpe et. al., 2011). For OPT imaging, the specimen is immersed in an index-matching benzyl-benzoate-benzyl alcohol solution (BABB, in 2:1 proportion) to decrease the light scattering. The specimen is rotated on a 360° rotation axis perpendicular to the optical axis (Figure1-A, Sharpe et. al., 2002). OPT positions the focal plane halfway between the rotation axis and the edge of the specimen that is closest to the lenses. This maximizes the acquisition of focused information from the specimen and minimizes the imaging time (Sharpe et. al., 2002).

Light passes through the specimen in straight lines, which allows creation of high-resolution images back-projection algorithm (Figure1-B, Sharpe et. al., 2002) and visualization of gene expression or protein localization patterns.

6.1.2 Analysing tissue development with OPT

The OPT has two imaging modes: the bright-field-OPT and fluorescent-OPT. The bright-field-OPT enables imaging of colored stains for β-Galactosidaase and WISH (Figure 1-C-G). I found that the maximum intensity projection rendering of 3-D images (Figure 1-E) enables excellent visualization in comparison to the manual adjustment of the signal in two channels (Figure1-D). The organs of interest can be analyzed by image cropping and segmentation and processed further (Figure 1-E). However, I realized that the dissection of the limb buds and imaging of single limbs result in better images for the following reason: On the one hand, the rotation axis and adjustment of the focal point are improved. On the other hand, due to the smaller size of the specimen, higher zoom and lower voxel size can be used (data not shown). Adult tissues up to 5 mm can also be imaged at high quality using this technique (Figure 1-G). The second mode, the fluorescent-OPT, enables the imaging of fluorescent specimens such as lung buds. These were stained using whole mount immunofluorescence detection of E-CADHERIN to visualize the lung bud epithelium (Figure 1-H).

6.1.3 Virtual sections and isosurfaces of OPT images

OPT allows not only to image 3-D gene expression patterns but also to inspect optical sections in any plane of virtual section, which provides a powerful tool to analyze phenotypes. OPT analysis of whole-mount *Decorin*

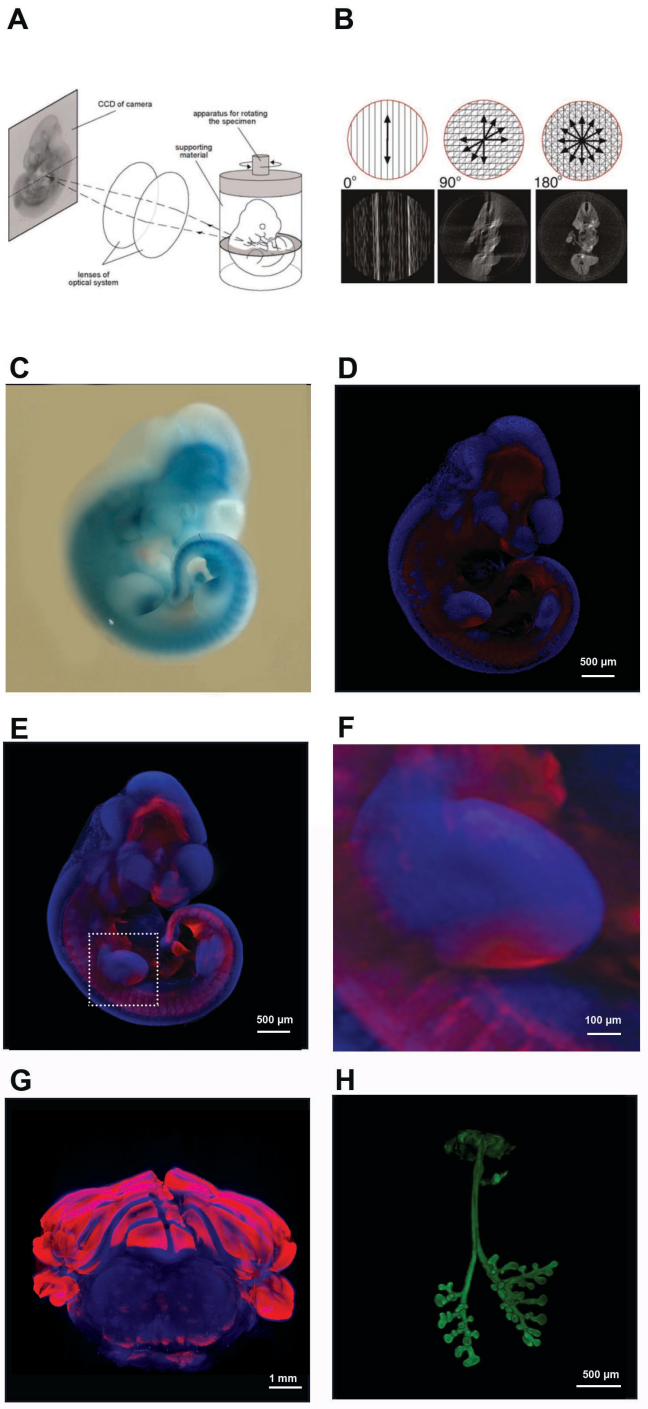

Figure 1. OPT imaging

(A) An OPT specimen is embedded in an agarose gel and cleared prior to imaging in BABB medium. The specimen is rotated around 360° and a CCD camera records 400 images at 0.9 degrees intervals. **(B)** The projections accumulated form a reconstructed image (0°, 90° and 180° are indicated). **(C)** An E10.75 embryo stained for *Ptch1* expression using LacZ staining. **(D)** OPT imaging allows the production of high quality 3-D images from the embryos: the OPT image of the embryo from (C). **(E)** Maximum intensity projection rendering provides higher signal to noise ratio and improved visualization. **(F)** The high magnification image of the right forelimb bud of the embryo shown in (E). **(G)** Cerebellum of a 6-week old Ptch1-LacZ mouse reveals the distribution of *β-galactosidase*. **(H)** Fluorescent-OPT imaging of a lung bud epithelium from an E11.5 mouse embryo stained for E-CADHERIN (provided by D. Menshykau). (The panels A and B adapted from Quintana and Sharpe, 2011)

expression in E12.5 limb buds represent a good example for the importance of the virtual sections analysis (Figure 2-A). DECORIN is a major component of connective tissue and organizes collagen fibers. Using OPT analysis, we discovered that *Decorin* expression is excluded from the cartilage condensations in limb buds in the digit forming territory and from the condensations in the stylopod and zygopod (Figure 2-B). This specific localization was completely lost in the *Smad4*-deficient forelimb buds, which fail to form cartilage condensations (Appendix, Figure-8 in Publication 1). Additionally, using OPT, we have also been able to show *Ptch1* expression is not upregulated in the mesenchyme of the bovine limb buds (Appendix, Figure-3 in Publication 2).

Iso-surfaces rendering can be used to visualize the anatomy of the limb buds as solid structure and colors. This technique increases visibility of diffuse staining and expression in e.g. the core mesenchyme (Figure 2-C,D). This is especially important when comparing gene expression patterns of WT and mutant specimens. Iso-surface rendering enables analyzing the localized gene expression. Using iso-surface rendering, we have discovered that *Sox9* expression is progressively reduced in the distal arch that normally forms digit primordia in *Smad4*-deficient forelimb buds. In contrast, *Sox9* expression domain was thickened in the primordia that will form the zeugopod elements (Figure 4 in Appendix, Paper 1).

In addition to virtual section and iso-surface rendering, OPT enables calculating the volumes and measuring the axis lengths of embryonic samples accurately.

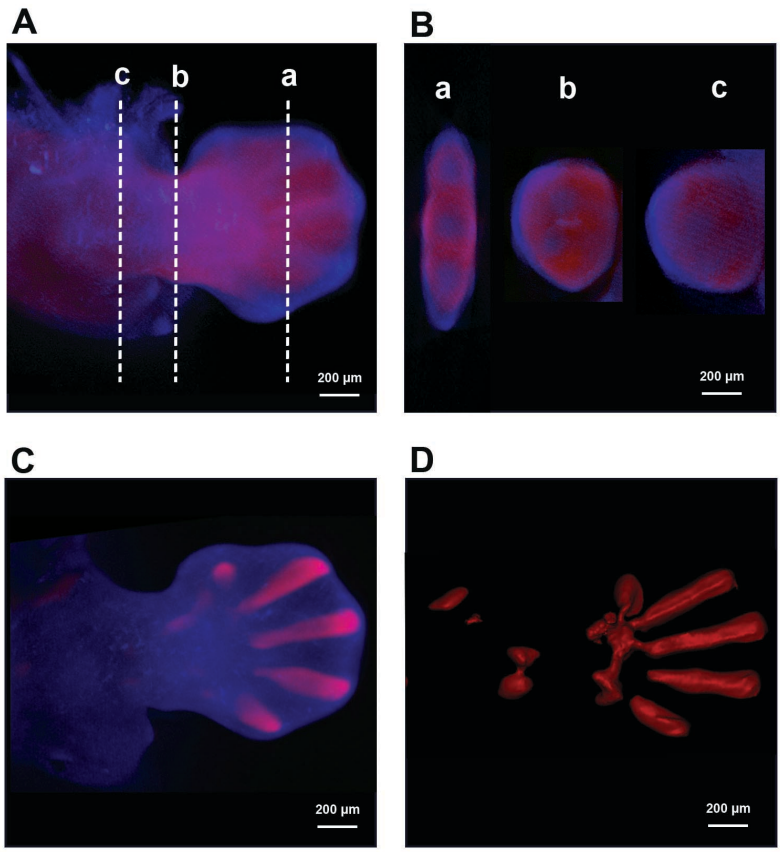

Figure 2. Optical Sectioning and isosurface production from 3-D images

(A) A mouse forelimb bud at E12.5 (60S) and detection of the *Decorin* transcript distribution by OPT. a,b,c indicate the sections shown in **(B). (C)** *Sox9* expression in a WT E12.5. **(D)** Isosurface rendering of the *Sox9* expression domains shown in panel (C).

6.2 A quantitative analysis of limb bud growth and proliferation

We took a quantitative approach to characterize limb bud outgrowth and the underlying cellular dynamics. We assessed the proliferation rates of the limb buds at different stages and determined the numbers of limb bud mesenchymal cells. We found that the expansion of limb bud cells shows an exponential behavior and that there are two distinct phases of this proliferative expansion. Careful analysis of the quantitative data indicated that the data

sets can be explained an exponential decay model in the underlying growth rates.

6.2.1 Quantitative analysis of volumetric growth reveals the decrease in limb bud outgrowth

To study the limb bud growth kinetics, we used OPT imaging (Sharpe, 2002) of limb buds whose mesenchyme was marked by Prx-Cre (Logan et. al, 2002) driven LacZ expression (R26-LacZ, Soriano et. al., 1999, Figure 3-A). The limb bud volume was determined from the 3-D morphologies using the AMIRA software package (Figure 3-B,C). We staged embryos according to the somite number (S). The resulting developmental sequence reveals how the limb bud grows as a bud, before assuming its paddle-like shape (Figure 1-F). By plotting the limb bud volume against the somite stages, we noticed an initial exponential expansion, which slowed down around the stages of hand plate formation (Figure 3-E). Overall, the limb bud volumetric growth data, *V*, could be fitted well with a biphasic exponential growth law

$$\frac{dV}{dt} = kV \qquad (1)$$

with k = 0.143 [S^{-1}] in the first phase and k = 0.053 [S^{-1}] in the second phase. This was necessary as a single exponential growth law fails to fit initial and late stages (Figure 3-F). The first pair of somites are formed at E 8.3 in the mouse, and additional somites are formed initially every our and at later stages every 2-3 hours (Tam , 1981). Therefore, from 22S to 30S 90 min was approximated for the formation of a somite pair and from 31S to 54S two hours were assumed for somite formation. In absolute times, the biphasic growth behaviour is thus even more pronounced.

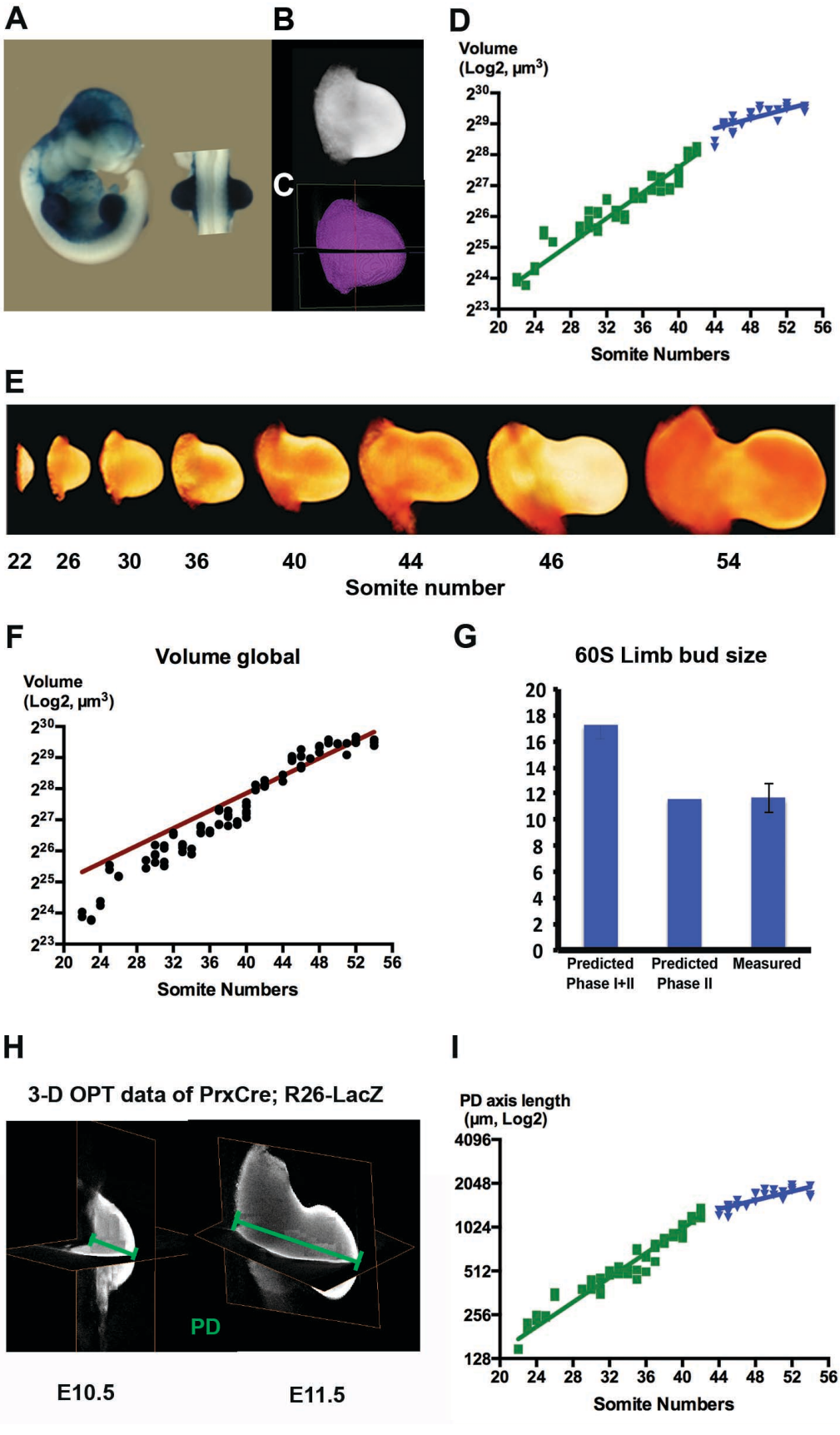
A
B
C
D
Volume
(Log2, µm3)
Somite Numbers
E
22 26 30 36 40 44 46 54
Somite number
F
Volume global
Volume
(Log2, µm3)
Somite Numbers
G
60S Limb bud size
Predicted Phase I+II
Predicted Phase II
Measured
H
3-D OPT data of PrxCre; R26-LacZ
PD
E10.5
E11.5
I
PD axis length
(µm, Log2)
Somite Numbers

Figure 3. Limb bud growth analysis in 3D shows biphasic behavior of volume and axis growth

(A) PrxCre; R26-LacZ limb buds were scanned using OPT and image segmentation and voxel quantification allowed calculation of the volumes. **(B)** Raw OPT image of a 37S limb bud. (C) Segmented 3-D image of a 37S limb bud. **(D)** The volume data was fitted to two different exponential graphs, with the values of =0.143 S^{-1} for the phase I and k=0.053 S^{-1} for the phase II. **(E)** Representative 3-D images of limb bud at the stages indicated (22S to 54S). **(F)** A Single exponential growth law fails to fit global data points. **(G)** Limb bud size at E12.5 (60S) was predicted correctly using the parameters from phase II, whereas a global fit overestimates the real limb bud size. **(H)** Using the oblique slicer tool, 3-D images were oriented and axis measurements performed. **(I)** The PD axis measurement data could also be fitted to two different exponential graphs, with values of k= 0,097 S^{-1} for the phase I and k = 0.034 S^{-1} for the phase II.

The extrapolation of limb bud size at 60S using phase II parameters correctly estimated the limb bud size, whereas phase I parameters significantly overestimate the size (Figure 3-G).

The 3-D morphology allowed us also to determine the expansion of the proximal-distal (PD), anterior-posterior (AP), and dorsal-ventral (DV) axes over time (Figure 4-A). This analysis showed that the main growth occurs along PD axis, whereas the DV axis remains within the range of 200-350 µm. The AP axis expands predominantly after 35S and approximately doubles in length. The AP and DV axis display heterogeneities due to curvature (Figure 4-C-F). The previously mentioned biphasic expansion was also observed for the PD axis (Figure 3-G,H). In particular, the length of the PD axis can be fitted with an exponential growth (see Eq. 1) with k = 0.097 [S^{-1}] during the initial phase and k = 0.034 [S^{-1}] in advanced limb buds.

Intriguingly, the switch from phase I to phase II occurs when the hand plate emerges (S40-S45) and the Sox9 positive condensations are formed. IF analysis suggested that the Sox9-positive mesenchymal progenitors in the

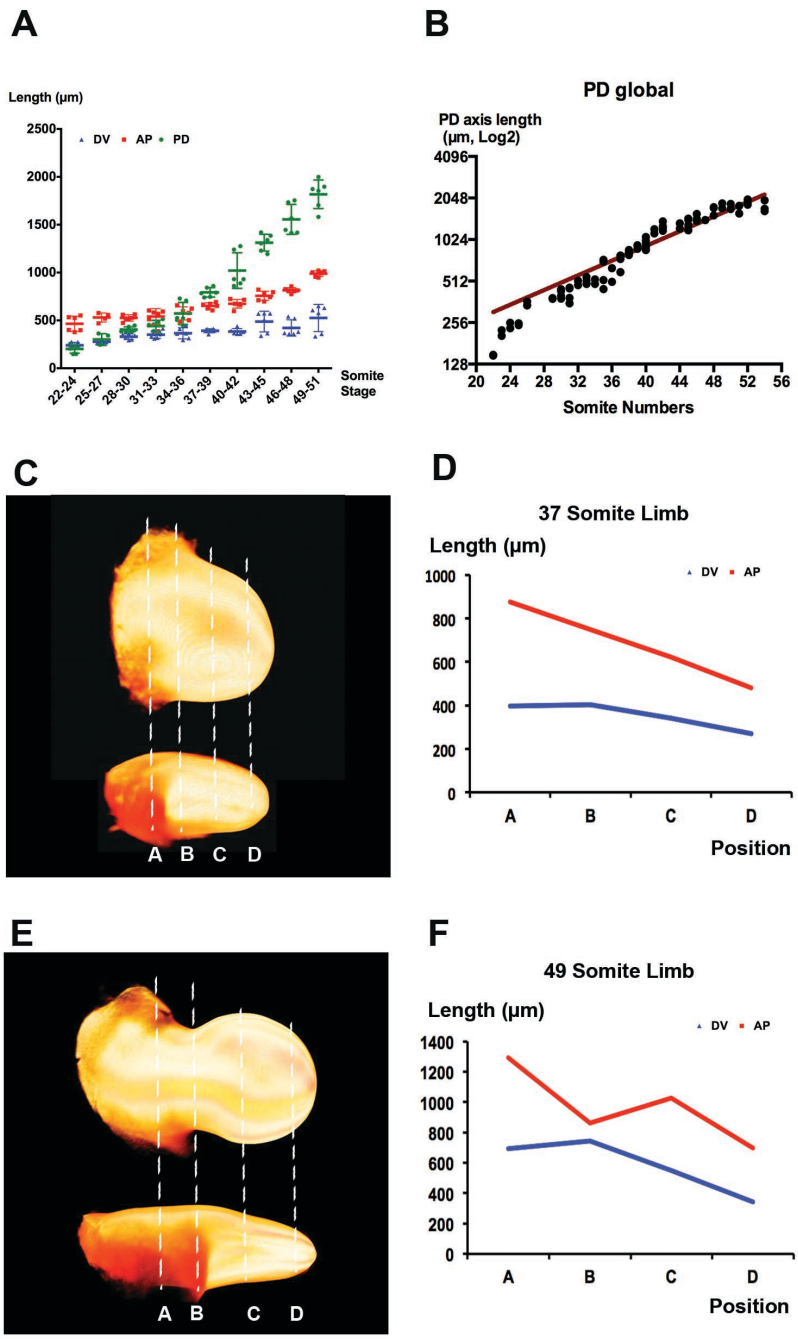

Figure 4. Quantitative analysis of limb bud outgrowth dynamics

(A) The mouse limb bud PD axis expands in an order of magnitude from E9 (22S) to E12 (54S) in three days of development. In contrast, DV and AP axis do not show a comparable expansion. **(B)** PD axis outgrowth appears exponential and a single fit fails to capture all datasets. **(C, D)** Measurement of a E10.5 (37S) forelimb bud AP and DV axes in different limb bud regions suggests dependence of the value on the measurement point. The values A-D in panel (C) are plotted in panel (D). **(E, F)** Analysis of a E11.5 (49S) mouse forelimb bud.

condensations proliferate at lower rates (tenBerge et. al., 2008). Thus, we wondered whether the observed switch in growth rates could be caused by such a change in proliferation of condensing and/or differentiating cells.

6.2.2 Quantitative analysis of cell numbers reveals the reduction in proliferation of limb bud mesenchymal progenitors

To quantify the cell numbers in the limb bud mesenchyme, we used Prx-Cre mice to conditionally activate GFP expression (β-actin-GFP mouse, Jägle et. al., 2007, Figure 5-A). A single cell suspension was prepared from dissected limb buds directly in the FACS tubes to avoid cell losses (See methods section). Dissociated mesenchymal progenitors were neither washed, nor filtered or centrifuged to avoid re-aggregation and/or loss of cells. To determine cell numbers, timed counting of cells in defined subfraction volumes calibrated using TruCount^{TM} tubes with polystyrene fluorescent beads was done. Non-limb cells, including the flank mesenchyme, are GFP negative (Figure 5-B). We also gated dead cells, which amounted to 8-12 % of all cells (Figure 2-B, red arrow-head). The GFP positive limb bud mesenchymal progenitors represented mostly singlets had a round morphology after sorting (Figure 5-B, green arrow-head).

Using this approach, we quantified cell numbers from 22S to 54S (Figure 5-C). As for the measurements of the limb bud volumes (Figure 3-D), we observe a biphasic exponential expansion rate is apparent (Figure 5-C). The doubling time in the two exponential phases can be calculated according to

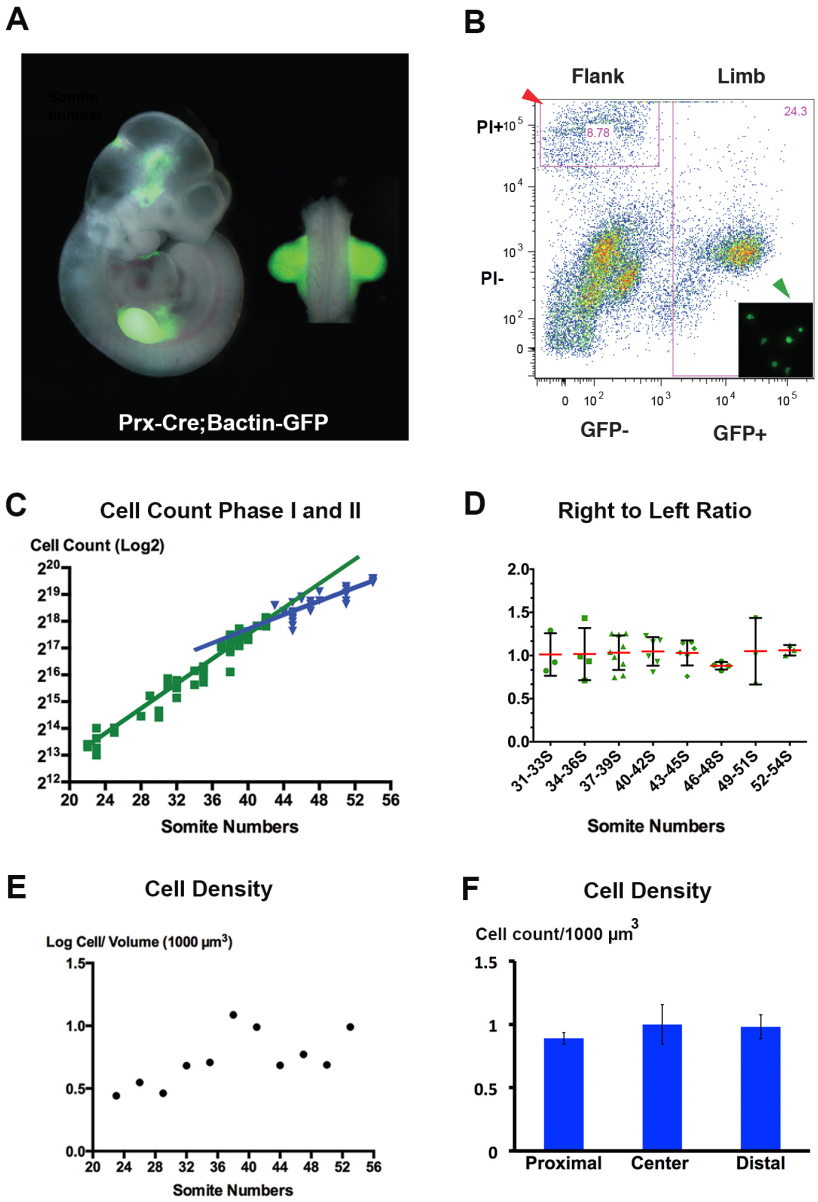

Figure 5. Quantitation of limb bud mesenchymal cells indicates that the increase in cell numbers shows a biphasic behavior

(A) Prx-Cre driven GFP expression labels all forelimb bud mesenchymal cells. **(B)** GFP positive cells are gated and quantified. Imaging of sorted GFP+ cells confirms this single cell states (green arrow head). The procedure results in overall 8-12 % cell death (red arrow head). **(C)** Limb bud mesenchymal cell numbers can be fitted using an exponential function with two phases, k=0,165 S^{-1} for the phase I and k=0.087 S^{-1} for the phase II. **(D)** The exponential fit estimated the cell numbers at 18 somite stages as around 500 cells. Nuclei counting of all sections results in average 4512 cells (± 975, n=4) in the initial limb bud. **(E)** Cell density over indicated stages is calculated using volumetric measurements and cell numbers. Mesenchymal cell density increases constantly until E11 (40S) and decreases thereafter. **(F)** Confocal imaging aided estimation of cell densities at E10.5 (34-36S) points to similar values obtained by OPT/FACS analysis. No difference was observed in different regions of limb bud mesenchyme.

$$\frac{dC}{dt} = kC \quad (2)$$

$$t_2 = \frac{\ln(2)}{k}. \quad (3)$$

When we fitted the two phases with the switch between 42 and 46S (Figure 2-C), cell doubling times for the first phase are 7h and 16h for the second phase. Previously, the doubling time of mesenchymal progenitors was estimated to be 11h for E11 hind limb buds (Boehm et. al., 2010). This represents about the average of both phases that we now defined.

A single limb bud contains around 12000 mesenchymal cells at 22S and consists of about 30000-40000 cells at 28-30S, when *Shh* expression is initiated. Limb buds first emerge around 16S, and we extrapolated our measurements to estimate the number of mesenchymal cells around limb bud initiation. By extrapolating phase I to 18S the number of mesenchymal cells estimated to be around 5500 cells. Additionally, 7 µm sections of the whole limb bud at 18S was prepared and stained with Hoechst to reveal nuclei. Using nucleus segmentation, we quantified the total cell number in these limb buds, which were close to values extrapolated from FACS analysis (4512±974, n=4). Taken together, these results show that the initial limb bud consists of about a few thousand mesenchymal progenitors.

The proliferation rate is higher than the volume expansion rate, and the cell density (cells per volume) increases over time (Figure 5-E). In fact, cells undergo five doublings during 58 hours (the real time approximation of 22S to 54S), while the limb bud volume doubles only four times. However, proliferation is reduced earlier than the volume increase, such that the cell density declines around S40 and then stabilizes (Figure 5-E). The maximal

cell density corresponds to about 1 cell per 1000 μm^3. Interestingly, the volume of 1000 μm^3 corresponds the typical volume a fibroblast (Lang et. al., 1992), thus suggesting that from 37S onward, limb buds are densely packed with mesenchymal cells. We confirmed the estimated cell densities by counting nuclei in the proximal, center and distal regions of 34-36S limb buds, using the IMARIS software (Figure 5-F). Cell numbers on thick vibrotome sections were determined by counting the nuclei contained completely inside a 40x40x20 µm cube using z-stack confocal images of 30 µm of limb buds. The cell number per 1000 μm^3 volume was calculated, which corresponds to 0.96 ± 0.12 and no regional differences were observed (Figure 5-F). We obtain 0.70 ±0.18 this stage based on FACS-measured cell numbers and OPT volumes (Figure 5-E) but we note that already slightly later (37-39S), the cell densities has increased to 1.10 ± 0.26 cells per 1000 µm3 volume. The two methods thus yield comparable results.

We conclude that cell density is highest slightly just prior to the switch in the growth and proliferation rates. Around the time of the switch point, the hand plate emerges.

6.2.3 The increase in Sox9 positive progenitors does not correlate with reduction in proliferation in the limb bud mesenchymal progenitors

To determine the increase in Sox9 positive and Sox9 negative mesenchymal cell populations mice expressing GFP under the control of the Sox9 promotor were used. In addition, the relative proliferation rates were determined using BrdU labeling. BrdU is incorporated by cells into their DNA during S-phase,

and the fraction of BrdU positive cells is used to determine the relative length of the cell cycle (Nowakowski et. al., 1989). Pregnant mice were injected twice with BrdU 4h and 2h prior to dissection, non-apoptotic mesenchymal cells that are analysed and measured the fraction of BrdU-positive cells at 36-40S and 48-52S (Figure 6-A,B). In addition, the Sox9 positive population was revealed using an anti-GFP antibody to discriminate the positive and negative cells (Figure 6-A',B'). Next, we determined the proportion of cells fractions that are in the S-phase for the Sox9 positive and negative cell populations (Figure 6-A'',B''). As expected, Sox9 positive population contained a smaller fraction of BrdU positive cells than the Sox9 negative population (Figure 6-A'',B'',C). Detection of BrdU positive cells and SOX9 protein using immunofluorescence analysis confirmed these results (Figure 6-D,E). Intriguingly, there is a similar decrease in the fraction of BrdU positive cells in both Sox9 positive and Sox9 negative cells (Figure 6-C). Between 36-42S and 48-52S, the fraction of BrdU positive cells dis lowered by 17% in the negative and by 23% in the Sox9 positive population. Moreover, the Sox9 positive population is already significant at 37-42S (42% ± 3%, n=4) but only increases slightly by 48-52S (45% ± 3%, Figure 6-D). Also the Sox9+ domains assessed by OPT remains around 35-40% in both younger and older limb buds (Figure 6-F). As the *Sox9* negative cell population also showed the characteristic reduction in proliferation, we repeated the experiments using wild type embryos at the same stages and at 26-29S stage embryos (limb bud initation, Figure 6-H,I). The results at the later stages correspond to the averages of the both populations in Sox9-GFP limb buds. During the onset of limb bud development (26-29S) we observe 85% BrdU positive cells. This indicates

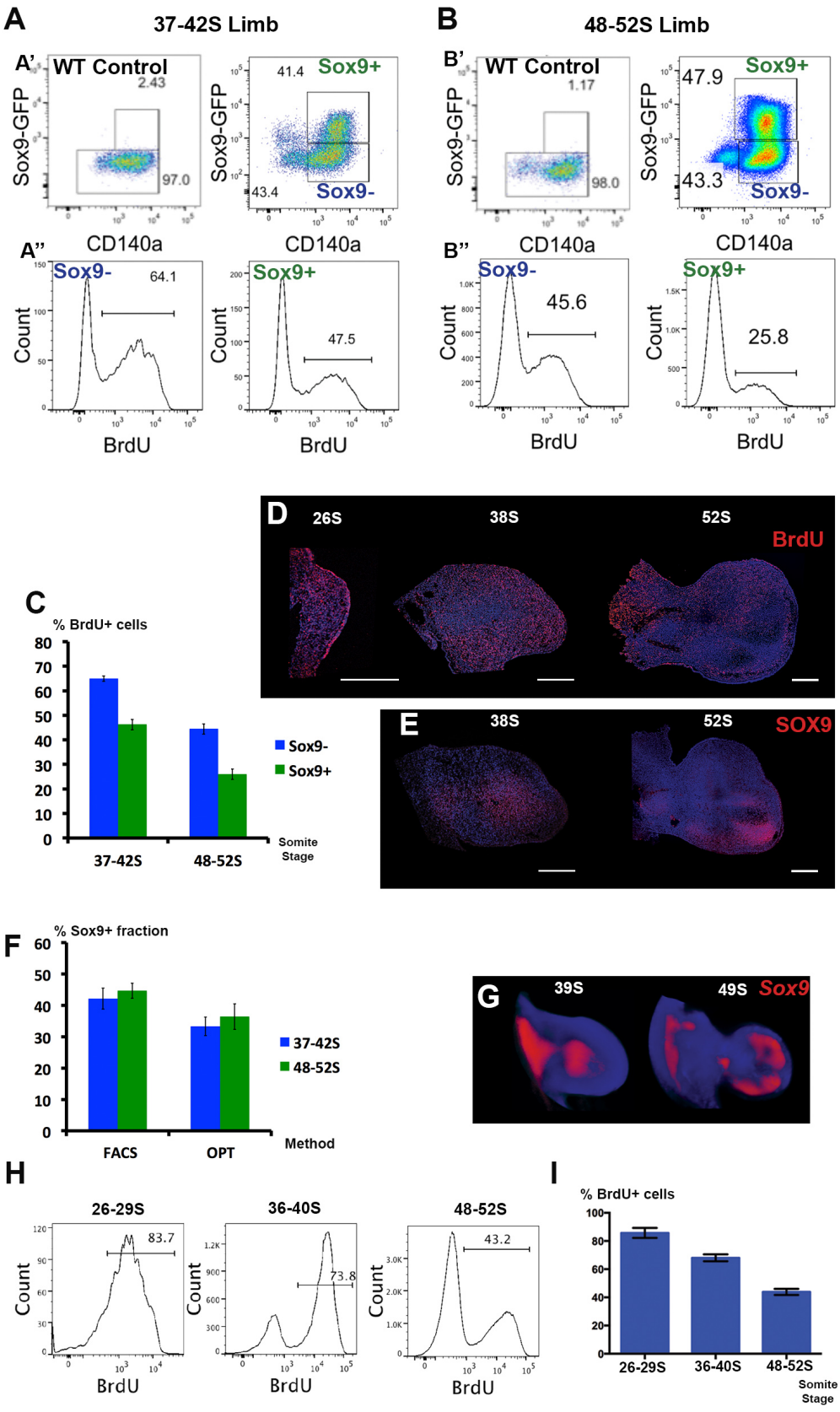
A
37-42S Limb
B
48-52S Limb
A'
WT Control
2.43
97.0
Sox9-GFP
41.4
Sox9+
43.4
Sox9-
B'
WT Control
1.17
98.0
47.9
Sox9+
43.3
Sox9-
A''
CD140a
Sox9-
64.1
Count
BrdU
Sox9+
47.5
B''
45.6
25.8
C
% BrdU+ cells
80
70
60
50
40
30
20
10
0
Sox9-
Sox9+
37-42S
48-52S
Somite Stage
D
26S
38S
52S
BrdU
E
38S
52S
SOX9
F
% Sox9+ fraction
60
50
40
30
20
10
0
37-42S
48-52S
FACS
OPT
Method
G
39S
49S
Sox9
H
26-29S
36-40S
48-52S
83.7
73.8
43.2
Count
BrdU
I
% BrdU+ cells
100
80
60
40
20
0
26-29S
36-40S
48-52S
Somite Stage

Figure 6: Sox9+ population shows decreased cell proliferation

37-42 S limb buds **(A)** and 48-52 S limb buds **(B)** were analyzed for the BrdU incorporation following injections of BrdU 4h and 2h prior to examination. The Sox9-GFP mouse enables sorting of osteo-chondro progenitors (A', B', right), where wild-type limbs serve as a negative control (A', B', left). CD140a (PDGFRα) marks limb bud mesenchymal cells. The S-Phase cells, which are BrdU positive cells are gated in the Sox9- (A'', B'', left) and Sox9+ populations (A'', B'', right). **(C)** Quantification of cell proliferation rates in the Sox9+ and Sox9- population. **(D)** Immunofluorescent analysis of BrdU incorporation into limb buds at 26-29S, 37-42S and 48-52S**. (E)** Localization of SOX9 in limb buds at the same age at 37-42S and 48-52S**. (F)** FACS and OPT analysis suggest that the percentages in the Sox9+ positive population is only slightly different when comparing limb buds from 37-42S and 48-52S. **(G)** Representative OPT images of *Sox9* WISH at the indicated stages. **(H,I)** FACS Analysis of wild-type limb buds for the BrdU incorporation shows that the reduction in proliferation apparent from early limb bud development.

that already from of 26-29S to 35-39S, proliferation rate is reduced (Figure 6-H,I). Thus, mesenchymal cell differentiation alone cannot explain the reduced in the proliferation rate we observe in our analysis.

6.3 The *In silico* limb: spatio-temporal computational model of limb bud development

The networks controlling limb bud growth and patterning are complex, and both spatial and temporal aspects have to be taken into account when studying the regulatory mechanisms. Various models of limb bud development have been proposed, but these models have focused mainly on digit formation and on cellular behavior. Moreover, these were simulated using idealized static domains (reviewed by Iber and Zeller, 2012). However, development is a very dynamic procedure, and growth and patterning are coupled.

Therefore, one major aspect of my PhD thesis aimed to develop a spatio-temporal model that is solved using real *in silico* limb shapes. To perform this

kind of modeling, a pipeline that combines high quality imaging and image processing is imperative. For the generation of accurate 3-D limb bud images with gene expression domains, I used Optical Projection Tomography (OPT).

6.3.1 *In silico* limb bud domains from 3-D OPT images

6.3.1.1 3-D image analysis suggests usage of single limb bud images rather than averages for each stage

Using Amira, I cropped the limb bud regions and segmented regions of interest. OPT images have a high signal to noise ratio that enables segmentation using a thresholding tool. The segmented images can be used to measure of volumes, lengths or for creation of surfaces. For limb buds of 21 to 60 somites (S), several limb buds labeled for that were stained for *Fgf8* (AER) and *Shh* (ZPA) expression were analyzed by OPT scanning. The variances in the shape and morphology in the limb buds of the same age were assessed by overlaying seven limb buds (at 40S). This allowed me to determine the average limb bud size and the variance of single limb buds. The variance of each individual limb bud was mapped onto an average domain using the distance function according to a color map (Figure 7-A-C). This analysis suggested that it is better to use a representative limb bud of each stage rather than an average limb bud. The usage of representative limb buds of each stage avoids the creation of non-biological variance in limb bud geometries. This is the preferred option for creating of 2-D and 3-D limb bud shapes for modeling.

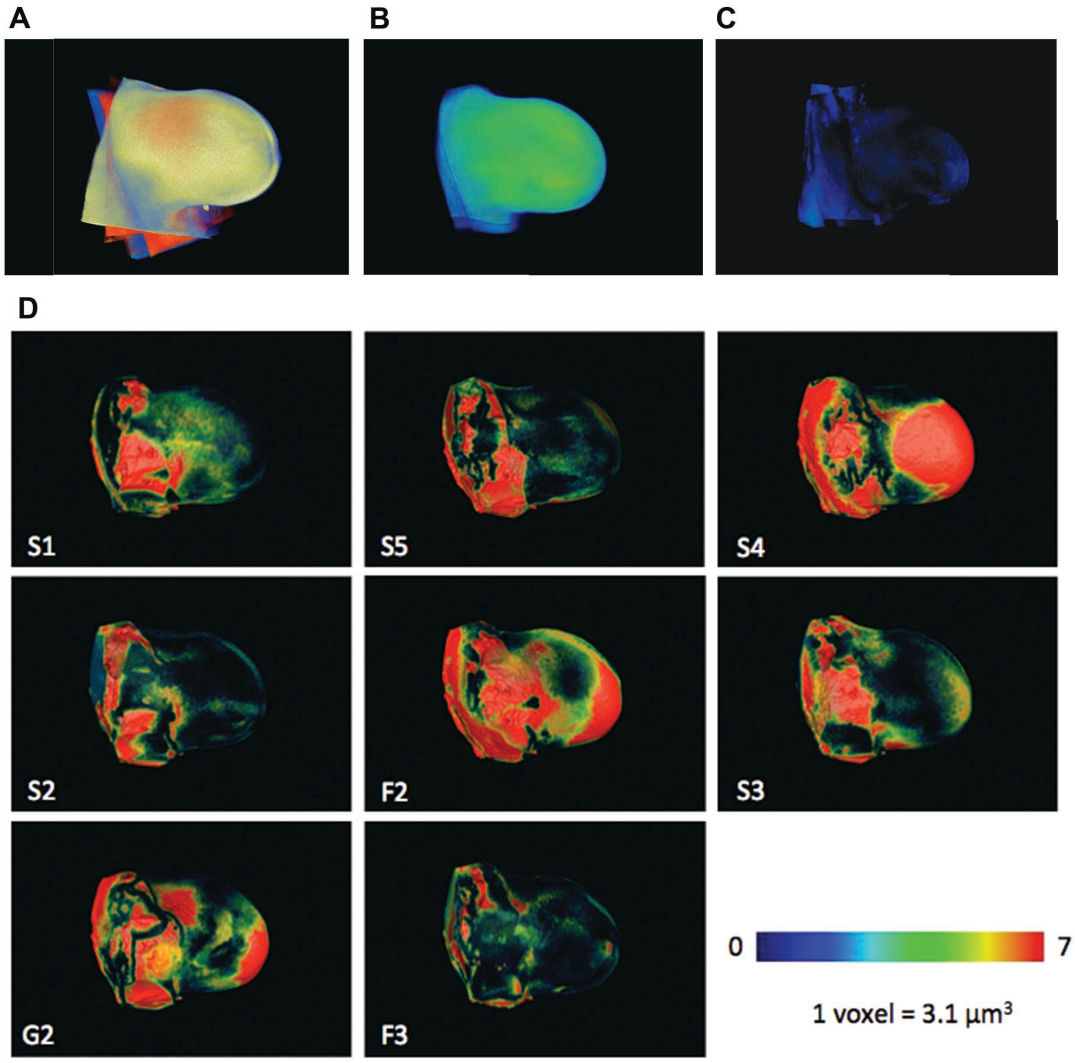

Figure 7. Evaluation of an averaged domain and deviation to single limbs

(A) Seven forelimb buds at E 10.75 are aligned. **(B)** The calculated averaged limb bud. **(C)** The deviation of the average limb shown as an intensity plot. **(D)** The differences in shapes are shown as shape distance for each limb bud to the averaged reference limb bud.

6.3.1.2 Creation of 3-D (2-D + t) gene expression domains

Segmented limb buds encompassing AER and ZPA domains were aligned and mapped onto the corresponding shape (Figure 8-A-D). From this, a surface mesh was created and mesh reduction steps were used to create smoother images. For limb buds of 21-40 S, 50000 mesh elements were created and for later stages (42-60S) 100000 mesh elements were used.

Limb buds were aligned in 3-D space using lateral mesenchymal trunk parts, the gene expression domains and curvature as landmarks. In order to create the 2-D domains, the center-most sagittal plane was constructed for each of the limb buds (Figure 8-E-F). The resulting virtual section shows the limb bud curvature boundaries and the ones of the expression patterns (Figure 8-G). Next, the boundaries of the surface were extracted and processed. The curves were uploaded as interpolation curves into COMSOL and domains were defined to simulate gene expression in the real gene domains (Figure 8-H). In addition to AER and ZPA domains, we also add an ectoderm of 20 μm thickness onto our mesenchymal shapes. The ectoderm domain required simulating e.g. the ectodermal WNT pathway. *In silico* domains of 21 to 60 S limbs were created in 3 somite steps to enable the real data-based simulations of limb bud shapes in an about 6 h interval. The growth vectors between these stages were calculated using methods that were developed by my collaborators (Schwaninger et. al., 2014, Karimaddini et. al., 2014, performed by Z. Karimaddini). Each point of the first stage was registered to the closest point in the next limb bud stage for each individual subdomain separately (Appendix, Publication 4). For intersecting points on curves like AER-limb, ZPA- limb or AER-ZPA, the exact same displacement vector was used for the shared points to avoid improper displacement, which would result in numerical errors.

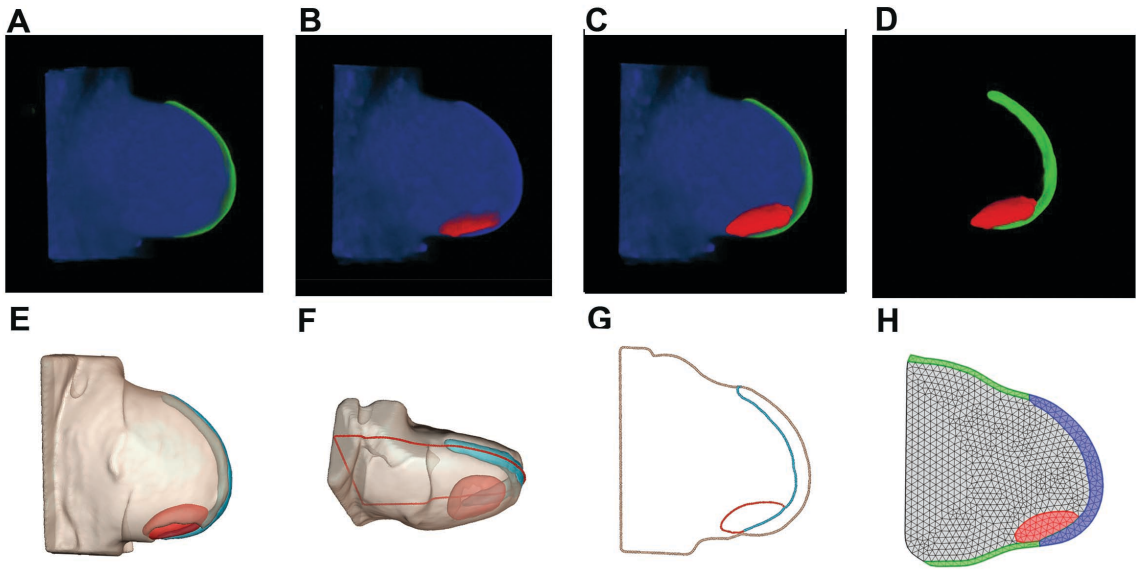

Figure 8. Production of *in silico* limb bud domains with gene expression

3-D images of the *Fgf8* **(A)** and *Shh* **(B)** expression domains were registered at the same stage **(C).** Gene expression domains without the limb bud shapes are shown in panel **(D).** Surface mesh generation using the Amira software results in 3-D geometries with the following domain identities: pink represents the limb bud shape, red the *Shh* and the blue *Fgf8* expression domains. **(F)** The 2-D clipping plane is shown as a red line. **(G)** The resulting 2-D boundaries for the domains are represented as lines. **(H)** The imported boundaries allow generation of a surface mesh using the simulation software Comsol. The AER is indicated in blue, ZPA in red and non-AER ectoderm in green. Representative limb bud shown in the figure is at E 10.5 (37S).

6.3.1.3 Creation and morphing of 4-D (3-D + t) gene expression domains

Simulations in 3-D domain over time (4-D) are computationally expensive. With improvements of computer processors and numerical methods to solve PDE's, 4-D modeling will become a standard to study geometrical and biophysical processes. To address the 4-D growth of the limb, 3-D limb buds were aligned using choosing landmarks on the AER, dorso-ventral ectoderm and along the anterio-posterior axis. Amira permits the use of a Bookstein algorithm (Bookstein, 1997) to calculate displacements between such landmarks. Landmarks were registered in the first and next limb bud stage

and vectors extracted. By registering 34 to 52 S limb buds, I created a 4-D movie of limb bud development that reveals the morphological changes during limb bud development, with particular emphasis on AER and ZPA (Figure 9).

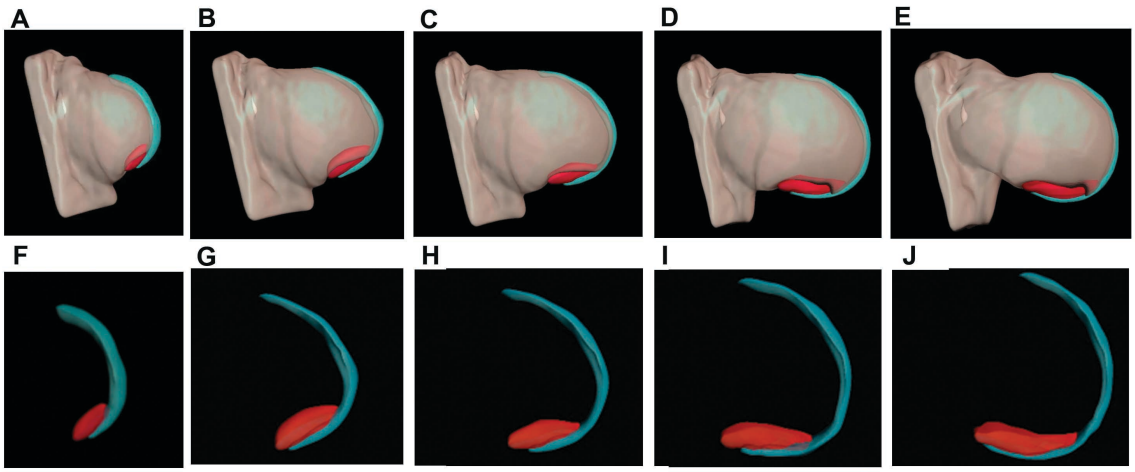

Figure 9. Generation of the 4-D *in silico* limb geometries

The 3-D limb bud geometry of each stage was morphed using Amira. Single frames of the resulting dynamic 4-D are shown for a mouse limb bud at E10.5 (34S) **(A)**, E10.5 (37S) **(B)**, (E10.75) 40S **(C)**, E11.5 (45S) **(D)**, E12 **(**50S) **(E).** AER and ZPA domains alone are shown below each stage in **(F-J).**

6.3.2 Development of an *in silico* model

After we created the 3-D (2-D + t) limb bud geometries, we developed the *in silico* limb bud model. By using reaction-diffusion equations, the components and their interactions were simulated following the steps described below.

6.3.2.1 Model formulation

Reaction-diffusion equations have the form:

$$\frac{\partial Ci}{\partial t} = Di\Delta Ci + Ri(C1, \dots Cn) \quad (4)$$

Here, Ci denotes the concentration of the component i, Di is the diffusion constant of Ci, Δ is the Laplace operator and DiΔCi describes the diffusion of Ci. In the 3-D limb bud shapes with growth vecrors, this equation was complemented with advection and dilution terms (Iber et. al., 2015):

$$\frac{\partial Ci}{\partial t} + u\nabla \mathrm{Ci} + \mathrm{Ci}\nabla \mathrm{u} = Di\Delta Ci + Ri(C1, \dots Cn) \quad (5)$$

Here, term u represents the velocity field of the deforming domain. The reactions that are described using Ri(C1, Cn), which encodes production, degradation, complex formation and activation inhibition dynamics.

The decay term is described as:

$$Rx = -\delta X \quad (6)$$

δ is the decay constant. The activation and inhibition dynamics were formulated using Hill functions, where activation (σ) and inhibition ($\bar{\sigma}$) are:

$$\sigma = X^n / (X^n + K^n) \quad (7)$$

$$\bar{\sigma} = K^n / (X^n + K^n) \quad (8)$$

Zero flux boundary conditions were applied as $\vec{n}\ \nabla C_i = 0$ for all reactions.

6.3.2.2 The network

In our model we used the real limb bud domains with accurate sizes including the AER, ZPA and ectoderm subdomains enabling us to model key aspects of the limb bud development such as establishment of the AER and ZPA activation and SHH pathway kinetics and expression domains of key genes.

We built our gene network based on following published interactions (Figure 10 and Table 1):

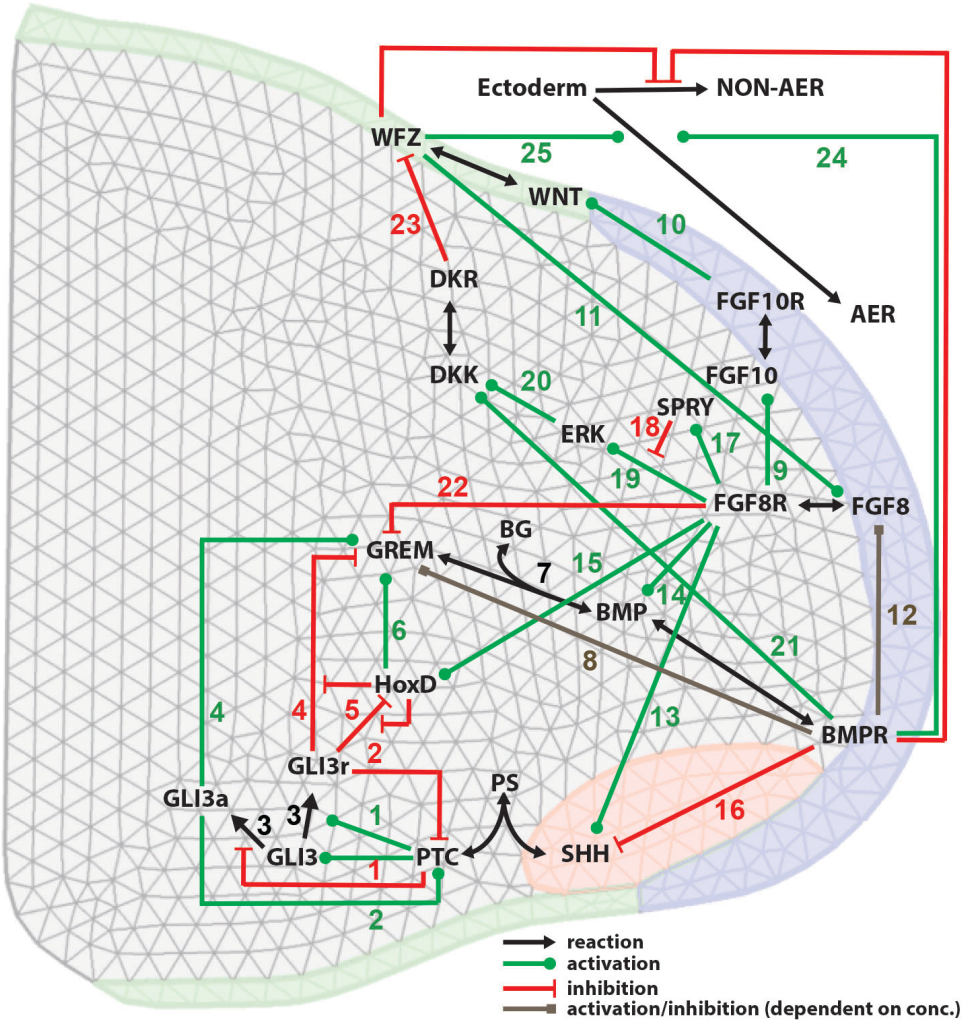

Figure 10. The gene network used for the *in silico* limb model

The network incorporates the major pathways regulating the proliferation, outgrowth and differentiation of the limb bud mesenchymal cells. The mesenchyme (grey), AER (blue), ZPA (red) and the non-AER ectoderm (green) are outlined as subdomains. Positive interactions (e.g. transcriptional up-regulation) are indicated by green lines with a circular arrowhead. Negative regulation (e.g. repression) are indicated by red lines with closed arrowhead. Direct interaction of two molecules like receptor ligand binding interactions (FGF-FGFR, SHH-PTCH, BMP-BMPR, WNT-FZ or sequestration by antagonist (BMP-GREM1) are indicated by red arrows. The PDE's describing the interactions were solved in the growing using somite formation as biological time units.

Interaction number	Publication
1	Wang et. al., 2000
2	Marigo et. al., 2006
3	Wang et. al., 2000
4	teWelscher et. al, 2002
5	teWelscher et. al, 2002
6	Sheth et. al., 2013
7	Zuniga et. al, 1999
8	Benazet. al, 2009, Nissim et. al., 2006
9	Kawakami et. al., 2001
10	Ohuchi et. al., 1997
11	Soshnikova et. al, 2003, Barrow et. al., 2003, Kawakami et. al., 2001
12	Bastida et. al., 2009, Verheyden and Sun, 2008
13	Laufer et. al, 1994
14	Verheyden and Sun, 2008
15	Sheth et. al., 2013
16	Benazet et. al, 2009 Bastida et. al, 2009
17	Minowada et. al., 1999
18	Minowada et.al., 1999
19	Kawakami et. al., 2003
20	Mariani group, in preparation
21	Grotewold , 2002
22	Verheyden and Sun, 2008
23	Mukhopadyhyay , 2001
24	Pizette et. al., 2001
25	Kengaku et. al., 1998

6.3.2.3 Reaction terms

Reaction terms were formulated as described in the previous section. Depending on the gene and interaction of interest the simulations of reactions restricted to the ectoderm, mesenchyme or whole limb bud.

Component R(X)	**Reaction term**
FGF10	$\rho_{FGF10}p_{FGF10}$-d_{FGF10}+(1-1_{MES}) (koff*F10R-konF10(RT_{F10} – F10R))
FGF10R	konR*F10*(RT_F10-max(F10R,0))-(koff+dF10R)*max(F10R,0)
FGF8(F8)	$\rho_{F8}p_{F8}$-d_{F8}+(1_{MES})(koff*F8R)
FGF8R(F8R)	konR*F*(RT_F8-max(F8R,0))-(koff+dF8R)*F8R
WNT	$\rho_{WNT}p_{WNT}$-d_{WNT}+(k_{onR}WNT*(RT-WFZ)+koffWFZ
WFZ	konR*WNT*max(RT-max(WFZ,0),0)-(koff+dWFZ)*max(WFZ,0)
BMP	$\rho_{BMP}p_{BMP}$-d_{BMP}+(k_{onR}BMP*(RT_{BRa}-BRa)+koffBRa
BMPRa (BRa)	konR*BMP*max(RT_BRa-max(BRa,0),0)-(koff_BR+dBR)*max(BRa,0)
GREMLIN (GRM)	ρ_{GRM}*p_{GRM}-(kon*BMP*GRM-$koff_{BG}$*BG)-d_{GRM}*GRM
BMP-GREMLIN	
Complex (BG)	(kon*BMP*GRM-koff_BG*BG-dBG*BG)
SHH	ρ_{SHH}*p_{SHH} –d_{SHH}*SHH-R_PS-d_{SHH}*PS
PATCHED1 (PTC)	ρ_{PTC}*p_{PTC} – R_PS-d_{SHH}*PS
PATCHED1-SHH	
Complex (PS)	konR*PTC*SHH-koff*PS-d_{SHH}*PS
SHH Descendents	
(SDES)	ρ_{DES}*max(RT_DES-min(max(DES,0),RT_DES),0)*(p_{SHH}+0.1*DES)
	d_{DES}*DES
GLI3(GL3)	ρ_{GL3}*p_{GL3}-(d_{GLI3}+kcat)*max(GL3,0)
GLI3R (G3R)	kcat*σ(PTC, K_PTC_GL3)*max(GL3,0)-d_{GLI3}*max(G3R,0)
GLI3A (G3A)	kcat*¯σ(PTC, K_PTC_GL3)*max(GL3,0)-d_{GLI3}*max(G3A,0)
5'HOXD(HXD)	ρ_{HXD}*p_{HXD} -d_{GLI3}*HXD
HAND2 (H2)	ρ_{H2}*p_{H2} - d_{H2}*H2

FACTORX (FX)	ρ_{FX}*p_{FX} - d_{FX}*F_X
FACTORXR	konR*F_X*max(RT-max(RFX,0),0)-(koff+dWFZ)*max(RFX,0)
ERK	ρ_{ERK}*p_{ERK} - d_{ERK}*ERK
DKK	ρD_{KK}*pD_{KK} -R_DKR-d_{DKR}*DKR-d*DKK
DKKR (DKR)	konR*DKK*max(RT-max(DKR,0),0)-(koff+d_{DKR})*max(DKR,0)
SPROUTY (SPY)	ρ_{Spy}*pS_{PY} -d_{SPY}*SPY
AER	if(isnan(AER),0, ρ_{AER}*σ(max(WFZ,0),K_WNT*(1+max(DKR,0)/K_DKR))*σ(BRa,K_BRa_AER)*max(ECT,0)- d_{AER}*$\bar{}$σ(max(WFZ,0),K_WNT1*(1+max(DKR,0)/K_DKR))*$\bar{}$σ(BRa, K_BRi_Apo)*max(AER,0))')
ECT	if(isnan(AER),0,- ρ_{AER}*σ(max(WFZ,0),K_WNT*(1+max(DKR,0)/K_DKR))*σ(BRa,K_BRa_AER)*max(ECT,0)- 0*d_{AER}*$\bar{}$σ(max(WFZ,0),K_WNT1*(1+max(DKR,0)/K_DKR))*$\bar{}$σ(BRa, K_BRi_Apo)*max(ECT,0))
APO	if(isnan(AER),0, d_{AER}*$\bar{}$σ(max(WFZ,0),K_WNT1*(1+max(DKR,0)/K_DKR))*$\bar{}$σ(BRa, K_BRi_Apo)*(max(AER,0)+0*max(ECT,0)))

6.2.3.4 Expression rates

We use the term pSignal/Gene as the term simulating the gene expression patterns.

Component p(X)	**Expression Rate**
FGF10	if((isnan(AER)+isnan(Ecto))==2,(0.05*(Y<1700*factor_Geom1)+σ(max(F8R,0),K_F8R_F10)),0)
FGF8(F8)	if(isnan(AER),0,(ECT+AER)*σ(max(WFZ,0),K_WNT_FGF)*σ(BRa,K_BRa_AER1)*$\bar{}$σ(BRa, K_BRi))
WNT	if(isnan(AER),0, (ECT+AER)*σ(F10R,K_F10R))+if(isnan(Ecto),0, σ(F10R,K_F10R))

BMP	if((isnan(AER)+isnan(Ecto))==2,pBMP0+σ(max(F8R,0),K_F8R_Bmp)*¯σ(BRa, K_BRi_Bmp),σ(max(WFZ,0),K_WNT)*¯σ(BRa, K_BRi_Bmp))
GREMLIN1 (GRM)	if((isnan(AER)+isnan(Ecto))==2,pGRM0+ max(RT_DES-min(max(DES,0),RT_DES),0)*¯σ(F8R,K_F8R_Grm)*(σ(max(HXD,0), K_HXDGrem)*σ(BRa, K_BRa_Grm)*¯σ(BRa, K_BRi_Grm)+σ(G3A, K_G3A))*¯σ(G3R, K_G3R_Grem*(1+ HXD/K_HXDGrem)
SHH	ρSHH*pSHH –dSHH*SHH-R_PS-dSHH*PS
PATCHED1 (PTC)	max((0.01+r_Ptch*σ(G3A, K_G3A_PTC)*¯σ(G3R, K_G3R_PTC)),0)
GLI3(GL3)	σ(PTC, K_PTC)*if((isnan(AER)+isnan(Ecto))==2,¯σ(H2, K_H2),1)
5'HOXD(HXD)	if((isnan(AER)+isnan(Ecto))==2,σ(max(F8R,0),K_F8R_Hxd)*¯σ(G3R, K_G3R_HoxD*(1+ max(HXD,0)/K_HXD)),0)
HAND2 (H2)	if((isnan(AER)+isnan(Ecto))==2,σ(max(RFX,0),K_RFX)*¯σ(G3R, K_G3R),0)
FACTORX (FX)	if(isnan(Ecto_P),0, 1)
ERK	if((isnan(AER)+isnan(Ecto))==2,σ(max(F8R,0), K_F8R_Erk*(1+SPY/K_SPY)), 0*σ(max(F10R,0), K_F10R))
DKK	σ(ERK,K_ERK_DKK)*σ(BRa,K_BRa_DKK)
SPROUTY (SPY)	σ(max(F8R,0),K_F8R_Spy)

6.3.2.5 Limb Bud Geometries

The limb bud geometries and subdomains in this framework are real and accurate biological size. Additionally, the growth data is a realistic approximation. The availability of the ISH data of morphogen readouts and target genes allowed for the adjustment of correct activity thresholds and diffusion reach of the morphogens.

6.3.2.5 Diffusion coefficients

In the limb bud, the diffusion coefficients cannot yet be measured accurately. Measured diffusion coefficients for diffusible proteins in tissue are typically in

the range 0.1-20 μm^2/sec (Kicheva et. al., 2007, Yu et. al., 2008). A diffusion coefficient of D = 1 μm^2/sec was used for diffusible signaling molecules and antagonist, while for transcription factors and receptors D_R = 0.01 μm^2/sec was applied.

6.3.2.6 Production rates

Production rate	Value
ρ	10^{-4}
ρ_{F8}	10^{-4}
ρ_{F10}	$1.5x10^{-4}$
ρ_{WNT}	10^{-4}
ρ_{DKK}	$2x10^{-3}$
ρ_{BMP}	$5x10^{-3}$
ρ_{GRM}	20
ρ_{PTC}	10^{-3}
ρ_{SHH}	$2.5x10^{-3}$
ρ_{DES}	$2x10^{-4}$
ρ_{GL3}	10^{-3}
ρ_{ERK}	$3x10^{-4}$
ρ_{SPY}	10^{-3}
ρ_{HXD}	10^{-6}
ρ_{FX}	10^{-6}
ρ_{H2}	10^{-4}

6.3.2.7 Decay rates

For most of the variables a decay rate of d = 10^{-6} mM/sec was used. However, different decay rates were used for the following molecules:

Component d_x	Decay Rate
d_{SHH}	10^{-5}
d_{H2}	10^{-4}
d_{SHH}	10^{-5}
d_{GRM}	10^{-2}
d_{BG}	10^{-2}
d_{ERK}	10^{-4}
d_{SPY}	10^{-4}
d_{BR}	10^{-6}
d_{WFZ}	$5x10^{-6}$
d_{F8R}	$8x10^{-5}$
d_{F10R}	10^{-4}
d_{DKR}	10^{-4}
d_{GLI3}	$4x10^{-5}$

6.3.2.8 Hill constants

Component K_x_y	**Hill Constant**
K_F8R	0.025
K_F8R_Bmp	0.5
K_F8R_F10	0.025
K_F8R_Erk	15
K_F8R_Spy	0.16
K_F8R_SHH	0.025
K_F8R_Hxd	0.004
K_F8R_Grm	0.25
K_F10R	1
K_SPY	1
K_ERK	0.01
K_ERK_DKK	0.01

K_ERK_BMP	0.001
K_ERK_F10	0.01
K_BRa_DKK	0.01
K_BRa_AER	0.05
K_BRa_AER1	0.001
K_BRa_Grm	0.05
K_BRa_SHH	0.3
K_BRi	4
K_BRi_Apo	0.3
K_BRi_Bmp	100
K_BRi_Grm	100
K_PTC	1
K_PTC_GL3	1
K_G3A	0.5
K_G3A_PTC	1
K_G3R	3
K_G3R_PTC	0.5
K_G3R_Grem	0.33
K_G3R_HoxD	0.03
K_SHH	1000
K_DKR	0.001
K_HXD	0.1
K_HXDGrem	0.1
K_HXDself	1000
K_WNT_Dkk	0.01
K_WNT	0.1
K_WNT_FGF	0.1
K_WNT1	0.05
K_WNT_Grem	1
K_WNT_Bmp	0.01

K_RFX	2
K_H2	0.02

6.3.2.9 Initial values

Component init_x	**Value**
init_Ptch	2.5
init_Bmp	100
init_Gli3	5
init_F10	0.05

6.3.2.10 Association and dissociation constants

Component K_{on}, K_{off}	**Value**
K_{cat}	$4x10^{-5}$
K_{on}	10^{-3}
K_{off}	10^{-6}
K_{offBR}	$6x10^{-4}$
K_{offBG}	10^{-4}

6.3.3 *In silico* simulations of limb bud networks and growth characteristics

6.3.3.1 The Simulations of AER, ZPA and ectodermal domains

We took our *in silico* domains derived from real gene expression domains to study growth characteristics between 21 until 60 somites (S) computationally. This allowed us to simulate the spatio-temporal dynamics of AER-*Fgf*, *Shh* and *Wnt* expression during limb bud outgrowth (Figure 11-14)

6.3.3.2 Simulation of limb bud initiation

Limb bud initiation is regulated by *Fgf10*, which is expressed by the lateral plate mesenchyme (Ohuchi et. al., 1997). In *Fgf10* deficient limb buds *Fgf8* expression is not activated and outgrowth is disrupted (Sekine et. al, 1999, Min et. al., 1998). A feedback loop between FGF10 and FGF8 coordinates the interaction between the mesenchyme and the ectoderm (Ohuchi et. al., 1997). This feedback loop has an additional intermediate mediator, the *Wnt3a* signal (Kawakami et.al., 2001). FGF10 activates *Wnt3a*, which in turn upregulates *Fgf8* expression. *Fgf8* in turn propagates *Fgf10* expression in the mesenchyme (Kawakami et. al., 2001). This *Fgf10*-*Wnt*-*Fgf8* feedback loop is an integral part of our model simulations (Figure 10, Figure 11-A). The mesenchymal FGF10 is the signal activated first in the mesenchyme. FGF10 binds to its receptor FGFR2IIIb in the ectoderm (Figure 11-B) and activates the expression of the *Wnt3*a ligand. The latter activates canonical WNT signaling in the ectoderm and underlying mesenchyme (Figure 11-C). WNT upregulates *Fgf8* expression in the AER in a *β-Catenin* dependent manner. (Figure 11-D). The AER-FGFs signal from the AER to the underlying mesenchyme by binding to its receptor FGFR2IIIc (Xu et. al., 1998, Arman et. al., 1998, Figure 11-D). Previous analysis has shown that *β-Catenin* deficient limb buds lose *Fgf8* expression at very early stages (Barrow et. al., 2003). This can be simulated by our model: simulations of *Wnt* deficient limb buds results in loss of *Fgf8* expression (Figure 11-E) and inactivation of *Fgf10* results in absence of AER-*Fgf* and disrupts limb bud outgrowth (Figure11-F).

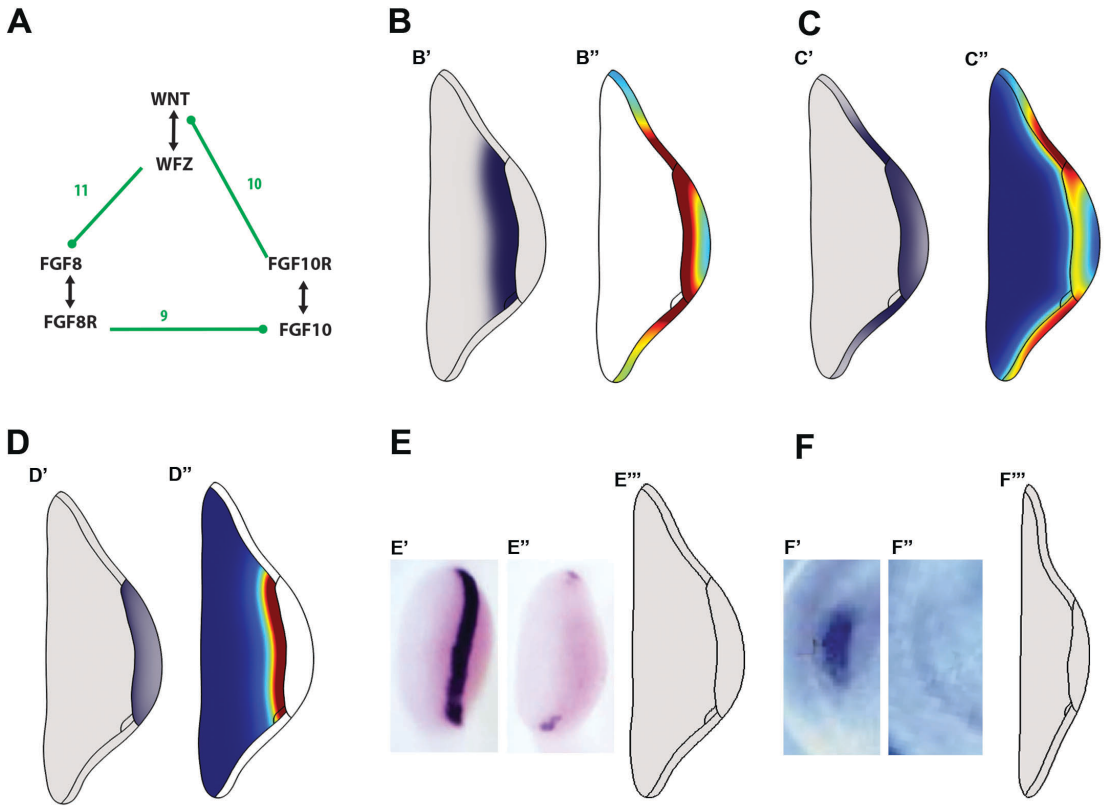

Figure 11. Simulations of the Fgf10-Wnt-Fgf8 feedback loop interaction

(A) Feedback loop interactions. WFZ, FGF10R and FGF8R are complexes with the receptors. **(B)** The simulated mesenchymal *Fgf10* expression domain (left). FGF10 signals to ectoderm by interacting with its receptor FGFR2IIIb in the ectoderm (right). This activates ectodermal WNT signaling. **(C)** The simulated ectodermal *Wnt* expression (left) signals to both in ectoderm and underlying mesoderm (right). **(D)** AER-*Fgf8* expression is positively regulated by ectodermal Wnt signaling. Simulated *AER-Fgf* expression (left) and AER-FGF-FGFR2IIIc interactions (right) are shown. **(E)** In β-catenin deficient limb buds the Fgf8 expression is lost (Borrow et. al., 2003, left). Simulation of Wnt deficient limb buds reproduces as the loss of AER-FGF expression (right) shows also lack of Fgf expression (right). **(F)** Limb bud initiation and activation of AER-Fgf expression is disrupted in *Fgf10* deficient limb buds (Sekine et. al., 1999, left). The simulations reproduce these results (right).

6.3.3.3 The AER-FGF pathway

Four *Fgf* genes are expressed by the AER, namely *Fgf8*, *Fgf4*, *Fgf9* and *Fgf17* (AER-*Fgf's,* Martin, 1998). *Fgf8* is expressed by the entire AER in

whole AER and the other three within a posterior to anterior progressing fashion (Figure 12-A, data not shown). Genetic inactivation of different combinations of *Fgf* genes has shown that in mouse limb buds the four FGF ligands constitute a total AER-FGF signal with partially redundant functions (Mariani et. al., 2008). Therefore we define one variable encompassing all four AER-*Fgf*s. Simulating this AER-*Fgf* expression results in stronger posterior than anterior AER expression (Figure 12-B).

The FGF ligands signal from the AER to the underlying mesenchyme by binding to the FGFR2IIIc receptor isoform (Xu et. al., 1998, Arman et. al., 1998, Figure 12-C-E). *Spry4* is a direct target transcriptional readout of AER-FGFs. We set the activation threshold for AER-FGFs such that it reproduces *Spry4* expression in the limb mesenchyme (Figure 12-F). The simulation of AER-*Fgf* activities over 3 developmental days is shown in Figure 12-G.

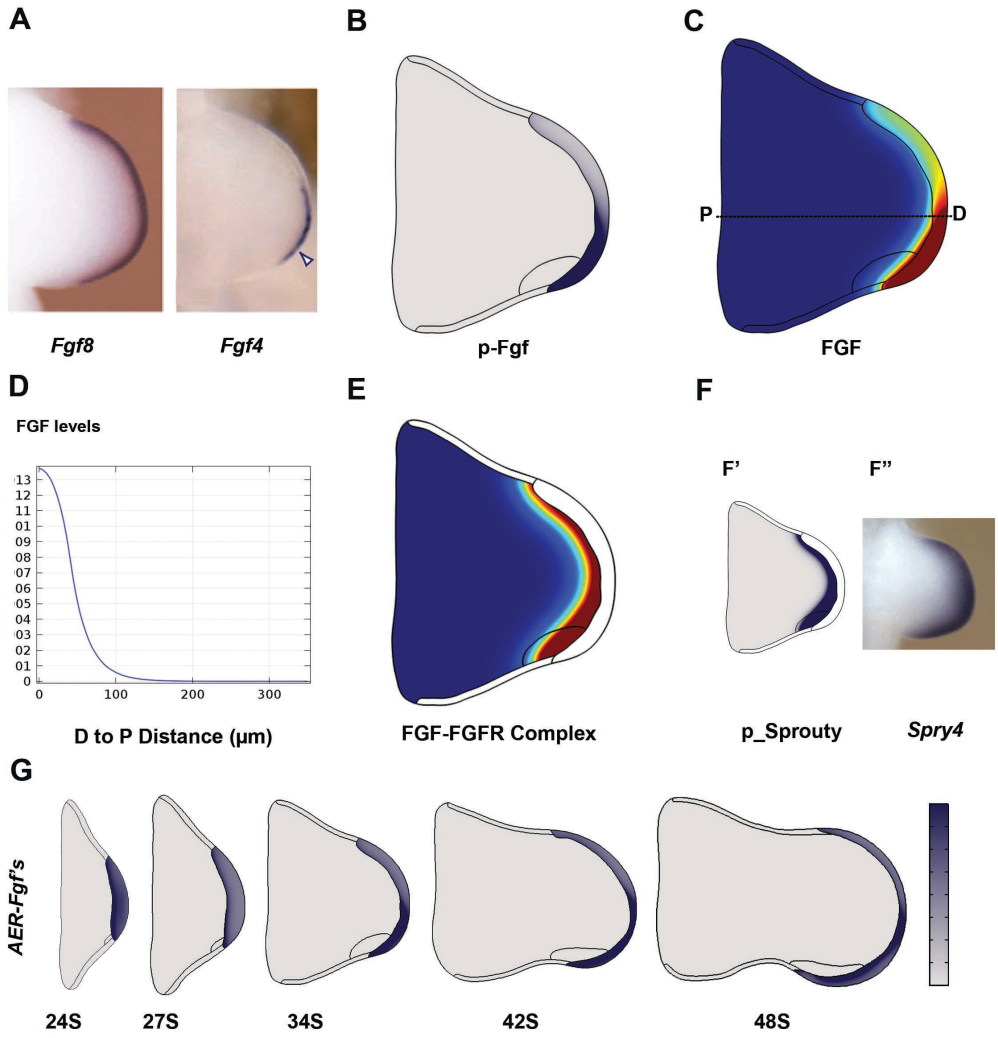

Figure 12. FGF pathway simulations

(A) *Fgf8* is expressed by the entire AER (left) and *Fgf4* extends from posterior to anterior during progression of limb bud development (right). The left panel was modified from Benazet et. al., 2012 and the right panel was modified from Zuniga et. al., 1999. **(B)** The simulation of AER-*Fgf* is representative of all four AER-*Fgf*s. **(C)** Free FGF ligand diffuses into mesenchyme. **(D)** The diffusion range extend is plotted in 1-D from distal to proximal along the PD axis indicated in panel (C). **(E)** AER-FGF's bind to the FGFR2IIIc receptor isoform in the mesenchyme. **(F)** The expression of *Spry4* serves as a read-out of FGF signaling. Note the similarities between the real limb bud expression and simulated domain (left). The right panel is modified from Probst et. al., 2012. **(G)** Dynamic simulation of AER-*Fgf* domains at selected time points.

6.3.3.4 SHH signaling

The SHH morphogen binds its receptor PTCH1 to activate the pathway and *Ptch1* itself is a direct transcriptional target of SHH signal transduction (Chen and Struhl, 1996, Marigo et. al., 1996, interaction 2, Figure 13-A). This positive feedback regulates the pathway by enhanced sequestering of SHH by PTCH1 and restricts the diffusion of the SHH morphogen (Briscoe et. al., 2001). In vertebrates, SHH target genes are regulated by the GLI1 to GLI3 transcription factors. The SHH signal transduction inhibits the proteolytic processing of GLI3 to its receptor, GLI3R at primary cilia (Wen et. al., 2003, Figure 13-A). Since GLI3 is the only transcriptional regulator required on its own (Park et. al., 2000, Cao et. al., 2013), this allowed us to simplify the simulations by using GLI3 as sole transcriptional regulator of SHH signal transduction (Figure 13-A, interaction 1, 2). *Shh* is expressed by the ZPA and the SHH ligand diffuses from its posterior source toward anterior mesenchyme (Figure 13-B, C). The simulated range of the SHH morphogen reproduces the SHH protein distribution localization detected by immunofluorescence (Figure 13-C, D; Gritli -Linde et.al, 2001, Lopez -Rios et. al., 2014). GLI3R is localizes to the anterior mesenchyme where no significant SHH signal transduction is detected (Figure 13-F). The *Shh* expression starts around somite stage 28-30S and its expression domain expands until about 45S. *Shh* expression terminates around 55-58 S in the simulations (Data not shown).

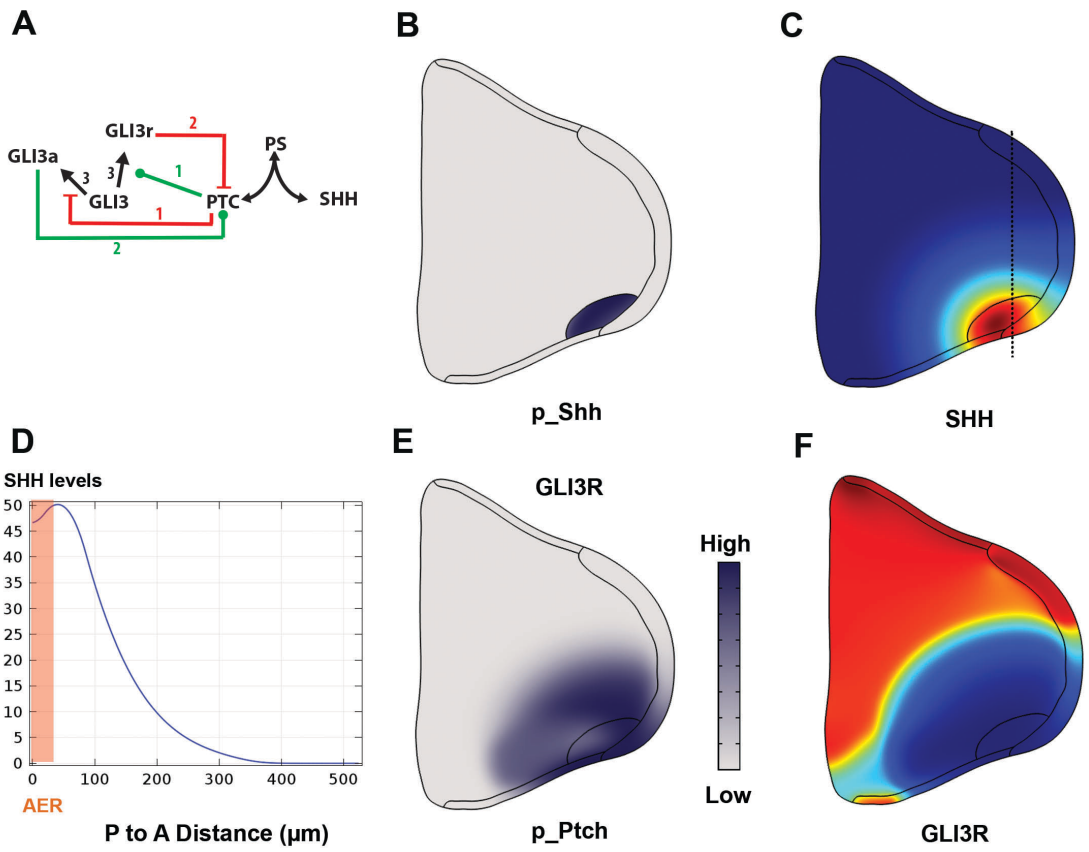

Figure 13. SHH pathway simulations

(A) SHH interacts with its receptor PTCH1 to activate SHH signal transduction. *Ptch1* itself is a direct target of the pathway. GLI transcription proteins are mediators of SHH signal transduction. In presence of SHH, GLI3 is in an activator that positively regulates SHH target genes. In the anterior part of limb bud mesenchyme, GLI3R represses target genes in the absence of SHH. **(B)** Simulated *Shh* expression is restricted to ZPA. **(C)** Produced SHH protein diffuses in the mesenchyme in a anterior direction and to the AER. **(D)** 1-D plot of SHH diffusion. **(E)** Simulated *Ptch1* expression pattern. **(F)** GLI3R is present in the anterior limb bud, where SHH signaling is very low or not present.

6.3.3.5 The BMP pathway activity

Bone morphogenic proteins (BMPs) play essential roles for the several stages of the limb bud development: during AER establishment and dorso-ventral patterning (Selever et. al., 2004, Pizette et. al., 2001, Benazet et. al., 2009), fine tuning of the e-m feedback loop (Pizette and Niswander, 1999, Benazet

et. al., 2009), chondrogenic differentiation (Pizette and Niswander, 2000, Benazet et. al., 2009, Badugu et. al., 2012), interdigital cell death (Dahn and Fallon, 2000), and finally for termination of the e-m feedback loop (Bastida et. al., 2009, Germann et. al., in revision). BMP activity is regulated by its antagonist GREM1 during progression of limb bud development (Michos et. al., 2004). GREM1 physically binds to BMPs and sequesters them (Hsu et . al., 1998, interaction 7, Figure 14-A). BMP activity is initially high in the limb bud mesenchyme (Benazet et. al., 2009, Figure 14-D). *Grem1* expression is activated by BMP4 signal transduction and upregulated subsequently by SHH, which lowers BMP activity as part of the SHH/GREM1/AER-FGF signaling system (Figure 14-E,F; interaction 8). The simulations could reproduce dynamic expression pattern of *Bmp4* and *Grem1* realistically (Figure 14-G, data not shown)

6.4 Cross-talk between BMP and WNT signaling pathways: regulation of *Grem1* expression by WNT signal transduction

Using the *in silico* limb simulations of the gene regulatory networks, we could reproduce most of the gene expression patterns in limb bud development (Figure 11-14). The *Grem1* has one of the most dynamic gene expression patterns in the limb and its expression is controlled by various pathways. In addition to its dynamic AP pattern, its expression is restricted to the dorsal and ventral subectodermal mesenchyme (Figure 15-B-D). This pattern suggests two possible regulatory mechanisms: possibly, an ectodermal signal diffuses into the mesenchyme that positively controls *Grem1* expression in the subectodermal mesenchyme. Alternatively, a repressor is present in the core

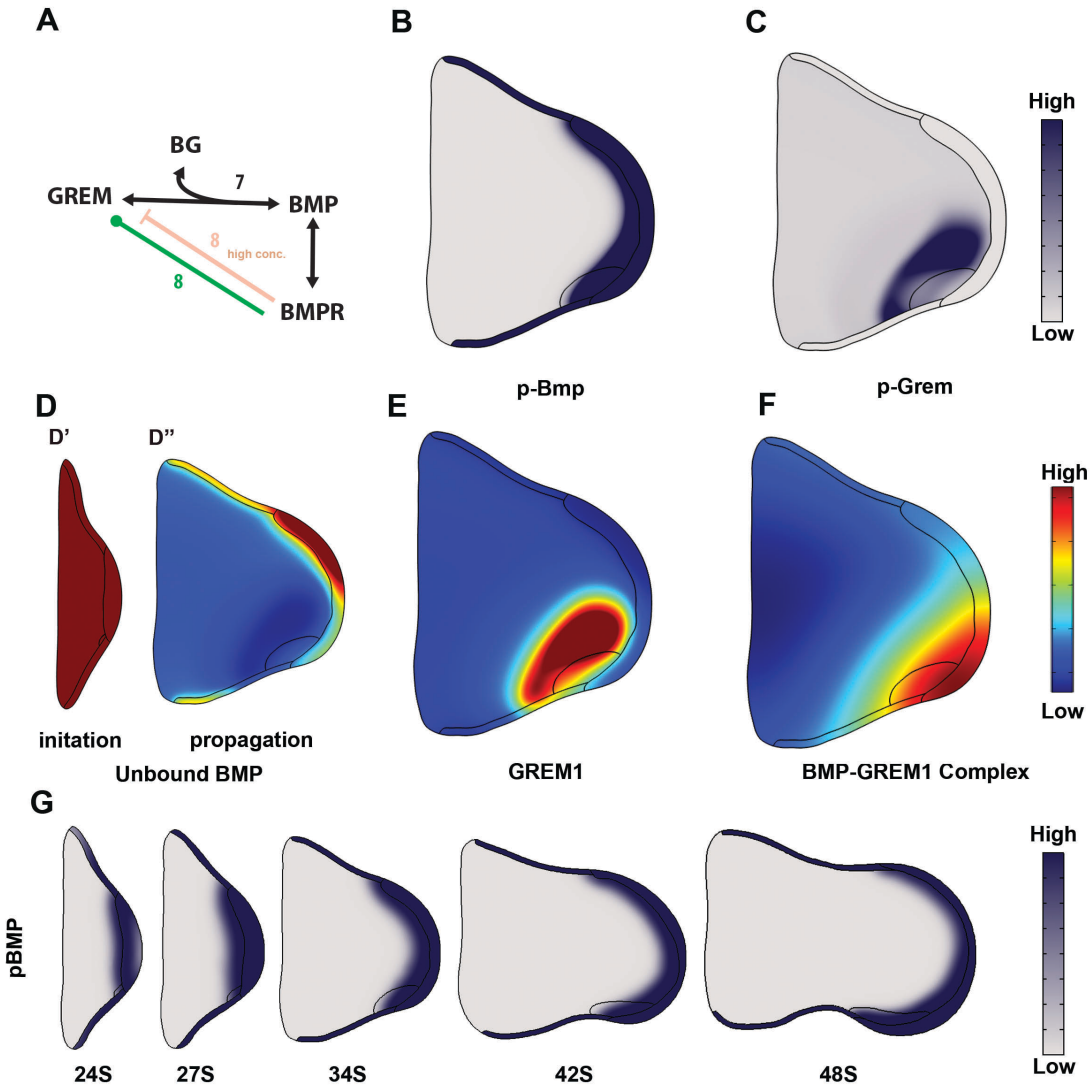

Figure 14. BMP pathway simulations

(A) BMP proteins interact with BMP receptor to induce cell differentiation and/or cell death in advanced limb buds. BMP is sequestered by its antagonist GREM1 during the limb bud outgrowth. *Grem1* is a direct transcriptional target of BMP signal transduction. However, bead experiments have shown that high concentrations of BMP can also inhibit the *Grem1* expression. Simulated BMP **(B)** and Gremlin **(C)** expression domains are similar to the real domains observed in limb buds. **(D)** Simulation of unbound BMP during the onset (high) and propagation (low) of limb bud outgrowth. **(E)** GREM1 protein. **(F)** The BMP-GREM1 complex. **(G)** Dynamic simulation of *Bmp* expression domains at selected time points.

mesenchyme thereby restricting *Grem1* expression to the subectodermal mesenchyme. However, none of the currently known pathways controlling *Grem1* expression in limb buds are expressed ectodermally or in the subectodermal mesenchyme. Since the testing of the second hypothesis would be more difficult, I focused on the first on the possibility of an unknown ectodermal signal regulating *Grem1* expression.

Using 3-D imaging and optical sectioning of *Grem1* expression domains, I determined that *Grem1* expression extends around 100 μm into the mesoderm below the dorsal and ventral ectoderm (Figure 16-C, D). This suggested that *Grem1* might be regulated by unknown ectodermal factors, possibly ectodermal WNTs. I decided to assess the potential impact of the WNT signal transduction on *Grem1* expression. Initially, I used the limb bud culture system (Zuniga et. al., 1999, Panman et. al., 2006) to block WNT signal transduction by utilizing a very well characterized specific inhibitor called: the Inhibitor of WNT Production compound 2 (IWP-2, Chen et. al., 2009, tenBerge et. al., 2011, Raspopovic et. al., 2014). This compound blocks the membrane bound O-acyltransferase PORCUPINE (Porcn), which normally functions to add a palmitoyl group to WNT proteins, which is essential for their activation and secretion (Chen et. al., 2009). Initially, a dose-response experiment was done to determine the optimal concentration and incubation time (data not shown). This resulted in limb buds being cultured at at 2 μM IWP2 for 6 hours. The 6 hours incubation was chosen to monitor possible direct regulation of *Grem1* transcription by WNT signaling.

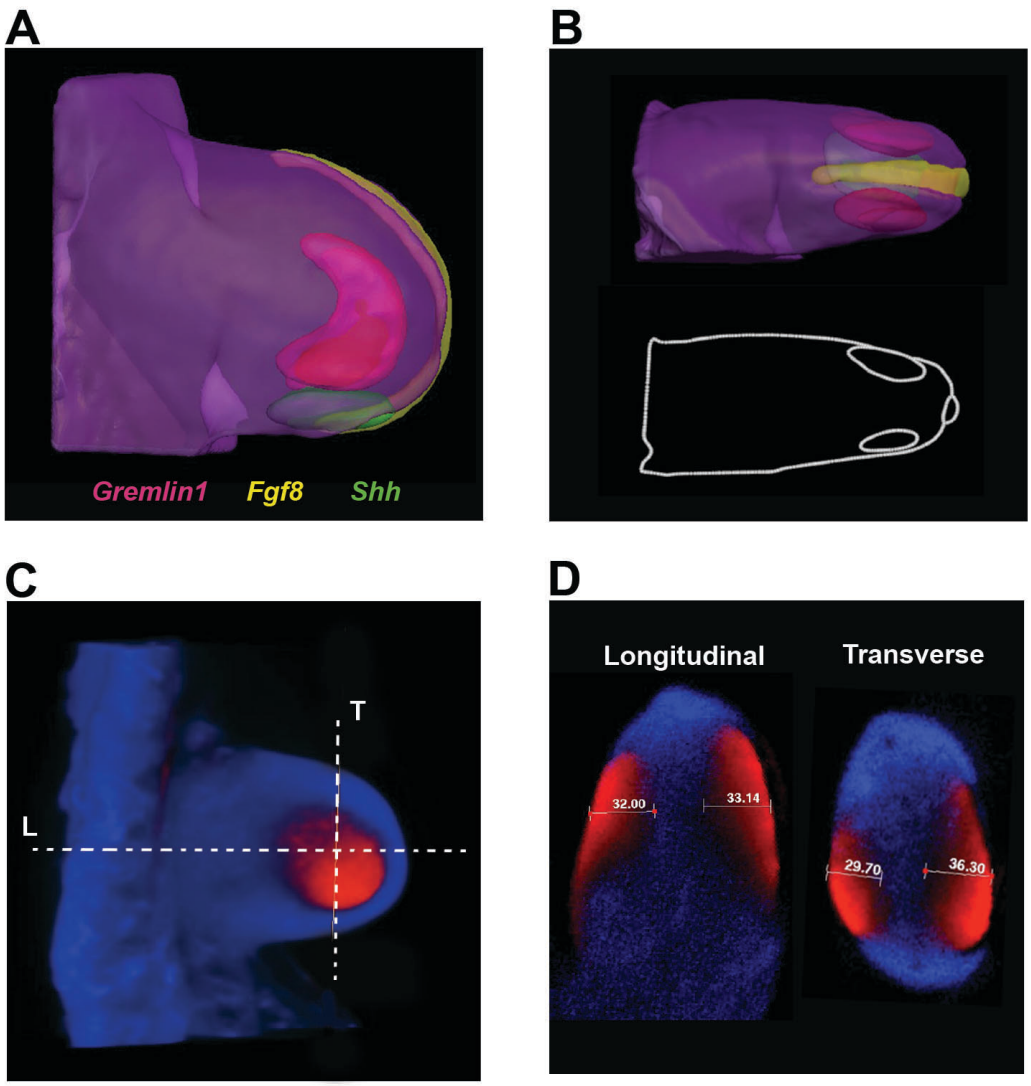

Figure 15. 3-D analysis of the *Grem1* expression domain

(A) 3-D representation of expression patterns of *Gremlin1*, *Fgf8* and *Shh* overlaid in the same forelimb bud (E10.5, 37S). **(B)** Side-view of the posterior limb bud. Gremlin1 expression is restricted to the dorsal and ventral side (top), which is more evident in the surface section (bottom). **(C)** The DV extend of the *Grem1* expression domain was measured on longitudinal (L) and transverse (T) sections. **(D)** The *Grem1* expression domain extended around 100 µm into the dorsal and ventral subectodermal mesenchyme. These values were determined using voxel values.

Limb buds cultured with 2 μM IWP-2 show decreased expressions of *Axin2 and N-Myc,* which are both direct transcriptional targets of WNT signaling (Figure 16-B, C, tenBerge et. al., 2008). *Sox9*, which is inhibited by WNT signaling, was expanded distally and dorso-ventrally (Figure 16-D). *Gremlin1* expression was decreased in a striking manner by inhibiting WNT signaling (Figure 16-A). In particular, expansion of *Gremlin1* to the anterior limb bud mesenchyme was blocked. This indicated that WNT signaling regulates the distal-anterior expansion of Grem1 expression. The remaining expression in the posterior mesenchyme is likely a consequence of the remaining positive inputs of SHH, BMP and AER-FGF pathways (Figure 16-A). Indeed, the expression of *Shh, Gli1 and Fgf8* were not altered by blocking WNT signaling (Figure 16-E,F). Additionally, the mesenchymal *Msx2* expression remained, which is indicative of continued BMP signal transduction (Benazet et. al., 2009). The expression of *Hoxd13* expression was also remained as in untreated limb buds. Thus, the loss of *Grem1* expression in distal-anterior mesenchyme appeared as specific consequence of blocking WNT pathway. Additionally, 6 hours of WNT inhibition results in reduced *Grem1* expression, which points for a likely direct effect.

To genetically assess this novel regulatory interaction, we genetically inactivated the WNT signal transduction by conditional deletion of the signaling mediator *β-Catenin* from the limb bud mesenchyme in Prx-Cre; *β-Catenin*$^{fl/fl}$ mouse embryos. The forelimb buds of Prx-Cre; *β-Catenin*$^{\Delta c/\Delta c}$ embryos were truncated because of disrupted AER establishment and FGF10-WNT3-FGF8 feedback signaling (Figure18-A, compare to Figure 7-A, Kawakami et. al., 2001, Ohuchi et. al., 1997). Therefore, we analyzed hind

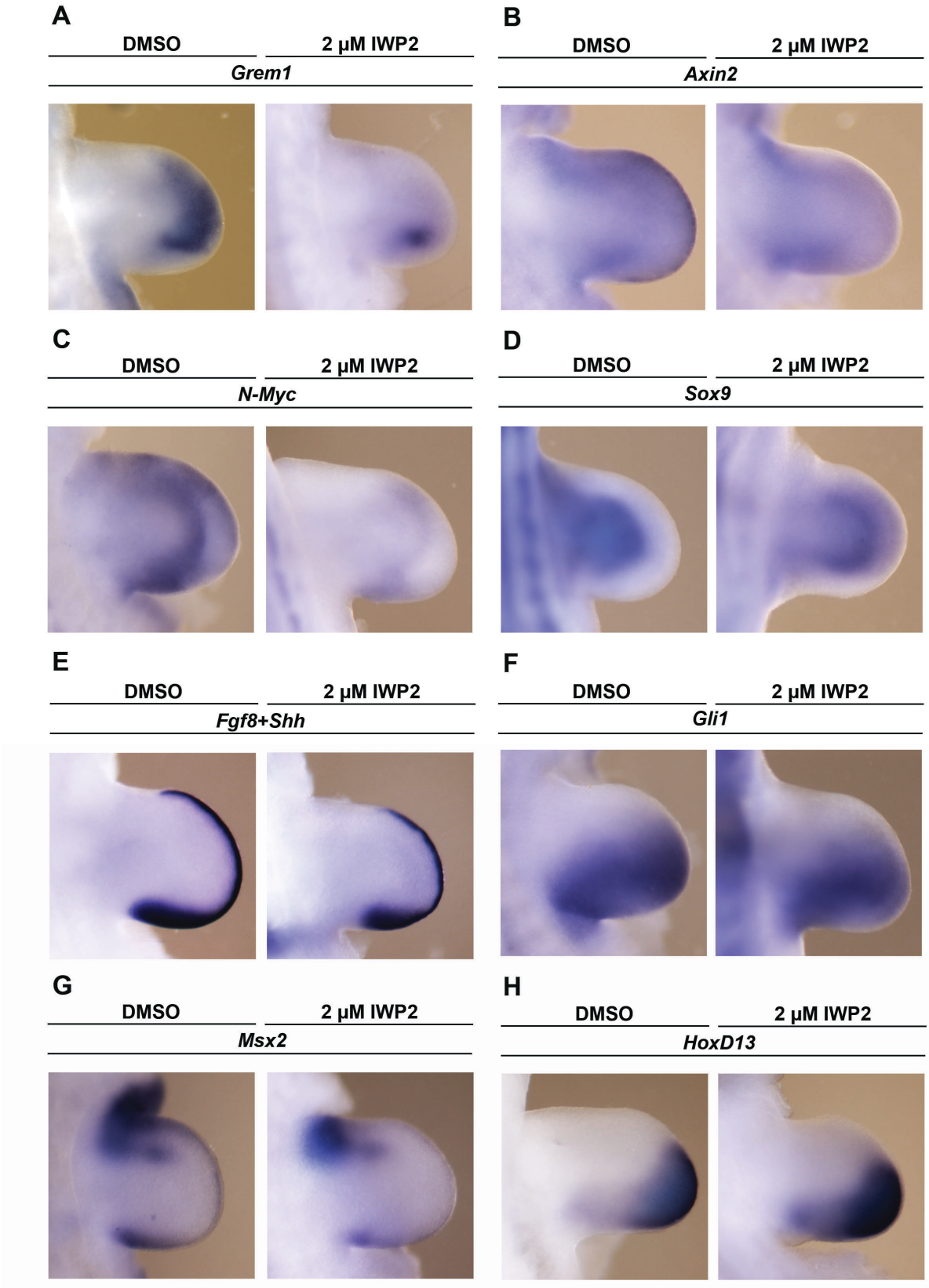
A
DMSO
2 µM IWP2
Grem1
B
DMSO
2 µM IWP2
Axin2
C
DMSO
2 µM IWP2
N-Myc
D
DMSO
2 µM IWP2
Sox9
E
DMSO
2 µM IWP2
Fgf8+Shh
F
DMSO
2 µM IWP2
Gli1
G
DMSO
2 µM IWP2
Msx2
H
DMSO
2 µM IWP2
HoxD13

Figure 16. Inhibition of WNT signaling results in loss of *Grem1* expression in the distal mesenchyme

(A) Limb buds exposed to IWP2 for 6 h show significantly reduced *Grem1* expression (right) in comparison to control limb buds exposed to DMSO. The WNT targets *Axin2* **(B)** and *N-Myc* **(C)** were also downregulated by IWP2 inhibition. **(D)** Expression of *Sox9*, which is normally repressed by WNT, was expanded following IWP2 treatment. The expression of *Fgf8*, *Shh* **(E)** *and Gli1* **(F)** was not altered by WNT inhibition. *Msx2* **(G)** and *HoxD13* **(H)** expression was also not altered.

limb buds, in which the activation of Prx-Cre activity is delayed by about 12 hours. These limb buds showed normal outgrowth (Figure 17-B), while the expression of the WNT target *Axin2* was decreased (Figure 17-C). In comparison to wild type limb buds, the expression of *Sox9* gene was expanded (Figure 17-D), while *Hoxd13* and *Gli1* expression remained (Figure 17-E, F). *Bmp4* expression and expression of the direct target remained at wild-type levels upon *Id-1* also stayed at WT levels upon *β-Catenin* inactivation (Figure 17-G, H). In contrast, *Grem1* expression was lost from the anterior mesenchyme and reduced and patchy in the posterior mesenchyme (Figure 17-A). In addition, *β-Catenin* was inactivated during hand plate development using Hoxa13-Cre transgene. In Hoxa13Cre; *β-Catenin*$^{\Delta c/\Delta c}$ limb buds the expression of *Axin2* levels in the hand plate was decreased (Figure 18-B). The normally distal *Grem1* expression domain was completely lost from the hand plates of mutant limb buds (Figure 18-A).

These results show that WNT signaling is crucial for *Grem1* in the distal dorsal and ventral mesenchyme and its propagation and maintenance during hand plate development. The *Sox9* expression was extended to distal limb (Figure 18-C). The embryos showed aberrant digit identities and fusions

indicating that WNT signaling is essential during hand plate formation. Skeletal stainings of the mutant limbs reveal the fusion of digits 2-3-4 (Figure 18-D). Taken together, this analysis using limb bud culture and genetics show that *Grem1* expression in the distal mesenchyme depends on WNT signal transduction.

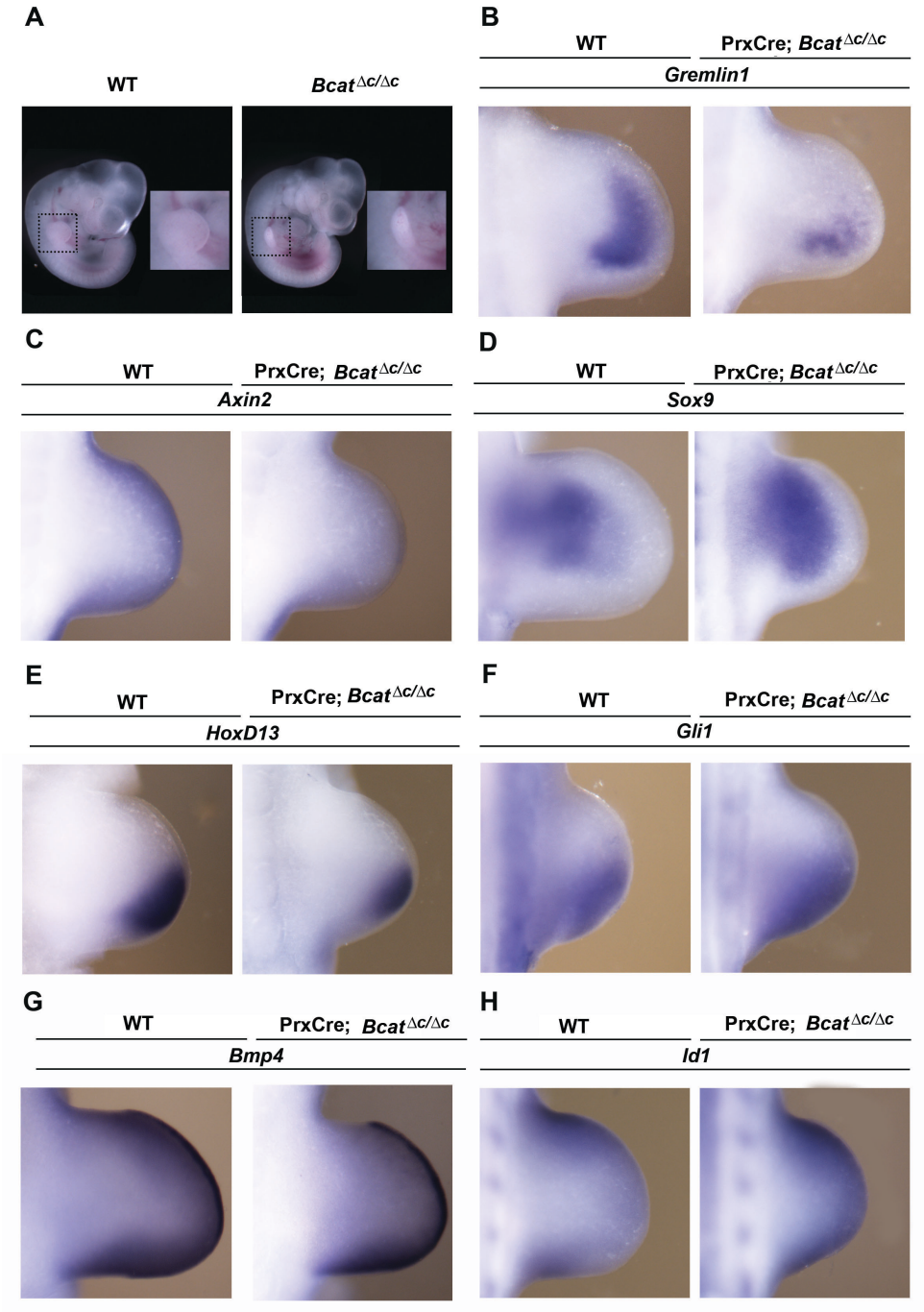

Figure 17. Genetic inactivation of *βcatenin* in the hindlimb bud mesenchyme results in loss of *Grem1* expression in the distal limb mesenchyme

(A) *Grem1* expression was downregulated in the limb buds of PrxCre; *βcatenin*$^{\Delta c/\Delta c}$ mouse embryos. In particular, the expression in the distal-anterior mesenchyme was lost. (**C)** *Axin2* was also downregulated. **(D)** In contrast, *Sox9* expression was expanded. *HoxD13* **(E),** *Gli1* **(F),** *Bmp4* **(G)** and *Id1* **(H)** levels were not altered in the hind limb buds.

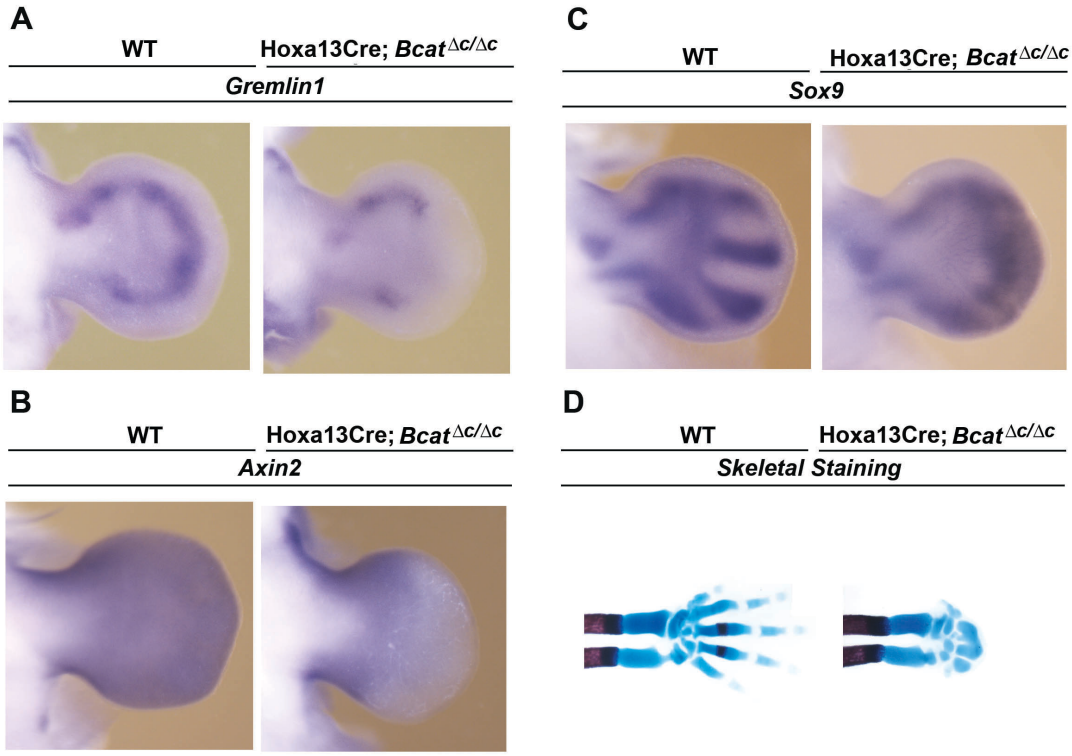

Figure 18. Specific inactivation of WNT signaling in the mesenchyme of advanced limb buds reveals the requirement of WNT for *Grem1* during hand plate development

(A) *Grem1* expression was lost from hand plates of Hoxa13Cre; *βcatenin*$^{\Delta c/\Delta c}$ mouse embryos. (**B)** *Axin2* was also down-regulated WNT signaling activity in the hand plate mesenchyme. **(C)** *Sox9* expression marks the digit ray progenitors in the WT (left). In the *βcatenin* deficient hand plates, single digit primoridas were not formed and *Sox9* expanded to into the distal mesenchyme (right). **(D)** Skeletal staining of the WT (left) and mutant (right) limbs. The *βcatenin* deficiency in the hand plate results in 2-3 digits, which are fused.

7. DISCUSSION

Vertebrate organogenesis has long fascinated researchers and is still intensively investigated to understand how the shape of an organ is built from proliferating progenitors. These progenitors undergo complex changes and they divide, migrate, differentiate and/or initiate apoptosis, which ultimately defines shape of an organ. Insights from classical experimental manipulation were complemented by molecular analysis, which identified the underlying key genes and signaling networks. Now, the major aim is to integrate this knowledge into complex-systems analysis including model simulations to gain more understanding of the relevant processes.

I focused on studying development of the vertebrate limb from initiation of limb buds to pattern formation. To that aim, I collected high quality quantitative data describing limb bud growth. This quantitative analysis allowed me to study the changes in the growth behavior. In addition, I collected growth data of the chicken wing buds, which uncovered what appear to be evolutionary conserved growth rules. This data was also compared with published growth data on *Drosophila* wing disc growth. Our analysis suggests that differentiation alone cannot explain the changes in the growth dynamics and the size changes of limb buds and that an unknown a more general mechanism likely controls the constant decrease proliferation and growth of limb buds. Using the *in silico* model simulations of limb bud development, we simulated a core gene regulatory network that controls key interactions during of the limb bud development. We used the computational power of simulations to model the behavior of gene networks by *in silico* mimicking of mutant conditions. This was done by setting the expression and the

production rate of the gene to zero. We compared the simulated gene expression of targets with the published qPCR and microarray data. The insights from 4-D image analysis and computational modeling led me to realize that an unknown additional interaction controls the expression of *Grem1*.

7.1 Quantitative analysis of limb bud development and growth control

Proliferation is key to produce sufficient mesenchymal progenitors and to correct pattern limb bud. During the limb bud development, progenitor cells are expanded in a controlled manner to generate e.g. the pools of chondrogenic progenitors for the skeletal elements. Defective proliferation or altered cell survival will result in severe limb skeletal defects (Chiang et. al., 2001, Michos et. al., 2004, Khoka et. al., 2003). Increased proliferation or delayed exit to chondrogenic differentiation results in formation of additional skeletal elements, particular digit polydactyl (Hui and Joyner, 1993, Lopez-Rios et. al., 2012).

We quantified limb bud volumes, limb bud axis expansion and the number of mesenchymal progenitors to gain insights into the proliferative expansion kinetics of mouse limb buds. In particular, I determined the average and stage specific cell doubling times in limb buds. This analysis reveals exponential proliferation and bi-phasic behavior because of proliferation slowed-down in all measured datasets. I then investigated if this decrease occurs at the phase-switch stage of limb bud development or if there is a gradual decrease in proliferative expansion. Using BrdU incorporation, the proliferative index of

Sox9+ and Sox9- cell populations were measured. The difference in the proliferation index was similar in both populations decreased by about 20% decrease in S-phase between the two phases. Interestingly, this decrease in proliferation was also seen in Sox9- population. In addition, I observed a decrease by comparing limb buds from 26-29S and 36-40S mouse embryos, which pointed to a continued decrease in cell proliferation. This decrease in the proliferation might be a consequence of the activation of *Sox9* expression, which appears around E10 (30S, Benazet et. al., 2012). The two distinct phases of proliferation could be due to the increase in Sox9+ cells, which amounts for about 45% ± 3% in the E 11.75 (48-52S).

A recent report suggested that proliferation and differentiation of mesenchymal progenitors were coupled through the ectodermal WNT signaling (tenBerge, et. al., 2008). Intriguingly, limb buds lacking *N-myc* have reduced proliferation, resulting in a reduced chondrogenic core, although the non-chondrogenic region remained the same, namely around 100 µm. The limb buds that overexpressed *N-myc* had larger limbs and thus much larger chondrogenic core, where non-chondrogenic core remained still around 100 µm (tenBerge et.al., 2008). This coupling indicated that the Sox9+ population giving rise to the chondrogenic core is most sensitive to molecular alterations in proliferation, which is coordinated by WNT signaling and its target *N-Myc* (ten Berge et. al., 2008).

7.2 OPT imaging as powerful 3-D imaging tool

By establishing OPT in the laboratory, I created a fast and efficient imaging and visualization pipeline. This enabled me to create high quality images and

snapshots by cutting virtual sections to pinpoint the alterations of gene expression in mutant limb buds and limb buds from different species (Lopez-Rios et. al., 2012, Benazet et. al., 2012, Lopez-Rios et. al., 2014).

With respect to 3-D imaging of large samples such as limb buds, confocal imaging tends to generate distorted 3-D shapes upon reconstruction from sections, while μCT imaging produces only low-resolution images. In contrast, OPT imaging provides higher quality images, especially for thick tissue specimens or embryonic samples (Sharpe et. al., 2002).

OPT imaging thus become a widely used tool for the analysis of 3-D spatio-temporal kinetics of gene expression in vertebrate embryos (Summerhurst et. al., 2008). Using OPT analysis, gene expression atlases like e-mouse atlas of gene expression (EMAGE) were created (Baldock et. al., 2003). The OPT analysis is also used to warp gene expression domains and perform cluster analysis of gene networks in developing chicken limb buds (Fisher et. al., 2008). In addition, transcription factors were compared to the fate maps of digits during chicken limb bud development (Fisher et. al., 2011).

7.3 The *In silico* limb bud gene network simulations

We used OPT to create an *in silico* limb bud model that allows simulation of large networks based on datasets collected by OPT. By combining OPT gene expression domains and limb bud shapes with the simulation of gene networks based on published and validated interactions, I was able to simulate key interactions in a realistic manner. Additionally, our *in silico* limb

model well captured the alterations in down-stream gene expression domains in different types of limb bud mutants.

Classical experiments and models have identified the morphogenetic signals that control limb bud outgrowth and patterning. Molecular analysis in combination with experimental and genetic manipulation has provided important insights about signaling pathways and the complexity of the signal transduction (see Introduction). The next step is to understand how information is integrated from different signaling pathways in a spatial and temporally coordinated manner. Modeling efforts such as *in silico* limb bud model developed as part of the PhD studies are central to this integrative approach (Zeller et. al., 2009, Iber and Zeller, 2012).

By creating 4-D limb bud growth domain, I was able to model the changes in the size, shape and relative position of the two main limb bud signaling centers in the mouse. However, 2-D sagittal sections of the OPT images capture limb bud dynamics well in both PD and AP directions and the limb bud curvature, AER and ZPA are well defined. The simulations of gene networks in 2-D growing domains over time were achieved by using previously described displacement calculation algorithms of limb bud shapes (Schwaninger et. al., 2014, Karimaddini et. al., 2014, Iber et. al., 2015). A previous study showed that mesenchymal cells have biased movements in the PD direction (Gros et. al., 2010), this agrees with the growth vectors of the limb bud boundaries used in this study. This is due to the fact that the shape extraction from accurately staged mouse embryos at 4.5-6 hour intervals was very precise.

In a previous attempt, a rather complex gene regulatory network was simulated on 2-D static domains to analyze e-m feedback loop, its termination and AP axis patterning in limb buds (Germann and Iber, in revision). We took this model further by simulating a more comprehensive gene network, also including ectodermal WNT signaling, mesenchymal-FGF10 and other key factors (For detail, see Figure 10). As limb bud size increases about an order of magnitude along the PD axis during the time window of simulation. The impact of growth on gene expression requires the incorporation of the real limb bud geometries. In particular limb bud initiation was simulated, during which the ectoderm-mesoderm crosstalk is initiated and the AER-*Fgf* expression domains are established. Next, we assessed the dynamics of the e-m feedback loop by including the interactions that control *Grem1* expression and incorporating the real domain dynamics of the ZPA, ectoderm and AER in the simulations. The published quantitative PCR analysis of *Bmp*, *Grem1* and *Shh* deficient limb buds provided a solid basis for adjusting the strength of the interactions using the appropriate hill constants (Benazet et. al., 2009). There are several mechanisms that contribute to termination of the self regulatory limb bud signaling system (Benazet et.al., 2009): first, the increasing inhibitory effects of AER-*Fgf* on *Grem1* (Verheyden and Sun, 2008), second, the negative impact of BMPs on *Shh* expression (Bastida et. al., 2009) and third, the increasing gap between *Shh* and *Grem1* domain all contribute to termination of signaling (Scherz et. al., 2006). The simulations included *Shh*-descendants, which do not express *Grem1* and establish the widening *Shh*-*Grem1* gap. These simulations based on real data significantly aided to the

adjustment of the gene interaction strength. If not properly adjusted, the feedback signaling system fails to terminate.

7.4: Genetic regulation of *Grem1* and digit patterning by WNT signaling

During my studies, I identified a critical role for WNT signaling in regulating *Grem1* expression in limb bud mesenchyme. Genetic inactivation or small molecule blocking of WNT signal transduction leads to a loss of Grem1 expression in the distal mesenchyme.

In a previous study, mutants of *Hox A* and *D* cluster (PrxCre; $HoxA^{c/c}$; $D^{-/-}$) were shown to disrupt distal-anterior expansion of the *Grem1* expression (Sheth et. al., 2013). However, in these mutant mouse embryos hand plate formation was altered and additionally *Fgf8* expression was absent from the anterior AER, revealing a general disruption in AP axis polarity. Removing the *Gli3* gene from the above mentioned genetic background restores the posterior *Grem1* expression domain, implying that the late dependency of *Grem1* expression in the anterior mesenchyme is secondary to its initial expression in limb buds.

Previous experiments using genetic manipulation of the WNT pathway revealed the requirement of the WNT pathway for the limb bud outgrowth (Hill et. al., 2005). The constitutive activation of WNT signal transduction by deletion of the *β-Catenin* exon3 in mouse embryos led to the up-regulation of *Bmp* and *Grem1* expression in the limb buds. The authors concluded that the increase in *Grem1* expression is secondary effect to the up-regulation of *Bmps*. My analysis provides good evidence in favor of a direct dependence of

Grem1 on WNT signaling in the distal mesenchyme, as *Grem1* expression is rapidly lost while Bmp expression remains. In colon cancer, a synergistic effect of aberrant WNT signaling on *Grem1* expression was recently established (Davis et. al., 2015). The colorectal mouse model $Apc^{Min/+}$ (with a truncated adenomatous polyposis coli gene) develops tumors due to activation of the WNT pathway. Specific conditional deletion of *Grem1* led to a reduction of polyp burden in $Apc^{Min/+}$ mice (Davis et. al., 2015). This effect might be due to the regulation of *Grem1* levels by the WNT pathway. In agreement, it was shown that the WNT effector TCF7L2 and intestine specific transcription factor CDX2 interact with an enhancer element upstream of *Grem1* gene to upregulate its expression as it associates with *Grem1* overexpression in colorectal cancer patients (Lewis et. al., 2014).

Thus, crosstalk between WNT and BMP signaling pathways is important during development and disease. In fact, additional studies have revealed the importance of the crosstalk of these two pathways for limb bud morhogenesis. The expression of WNT antagonist *Dkk1* is regulated by *Bmp4* during apoptosis (Groteworld and Rüther, 2002, Mukhopadhyay et. al., 2001). *Dkk1* mutant limbs are syndactylous (Mukhopadhyay et. al., 2001). Bmp-Sox9-Wnt Turing model in combination with limb bud culture system indicated the interactions between BMP and WNT are essential correct patterning of the digits, where SOX9 was in the core of the model (Raspopovic et. al., 2014). Our genetic analysis by inhibiting *β-Catenin* in the hand plate pointed to similar experimental and simulation results from this study, where WNT pathway was inhibited specifically in the digit forming stages (Raspopovic et. al., 2014).

8. CONCLUSIONS AND OUTLOOK

I followed two main lines of investigations as part of my systems analysis of limb bud development. Firstly, I quantitated cell numbers, proliferation and growth rate to gain insights into the volume and shape change dynamics during limb bud development. The use of OPT imaging was also an important technique to gain an understanding of the shape and gene expression domains in mutant limb buds. In addition, the OPT analysis provided the basis for the second aim of my PhD thesis namely the generation of a realistic limb bud shape frame for gene network simulations.

However, OPT precludes cellular resolution, which is becoming important to understand the cellular dynamics of organogenesis. With the recent development the light sheet microscopy (LSM), cellular resolution can now be achieved for live imaging of small embryos such as zebra fish (Huisken et. al., 2004). By merging LSM with OPT, the high-resolution tracking of fluorescent signals can be combined with good anatomy structure resolution (Bassi et. al., 2015). The method applies a spiral rotation for OPT with focal depth of LSM and LED back illumination in combination with sCMOS cameras allow rapid image acquisition. This multimodal-imaging platform enables much faster creation of live images than OPT (Bassi et. al., 2015). This and similar live imaging methods will enable imaging of mouse embryos and in particular limb bud development with cellular resolution. This might provide even better tools for real data acquision for *in silico* simulations of limb bud development. However, culturing mouse limb buds for prolonged periods remain challenging (Raspopovic et .al., 2014).

Our *in silico* limb bud model simulations allow testing the robustness and the scaling of the molecular networks and the limb bud development. Robustness is a central and essential feature of evolvable systems (Kitano, 2004). The flexibility of a robust system favors its evolvability and robust traits are often co-selected during evolution (Kitano , 2004). The gene expression patterns of limb bud at early stages are similar among rather different species such as the mouse, chicken and bovine although limb bud sizes are rather different. These similarities are termed scaling among different species. The exact mechanisms of scaling among differently sized embryonic structures from different species are still rather elusive. Determination of the accurate spatial dynamics of mouse and chicken limb bud development will allow the geometry and impact on scaling, thus allow the analysis of evolutionary aspects. Recent analysis of Drosophila wing discs development suggests that pre-steady-state dynamics and the advection of cell-bound ligand in a growing tissue can underline scaling (Fried and Iber, 2014). We have initiated similar simulations of chicken limb bud development as presented here for in mouse limb buds, which should enable us to test for scaling. However, manual model creation, parameterization and parameter screening are all very laborious. Therefore we have initiated attempts toward automated parameter inference for the initial stages of limb bud development (Velten et. al., 2014; Appendix, Publication 5). The implementation of automated parameter screens and sensitivity analysis might be able to improve our *in silico* limb bud gene network simulations and gain more insight into scaling and the robustness of the systems and gene interactions.

Our OPT analysis and modeling approach has facilitated the formulation of a novel mechanism for the regulation of the *Grem1* by ectodermal factors. The regulation of *Grem1* by WNTs likely provides an additional AER ectoderm to the DV restricted *Grem1* expression with in turn will feed into the SHH/GREM1/AER-FGF feedback signaling system. Its modulation by WNT signaling might be essential for the proliferative expansion of progenitors and/or for initiating chondrogenesis and digit identities at later stages.

Finally, our *in silico* model and the quantitative datasets will be an asset to understand the dynamics of growth control and patterning during progression of limb bud development. Cell-based models of the limb bud development can be implemented using numbers of proliferating mesenchymal progenitors to address cell division rates and to model the potential effects of this expansion on morphogen gradients. These models should aid the understanding of cellular dynamics during limb bud outgrowth and condensation of the cells during initiating chondrogenesis. With increasingly realistic multi scale modeling, *in silico* genetics will be likely become a possibility and powerful tool for improved experimental designs (Iber and Zeller, 2012).

9. ACKNOWLEDGEMENTS

I would like to thank Prof. Rolf Zeller and Prof. Dagmar Iber for enabling me to work in this fascinating and challenging iPhD project. They supervised and mentored me during my studies. They motivated me throughout my PhD, by teaching the scientific approach and enthusiasm. Thanks to their input and critic I developed myself scientifically and personally.

Also many thanks to Denis Menshykau for the initial 3-D software screening, and discovering Amira.

Many thanks to Gretel Nusspaumer and Sumit Jaiswal for the proliferation assays in the last six months of my PhD and Jannik Vollmer with the analysis of the growth models.

Thanks to Zahra Karimaddini for the limb bud domain and growth vector calculations.

Special thanks go to Prof. Savas Tay and Prof. Markus Affolter for being members in my thesis committee.

Many thanks to Javier Lopez-Rios for sharing his know-how and scientific passion.

Thanks to Marco Osterwalder for his friendship, passion of science and fun times during the Maus im Haus short film production.

Many thanks to Pascal Lorentz for the microscopy assistance, Angelika Offinger and her team for the excellent mouse care and Diana Barac for the language correction of this dissertation and continuing limb modeling project.

I thank my PhD-Bros Sumit Jaiswal, Frédéric Laurent for the nice time in the lab, retreats, Wednesdays in McDonald's or outside of the lab. We had valuable and fun discussions. Thanks to Emmanuele Pignatti, Marco

Osterwalder, Nathalie Riesen, Dario Speziale, Julie Leclercq, Marion Bétizeau and Jorge Dorado for the good moments in the lab and scientific support.

Many thanks to Aimée Zuniga Ashleigh Nugent, Simon Tanaka, Patrick Fried, Paola Valdivieso, Rosaria Costa, Sandro Nuciforo, Philipp Germann, Patrick Schlenker, Christine Mueller-Thompson, Barbara Widmer, Virginie Tissières, Sami Ben Said, Harold Gomez, Robert Croce, for the nice working environment.

I thank to my parents for believing in me and supporting me for everything. I thank my sisters for their motivation and cheering me up. Special thanks to my fiancé Désirée for being with me, for her amazing support and motivation and also great helps during writing this thesis.

10. REFERENCES

Akiyama, H., Chaboissier, M.C., Martin, J.F., Schedl, A., and de Crombrugghe, B. (2002). The transcription factor Sox9 has essential roles in successive steps of the chondrocyte differentiation pathway and is required for expression of Sox5 and Sox6. Genes & development *16*, 2813-2828.

Akiyama, H., Lyons, J.P., Mori-Akiyama, Y., Yang, X., Zhang, R., Zhang, Z., Deng, J.M., Taketo, M.M., Nakamura, T., Behringer, R.R.*, et al.* (2004). Interactions between Sox9 and beta-catenin control chondrocyte differentiation. Genes & development *18*, 1072-1087.

Arman, E., Haffner-Krausz, R., Chen, Y., Heath, J.K., and Lonai, P. (1998). Targeted disruption of fibroblast growth factor (FGF) receptor 2 suggests a role for FGF signaling in pregastrulation mammalian development. Proceedings of the National Academy of Sciences of the United States of America *95*, 5082-5087.

Badugu, A., Kraemer, C., Menshykau, D., Germann, P., and Iber, D. (2012). Digit patterning during limb development by a Turing mechanism. PloS Computational Biology.

Baldock, R.A., Bard, J.B., Burger, A., Burton, N., Christiansen, J., Feng, G., Hill, B., Houghton, D., Kaufman, M., Rao, J.*, et al.* (2003). EMAP and EMAGE: a framework for understanding spatially organized data. Neuroinformatics *1*, 309-325.

Barna, M., and Niswander, L. (2007). Visualization of cartilage formation: insight into cellular properties of skeletal progenitors and chondrodysplasia syndromes. Developmental cell *12*, 931-941.

Barrow, J.R., Thomas, K.R., Boussadia-Zahui, O., Moore, R., Kemler, R., Capecchi, M.R., and McMahon, A.P. (2003). Ectodermal Wnt3/beta-catenin signaling is required for the establishment and maintenance of the apical ectodermal ridge. Genes & development *17*, 394-409.

Bassi, A., Schmid, B., and Huisken, J. (2015). Optical tomography complements light sheet microscopy for in toto imaging of zebrafish development. Development *142*, 1016-1020.

Bastida, M.F., Sheth, R., and Ros, M.A. (2009). A BMP-Shh negative-feedback loop restricts Shh expression during limb development. Development *136*, 3779-3789.

Benazet, J.D., Bischofberger, M., Tiecke, E., Goncalves, A., Martin, J.F., Zuniga, A., Naef, F., and Zeller, R. (2009). A Self Regulatory System of Interlinked Signaling Feedback Loops Controls Mouse Limb Patterning. Science *323*, 1048-1050.

Benazet, J.D., Pignatti, E., Nugent, A., Unal, E., Laurent, F., and Zeller, R. (2012). SMAD4 Controls the Induction of Digit Ray Progenitors and the Condensation of Skeletal Primordia in Mouse Limb Buds. Development.

Benazet, J.D., and Zeller, R. (2009). Vertebrate Limb Development: Moving from Classical Morphogen Gradients to an Integrated 4-Dimensional Patterning System. Cold Spring Harbor Perspectives in Biology *1*, a001339-a001339.

Bi, W., Huang, W., Whitworth, D.J., Deng, J.M., Zhang, Z., Behringer, R.R., and de Crombrugghe, B. (2001). Haploinsufficiency of Sox9 results in defective cartilage primordia and premature skeletal mineralization. Proceedings of the National Academy of Sciences of the United States of America *98*, 6698-6703.

Boehm, B., Westerberg, H., Lesnicar-Pucko, G., Raja, S., Rautschka, M., Cotterell, J., Swoger, J., and Sharpe, J. (2010). The role of spatially controlled cell proliferation in limb bud morphogenesis. PLoS biology *8*, e1000420.

Bookstein, F.L. (1989). Principal warps: thin-plate splines and the decomposition of deformations. IEEE Transactions on Pattern Analysis and Machine Intelligence *11*, 567-585.

Brault, V., Moore, R., Kutsch, S., Ishibashi, M., Rowitch, D.H., McMahon, A.P., Sommer, L., Boussadia, O., and Kemler, R. (2001). Inactivation of the beta-catenin gene by Wnt1-Cre-mediated deletion results in dramatic brain malformation and failure of craniofacial development. Development *128*, 1253-1264.

Briscoe, J., Chen, Y., Jessell, T.M., and Struhl, G. (2001). A hedgehog-insensitive form of patched provides evidence for direct long-range morphogen activity of sonic hedgehog in the neural tube. Molecular cell *7*, 1279-1291.

Cao, T., Wang, C., Yang, M., Wu, C., and Wang, B. (2013). Mouse limbs expressing only the Gli3 repressor resemble those of Sonic hedgehog mutants. Dev Biol *379*, 221-228.

Chen, B., Dodge, M.E., Tang, W., Lu, J., Ma, Z., Fan, C.W., Wei, S., Hao, W., Kilgore, J., Williams, N.S.*, et al.* (2009). Small molecule-mediated disruption of Wnt-dependent signaling in tissue regeneration and cancer. Nature chemical biology *5*, 100-107.

Chen, Y., and Struhl, G. (1996). Dual roles for patched in sequestering and transducing Hedgehog. Cell *87*, 553-563.

Chiang, C., Litingtung, Y., Harris, M.P., Simandl, B.K., Li, Y., Beachy, P.A., and Fallon, J.F. (2001). Manifestation of the limb prepattern: limb development in the absence of sonic hedgehog function. Dev Biol *236*, 421-435.

Chiang, C., Litingtung, Y., Lee, E., Young, K.E., Corden, J.L., Westphal, H., and Beachy, P.A. (1996). Cyclopia and defective axial patterning in mice lacking Sonic hedgehog gene function. Nature *383*, 407-413.

Cooper, K.L., Hu, J.K., ten Berge, D., Fernandez-Teran, M., Ros, M.A., and Tabin, C.J. (2011). Initiation of proximal-distal patterning in the vertebrate limb by signals and growth. Science *332*, 1083-1086.

Corson, L.B., Yamanaka, Y., Lai, K.M., and Rossant, J. (2003). Spatial and temporal patterns of ERK signaling during mouse embryogenesis. Development *130*, 4527-4537.

Cunningham, T.J., Chatzi, C., Sandell, L.L., Trainor, P.A., and Duester, G. (2011). Rdh10 mutants deficient in limb field retinoic acid signaling exhibit normal limb patterning but display interdigital webbing. Developmental dynamics : an official publication of the American Association of Anatomists *240*, 1142-1150.

Dahn, R.D., and Fallon, J.F. (2000). Interdigital regulation of digit identity and homeotic transformation by modulated BMP signaling. Science *289*, 438-441.

Davis, H., Irshad, S., Bansal, M., Rafferty, H., Boitsova, T., Bardella, C., Jaeger, E., Lewis, A., Freeman-Mills, L., Giner, F.C.*, et al.* (2015). Aberrant epithelial GREM1 expression initiates colonic tumorigenesis from cells outside the stem cell niche. Nature medicine *21*, 62-70.

Dudley, A.T., Ros, M.A., and Tabin, C.J. (2002). A re-examination of proximodistal patterning during vertebrate limb development. Nature *418*, 539-544.

Ede, D.A., and Law, J.T. (1969). Computer simulation of vertebrate limb morphogenesis. Nature *221*, 244-248.

Fernandez-Teran, M.A., Hinchliffe, J.R., and Ros, M.A. (2006). Birth and death of cells in limb development: a mapping study. Developmental dynamics : an official publication of the American Association of Anatomists *235*, 2521-2537.

Fisher, M., Downie, H., Welten, M.C., Delgado, I., Bain, A., Planzer, T., Sherman, A., Sang, H., and Tickle, C. (2011). Comparative analysis of 3D expression patterns of transcription factor genes and digit fate maps in the developing chick wing. PloS one *6*, e18661.

Fisher, M.E., Clelland, A.K., Bain, A., Baldock, R.A., Murphy, P., Downie, H., Tickle, C., Davidson, D.R., and Buckland, R.A. (2008). Integrating technologies for comparing 3D gene expression domains in the developing chick limb. Dev Biol *317*, 13-23.

Fried, P., and Iber, D. (2014). Dynamic scaling of morphogen gradients on growing domains. Nature communications *5*, 5077.

Galli, A., Robay, D., Osterwalder, M., Bao, X., Benazet, J.D., Tariq, M., Paro, R., Mackem, S., and Zeller, R. (2010). Distinct roles of Hand2 in initiating polarity and posterior Shh expression during the onset of mouse limb bud development. PLoS Genet *6*, e1000901.

Gritli-Linde, A., Lewis, P., McMahon, A.P., and Linde, A. (2001). The whereabouts of a morphogen: direct evidence for short- and graded long-range activity of hedgehog signaling peptides. Dev Biol *236*, 364-386.

Gros, J., Hu, J.K., Vinegoni, C., Feruglio, P.F., Weissleder, R., and Tabin, C.J. (2010). WNT5A/JNK and FGF/MAPK pathways regulate the cellular events shaping the vertebrate limb bud. Current biology : CB *20*, 1993-2002.

Grotewold, L., and Ruther, U. (2002). The Wnt antagonist Dickkopf-1 is regulated by Bmp signaling and c-Jun and modulates programmed cell death. The EMBO journal *21*, 966-975.

Harfe, B.D., Scherz, P.J., Nissim, S., Tian, H., McMahon, A.P., and Tabin, C.J. (2004). Evidence for an expansion-based temporal Shh gradient in specifying vertebrate digit identities. Cell *118*, 517-528.

Hentschel, H.G., Glimm, T., Glazier, J.A., and Newman, S.A. (2004). Dynamical mechanisms for skeletal pattern formation in the vertebrate limb. Proceedings Biological sciences / The Royal Society *271*, 1713-1722.

Hill, T.P., Spater, D., Taketo, M.M., Birchmeier, W., and Hartmann, C. (2005). Canonical Wnt/beta-catenin signaling prevents osteoblasts from differentiating into chondrocytes. Developmental cell *8*, 727-738.

Hornbruch, A., and Wolpert, L. (1970). Cell division in the early growth and morphogenesis of the chick limb. Nature *226*, 764-766.

Hsu, D.R., Economides, A.N., Wang, X., Eimon, P.M., and Harland, R.M. (1998). The Xenopus dorsalizing factor Gremlin identifies a novel family of secreted proteins that antagonize BMP activities. Molecular cell *1*, 673-683.

Hui, C.C., and Joyner, A.L. (1993). A mouse model of greig cephalopolysyndactyly syndrome: the extra-toesJ mutation contains an intragenic deletion of the Gli3 gene. Nature genetics *3*, 241-246.

Huisken, J., Swoger, J., Del Bene, F., Wittbrodt, J., and Stelzer, E.H. (2004). Optical sectioning deep inside live embryos by selective plane illumination microscopy. Science *305*, 1007-1009.

Iber, D., Tanaka, S., Fried, P., Germann, P., and Menshykau, D. (2015). Simulating tissue morphogenesis and signaling. Methods in molecular biology *1189*, 323-338.

Iber, D., and Zeller, R. (2012). Making sense-data-based simulations of vertebrate limb development. Current opinion in genetics & development *22*, 570-577.

Jagle, U., Gasser, J.A., Muller, M., and Kinzel, B. (2007). Conditional transgene expression mediated by the mouse beta-actin locus. Genesis *45*, 659-666.

Karimaddini, Z., Ünal, E., Menshykau, D., and Iber, D. (2014). Simulating Organogenesis in COMSOL: Image-based Modeling. Proceedings of Comsol Conference

Kawakami, Y. (2013). Redefining the role of retinoic acid in limb development. Cell reports *3*, 1337-1338.

Kengaku, M., Capdevila, J., Rodriguez-Esteban, C., De La Pena, J., Johnson, R.L., Izpisua Belmonte, J.C., and Tabin, C.J. (1998). Distinct WNT pathways regulating AER formation and dorsoventral polarity in the chick limb bud. Science *280*, 1274-1277.

Khokha, M.K., Hsu, D., Brunet, L.J., Dionne, M.S., and Harland, R.M. (2003). Gremlin is the BMP antagonist required for maintenance of Shh and Fgf signals during limb patterning. Nature genetics *34*, 303-307.

Kicheva, A., Pantazis, P., Bollenbach, T., Kalaidzidis, Y., Bittig, T., Julicher, F., and Gonzalez-Gaitan, M. (2007). Kinetics of morphogen gradient formation. Science *315*, 521-525.

Kitano, H. (2004). Biological robustness. Nature reviews Genetics *5*, 826-837.

Kondo, S., and Asal, R. (1995). A reaction-diffusion wave on the skin of the marine angelfish Pomacanthus. Nature *376*, 765-768.

Lang, F., Ritter, M., Woll, E., Weiss, H., Haussinger, D., Hoflacher, J., Maly, K., and Grunicke, H. (1992). Altered cell volume regulation in ras oncogene expressing NIH fibroblasts. Pflugers Archiv : European journal of physiology *420*, 424-427.

Laufer, E., Nelson, C.E., Johnson, R.L., Morgan, B.A., and Tabin, C. (1994). Sonic hedgehog and Fgf-4 act through a signaling cascade and feedback loop to integrate growth and patterning of the developing limb bud. Cell *79*, 993-1003.

Lewis, A., Freeman-Mills, L., de la Calle-Mustienes, E., Giraldez-Perez, R.M., Davis, H., Jaeger, E., Becker, M., Hubner, N.C., Nguyen, L.N., Zeron-Medina, J.*, et al.* (2014). A polymorphic enhancer near GREM1 influences bowel cancer risk through differential CDX2 and TCF7L2 binding. Cell reports *8*, 983-990.

Li, Q., Lewandowski, J.P., Powell, M.B., Norrie, J.L., Cho, S.H., and Vokes, S.A. (2014). A Gli silencer is required for robust repression of gremlin in the vertebrate limb bud. Development *141*, 1906-1914.

Li, S., and Muneoka, K. (1999). Cell migration and chick limb development: chemotactic action of FGF-4 and the AER. Dev Biol *211*, 335-347.

Litingtung, Y., Dahn, R.D., Li, Y., Fallon, J.F., and Chiang, C. (2002). Shh and Gli3 are dispensable for limb skeleton formation but regulate digit number and identity. Nature *418*, 979-983.

Logan, M., Martin, J.F., Nagy, A., Lobe, C., Olson, E.N., and Tabin, C.J. (2002). Expression of Cre Recombinase in the developing mouse limb bud driven by a Prxl enhancer. Genesis *33*, 77-80.

Loomis, C.A., Harris, E., Michaud, J., Wurst, W., Hanks, M., and Joyner, A.L. (1996). The mouse Engrailed-1 gene and ventral limb patterning. Nature *382*, 360-363.

Lopez-Rios, J., Duchesne, A., Speziale, D., Andrey, G., Peterson, K.A., Germann, P., Unal, E., Liu, J., Floriot, S., Barbey, S.*, et al.* (2014). Attenuated sensing of SHH by Ptch1 underlies evolution of bovine limbs. Nature *511*, 46-51.

Lopez-Rios, J., Speziale, D., Robay, D., Scotti, M., Osterwalder, M., Nusspaumer, G., Galli, A., Hollander, G.A., Kmita, M., and Zeller, R. (2012). GLI3 constrains digit number by controlling both progenitor proliferation and BMP-dependent exit to chondrogenesis. Developmental cell *22*, 837-848.

MacCabe, J.A., Errick, J., and Saunders, J.W., Jr. (1974). Ectodermal control of the dorsoventral axis in the leg bud of the chick embryo. Dev Biol *39*, 69-82.

Mariani, F.V., Ahn, C.P., and Martin, G.R. (2008). Genetic evidence that FGFs have an instructive role in limb proximal–distal patterning. Nature *453*, 401-405.

Marigo, V., Davey, R.A., Zuo, Y., Cunningham, J.M., and Tabin, C.J. (1996). Biochemical evidence that patched is the Hedgehog receptor. Nature *384*, 176-179.

Martin, G.R. (1998). The roles of FGFs in the early development of vertebrate limbs. Genes & development *12*, 1571-1586.

Mercader, N., Leonardo, E., Piedra, M.E., Martinez, A.C., Ros, M.A., and Torres, M. (2000). Opposing RA and FGF signals control proximodistal vertebrate limb development through regulation of Meis genes. Development *127*, 3961-3970.

Michos, O., Panman, L., Vintersten, K., Beier, K., Zeller, R., and Zuniga, A. (2004). Gremlin-mediated BMP antagonism induces the epithelial-mesenchymal feedback signaling controlling metanephric kidney and limb organogenesis. Development *131*, 3401-3410.

Min, H., Danilenko, D.M., Scully, S.A., Bolon, B., Ring, B.D., Tarpley, J.E., DeRose, M., and Simonet, W.S. (1998). Fgf-10 is required for both limb and lung development and exhibits striking functional similarity to Drosophila branchless. Genes & development *12*, 3156-3161.

Minowada, G., Jarvis, L.A., Chi, C.L., Neubuser, A., Sun, X., Hacohen, N., Krasnow, M.A., and Martin, G.R. (1999). Vertebrate Sprouty genes are induced by FGF signaling and can cause chondrodysplasia when overexpressed. Development *126*, 4465-4475.

Mukhopadhyay, M., Shtrom, S., Rodriguez-Esteban, C., Chen, L., Tsukui, T., Gomer, L., Dorward, D.W., Glinka, A., Grinberg, A., Huang, S.P.*, et al.* (2001). Dickkopf1 is required for embryonic head induction and limb morphogenesis in the mouse. Developmental cell *1*, 423-434.

Newman, S.A., and Bhat, R. (2007). Activator-inhibitor dynamics of vertebrate limb pattern formation. Birth defects research Part C, Embryo today : reviews *81*, 305-319.

Newman, S.A., and Frisch, H.L. (1979). Dynamics of skeletal pattern formation in developing chick limb. Science *205*, 662-668.

Ng, L.J., Wheatley, S., Muscat, G.E., Conway-Campbell, J., Bowles, J., Wright, E., Bell, D.M., Tam, P.P., Cheah, K.S., and Koopman, P. (1997). SOX9 binds DNA, activates transcription, and coexpresses with type II collagen during chondrogenesis in the mouse. Dev Biol *183*, 108-121.

Nissim, S., Hasso, S.M., Fallon, J.F., and Tabin, C.J. (2006). Regulation of Gremlin expression in the posterior limb bud. Dev Biol *299*, 12-21.

Niswander, L., Tickle, C., Vogel, A., Booth, I., and Martin, G.R. (1993). FGF-4 replaces the apical ectodermal ridge and directs outgrowth and patterning of the limb. Cell *75*, 579-587.

Nowakowski, R.S., Lewin, S.B., and Miller, M.W. (1989). Bromodeoxyuridine immunohistochemical determination of the lengths of the cell cycle and the

DNA-synthetic phase for an anatomically defined population. Journal of neurocytology *18*, 311-318.

Ohuchi, H., Hori, Y., Yamasaki, M., Harada, H., Sekine, K., Kato, S., and Itoh, N. (2000). FGF10 acts as a major ligand for FGF receptor 2 IIIb in mouse multi-organ development. Biochemical and biophysical research communications *277*, 643-649.

Ohuchi, H., Nakagawa, T., Yamamoto, A., Araga, A., Ohata, T., Ishimaru, Y., Yoshioka, H., Kuwana, T., Nohno, T., Yamasaki, M.*, et al.* (1997). The mesenchymal factor, FGF10, initiates and maintains the outgrowth of the chick limb bud through interaction with FGF8, an apical ectodermal factor. Development *124*, 2235-2244.

Osterwalder, M., Speziale, D., Shoukry, M., Mohan, R., Ivanek, R., Kohler, M., Beisel, C., Wen, X., Scales, S.J., Christoffels, V.M.*, et al.* (2014). HAND2 targets define a network of transcriptional regulators that compartmentalize the early limb bud mesenchyme. Developmental cell *31*, 345-357.

Panman, L., Galli, A., Lagarde, N., Michos, O., Soete, G., Zuniga, A., and Zeller, R. (2006). Differential regulation of gene expression in the digit forming area of the mouse limb bud by SHH and gremlin 1/FGF-mediated epithelial-mesenchymal signalling. Development *133*, 3419-3428.

Park, H.L., Bai, C., Platt, K.A., Matise, M.P., Beeghly, A., Hui, C.C., Nakashima, M., and Joyner, A.L. (2000). Mouse Gli1 mutants are viable but

have defects in SHH signaling in combination with a Gli2 mutation. Development *127*, 1593-1605.

Parr, B.A., and McMahon, A.P. (1995). Dorsalizing signal Wnt-7a required for normal polarity of D-V and A-P axes of mouse limb. Nature *374*, 350-353.

Pizette, S., Abate-Shen, C., and Niswander, L. (2001). BMP controls proximodistal outgrowth, via induction of the apical ectodermal ridge, and dorsoventral patterning in the vertebrate limb. Development *128*, 4463-4474.

Pizette, S., and Niswander, L. (1999). BMPs negatively regulate structure and function of the limb apical ectodermal ridge. Development *126*, 883-894.

Pizette, S., and Niswander, L. (2000). BMPs are required at two steps of limb chondrogenesis: formation of prechondrogenic condensations and their differentiation into chondrocytes. Dev Biol *219*, 237-249.

Probst, S., Kraemer, C., Demougin, P., Sheth, R., Martin, G.R., Shiratori, H., Hamada, H., Iber, D., Zeller, R., and Zuniga, A. (2011). SHH propagates distal limb bud development by enhancing CYP26B1-mediated retinoic acid clearance via AER-FGF signalling. Development *138*, 1913-1923.

Prum, R.O., and Williamson, S. (2002). Reaction-diffusion models of within-feather pigmentation patterning. Proceedings Biological sciences / The Royal Society *269*, 781-792.

Quintana, L., and Sharpe, J. (2011). Optical projection tomography of vertebrate embryo development. Cold Spring Harbor protocols *2011*, 586-594.

Raspopovic, J., Marcon, L., Russo, L., and Sharpe, J. (2014). Modeling digits. Digit patterning is controlled by a Bmp-Sox9-Wnt Turing network modulated by morphogen gradients. Science *345*, 566-570.

Riddle, R.D., Johnson, R.L., Laufer, E., and Tabin, C. (1993). Sonic hedgehog mediates the polarizing activity of the ZPA. Cell *75*, 1401-1416.

Rosello-Diez, A., Ros, M.A., and Torres, M. (2011). Diffusible signals, not autonomous mechanisms, determine the main proximodistal limb subdivision. Science *332*, 1086-1088.

Salazar-Ciudad, I., and Jernvall, J. (2002). A gene network model accounting for development and evolution of mammalian teeth. Proceedings of the National Academy of Sciences of the United States of America *99*, 8116-8120.

Saunders, J.W., and Gasseling, M.T. (1968). Ectodermal-mesenchymal interactions in the origin of limb symmetry. In Epithelial-Mesen- chymal Interactions, 78-97.

Scherz, P.J., Harfe, B.D., McMahon, A.P., and Tabin, C.J. (2004). The limb bud Shh-Fgf feedback loop is terminated by expansion of former ZPA cells. Science *305*, 396-399.

Schwaninger, A., Menshykau, D., and Iber, D. (2015). Simulating Organogenesis: Algorithms for the Image-based Determination of Growth Fields. TOMACS *in press*.

Sekine, K., Ohuchi, H., Fujiwara, M., Yamasaki, M., Yoshizawa, T., Sato, T., Yagishita, N., Matsui, D., Koga, Y., Itoh, N.*, et al.* (1999). Fgf10 is essential for limb and lung formation. Nature genetics *21*, 138-141.

Selever, J., Liu, W., Lu, M.F., Behringer, R.R., and Martin, J.F. (2004). Bmp4 in limb bud mesoderm regulates digit pattern by controlling AER development. Dev Biol *276*, 268-279.

Sharpe, J., Ahlgren, U., Perry, P., Hill, B., Ross, A., Hecksher-Sorensen, J., Baldock, R., and Davidson, D. (2002). Optical projection tomography as a tool for 3D microscopy and gene expression studies. Science *296*, 541-545.

Sheth, R., Gregoire, D., Dumouchel, A., Scotti, M., Pham, J.M., Nemec, S., Bastida, M.F., Ros, M.A., and Kmita, M. (2013). Decoupling the function of Hox and Shh in developing limb reveals multiple inputs of Hox genes on limb growth. Development *140*, 2130-2138.

Sheth, R., Marcon, L., Bastida, M.F., Junco, M., Quintana, L., Dahn, R., Kmita, M., Sharpe, J., and Ros, M.A. (2012). Hox genes regulate digit patterning by controlling the wavelength of a Turing-type mechanism. Science *338*, 1476-1480.

Sick, S., Reinker, S., Timmer, J., and Schlake, T. (2006). WNT and DKK determine hair follicle spacing through a reaction-diffusion mechanism. Science *314*, 1447-1450.

Soriano, P. (1999). Generalized lacZ expression with the ROSA26 Cre reporter strain. Nature genetics *21*, 70-71.

Soshnikova, N., Zechner, D., Huelsken, J., Mishina, Y., Behringer, R.R., Taketo, M.M., Crenshaw, E.B., 3rd, and Birchmeier, W. (2003). Genetic interaction between Wnt/beta-catenin and BMP receptor signaling during formation of the AER and the dorsal-ventral axis in the limb. Genes & development *17*, 1963-1968.

Summerbell, D., Lewis, J.H., and Wolpert, L. (1973). Positional information in chick limb morphogenesis. Nature *244*, 492-496.

Summerbell, D., and Wolpert, L. (1972). Cell density and cell division in the early morphogenesis of the chick wing. Nature: New biology *239*, 24-26.

Summerhurst, K., Stark, M., Sharpe, J., Davidson, D., and Murphy, P. (2008). 3D representation of Wnt and Frizzled gene expression patterns in the mouse embryo at embryonic day 11.5 (Ts19). Gene expression patterns : GEP *8*, 331-348.

Sun, X., Mariani, F.V., and Martin, G.R. (2002). Functions of FGF signalling from the apical ectodermal ridge in limb development. Nature *418*, 501-508.

Tabin, C., and Wolpert, L. (2007). Rethinking the proximodistal axis of the vertebrate limb in the molecular era. Genes & development *21*, 1433-1442.

Tam, P.P. (1981). The control of somitogenesis in mouse embryos. Journal of embryology and experimental morphology *65 Suppl*, 103-128.

te Welscher, P., Fernandez-Teran, M., Ros, M.A., and Zeller, R. (2002a). Mutual genetic antagonism involving GLI3 and dHAND prepatterns the vertebrate limb bud mesenchyme prior to SHH signaling. Genes & development *16*, 421-426.

te Welscher, P., Zuniga, A., Kuijper, S., Drenth, T., Goedemans, H.J., Meijlink, F., and Zeller, R. (2002b). Progression of vertebrate limb development through SHH-mediated counteraction of GLI3. Science *298*, 827-830.

ten Berge, D., Brugmann, S.A., Helms, J.A., and Nusse, R. (2008). Wnt and FGF signals interact to coordinate growth with cell fate specification during limb development. Development *135*, 3247-3257.

ten Berge, D., Kurek, D., Blauwkamp, T., Koole, W., Maas, A., Eroglu, E., Siu, R.K., and Nusse, R. (2011). Embryonic stem cells require Wnt proteins to prevent differentiation to epiblast stem cells. Nature cell biology *13*, 1070-1075.

Towers, M., and Tickle, C. (2009). Growing models of vertebrate limb development. Development *136*, 179-190.

Trumpp, A., Refaeli, Y., Oskarsson, T., Gasser, S., Murphy, M., Martin, G.R., and Bishop, J.M. (2001). c-Myc regulates mammalian body size by controlling cell number but not cell size. Nature *414*, 768-773.

Turing, A.M. (1990). The chemical basis of morphogenesis. 1953. Bulletin of mathematical biology *52*, 153-197; discussion 119-152.

Turner, N., and Grose, R. (2010). Fibroblast growth factor signalling: from development to cancer. Nature reviews Cancer *10*, 116-129.

Vargesson, N., Clarke, J.D., Vincent, K., Coles, C., Wolpert, L., and Tickle, C. (1997). Cell fate in the chick limb bud and relationship to gene expression. Development *124*, 1909-1918.

Velten, B., Ünal, E., and Iber, D. (2014). Image-based Parameter Inference for Spatio-temporal models of Organogenesis. NOLTA 2014, International Symposium on Nonlinear Theory & its Applications.

Verheyden, J.M., and Sun, X. (2008). An Fgf/Gremlin inhibitory feedback loop triggers termination of limb bud outgrowth. Nature *454*, 638-641.

Vokes, S.A., Ji, H., Wong, W.H., and McMahon, A.P. (2008). A genome-scale analysis of the cis-regulatory circuitry underlying sonic hedgehog-mediated patterning of the mammalian limb. Genes & development *22*, 2651-2663.

Wang, B., Fallon, J.F., and Beachy, P.A. (2000). Hedgehog-regulated processing of Gli3 produces an anterior/posterior repressor gradient in the developing vertebrate limb. Cell *100*, 423-434.

Wen, X., Lai, C.K., Evangelista, M., Hongo, J.A., de Sauvage, F.J., and Scales, S.J. (2010). Kinetics of hedgehog-dependent full-length Gli3 accumulation in primary cilia and subsequent degradation. Molecular and cellular biology *30*, 1910-1922.

Wolpert, L. (1969). Positional information and the spatial pattern of cellular differentiation. Journal of theoretical biology *25*, 1-47.

Xu, X., Weinstein, M., Li, C., Naski, M., Cohen, R.I., Ornitz, D.M., Leder, P., and Deng, C. (1998). Fibroblast growth factor receptor 2 (FGFR2)-mediated reciprocal regulation loop between FGF8 and FGF10 is essential for limb induction. Development *125*, 753-765.

Yoon, B.S., Ovchinnikov, D.A., Yoshii, I., Mishina, Y., Behringer, R.R., and Lyons, K.M. (2005). Bmpr1a and Bmpr1b have overlapping functions and are essential for chondrogenesis in vivo. Proceedings of the National Academy of Sciences of the United States of America *102*, 5062-5067.

Yu, S.R., Burkhardt, M., Nowak, M., Ries, J., Petrasek, Z., Scholpp, S., Schwille, P., and Brand, M. (2009). Fgf8 morphogen gradient forms by a source-sink mechanism with freely diffusing molecules. Nature *461*, 533-536.

Zeller, R., Lopez-Rios, J., and Zuniga, A. (2009). Vertebrate limb bud development: moving towards integrative analysis of organogenesis. Nature Reviews Genetics *10*, 845-858.

Zhao, X., Sirbu, I.O., Mic, F.A., Molotkova, N., Molotkov, A., Kumar, S., and Duester, G. (2009). Retinoic acid promotes limb induction through effects on body axis extension but is unnecessary for limb patterning. Current biology : CB *19*, 1050-1057.

Zhu, J., Nakamura, E., Nguyen, M.T., Bao, X., Akiyama, H., and Mackem, S. (2008). Uncoupling Sonic hedgehog control of pattern and expansion of the developing limb bud. Developmental cell *14*, 624-632.

Zuniga, A., Haramis, A.P., McMahon, A.P., and Zeller, R. (1999). Signal relay by BMP antagonism controls the SHH/FGF4 feedback loop in vertebrate limb buds. Nature *401*, 598-602.

Zuniga, A., Laurent, F., Lopez-Rios, J., Klasen, C., Matt, N., and Zeller, R. (2012). Conserved cis-regulatory regions in a large genomic landscape control SHH and BMP-regulated Gremlin1 expression in mouse limb buds. BMC developmental biology *12*, 23.

Zuniga, A., Michos, O., Spitz, F., Haramis, A.P., Panman, L., Galli, A., Vintersten, K., Klasen, C., Mansfield, W., Kuc, S.*, et al.* (2004). Mouse limb deformity mutations disrupt a global control region within the large regulatory

landscape required for Gremlin expression. Genes & development *18*, 1553-1564.

Zwilling, E. (1956). Genetic mechanism in limb development. Cold Spring Harbor symposia on quantitative biology *21*, 349-354.

11. APPENDIX

Publication 1: *Smad4* is required to induce digit ray primordia and to initiate the aggregation and differentiation of chondrogenic progenitors in the mouse limb buds

In this manuscript, limb buds that are deficient for *Smad4* in the limb bud mesenchyme were studied. This conditional deletion was done by Prx-Cre mediated *Smad4* deletion. I performed OPT analysis that are in the Figures 4 and 8 and found that the *Sox9* expression in the mutant limbs are thickened in the mutant limbs in the early stages onwards. Additionally, I showed that *Decorin* expression is excluded from the digit condensation regions in the WT limbs, where as it was expressed throughout the hand plate in the mutants.

Development 139, 4250-4260 (2012) doi:10.1242/dev.084822

Smad4 is required to induce digit ray primordia and to initiate the aggregation and differentiation of chondrogenic progenitors in mouse limb buds

Jean-Denis Bénazet[1,*,‡], Emanuele Pignatti[1,‡], Ashleigh Nugent[1], Erkan Unal[1,2], Frédéric Laurent[1] and Rolf Zeller[1,§]

SUMMARY

SMAD4 is an essential mediator of canonical TGFβ/BMP signal transduction and we inactivated *Smad4* in mouse limb buds from early stages onward to study its functions in the mesenchyme. While this *Smad4* inactivation did not alter the early *Sox9* distribution, prefiguring the chondrogenic primordia of the stylopod and zeugopod, it disrupted formation of all *Sox9*-positive digit ray primordia. Specific inactivation of *Smad4* during handplate development pointed to its differential requirement for posterior and anterior digit ray primordia. At the cellular level, *Smad4* deficiency blocked the aggregation of *Sox9*-positive progenitors, thereby preventing chondrogenic differentiation as revealed by absence of collagen type II. The progressive loss of SOX9 due to disrupting digit ray primordia and chondrogenesis was paralleled by alterations in genes marking other lineages. This pointed to a general loss of tissue organization and diversion of mutant cells toward non-specific connective tissue. Conditional inactivation of *Bmp2* and *Bmp4* indicated that the loss of digit ray primordia and increase in connective tissue were predominantly a consequence of disrupting SMAD4-mediated BMP signal transduction. In summary, our analysis reveals that SMAD4 is required to initiate: (1) formation of the *Sox9*-positive digit ray primordia; and (2) aggregation and chondrogenic differentiation of all limb skeletal elements.

KEY WORDS: BMP signaling, Limb bud, Mouse

INTRODUCTION

Bone morphogenetic proteins (BMPs) are ligands belonging to the transforming growth factor beta (TGFβ) superfamily, which control inductive processes in early embryos and during organogenesis (reviewed by Zakin and De Robertis, 2010) and are required for chondrogenesis, growth and ossification of bones in vertebrates (reviewed by Wu et al., 2007). BMP ligands interact with two types of BMP receptors (BMPR1 and BMPR2), which in turn trigger intracellular signal transduction by phosphorylation of the receptor-associated SMAD1, -5 and -8 proteins. These in turn form a complex with SMAD4, an essential mediator of both canonical BMP and TGFβ signal transduction (Yang et al., 2002). These SMAD complexes translocate to the nucleus and regulate the expression of target genes in concert with other transcriptional regulators (Feng and Derynck, 2005). Genetic and functional analysis of mouse and chicken limb bud development has uncovered important morphoregulatory functions of the BMP pathway in the establishment and functioning of the two limb bud signaling centers, namely sonic hedgehog (SHH) signaling by the posterior mesenchymal organizer and fibroblast growth factor (FGF) signaling by the apical ectodermal ridge (AER).

During limb bud outgrowth, BMPs and the BMP antagonist gremlin 1 (GREM1) control the epithelial-mesenchymal signaling interactions that coordinate outgrowth with patterning and determination of digit identities (reviewed by Zeller et al., 2009). During the onset of limb bud development, BMP4 is first required in the mesenchyme and BMPR1A in the ectoderm for formation of the AER, as inactivation of these molecules disrupts establishment of the AER-FGF signaling centre, which results in limb truncations and loss of dorsoventral polarity (Ahn et al., 2001; Pizette et al., 2001; Pajni-Underwood et al., 2007; Bénazet et al., 2009). During initiation of limb bud outgrowth, the SHH signaling centre is established and restricted to the posterior mesenchyme under the influence of BMP signaling (Bastida et al., 2004). Concurrently, BMP4 triggers expression of the BMP antagonist *Grem1* in the posterior limb bud mesenchyme, which causes rapid lowering of mesenchymal BMP activity (Nissim et al., 2006; Bénazet et al., 2009). The subsequent distal-anterior expansion of the *Grem1* expression domain depends largely on its positive regulation by AER-FGF and SHH signaling. This self-regulatory SHH/GREM1/AER-FGF feedback loop coordinates anteroposterior (AP) with proximodistal (PD) limb bud outgrowth and patterning (Zúñiga et al., 1999; Michos et al., 2004; Panman et al., 2006; Bénazet et al., 2009; Probst et al., 2011).

During limb bud outgrowth, low mesenchymal BMP activity is required to restrict the length of the AER, as inactivation of *Bmp4* during this developmental period results in extended AER-FGF signaling and digit polydactyly (Selever et al., 2004; Bénazet et al., 2009). As inactivation of *Bmpr1a* in the mesenchyme also disrupts limb bud outgrowth (Ovchinnikov et al., 2006), tight control of BMP activity is required for normal progression of limb development (reviewed by Zeller et al., 2009).

These signaling interactions are terminated as the SHH/GREM1/AER-FGF feedback signaling system breaks down owing to progressive inhibition of *Grem1* expression by high AER-FGF levels and the increasing separation of the *Shh* and *Grem1*

[1]Developmental Genetics, Department of Biomedicine, University of Basel, Mattenstrasse 28, CH-4058 Basel, Switzerland. [2]Department of Biosystems Science and Engineering (D-BSSE), ETH Zurich, Mattenstrasse 26, CH-4058 Basel, Switzerland.

*Present address: Broad Center for Regenerative Medicine and Stem Cell Research, University of Southern Carolina, 1425 San Pablo Street, Los Angeles, CA 90089, USA
‡These authors contributed equally to this work
§Author for correspondence (rolf.zeller@unibas.ch)

Accepted 18 August 2012

expression domains (Scherz et al., 2004; Verheyden and Sun, 2008). This termination results in a renewed increase in BMP activity during development of the digit ray primordia (giving rise to metacarpals and phalanges) (Bénazet et al., 2009), which probably serves two purposes: first, to control digit identity by signaling from the interdigit mesenchyme to the distal phalanx-forming region (PFR) (Dahn and Fallon, 2000; Suzuki et al., 2008; Witte et al., 2010), and second, to induce apoptosis of the interdigit mesenchyme (Bandyopadhyay et al., 2006; Pajni-Underwood et al., 2007; Maatouk et al., 2009; Wong et al., 2012). In agreement with these dynamic changes in BMP activity, BMPs inhibit chondrogenic differentiation of early limb bud mesenchymal progenitors while promoting chondrogenesis at late stages (Karamboulas et al., 2010). Noggin-mediated BMP antagonism under experimental conditions showed that BMPs are required to initiate compaction and chondrogenic differentiation of *Sox9*-positive mesenchymal progenitors (Brunet et al., 1998; Pizette and Niswander, 2000; Barna and Niswander, 2007). Genetic inactivation of both *Bmp2* and *Bmp4* in the limb bud mesenchyme disrupted formation of the two posterior-most digit primordia and the ulna (Bandyopadhyay et al., 2006). Experimental evidence indicated that BMPs participate in activating *Sox9* expression in prechondrogenic progenitors, and *Sox9* not only marks the chondrogenic lineage but is essential to initiate chondrogenesis during formation of skeletal elements (Bi et al., 1999; Akiyama et al., 2005; Pan et al., 2008).

Genetic analysis of the BMP pathway during chondrogenesis established that BMP signaling and antagonism are required recurrently for the proliferation of prechondrogenic progenitors, chondrocyte differentiation, shaping the skeletal primordia and formation of the endochondral growth plate (Brunet et al., 1998; Kobayashi et al., 2005; Yoon et al., 2005). In parallel, mesenchymal cells receiving different signals are specified as tendons, ligaments and connective tissues. For example, chondrogenic differentiation is inhibited and mesenchymal cells remain in a proliferative, undifferentiated state when they are exposed to both ectodermal WNT and AER-FGF signaling, whereas WNT signaling alone promotes the development of non-specific connective tissue (ten Berge et al., 2008; Gros et al., 2010).

TGFβ ligands are expressed from early limb bud stages onward, and inhibition of TGFβ signal transduction in cultured mesenchymal cells provided evidence that TGFβ signaling functions in early limb buds to alleviate the inhibitory effects of BMPs on initiation of chondrogenic differentiation (Karamboulas et al., 2010). Therefore, brief exposure of mesenchymal progenitors to TGFβ signaling seems necessary to allow subsequent induction of chondrogenesis by BMPs (Roark and Greer, 1994; Karamboulas et al., 2010). Furthermore, implantation of TGFβ1-loaded beads into the interdigit mesenchyme of chicken limb buds is able to induce formation of ectopic digit phalanges, i.e. trigger ectopic chondrogenesis (Merino et al., 1999; Lorda-Diez et al., 2011). Genetic analysis of TGFβ ligands and receptors in mouse embryos has revealed their essential roles during limb long bone, joint and tendon morphogenesis (Sanford et al., 1997; Seo and Serra, 2007)]. Although this genetic analysis revealed essential functions during limb skeletal development, it is possible that earlier functions in initiating chondrogenesis were masked by functional complementation among TGFβ and/or BMP ligands and receptors (see e.g. Karamboulas et al., 2010).

As *Smad4*-deficient ($Smad4^{\Delta/\Delta}$) embryos die during gastrulation (Chu et al., 2004), we used a conditional loss-of-function allele (Yang et al., 2002) to study its requirement in the limb bud mesenchyme. *Prx1*-Cre-mediated conditional inactivation of *Smad4* in limb bud mesenchyme resulted in the clearance of SMAD4 protein during early limb bud outgrowth, and the distribution of *Sox9* transcript and SOX9 protein was normal until at least embryonic day (E) 11.0 in the proximal mesenchyme. By contrast, *Sox9* expression was not activated in the distal *Smad4*-deficient limb bud mesenchyme that would normally give rise to the digit ray primordia. The analysis of SOX9 also indicated that with the exception of a small proximal aggregate, the aggregation and condensation of all mesenchymal progenitors to form the cartilage elements was disrupted in *Smad4*-deficient limb buds. Mutant cells failed to deposit extracellular collagen type II (COL type II) fibres, a hallmark of chondrogenesis, and progressively lost SOX9, i.e. chondrogenic lineage. In parallel, the expression of markers for other mesenchymal lineages was upregulated in *Smad4*-deficient limb buds without their normal spatial restriction, which provided evidence for a diversion of *Smad4*-deficient progenitors toward non-specific connective tissue.

MATERIALS AND METHODS

Ethics statement concerning animal experiments and mouse strains

Animal experiments were approved by the legally required regional commission in strict accordance with Swiss law. All studies were classified as grade zero, which implies minimal suffering. The 3R and Basel Declaration principles were implemented. The *Prx1*-Cre was used to conditionally inactivate *Smad4* ($Smad4^{flox}$) (Yang et al., 2002) in the mesenchyme from early limb bud stages onward (Logan et al., 2002), and the $Hoxa13^{Cre/+}$ knock-in allele was used for autopod specific inactivation (Lopez-Rios et al., 2012; Scotti and Kmita, 2012). *Prx1-Cre*-mediated inactivation of *Bmp2* and *Bmp4* was done as described (Bandyopadhyay et al., 2006).

In situ hybridization and skeletal preparations

Whole-mount in situ hybridization was performed using standard protocols. Control and experimental embryos were age-matched by counting somites. To assess the clearance of *Smad4* transcript in *Smad4*-deficient limb buds, a probe against the deleted region, coding exon 8 (Yang et al., 2002) was used for hybridization. Depending on the analysis, $Smad4^{+/+}$, $Smad4^{+/flox}$, $Smad4^{flox/flox}$ or $Smad4^{\Delta M/+}$ *Prx1*-$Cre^{tg/+}$ or $Hoxa13^{Cre/+}$ heterozygous embryos were used as controls and collectively referred to as 'wild-type controls'. Alcian Blue and Alizarin Red were used to reveal cartilage and bone.

Optical projection tomography

Optical projection tomography (OPT) imaging (Sharpe et al., 2002) was used to acquire 3D images and prepare optical sections. RNA hybrids were detected using nitro-blue tetrazolium and 5-bromo-4-chloro-3′-indolyphosphate (NBT/BCIP, Roche). Whole-mount immunofluorescence analysis was done as follows: embryos were permeabilized in cold acetone (15-30 minutes) and then incubated in blocking solution (PBT with 1% bovine serum albumin, 1% dimethyl sulfoxide and 5% inactivated bovine serum) for 20 minutes. SMAD4 was detected using rabbit monoclonal anti-SMAD4 antibodies, 1:50 in blocking solution (Abcam; 12 hour incubation at 4°C). Samples were washed extensively and incubated with secondary antibodies Alexa Fluor 594-conjugated anti-rabbit antibody, 1:250 (Invitrogen; overnight at 4°C). Subsequently, samples were embedded in 1% low melting point agarose (Sigma), dehydrated in 100% methanol and cleared in BABB. Samples were scanned either at high (1024×1024 pixels) or intermediate resolution (512×512 pixels) in the Bioptonics OPT scanner using Skyscan software (Bioptonics, MRC Technology). The GFP1 filter (425/40 nm, 475 nm LP) was used to detect sample anatomy. No filter (bright field) or the TXR filter (560/40 nm, 610 nm LP) was used to image NBT/BCIP signals or fluorescently labeled samples, respectively. OPT scans were reconstructed using NRecon software (SkyScan) and analysed using the Bioptonics Viewer. Rendering images were taken using the maximum intensity projection function. For generation of iso-surfaces, the iso-surface editor of the Bioptonics viewer program was used at 25%

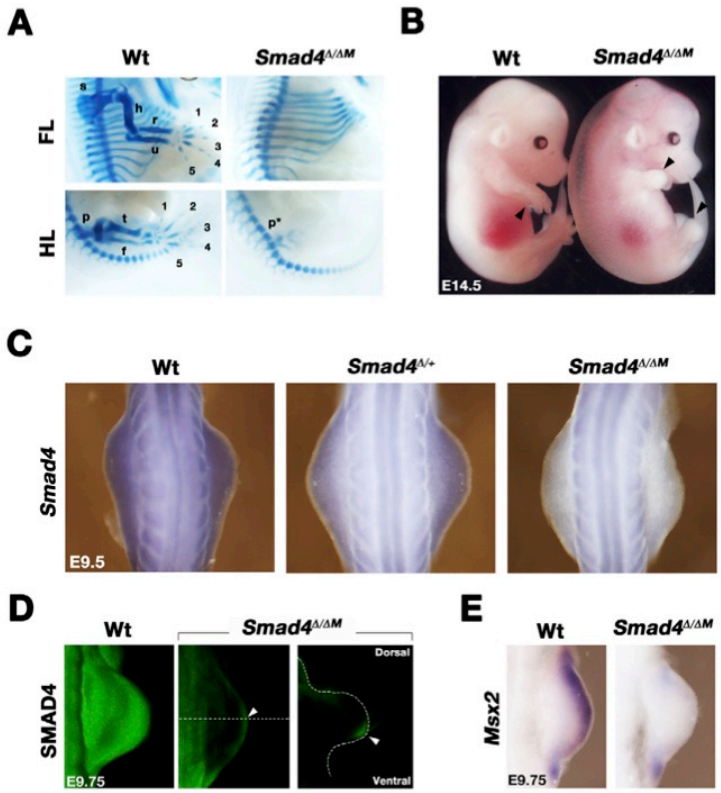

Fig. 1. *Prx1*-Cre-mediated inactivation of *Smad4* in mouse forelimb bud mesenchyme. (**A**) Skeletal preparations at embryonic day E14.5. Note the absence of all skeletal elements including the scapula in $Smad4^{\Delta/\Delta M}$ forelimbs (FL) and formation of only a rudimentary pelvic girdle in mutant hindlimbs (HL). (**B**) Brightfield images of wild-type and $Smad4^{\Delta/\Delta M}$ embryos at E14.5 to reveal the paddle-like limb morphology. (**C**) *Smad4* transcript distribution (blue-purple staining) in wild-type, $Smad4^{\Delta/+}$ and $Smad4^{\Delta/\Delta M}$ forelimb buds at E9.5 (23-24 somites). *Smad4* transcript levels are reduced in $Smad4^{\Delta/+}$ forelimb buds and cleared in $Smad4^{\Delta/\Delta M}$ forelimb buds. (**D**) Detection of SMAD4 protein (green fluorescence) by whole-mount antibody staining in wild-type (29 somites) and $Smad4^{\Delta/\Delta M}$ forelimb buds at E9.75 (27 somites). SMAD4 levels are also reduced along the primary axis, as only one *Smad4* allele is functional in $Smad4^{\Delta/\Delta M}$ embryos. The broken line indicates the approximate position of the virtual OPT section shown in the right-most panel. SMAD4 is lost from the mutant mesenchyme, whereas AER expression remains (arrowheads). (**E**) *Msx2*, a direct transcriptional target of BMP signaling, is downregulated in $Smad4^{\Delta/\Delta M}$ forelimb buds by E9.75 (26 somites). 1-5: digits 1-5; f, femur; h, humerus; p, pelvis; p*, rudimentary pelvis; r, radius; s, scapula; t, tibia; u, ulna.

iso-surface quality and 50% Gaussian smoothing parameters. Iso-surface values were determined and compared with the strength and distribution of the original signal to exclude aberrant iso-surfaces.

Quantification of transcript levels by quantitative real-time PCR

Forelimbs were isolated at E10.5 (35-39 somites) and E11.75 (51-53 somites) and analysed (Bénazet et al., 2009) using the primers listed in supplementary material Table S1. At least eight samples per stage and genotype were analysed. All results shown are mean±SD; each dot represents one sample, and the significance of all differences was verified using the two-tailed non-parametric Mann-Whitney U-test.

Immunofluorescence analysis

Embryos or forelimb buds were isolated and fixed in 4% PFA overnight at 4°C. Samples were dehydrated stepwise into 100% ethanol, then transferred to xylene. Subsequently, samples were embedded in Paraplast wax (Sigma) and sectioned following standard procedures. For most antibodies, antigen retrieval was achieved by heating the dewaxed sections at 121°C in 1 atm for 6 minutes in a desktop autoclave. The COL type II antigen was retrieved by digesting sections with pepsin (1 mg/ml in 10 mM HCl, pH 2.0) for 15 minutes (37°C). Sections were blocked using PBS containing 0.3% Triton X-100 and 1% BSA (blocking solution; 1 hour at room temperature). Following pre-treatment, sections were incubated with primary antibodies (blocking solution overnight at 4°C). The following primary antibodies were used: rabbit polyclonal anti-Ki67 1:200 (Millipore); rabbit polyclonal anti-Sox9 1:500 (Millipore); mouse monoclonal anti-collagen type-II 1:100 (Thermo Scientific); rabbit polyclonal anti-collagen type-I 1:500 (Abcam). Immunocomplexes were detected using the following secondary antibodies (1 hour at room temperature): goat anti-rabbit Alexa Fluor 594 1:500 (Invitrogen), goat anti-mouse Alexa Fluor 488 1:200 (Invitrogen). Apoptotic cells were detected by whole-mount Lysotracker analysis (Invitrogen) as previously described (Benazet et al., 2009).

Limb mesenchymal cell culture and immunofluorescence

Forelimbs were dissected in ice-cold PBS, and 2% trypsin digestion (25 minutes at 4°C) in combination with gently pipetting resulted in single cell preparations of mesenchymal cells that were plated in DMEM/F12 medium (supplemented with 0.5% penicillin/streptomycin and 10% FBS, Gibco-BRL) at 7.5×10^5 cells/300 μl in eight-well chamber slides (Ibidi). After 48 hours' culturing, samples were washed in PBS and fixed in 4% PFA (30 minutes at room temperature) before permeabilization and antigen detection as described above. BMP signaling was specifically inhibited by adding 10 μM dorsomorphin (Yu et al., 2008) and TGFβ signaling was inhibited by adding 10 μM SB431542 (Inman et al., 2002) in 0.1% DMSO (final concentration in medium). Control cells were cultured in medium containing 0.1% DMSO. Media were refreshed every 24 hours. The results shown are representative of eight independent experiments (supplementary material Fig. S5). Inhibition of p38, which is involved in non-canonical BMP signal transduction, had no effect on cell aggregation and the onset of chondrogenic differentiation (data not shown).

RESULTS

Requirement of mesenchymal *Smad4* for propagation of the SHH/GREM1/AER-FGF feedback loop during mouse limb bud development

Prx1-Cre-mediated conditional inactivation of *Smad4* in the mesenchyme ($Smad4^{\Delta/\Delta M}$) resulted in fore- and hindlimbs lacking skeletal elements (Fig. 1A). Stunted paddles replaced the autopod with digits at embryonic day E14.5 (Fig. 1B, arrowheads). As this initial analysis pointed to a late onset phenotype, the clearance of *Smad4* gene products was assessed (Fig. 1C,D; supplementary material Fig. S1A). Mesenchymal transcripts were undetectable by ~E9.5 (Fig. 1C) and proteins from ~E9.75 onward in $Smad4^{\Delta/\Delta M}$ forelimb buds (Fig. 1D). As the *Prx1*-Cre transgene is activated in

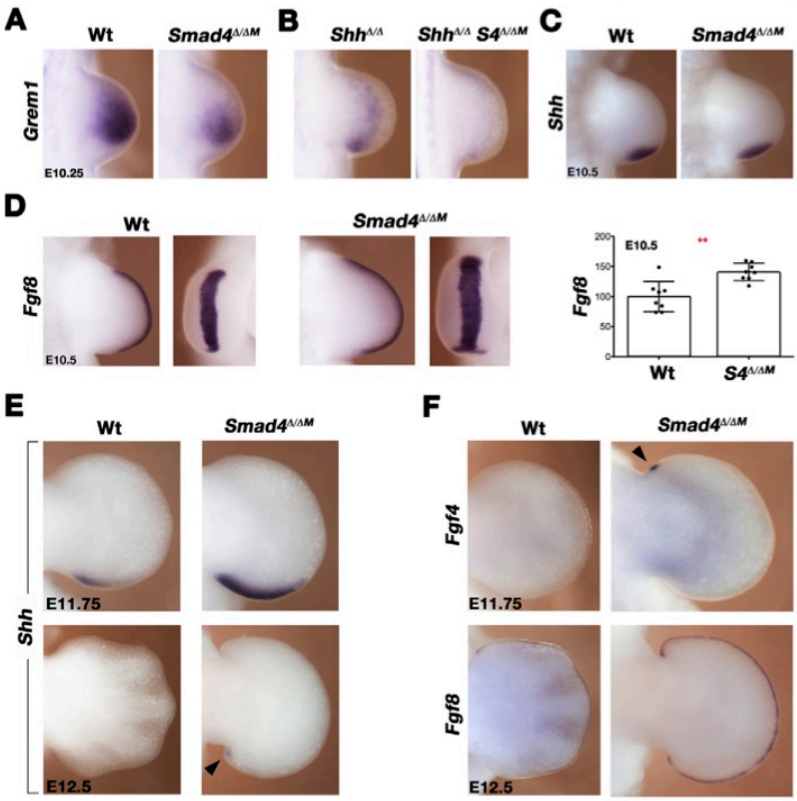

Fig. 2. Effect of mesenchymal *Smad4* deficiency on the SHH/GREM1/AER-FGF feedback loop. (**A**,**B**) *Grem1* expression in wild-type, $Smad4^{\Delta/\Delta M}$, $Shh^{\Delta/\Delta}$ and $Shh^{\Delta/\Delta}$ $Smad4^{\Delta/\Delta M}$ forelimbs at E10.25 (31-32 somites). (**C**) *Shh* expression is not significantly altered in $Smad4^{\Delta/\Delta M}$ forelimb buds at E10.5 (35 somites). (**D**) Expression of *Fgf8* in wild-type and $Smad4^{\Delta/\Delta M}$ forelimb buds at E10.5 (35 somites). Right panel: qPCR-based quantification of *Fgf8* levels in forelimb buds at E10.5. Expression is significantly higher in $Smad4^{\Delta/\Delta M}$ than wild-type forelimbs ($P \leq 0.01$). Data are shown as mean±SD. (**E**,**F**) Termination of *Shh* (E) and AER-*Fgf* (F) expression is delayed in $Smad4^{\Delta/\Delta M}$ forelimb buds. The black arrowheads indicate the prolonged *Shh* (E11.75, 50 somites and E12.5, 60 somites) and anterior AER-*Fgf4* expression (at E11.75, 50 somites) in mutant limb buds.

the forelimb bud territory before E9.0 (Logan et al., 2002), the complete functional inactivation of *Smad4* in forelimb buds required ~18 hours. In agreement with these inactivation kinetics, the expression of the BMP target *Msx2* was reduced from ~E9.75 onward (Fig. 1E; supplementary material Fig. S1B). By contrast, the three main *Bmp* ligands were either unchanged or slightly increased in mutant limb buds (supplementary material Fig. S2).

Previous analysis provided evidence that activation and initial upregulation of *Grem1* expression in the limb bud mesenchyme depended on BMP4 signaling (Nissim et al., 2006; Bénazet et al., 2009). In $Smad4^{\Delta/\Delta M}$ forelimb buds, *Grem1* expression was reduced, but its posterior domain was maintained at E10.25 (Fig. 2A). To discriminate between SMAD4-independent regulation and the well-characterized positive regulation of *Grem1* expression by SHH signaling (Zúñiga et al., 1999; Panman et al., 2006), forelimb buds lacking both *Shh* and *Smad4* were analysed. In contrast to the low expression in $Shh^{\Delta/\Delta}$ forelimb buds (Fig. 2B, left panel), *Grem1* expression was lost from $Shh^{\Delta/\Delta}Smad4^{\Delta/\Delta M}$ forelimb buds (Fig. 2B, right panel). These results showed that *Grem1* expression in the limb bud mesenchyme is positively regulated by both SHH and SMAD4-mediated signal transduction. Contrary to *Grem1*, *Shh* expression and signal transduction appeared normal (Fig. 2C and data not shown), whereas the AER-*Fgf8* expression domain was broadened and levels increased from ~E10.5 onward in $Smad4^{\Delta/\Delta M}$ forelimb buds (Fig. 2D). This analysis showed that mesenchymal *Smad4* is either not required, or its functional inactivation occurred too late to disrupt establishment of the AER-*Fgf8* expression domain (Bénazet et al., 2009), in contrast to its direct requirement in the AER (Bénazet and Zeller, unpublished). As the SHH/GREM1/AER-FGF signaling system terminated in wild-type limb buds, the expression of both *Shh* (Fig. 2E) and AER-*Fgfs* (Fig. 2F) persisted in $Smad4^{\Delta/\Delta M}$ forelimb buds. Rather unexpected from previous analysis (Scherz et al., 2004; Verheyden and Sun, 2008), these results reveal that mesenchymal *Smad4* is required for correct termination of the epithelial-mesenchymal feedback signaling system. In agreement with the initially normal progression of limb bud development, no striking alterations in cell proliferation were apparent in $Smad4^{\Delta/\Delta M}$ forelimb buds (supplementary material Fig. S3A). However, apoptosis of core mesenchymal cells was increased up to ~E11.5, whereas apoptosis in mutant handplates was suppressed because of the absence of the interdigit mesenchyme (supplementary material Fig. S3B; Fig. 3).

The spatiotemporal expression of the 5′-most *HoxD* and *HoxA* genes, which regulate limb bud patterning and outgrowth (reviewed by Zakany and Duboule, 2007) was not significantly altered up to E11.5 (data not shown). Fig. 3 shows the expression of select markers for the autopod, digit and interdigit territories. *Hoxa13* correctly delineated the presumptive autopod territory in mutant limb buds, but none of the putative digit primordia were outlined (Fig. 3A). *Cyp26b1* is normally expressed in the distal part of all digit primordia including the PFRs (Fig. 3B) (Yashiro et al., 2004). $Smad4^{\Delta/\Delta M}$ forelimb buds lacked these PFR-like expression domains and *Cyp26b1* was largely confined to the anterior and posterior margins (Fig. 3B). *Dlx5* is normally expressed by the AER and interdigit mesenchyme in wild-type limb buds (Robledo et al., 2002), but its expression was confined largely to the AER in $Smad4^{\Delta/\Delta M}$ forelimb buds (Fig. 3C). These results indicated that

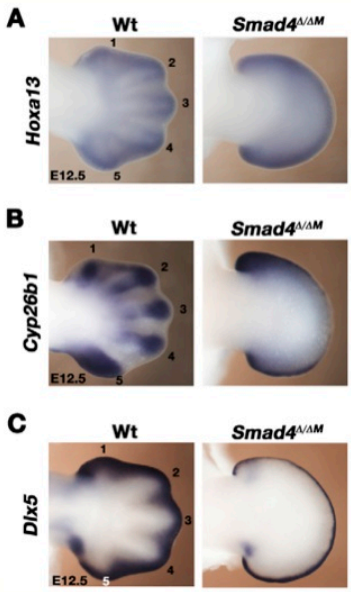

Fig. 3. Mesenchymal *Smad4* inactivation disrupts the spatial distribution of genes that mark specific autopod territories. (**A**) *Hoxa13* expression at E12.5 (60 somites). In wild-type forelimb buds, the distal parts of the developing digits and perichondria express the highest levels of *Hoxa13* transcript. In $Smad4^{\Delta/\Delta M}$ forelimb buds, *Hoxa13* expression is distally restricted but not localized to specific structures. (**B**) *Cyp26b1* marks the PFRs of all developing digit primordia in wild type, whereas no differential expression is apparent in $Smad4^{\Delta/\Delta M}$ forelimb buds. (**C**) *Dlx5* is expressed by the AER, subectodermal mesenchyme, and the interdigit mesenchyme in wild type, which is lacking in $Smad4^{\Delta/\Delta M}$ forelimb buds. The wild-type digit ray primordia are labelled 1 (thumb) to 5 (little finger).

separation of the mutant mesenchyme into digit ray primordia and interdigit mesenchyme was disrupted in $Smad4^{\Delta/\Delta M}$ autopods.

Smad4 is required to induce formation of the *Sox9*-positive digit ray primordia

Sox9 marks prechondrogenic progenitors from early limb bud stages onward. As *Sox9* prefigures the formation of all mesenchymal condensations that initiate chondrogenesis and give rise to the skeletal primordia (Bi et al., 1999; Akiyama et al., 2005), its expression was assessed (Fig. 4). Despite the early mesenchymal loss of *Smad4* and disruption of BMP signal transduction (Fig. 1B-D), the *Sox9* transcript distribution remained comparable to wild-type controls until at least E11.0 (Fig. 4A, left panels). These results indicated that SMAD4 is not required for activation and patterning of *Sox9* during the developmental period characterized by low BMP activity (Bénazet et al., 2009). The *Sox9*-positive progenitors in the proximal mesenchyme normally give rise to the cartilage elements of the scapula, stylopod (humerus) and zeugopod (radius and ulna). In wild-type forelimb buds, the *Sox9*-positive progenitors giving rise to the carpals and digit rays (metacarpals and phalanges) were apparent by ~E11.5, and the *Sox9*-positive digit ray primordia of all except digit 1 had formed by ~E12.25 (Fig. 4A, upper right panels) (Zhu et al., 2008). In $Smad4^{\Delta/\Delta M}$ limb buds, the distalmost zone of *Sox9*-negative mesenchyme expanded (Fig. 4A, brackets) and *Sox9* expression was progressively lowered (Fig. 4A, right-most lower panel). This downregulation was paralleled by a complete loss of the *Sox9*-positive primordia corresponding to carpals and digit rays (Fig. 4A,B). By E12.25, the characteristic *Sox9*-positive domains prefiguring all of the chondrogenic limb skeletal elements were largely lost from $Smad4^{\Delta/\Delta M}$ limb buds (Fig. 4A, right-most panels). By E13.5, only very low *Sox9* expression remained in $Smad4^{\Delta/\Delta M}$ limb buds, whereas *Sox9* was abundant in the PFRs and phalanges of all wild-type digits (supplementary material Fig. S4A). To gain further insight, OPT (Sharpe et al., 2002) was used in combination with iso-surface rendering for comparative analysis of the *Sox9* transcript distribution in wild-type and $Smad4^{\Delta/\Delta M}$ forelimb buds. This analysis revealed thinning of the distal arch of *Sox9*-positive cells (Fig. 4B, brackets), whereas the proximal domain was enlarged in $Smad4^{\Delta/\Delta M}$ forelimb buds (Fig. 4B, arrowheads; better seen in supplementary material Movie 1).

The requirement of *Smad4* for formation of the *Sox9*-positive digit rays could be transient, as evidenced by the kinetics of $Hoxa13^{Cre/+}$-mediated conditional inactivation of either one ($Smad4^{\Delta/\Delta A13}$) or both *Smad4* alleles (Fig. 4C, $Smad4^{\Delta A13/\Delta A13}$; supplementary material Fig. S4). Inactivation of *Smad4* using the $Hoxa13^{Cre/+}$ knock-in allele (Scotti and Kmita, 2012) resulted in the progressive clearance of *Smad4* transcripts during autopod development and specific agenesis of the autopod skeleton (supplementary material Fig. S4B,C). The functional loss of *Smad4* should be faster in $Smad4^{\Delta/\Delta A13}$ than $Smad4^{\Delta A13/\Delta A13}$ forelimb buds, as two conditional alleles have to be inactivated and twice as much SMAD4 proteins cleared in the latter (Bénazet et al., 2009). As only one *Hoxa13* allele is functional in mouse embryos carrying the $Hoxa13^{Cre/+}$ knock-in, we first established that formation of digit ray primordia was not altered in $Hoxa13^{Cre/+}$ and $Hoxa13^{Cre/+}Smad4^{\Delta A13/+}$ forelimb buds (Fig. 4C). However, only the two posteriormost digit ray primordia were apparent in $Smad4^{\Delta/\Delta A13}$ forelimb buds, whereas the primordia of digit rays 2-5 formed in all $Smad4^{\Delta A13/\Delta A13}$ forelimb buds (Fig. 4D). These results indicated that morphogenesis of anterior digit ray primordia could require *Smad4* for longer or at a later stage than posterior primordia.

SOX9-positive mesenchymal progenitors fail to aggregate and initiate chondrogenic differentiation of all cartilage elements in $Smad4^{\Delta/\Delta M}$ limb buds

As whole-mount RNA in situ hybridization analysis did not provide cellular resolution, the SOX9 protein distribution was analysed on serial sections of forelimb buds (Fig. 5, red fluorescence). At E10.5, scattered SOX9-positive mesenchymal cells were detected mainly in the core of both wild-type and $Smad4^{\Delta/\Delta M}$ forelimb buds (Fig. 5A,B). By E11.75, SOX9-positive progenitors condensed to initiate formation of the cartilage elements of the humerus and the ulna/radius and the posterior digit 4 in wild-type limb buds (Fig. 5C) (Zhu et al., 2008). In $Smad4^{\Delta/\Delta M}$ forelimb buds, a small proximal condensation was apparent (Fig. 5D, arrowhead), but most SOX9-positive cells remained loose and in a pattern reminiscent of the *Sox9*-positive distal arch (compare Fig. 5D and Fig. 4A). During subsequent development, no organized mesenchymal condensations and cartilage elements formed in $Smad4^{\Delta/\Delta M}$ forelimb buds (Fig. 5E-H). Rather, the small proximal condensation disappeared and SOX9-positive cells dispersed throughout the distal mesenchyme (Fig. 5F,H). Taken together, this analysis indicated that aggregation of the SOX9-positive progenitors to initiate chondrogenic differentiation and

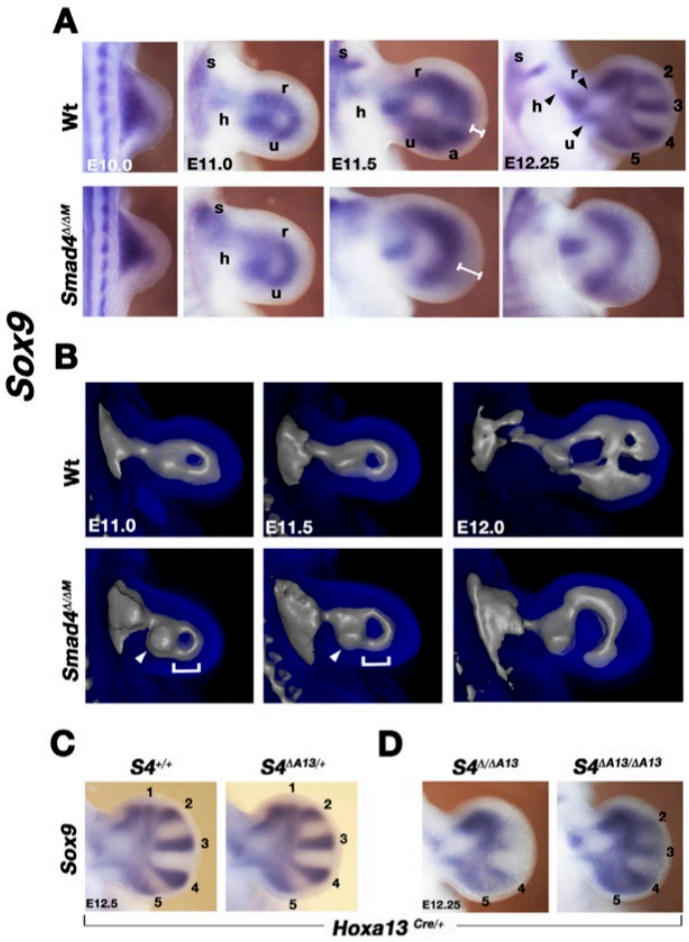

Fig. 4. Induction of *Sox9*-positive digit progenitors and maintenance of *Sox9* expression are disrupted in *Smad4*$^{\Delta/\Delta M}$ forelimb buds. (**A**) Spatial distribution of *Sox9* transcript in wild-type (upper panels) and *Smad4*-deficient forelimb buds. (**B**) Iso-surface rendering of the *Sox9* expression domains by OPT analysis. This reveals the progressive thinning of the distal arch (white brackets) and absence of *Sox9*-positive digit primordia in *Smad4*-deficient forelimb buds. By contrast, the *Sox9* expression domain probably corresponding to the zeugopod appears thickened (white arrowheads). (**C**) Heterozygosity for the *Hoxa13*$^{Cre/+}$ allele alone (*S4*$^{+/+}$) or in combination with inactivation of one *Smad4* allele (*S4*$^{\Delta A13/+}$) has no effect on *Sox9*-positive digit ray primordia. (**D**) *Hoxa13*$^{Cre/+}$-mediated conditional inactivation of either one (*S4*$^{\Delta/\Delta A13}$) or both *Smad4* alleles (*S4*$^{\Delta A13/\Delta A13}$) during autopod development reveals the differential effects on posterior and anterior digit ray primordia. E10.0: 30-32 somites; E11.0: 41 somites; E11.5: 44 somites; E12.0: 50 somites. E12.25-12.5: 53-57 somites. Primordia are indicated as follows: 1-5, primordia of digit rays 1-5; a, autopod; h, humerus; r, radius; s, scapula; u, ulna;.

formation of cartilage elements was disrupted in *Smad4*-deficient forelimb buds.

To gain further insight into the underlying cellular defects, wild-type and mutant mesenchymal cells were dissociated from limb buds at E11.5 and high-density cultures were used to assess their chondrogenic differential potential (Barna and Niswander, 2007). A hallmark of chondrogenic differentiation is the transcriptional activation of *Col2a1*, a direct transcriptional target of SOX9 that encodes the pro-alpha1(II) chain of COL type II, which is cartilage-specific (Bell et al., 1997; Lefebvre et al., 1997). In wild-type mesenchymal cultures, cells aggregated and compacted to form the typical cell-dense condensations often paralleled by reduced SOX9 expression, and the onset of chondrogenesis was revealed by abundant COL type II (Fig. 6A). By contrast, no COL type II was detected in areas of less densely packed cells (Fig. 6A, enlargements), which revealed that chondrogenesis was initiated in regions with high mesenchymal cell density, i.e. after cells had aggregated. By contrast, slightly lower levels of SOX9 were consistently detected in mesenchymal cells isolated from *Smad4*$^{\Delta/\Delta M}$ forelimb buds, which failed to aggregate and produce COL type II fibres (Fig. 6B). This failure of *Smad4*-deficient mesenchymal cells to aggregate appeared more severe than the effects of Noggin-mediated inhibition of BMP activity in limb bud mesenchymal cells, which aggregate but fail to undergo subsequent compaction and initiation of chondrogenesis (Barna and Niswander, 2007). To gain further insight, we selectively inhibited BMP type I receptors and thereby BMP signal transduction using Dorsomorphin (Yu et al., 2008), which disrupted condensation and COL type II expression of wild-type cells similar to *Smad4*$^{\Delta/\Delta M}$ cells (compare supplementary material Fig. S5B and Fig. 6B). Inhibiting TGFβ receptors with the selective antagonist SB431542 (Inman et al., 2002) blocked cell aggregation and COL type II deposition to a similar extent (supplementary material Fig. S5B) (Karamboulas et al., 2010). These results indicated that BMP and TGFβ signal transduction were both required for initiating chondrogenesis of mesenchymal progenitors in culture.

As these experiments revealed striking effects on deposition of extracellular COL type II fibres, the extent to which *Col2a1* expression might be altered in *Smad4*$^{\Delta/\Delta M}$ forelimb buds was determined (Fig. 7A). At E11.5, the *Col2a1* transcript distributions in wild-type and mutant forelimb buds were similar and comparable to *Sox9* at this stage (compare Fig. 7A, left panels and Fig. 4A). As autopod development progressed, *Col2a1* was expressed abundantly by all skeletal elements including digit rays in wild-type limb buds (Fig. 7A, upper panels). By contrast, *Col2a1* expression remained diffuse and was progressively lost

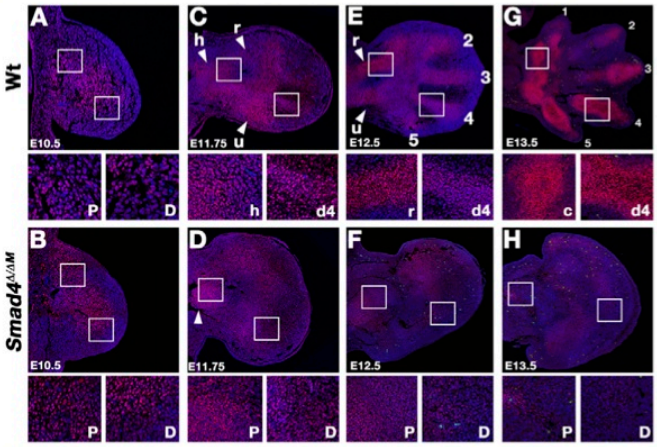

Fig. 5. SOX9 protein distribution in wild-type and *Smad4*$^{\Delta/\Delta M}$ forelimb buds. (**A-H**) The distribution of nuclear SOX9 protein (red) was determined on serial histological sections of limb buds from E10.5 to E13.5. Nuclei were counterstained using the DNA dye Hoechst (blue). (A,C,E,G) Wild-type forelimb buds. (B,D,F,H) In *Smad4*$^{\Delta/\Delta M}$ forelimb buds, the SOX9-positive cells fail to aggregate and initiate mesenchymal condensations. Only a small but transient proximal condensation is formed (arrowhead in D). White rectangles indicate the positions of the enlargements shown below. 1-5, digit ray primordia 1-5; c, carpal primordia; D, distal; d4, digit 4; h, humerus; P, proximal; r, radius; u, ulna.

from *Smad4*$^{\Delta/\Delta M}$ forelimb buds (Fig. 7A, lower panels). Indeed, high levels of COL type II protein were detected in all chondrogenic primordia of the skeletal elements in wild-type limb buds, whereas only few scattered positive clusters were detected in *Smad4*$^{\Delta/\Delta M}$ limb buds (Fig. 7B). Taken together, this analysis (Figs 5-7) revealed the disruption of chondrogenesis and absence of all cartilage elements prefiguring the limb skeleton in *Smad4*$^{\Delta/\Delta M}$ forelimb buds.

To determine the extent to which *Smad4*-deficient mesenchymal cells might acquire non-chondrogenic fates, genes marking other mesenchymal lineages were analysed. Collagen type I (COL type I) is expressed by diverse connective tissues such as skin, tendons, ligaments and bones, and muscle-associated connective tissues (see e.g. ten Berge et al., 2008). In wild-type limb buds, *Col1a2* was detected first in the proximal mesenchyme (Fig. 7C, E11.5). At later stages, *Col1a2* outlined the forming perichondria and tendons (Fig. 7C, arrowheads). In *Smad4*$^{\Delta/\Delta M}$ forelimb buds, *Col1a2* transcript and protein were detected throughout the mesenchyme (Fig. 7C,D, lower panels). COL type I localized to the perichondrium and developing dermis in wild type (Fig. 7D, upper panels), whereas its expression appeared more widespread and disorganized in *Smad4*$^{\Delta/\Delta M}$ forelimb buds (Fig. 7D, lower panels). As decorin (*Dcn*) regulates the assembly of collagen fibres (Danielson et al., 1997), its expression was analysed. In wild-type limb buds, the initially rather diffuse *Dcn* expression became excluded from the chondrogenic cores of all developing cartilage elements including digit rays (Fig. 8A, upper panels and data not shown). By contrast, *Dcn* expression was enhanced and persisted throughout the mesenchyme of *Smad4*$^{\Delta/\Delta M}$ forelimb buds (Fig. 8A, lower panels; supplementary material Fig. S6A). Possible effects on *Dcn* expression were also assessed in forelimb buds lacking both mesenchymal *Bmp2* and *Bmp4*, as the two posteriormost digit ray primordia are not formed (Fig. 8B) (Bandyopadhyay et al., 2006). Analogous to the *Smad4* deficiency (Fig. 8A), the absence of these two digit ray primordia results in uniformly increased expression of *Dcn* in the posterior mesenchyme of limb buds lacking both *Bmps* (Fig. 8B, posterior region indicated by a bracket). The striking similarity of these alterations indicates that formation of the posterior *Sox9*-positive digit ray primordia and restriction of *Dcn* expression depends on BMP signal transduction that is mediated by SMAD4.

In addition, the expression of the transcriptional regulator scleraxis (*Scx*, marking tendon and ligament progenitors) (Schweitzer et al., 2001) was also increased in *Smad4*$^{\Delta/\Delta M}$ forelimb buds (supplementary material Fig. S6B). While *Scx* marked both dorsal and ventral tendons in wild-type limb buds (Fig. 8C, upper panels), its expression was upregulated and diffuse in *Smad4*$^{\Delta/\Delta M}$ forelimb buds (Fig. 8C, lower panels). This was paralleled by widespread and diffuse expression of *Fjx1*, which normally marks the attachment points of the forming tendons and the developing joints (Rock et al., 2005), in *Smad4*-deficient forelimb buds (supplementary material Fig. S6C). In addition to tendons and ligaments, limb skeletal muscles form in concert with the limb skeletal elements. Analysis of the *MyoD* distribution (marking all limb muscle primordia) (Francis-West et al., 2003) showed that dysplastic skeletal muscles were present in the flank and proximal part of *Smad4*-deficient forelimb buds, whereas the distal mesenchyme was devoid of *MyoD*-expressing cells (supplementary

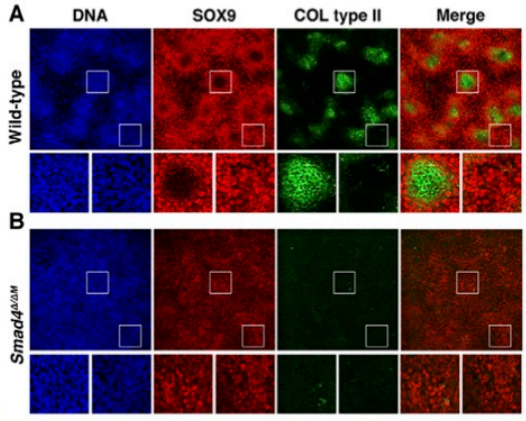

Fig. 6. Chondrogenic potential of wild-type and *Smad4*-deficient mesenchymal cells. (**A**) Wild-type limb bud mesenchymal cells (isolated at E11.5) form chondrogenic condensations after 48 hours in high-density culture. The peripheral cells of the chondrogenic condensations express the highest levels of SOX9 (red fluorescence). Cells in the core often express lower levels of SOX9 and produce COL type II (green fluorescence). (**B**) By contrast, *Smad4*$^{\Delta/\Delta M}$ mesenchymal cells fail to aggregate and produce COL type II. Cell nuclei were labelled by Hoechst (blue fluorescence). White rectangles indicate the positions of the enlargements shown below.

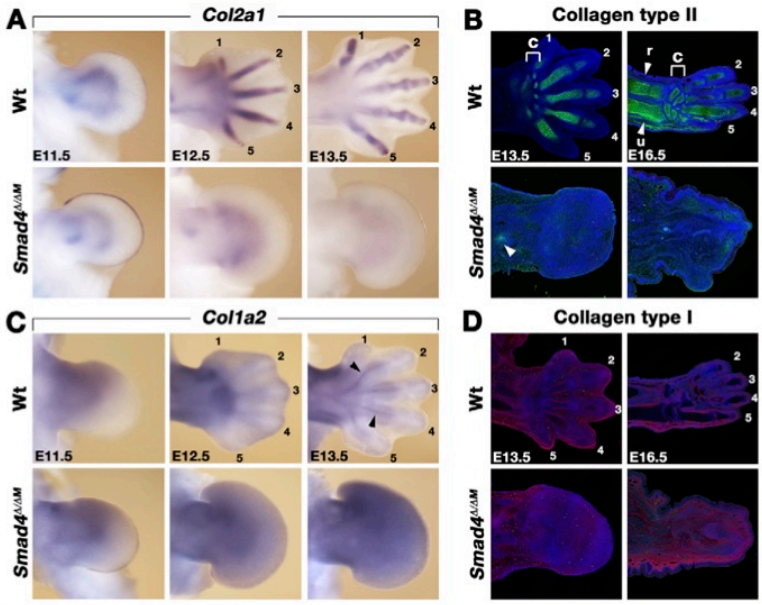

Fig. 7. Loss of cartilage-specific and increase of connective tissue-type collagens in *Smad4*$^{\Delta/\Delta M}$ forelimb buds. (**A**) *Col2a1* transcript distribution in wild-type and *Smad4*$^{\Delta/\Delta M}$ forelimb buds. In *Smad4*$^{\Delta/\Delta M}$ forelimb buds, mesenchymal *Col2a1* expression in the mesenchyme is similar to that of wild type up to E11.5, but is lost during subsequent stages. The *Col2a1* upregulation in the AER of *Smad4*$^{\Delta/\Delta M}$ forelimb buds was reproducibly detected at E11.5. (**B**) The COL type II distribution (green fluorescence) was assessed on serial histological sections. At E16.5, COL type II marks all developing limb skeletal elements. In *Smad4*$^{\Delta/\Delta M}$ forelimb buds, a small but transient cluster positive for COL type II was always detected (arrowheads). (**C**) *Col1a2* expression in wild-type forelimb buds marks connective tissue, perichondria and developing tendons (arrowheads, upper-right panel). In *Smad4*$^{\Delta/\Delta M}$ forelimb buds, *Col1a2* expression becomes increasingly widespread and diffuse (lower panels). (**D**) The COL type I distribution (red fluorescence) was assessed on serial histological sections. In wild-type forelimb buds, COL type I outlines the perichondria and dermis. The developing dorsal and ventral tendons are not apparent, as sections through the core mesenchyme are shown. In *Smad4*$^{\Delta/\Delta M}$ forelimb buds, most mesenchyme expresses this connective tissue-type collagen by E16.5. Labelling of primordia: 2-5, digit rays c, carpals; h, humerus; r, radius; u, ulna.

material Fig. S6D). Taken together, this analysis revealed the rather diffuse expression of genes marking diverse non-chondrogenic lineages and general disruption of tissue organization in *Smad4*$^{\Delta/\Delta M}$ forelimb buds, which pointed to diversion of chondrogenic to loose and non-specific connective tissue (Fig. 8D).

DISCUSSION

Our genetic analysis of mesenchymal *Smad4* during mouse limb bud development uncovers its dual requirement for initiating: (1) formation of the *Sox9*-positive digit ray primordia; and (2) aggregation and chondrogenic differentiation of all *Sox9*-positive prechondrogenic progenitors that give rise to the cartilage elements of the future limb skeleton (Fig. 8D). SMAD4 is essential to induce chondrogenesis because cell aggregation, which is the first step toward chondrogenic differentiation, is disrupted and mutant progenitors remain scattered in *Smad4*$^{\Delta/\Delta M}$ forelimb buds (Fig. 8D) (see also Pizette and Niswander, 2000; Barna and Niswander, 2007). By contrast, the expression of *Sox9*, which prefigures the primordia of the stylopod and zeugopod, is normal up to at least E11.0 in *Smad4*$^{\Delta/\Delta M}$ forelimb buds. A role of SMAD4 in activation of *Sox9* expression in early limb buds cannot be formally excluded, as the protein is only cleared around the time *Sox9* is activated in *Smad4*$^{\Delta/\Delta M}$ forelimb buds. Nevertheless, the *Smad4*-independent phase of *Sox9* expression coincides well with the period of low BMP activity in mouse limb buds (Bénazet et al., 2009), which corroborates the proposal that the spatiotemporal regulation of *Sox9* expression does not require SMAD4-mediated signal transduction before handplate formation (this study). Indeed, it has been proposed that BMPs inhibit *Sox9* expression and initiation of chondrogenic differentiation in the mesenchyme of early limb buds; an effect that can be alleviated by short-term exposure to TGFβ signaling in culture (Karamboulas et al., 2010). However, inhibition of BMP or TGFβ signal transduction in vitro disrupted chondrogenesis in a similar way to the genetic *Smad4* deficiency, but did not cause complete loss of SOX9 (this study).

In addition to *Sox9*, the mesenchymal expression of the early chondrocyte marker *Col2a1* is activated normally in *Smad4*$^{\Delta/\Delta M}$ forelimb buds. During distal progression of limb bud development, *Col2a1* expression is lost concurrent with the failure to refine SOX9 protein distribution, as expected from direct transcriptional regulation of *Col2a1* by SOX9 (Bell et al., 1997; Lefebvre et al., 1997). In *Smad4*$^{\Delta/\Delta M}$ forelimb buds, the progressive loss of *Sox9* and *Col2a1* was paralleled by widespread and diffuse expression of markers for other lineages and a general absence of tissue organization and differentiation. Therefore, SMAD4 appears to function in signaling networks that restrict non-chondrogenic progenitors and connective tissue lineages. In agreement with the diffuse *Scx* expression in *Smad4*$^{\Delta/\Delta M}$ forelimb buds, inhibition of BMP signaling results in ectopic *Scx* expression without the formation of additional tendons (Schweitzer et al., 2001). However,

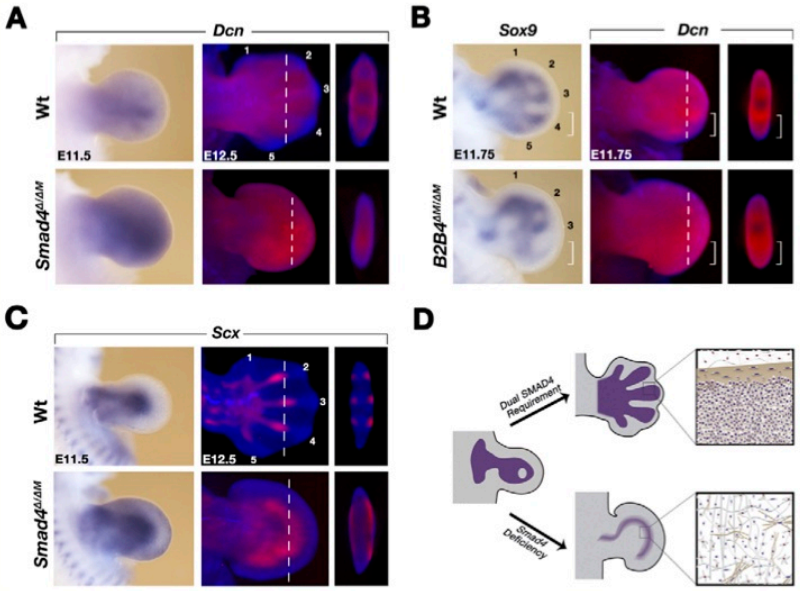

Fig. 8. General loss of tissue organization results in diversion towards fascia-like connective tissue in *Smad4*$^{\Delta/\Delta M}$ limb buds. (**A**) *Dcn* transcript distribution in wild-type and *Smad4*-deficient forelimb buds visualized by brightfield microscopy (left) and OPT analysis (right panels). The positions of the virtual OPT cross-sections are indicated by the broken white lines in the middle panels. (**B**) *Prx1*-Cre mediated inactivation of *Bmp2* and *Bmp4* in the forelimb bud mesenchyme (*B2B4*$^{\Delta M/\Delta M}$). Left panels show *Sox9* expression at E11.75 (51 somites). Middle and right panels show OPT analysis of *Dcn* distribution at E11.75. White brackets mark the relevant posterior part of *B2B4*$^{\Delta M/\Delta M}$ and wild-type forelimb buds. (**C**) *Scx* transcript distribution in wild-type and *Smad4*-deficient forelimb buds, which becomes normally restricted to the forming tendons by E12.5. OPT analysis reveals the diffuse *Scx* expression extending into the core mesenchyme of *Smad4*$^{\Delta/\Delta M}$ forelimb buds. (**D**) SMAD4 is required: (1) for digit ray formation in the distal mesenchyme; and (2) to induce aggregation and chondrogenic differentiation of all *Sox9*-positive mesenchymal progenitors. In *Smad4*$^{\Delta/\Delta M}$ limb buds, mutant mesenchymal cells remain loose and divert toward non-specific connective tissue lineages.

as both *Col1a1* and *Col1a2* are positively regulated by SCX (Cserjesi et al., 1995), the ectopic *Scx* expression in *Smad4*$^{\Delta/\Delta M}$ forelimb buds could contribute to the increased COL type I expression (this study). These molecular changes and the complete lack of tissue organization in *Smad4*-deficient limb buds (Fig. 8D) indicate that SMAD4 functions in the morphoregulatory networks that pattern diverse limb bud mesenchymal lineages and/or orchestrate coordinated tissue differentiation. Taken together, these studies uncover the recurrent differential requirement of SMAD4-mediated canonical BMP/TGFβ signal transduction during specification and aggregation of SOX9-positive prechondrogenic progenitors and initiation of their chondrogenic differentiation (Fig. 8D).

Although formation of the *Sox9*-positive primordia of the stylopod and zeugopod appears *Smad4*-independent, the induction of the *Sox9*-positive digit ray primordia depends critically on *Smad4* and increased BMP activity (Bandyopadhyay et al., 2006; Bénazet et al., 2009; Lopez-Rios et al., 2012; this study). As the proximal *Sox9*-positive domains are enlarged, the mutant pre-chondrogenic cells may contribute preferentially to proximal primordia as evidenced by thinning of the distal arch in *Smad4*$^{\Delta/\Delta M}$ forelimb buds (this study). Such a differential requirement of *Smad4* might be of evolutionary relevance as the autopod and digits of tetrapod limbs are so-called neomorphic structures, whose development may have relied on co-opting novel gene-regulatory networks (reviewed by Woltering and Duboule, 2010). Our analysis indicates that limb bud development and formation of *Sox9*-positive digit ray primordia become *Smad4* dependent as BMP activity rises owing to self-termination of the SHH/Grem1/AER-FGF signaling system (Scherz et al., 2004; Verheyden and Sun, 2008; Benazet et al., 2009). During this developmental period, differential BMP signaling appears to determine digit identities in both chicken and mouse (Dahn and Fallon, 2000; Suzuki et al., 2008; Witte et al., 2010). As extensive genetic analysis of TGFβ signaling in mouse embryos has not produced similar phenotypes (see e.g. Sanford et al., 1997; Seo and Serra, 2007), SMAD4-mediated BMP signal transduction is likely to be predominant during these advanced stages of digit ray primordia growth and patterning. It has been proposed that the progenitors giving rise to the digit ray primordia are recruited from the distalmost limb bud mesenchyme (Suzuki et al., 2008), which is defective in *Smad4*$^{\Delta/\Delta M}$ forelimb buds as revealed by the increasing gap of *Sox9*-negative cells in the distal mesenchyme (this study). In addition, temporally controlled *Smad4* inactivation in the autopod provided evidence for its possible differential requirement for posterior and anterior digit ray primordia. A region free of the BMP antagonist GREM1 is generated within the posterior limb bud mesenchyme by the population of *Shh* descendants, which is refractory to *Grem1* expression and increases as limb bud development progresses (Scherz et al., 2004). These results together with the differential requirement observed in this study indicate that BMP activity might first rise in the posterior mesenchyme, where *Bmp2* and *Bmp4* are co-expressed and required for digit ray formation (Bandyopadhyay et al., 2006). The

mechanism that controls BMP-dependent formation of the digit ray primordia was recently uncovered (Lopez-Rios et al., 2012). Inactivation of *Gli3* in the developing autopod promoted cell cycle entry and delayed the exit of digit progenitors to chondrogenesis due to prolonged GREM1-mediated BMP-antagonism in the anterior limb bud mesenchyme. Taken together, this indicates that two distinct mechanisms regulate digit ray formation in the posterior and anterior handplate via BMP-dependent SMAD4-mediated signal transduction. The spatiotemporal requirements of BMPs and SMAD4 for posterior and anterior digit ray primordia (Bandyopadhyay et al., 2006; Lopez-Rios et al., 2012; this study) is apparently at odds with the genetic analysis of the temporal requirement of *Shh* during mouse limb bud development (Zhu et al., 2008). This analysis showed that digit ray primordia form with alternating posterior to anterior sequence (starting with d4, d2, d5 and ending with d3), while digit 1 forms in a SHH-independent manner. However, these apparent discrepancies are resolved if BMPs and SMAD4 were transiently required to initiate a posterior and anterior mesenchymal condensation that would subsequently give rise to the primordia of digits 4 and 5 and digits 2 and 3, respectively, following the sequence defined by Zhu et al. (Zhu et al., 2008).

Finally, BMPs are widely used to induce chondrogenesis in ex vivo models of cartilage and bone engineering, but outcomes are often conflicting (Jiang et al., 2010; Sanchez-Adams and Athanasiou, 2012). In light of the complex regulation of chondrogenesis during limb bud development, ex vivo developmental engineering of cartilage and endochondral bone (Scotti et al., 2010) will probably require activation and inhibition of BMP signal transduction in a spatiotemporally controlled manner as revealed by the present study. In particular, this study highlights the temporal kinetics of the SMAD4 requirement during formation of the *Sox9*-positive digit ray primordia and its more general role in inducing aggregation of the mesenchymal progenitors during the onset of chondrogenesis, which is key to developmentally engineering cartilage and bone.

Acknowledgements

We are grateful to Chuxia Deng for providing us with the *Smad4* conditional allele and to Georg Holländer for colony founder mice, to Marie Kmita and Martina Scotti for providing us with the *Hoxa13*-Cre knock-in mouse strain, and to Phillipa Francis-West and Manfred Gesser for providing plasmids for RNA in situ hybridization probes. We are grateful to Angelika Offinger and Cornelia Meyer for excellent mouse care and to Chris Müller-Thompson for help in preparing this manuscript. Group members are thanked for helpful input into the manuscript.

Funding

This study was made possible by grants from the Swiss National Science Foundation [31003A-130803 to R.Z.], a EU Marie Curie International Incoming Fellowship [273304 to A.N.], a SystemsX.ch iPhD grant [20101078 to E.U. and R.Z.] and support by the University of Basel.

Competing interests statement

The authors declare no competing financial interests.

Supplementary material

Supplementary material available online at
http://dev.biologists.org/lookup/suppl/doi:10.1242/dev.084822/-/DC1

References

Ahn, K., Mishina, Y., Hanks, M. C., Behringer, R. R. and Crenshaw, E. B., 3rd (2001). BMPR-IA signaling is required for the formation of the apical ectodermal ridge and dorsal-ventral patterning of the limb. *Development* **128**, 4449-4461.

Akiyama, H., Kim, J. E., Nakashima, K., Balmes, G., Iwai, N., Deng, J. M., Zhang, Z., Martin, J. F., Behringer, R. R., Nakamura, T. et al. (2005). Osteo-chondroprogenitor cells are derived from Sox9 expressing precursors. *Proc. Natl. Acad. Sci. USA* **102**, 14665-14670.

Bandyopadhyay, A., Tsuji, K., Cox, K., Harfe, B. D., Rosen, V. and Tabin, C. J. (2006). Genetic analysis of the roles of BMP2, BMP4, and BMP7 in limb patterning and skeletogenesis. *PLoS Genet.* **2**, e216.

Barna, M. and Niswander, L. (2007). Visualization of cartilage formation: insight into cellular properties of skeletal progenitors and chondrodysplasia syndromes. *Dev. Cell* **12**, 931-941.

Bastida, M. F., Delgado, M. D., Wang, B., Fallon, J. F., Fernandez-Teran, M. and Ros, M. A. (2004). Levels of Gli3 repressor correlate with Bmp4 expression and apoptosis during limb development. *Dev. Dyn.* **231**, 148-160.

Bell, D. M., Leung, K. K., Wheatley, S. C., Ng, L. J., Zhou, S., Ling, K. W., Sham, M. H., Koopman, P., Tam, P. P. and Cheah, K. S. (1997). Sox9 directly regulates the type-II collagen gene. *Nat. Genet.* **16**, 174-178.

Bénazet, J. D., Bischofberger, M., Tiecke, E., Gonçalves, A., Martin, J. F., Zuniga, A., Naef, F. and Zeller, R. (2009). A self-regulatory system of interlinked signaling feedback loops controls mouse limb patterning. *Science* **323**, 1050-1053.

Bi, W., Deng, J. M., Zhang, Z., Behringer, R. R. and de Crombrugghe, B. (1999). Sox9 is required for cartilage formation. *Nat. Genet.* **22**, 85-89.

Brunet, L. J., McMahon, J. A., McMahon, A. P. and Harland, R. M. (1998). Noggin, cartilage morphogenesis, and joint formation in the mammalian skeleton. *Science* **280**, 1455-1457.

Chu, G. C., Dunn, N. R., Anderson, D. C., Oxburgh, L. and Robertson, E. J. (2004). Differential requirements for Smad4 in TGFbeta-dependent patterning of the early mouse embryo. *Development* **131**, 3501-3512.

Cserjesi, P., Brown, D., Ligon, K. L., Lyons, G. E., Copeland, N. G., Gilbert, D. J., Jenkins, N. A. and Olson, E. N. (1995). Scleraxis: a basic helix-loop-helix protein that prefigures skeletal formation during mouse embryogenesis. *Development* **121**, 1099-1110.

Dahn, R. D. and Fallon, J. F. (2000). Interdigital regulation of digit identity and homeotic transformation by modulated BMP signaling. *Science* **289**, 438-441.

Danielson, K. G., Baribault, H., Holmes, D. F., Graham, H., Kadler, K. E. and Iozzo, R. V. (1997). Targeted disruption of decorin leads to abnormal collagen fibril morphology and skin fragility. *J. Cell Biol.* **136**, 729-743.

Feng, X. H. and Derynck, R. (2005). Specificity and versatility in tgf-beta signaling through Smads. *Annu. Rev. Cell Dev. Biol.* **21**, 659-693.

Francis-West, P. H., Antoni, L. and Anakwe, K. (2003). Regulation of myogenic differentiation in the developing limb bud. *J. Anat.* **202**, 69-81.

Gros, J., Hu, J. K., Vinegoni, C., Feruglio, P. F., Weissleder, R. and Tabin, C. J. (2010). WNT5A/JNK and FGF/MAPK pathways regulate the cellular events shaping the vertebrate limb bud. *Curr. Biol.* **20**, 1993-2002.

Inman, G. J., Nicolás, F. J., Callahan, J. F., Harling, J. D., Gaster, L. M., Reith, A. D., Laping, N. J. and Hill, C. S. (2002). SB-431542 is a potent and specific inhibitor of transforming growth factor-beta superfamily type I activin receptor-like kinase (ALK) receptors ALK4, ALK5, and ALK7. *Mol. Pharmacol.* **62**, 65-74.

Jiang, Y., Chen, L. K., Zhu, D. C., Zhang, G. R., Guo, C., Qi, Y. Y. and Ouyang, H. W. (2010). The inductive effect of bone morphogenetic protein-4 on chondral-lineage differentiation and in situ cartilage repair. *Tissue Eng. Part A* **16**, 1621-1632.

Karamboulas, K., Dranse, H. J. and Underhill, T. M. (2010). Regulation of BMP-dependent chondrogenesis in early limb mesenchyme by TGFbeta signals. *J. Cell Sci.* **123**, 2068-2076.

Kobayashi, T., Lyons, K. M., McMahon, A. P. and Kronenberg, H. M. (2005). BMP signaling stimulates cellular differentiation at multiple steps during cartilage development. *Proc. Natl. Acad. Sci. USA* **102**, 18023-18027.

Lefebvre, V., Huang, W., Harley, V. R., Goodfellow, P. N. and de Crombrugghe, B. (1997). Sox9 is a potent activator of the chondrocyte-specific enhancer of the pro alpha1(II) collagen gene. *Mol. Cell. Biol.* **17**, 2336-2346.

Logan, M., Martin, J. F., Nagy, A., Lobe, C., Olson, E. N. and Tabin, C. J. (2002). Expression of Cre Recombinase in the developing mouse limb bud driven by a Prxl enhancer. *Genesis* **33**, 77-80.

Lopez-Rios, J., Speziale, D., Robay, D., Scotti, M., Osterwalder, M., Nusspaumer, G., Galli, A., Holländer, G. A., Kmita, M. and Zeller, R. (2012). GLI3 constrains digit number by controlling both progenitor proliferation and BMP-dependent exit to chondrogenesis. *Dev. Cell* **22**, 837-848.

Lorda-Diez, C. I., Montero, J. A., Diaz-Mendoza, M. J., Garcia-Porrero, J. A. and Hurle, J. M. (2011). Defining the earliest transcriptional steps of chondrogenic progenitor specification during the formation of the digits in the embryonic limb. *PLoS ONE* **6**, e24546.

Maatouk, D. M., Choi, K. S., Bouldin, C. M. and Harfe, B. D. (2009). In the limb AER Bmp2 and Bmp4 are required for dorsal-ventral patterning and interdigital cell death but not limb outgrowth. *Dev. Biol.* **327**, 516-523.

Merino, R., Macias, D., Gañan, Y., Rodriguez-Leon, J., Economides, A. N., Rodriguez-Esteban, C., Izpisua-Belmonte, J. C. and Hurle, J. M. (1999). Control of digit formation by activin signaling. *Development* **126**, 2161-2170.

Michos, O., Panman, L., Vintersten, K., Beier, K., Zeller, R. and Zuniga, A. (2004). Gremlin-mediated BMP antagonism induces the epithelial-mesenchymal feedback signaling controlling metanephric kidney and limb organogenesis. *Development* **131**, 3401-3410.

Nissim, S., Hasso, S. M., Fallon, J. F. and Tabin, C. J. (2006). Regulation of Gremlin expression in the posterior limb bud. *Dev. Biol.* **299**, 12-21.

Ovchinnikov, D. A., Selever, J., Wang, Y., Chen, Y. T., Mishina, Y., Martin, J. F. and Behringer, R. R. (2006). BMP receptor type IA in limb bud mesenchyme regulates distal outgrowth and patterning. *Dev. Biol.* **295**, 103-115.
Pajni-Underwood, S., Wilson, C. P., Elder, C., Mishina, Y. and Lewandoski, M. (2007). BMP signals control limb bud interdigital programmed cell death by regulating FGF signaling. *Development* **134**, 2359-2368.
Pan, Q., Yu, Y., Chen, Q., Li, C., Wu, H., Wan, Y., Ma, J. and Sun, F. (2008). Sox9, a key transcription factor of bone morphogenetic protein-2-induced chondrogenesis, is activated through BMP pathway and a CCAAT box in the proximal promoter. *J. Cell. Physiol.* **217**, 228-241.
Panman, L., Galli, A., Lagarde, N., Michos, O., Soete, G., Zuniga, A. and Zeller, R. (2006). Differential regulation of gene expression in the digit forming area of the mouse limb bud by SHH and gremlin 1/FGF-mediated epithelial-mesenchymal signaling. *Development* **133**, 3419-3428.
Pizette, S. and Niswander, L. (2000). BMPs are required at two steps of limb chondrogenesis: formation of prechondrogenic condensations and their differentiation into chondrocytes. *Dev. Biol.* **219**, 237-249.
Pizette, S., Abate-Shen, C. and Niswander, L. (2001). BMP controls proximodistal outgrowth, via induction of the apical ectodermal ridge, and dorsoventral patterning in the vertebrate limb. *Development* **128**, 4463-4474.
Probst, S., Kraemer, C., Demougin, P., Sheth, R., Martin, G. R., Shiratori, H., Hamada, H., Iber, D., Zeller, R. and Zuniga, A. (2011). SHH propagates distal limb bud development by enhancing CYP26B1-mediated retinoic acid clearance via AER-FGF signaling. *Development* **138**, 1913-1923.
Roark, E. F. and Greer, K. (1994). Transforming growth factor-beta and bone morphogenetic protein-2 act by distinct mechanisms to promote chick limb cartilage differentiation in vitro. *Dev. Dyn.* **200**, 103-116.
Robledo, R. F., Rajan, L., Li, X. and Lufkin, T. (2002). The Dlx5 and Dlx6 homeobox genes are essential for craniofacial, axial, and appendicular skeletal development. *Genes Dev.* **16**, 1089-1101.
Rock, R., Heinrich, A. C., Schumacher, N. and Gessler, M. (2005). Fjx1: a notch-inducible secreted ligand with specific binding sites in developing mouse embryos and adult brain. *Dev. Dyn.* **234**, 602-612.
Sanchez-Adams, J. and Athanasiou, K. A. (2012). Dermis isolated adult stem cells for cartilage tissue engineering. *Biomaterials* **33**, 109-119.
Sanford, L. P., Ormsby, I., Gittenberger-de Groot, A. C., Sariola, H., Friedman, R., Boivin, G. P., Cardell, E. L. and Doetschman, T. (1997). TGFbeta2 knockout mice have multiple developmental defects that are non-overlapping with other TGFbeta knockout phenotypes. *Development* **124**, 2659-2670.
Scherz, P. J., Harfe, B. D., McMahon, A. P. and Tabin, C. J. (2004). The limb bud Shh-Fgf feedback loop is terminated by expansion of former ZPA cells. *Science* **305**, 396-399.
Schweitzer, R., Chyung, J. H., Murtaugh, L. C., Brent, A. E., Rosen, V., Olson, E. N., Lassar, A. and Tabin, C. J. (2001). Analysis of the tendon cell fate using Scleraxis, a specific marker for tendons and ligaments. *Development* **128**, 3855-3866.
Scotti, C., Tonnarelli, B., Papadimitropoulos, A., Scherberich, A., Schaeren, S., Schauerte, A., Lopez-Rios, J., Zeller, R., Barbero, A. and Martin, I. (2010). Recapitulation of endochondral bone formation using human adult mesenchymal stem cells as a paradigm for developmental engineering. *Proc. Natl. Acad. Sci. USA* **107**, 7251-7256.
Scotti, M. and Kmita, M. (2012). Recruitment of 5′ Hoxa genes in the allantois is essential for proper extra-embryonic function in placental mammals. *Development* **139**, 731-739.
Selever, J., Liu, W., Lu, M. F., Behringer, R. R. and Martin, J. F. (2004). Bmp4 in limb bud mesoderm regulates digit pattern by controlling AER development. *Dev. Biol.* **276**, 268-279.
Seo, H. S. and Serra, R. (2007). Deletion of Tgfbr2 in Prx1-cre expressing mesenchyme results in defects in development of the long bones and joints. *Dev. Biol.* **310**, 304-316.
Sharpe, J., Ahlgren, U., Perry, P., Hill, B., Ross, A., Hecksher-Sørensen, J., Baldock, R. and Davidson, D. (2002). Optical projection tomography as a tool for 3D microscopy and gene expression studies. *Science* **296**, 541-545.
Suzuki, T., Hasso, S. M. and Fallon, J. F. (2008). Unique SMAD1/5/8 activity at the phalanx-forming region determines digit identity. *Proc. Natl. Acad. Sci. USA* **105**, 4185-4190.
ten Berge, D., Brugmann, S. A., Helms, J. A. and Nusse, R. (2008). Wnt and FGF signals interact to coordinate growth with cell fate specification during limb development. *Development* **135**, 3247-3257.
Verheyden, J. M. and Sun, X. (2008). An Fgf/Gremlin inhibitory feedback loop triggers termination of limb bud outgrowth. *Nature* **454**, 638-641.
Witte, F., Chan, D., Economides, A. N., Mundlos, S. and Stricker, S. (2010). Receptor tyrosine kinase-like orphan receptor 2 (ROR2) and Indian hedgehog regulate digit outgrowth mediated by the phalanx-forming region. *Proc. Natl. Acad. Sci. USA* **107**, 14211-14216.
Woltering, J. M. and Duboule, D. (2010). The origin of digits: expression patterns versus regulatory mechanisms. *Dev. Cell* **18**, 526-532.
Wong, Y. L., Behringer, R. R. and Kwan, K. M. (2012). Smad1/Smad5 signaling in limb ectoderm functions redundantly and is required for interdigital programmed cell death. *Dev. Biol.* **363**, 247-257.
Wu, X., Shi, W. and Cao, X. (2007). Multiplicity of BMP signaling in skeletal development. *Ann. N. Y. Acad. Sci.* **1116**, 29-49.
Yang, X., Li, C., Herrera, P. L. and Deng, C. X. (2002). Generation of Smad4/Dpc4 conditional knockout mice. *Genesis* **32**, 80-81.
Yashiro, K., Zhao, X., Uehara, M., Yamashita, K., Nishijima, M., Nishino, J., Saijoh, Y., Sakai, Y. and Hamada, H. (2004). Regulation of retinoic acid distribution is required for proximodistal patterning and outgrowth of the developing mouse limb. *Dev. Cell* **6**, 411-422.
Yoon, B. S., Ovchinnikov, D. A., Yoshii, I., Mishina, Y., Behringer, R. R. and Lyons, K. M. (2005). Bmpr1a and Bmpr1b have overlapping functions and are essential for chondrogenesis in vivo. *Proc. Natl. Acad. Sci. USA* **102**, 5062-5067.
Yu, P. B., Hong, C. C., Sachidanandan, C., Babitt, J. L., Deng, D. Y., Hoyng, S. A., Lin, H. Y., Bloch, K. D. and Peterson, R. T. (2008). Dorsomorphin inhibits BMP signals required for embryogenesis and iron metabolism. *Nat. Chem. Biol.* **4**, 33-41.
Zakany, J. and Duboule, D. (2007). The role of Hox genes during vertebrate limb development. *Curr. Opin. Genet. Dev.* **17**, 359-366.
Zakin, L. and De Robertis, E. M. (2010). Extracellular regulation of BMP signaling. *Curr. Biol.* **20**, R89-R92.
Zeller, R., López-Ríos, J. and Zuniga, A. (2009). Vertebrate limb bud development: moving towards integrative analysis of organogenesis. *Nat. Rev. Genet.* **10**, 845-858.
Zhu, J., Nakamura, E., Nguyen, M. T., Bao, X., Akiyama, H. and Mackem, S. (2008). Uncoupling Sonic hedgehog control of pattern and expansion of the developing limb bud. *Dev. Cell* **14**, 624-632.
Zúñiga, A., Haramis, A. P., McMahon, A. P. and Zeller, R. (1999). Signal relay by BMP antagonism controls the SHH/FGF4 feedback loop in vertebrate limb buds. *Nature* **401**, 598-602.

Publication 2: Attenuated sensing of SHH by *Ptch1* underlies evolution of bovine limbs

In this manuscript, I performed OPT analysis of the mouse and bovine limbs and confirmed that Ptch1 is not up-regulated in the bovine limb bud mesenchyme. The results are published as part of Figure 3 and extended Figures 3 and 4.

ARTICLE

doi:10.1038/nature13289

Attenuated sensing of SHH by *Ptch1* underlies evolution of bovine limbs

Javier Lopez-Rios[1]*, Amandine Duchesne[1,2]*, Dario Speziale[1], Guillaume Andrey[3], Kevin A. Peterson[4], Philipp Germann[5], Erkan Ünal[1,5], Jing Liu[4], Sandrine Floriot[2], Sarah Barbey[6], Yves Gallard[6], Magdalena Müller-Gerbl[7], Andrew D. Courtney[8], Christophe Klopp[9], Sabrina Rodriguez[2]†, Robert Ivanek[1,10], Christian Beisel[5], Carol Wicking[8], Dagmar Iber[5], Benoit Robert[11], Andrew P. McMahon[4], Denis Duboule[3,12] & Rolf Zeller[1]

The large spectrum of limb morphologies reflects the wide evolutionary diversification of the basic pentadactyl pattern in tetrapods. In even-toed ungulates (artiodactyls, including cattle), limbs are adapted for running as a consequence of progressive reduction of their distal skeleton to symmetrical and elongated middle digits with hoofed phalanges. Here we analyse bovine embryos to establish that polarized gene expression is progressively lost during limb development in comparison to the mouse. Notably, the transcriptional upregulation of the *Ptch1* gene, which encodes a Sonic hedgehog (SHH) receptor, is disrupted specifically in the bovine limb bud mesenchyme. This is due to evolutionary alteration of a *Ptch1 cis*-regulatory module, which no longer responds to graded SHH signalling during bovine handplate development. Our study provides a molecular explanation for the loss of digit asymmetry in bovine limb buds and suggests that modifications affecting the *Ptch1 cis*-regulatory landscape have contributed to evolutionary diversification of artiodactyl limbs.

A prime example of morphological evolution is the diversification of pentadactylous (five digits) limbs in tetrapods to serve a multitude of specialized needs such as grasping, digging, swimming, flying and running[1]. Artiodactyls (even-toed ungulates, including cattle, deer, giraffe, hippopotamus, whale, dolphin, pig and camel) are a diversified order of mammals that underwent highly successful radiation from the early Eocene; that is, from ~55 million years ago[2,3]. In the order Artiodactyla, Bovidae represent the largest extant family, and their domestication was pivotal to human agricultural settlement[4]. One key feature of terrestrial artiodactyls is the significant lengthening and streamlining of their distal limb skeleton, an adaption to walking and running on different terrains. Artiodactyl limbs are paraxonic, which means that the weight-bearing axis has shifted to between digits III and IV. The major morphological feature is that both middle digits are of equal length to facilitate walking on the distal-most phalanges (unguligrade posture). These evolutionary modifications in digit length and morphology are paralleled by varying degrees of digit loss (oligodactyly) and secondary fusions[2,3,5].

Analysis of *Bos taurus* (referred to as bovine) and *Mus musculus* (mouse) at equivalent developmental stages (Extended Data Fig. 1a) reveals the marked differences in their distal limb skeletons. In contrast to the mouse, only two elongated metacarpal primordia form in bovine handplates (autopod; Fig. 1a) and give rise to the cannon bone (Extended Data Fig. 1b)[2,5]. The middle digits that give rise to the cloven hoof are symmetrical and of identical length (digits III and IV). The vestigial lateral condensations (digits II and V) form the dewclaws and the anterior-most digit I is absent (Fig. 1a), as in many other tetrapods[6,7]. The oligodactyly of the bovine autopod could result from elimination of digit progenitors, but no apoptosis of cartilage precursors was detected (Extended Data Fig. 2a). This excludes cell death as the probable cause of the oligodactyly, in agreement with previous analysis of pig limb buds, which represent Suidae, another major artiodactyl family[8].

To circumvent pleiotropic and possibly lethal phenotypes, alterations underlying the unguligrade nature of the bovine limb skeleton should be limb-bud specific and probably alter the robust signalling systems that control vertebrate limb development[9–12]. Anterior–posterior polarization of the nascent limb bud mesenchyme, activation of *Shh* expression, and upregulation of the SHH receptor *Ptch1* and the *Gli1* transcriptional regulator in responding mesenchymal cells occur without apparent differences in both mouse and bovine forelimb buds (Fig. 1b and Extended Data Fig. 2b)[13–15]. In both species, expression of the extracellular BMP antagonist *Grem1* is upregulated in mesenchymal cells in response to SHH and keeps BMP activity low (Fig. 1b and Extended Data Fig. 2b)[9]. GREM1-mediated antagonism of BMPs contributes to maintaining *Fgf* expression in the apical ectodermal ridge (AER; Fig. 1b) as part of an epithelial–mesenchymal feedback loop[11]. This analysis shows that the mesenchymal SHH and AER–FGF signalling centres and mesenchymal SHH targets are activated in an identical manner in limb buds of both species[16,17]. Remarkably, expression domains scale perfectly in bovine limb buds, which are ~1.8-fold larger than mouse limb buds.

Molecular anterior–posterior limb-bud asymmetry loss

The first molecular differences become apparent as the posterior *Grem1* expression domain expands anteriorly in the mouse autopod (embryonic day (E) ~10.75). At equivalent bovine stages (D32), the shape of the *Grem1* domain appears symmetrical and distalized in bovine forelimb

[1]Developmental Genetics, Department Biomedicine, University of Basel, CH-4058 Basel, Switzerland. [2]Institut National de la Recherche Agronomique, Génétique Animale et Biologie Intégrative, F-78350 Jouy-en-Josas, France. [3]School of Life Sciences, Federal Institute of Technology Lausanne, CH-1015 Lausanne, Switzerland. [4]Department of Stem Cell Biology and Regenerative Medicine, Eli and Edythe Broad Center for Regenerative Medicine and Stem Cell Research, Keck School of Medicine, University of Southern California, Los Angeles, California 90089, USA. [5]Department for Biosystems Science and Engineering, Federal Institute of Technology Zurich and Swiss Institute of Bioinformatics, CH-4058 Basel, Switzerland. [6]Institut National de la Recherche Agronomique, Domaine Expérimental du Pin au Haras, F-61310 Exmes, France. [7]Institute of Anatomy, Department Biomedicine, University of Basel, CH-4056 Basel, Switzerland. [8]Institute for Molecular Bioscience, The University of Queensland, St Lucia, Queensland 4072, Australia. [9]Institut National de la Recherche Agronomique, Biométrie et Intelligence Artificielle, F-31326 Castanet-Tolosan, France. [10]Swiss Institute of Bioinformatics, CH-4058 Basel, Switzerland. [11]Institut Pasteur, Génétique Moléculaire de la Morphogenèse and Centre National de la Recherche Scientifique URA-2578, F-75015 Paris, France. [12]Department of Genetics and Evolution, University of Geneva, CH-1211 Geneva, Switzerland. †Present address: Institut National de la Recherche Agronomique, Laboratoire d'Ingénierie des Systèmes Biologiques et des Procédés, F-31077 Toulouse, France.

*These authors contributed equally to this work.

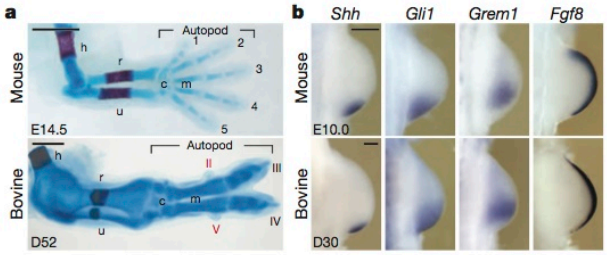

Figure 1 | Comparative analysis of mouse and bovine forelimb bud development. **a**, Forelimb skeletons at equivalent developmental stages in mouse (E14.5) and bovine (D52) embryos. 1–5 (mouse) and II–V (bovine), digits; c, carpus; h, humerus; m, metacarpus; r, radius; u, ulna. Vestigial digits II and V in bovine limbs are indicated in red. Scale bars, 1 mm. **b**, Comparative RNA *in situ* hybridization analysis during the onset of bovine and mouse forelimb bud development. Per gene and species, the transcript distribution was reproduced in at least $n = 3$ independent limb bud samples in independent experiments. In all figures, the images were scaled (scale bars, 0.25 mm) to enable direct comparison of both species and limb buds are always oriented with anterior to the top and posterior to the bottom.

buds, as illustrated by the reduction of the gap separating the dorsal and ventral *Grem1* domains (Fig. 2a). This distalization and loss of asymmetry is corroborated by *Hoxd13* expression in bovine forelimb buds (Fig. 2b and Extended Data Fig. 3a, b). These alterations are functionally relevant as the 5′ *Hoxd* transcription factors, and in particular *Hoxd13*, regulate digit number and identity[18]. Concurrently, *Fgf8* expression in the AER is displaced distally and becomes symmetrical during bovine handplate development (Fig. 2c, d). AER FGFs regulate both limb-bud outgrowth and digit length during chondrogenesis[19–21]. Therefore, the vestigial nature of digits II and V and loss of digit I in bovine can be explained by their territories getting precociously out of the AER FGF signalling range (Fig. 2d). All alterations in gene expression are limb-bud specific (Figs 2 and 3), as no differences were detected in other bovine tissues (Extended Data Fig. 3c).

Shh is essential for formation of digits 2–5 in the mouse and its expression in limb buds is controlled by a limb-specific *cis*-regulatory region[16,22,23]. Genetic inactivation or evolutionary loss of this enhancer correlates with loss of limbs in different species[24,25]. In lizards, the precocious down-regulation of *Shh* has been associated with digit loss[26]. Therefore, we analysed the kinetics of *Shh* expression, but no marked differences between bovine and mouse were observed (Fig. 3a; see also Fig. 1b). As SHH acts in a graded manner to pattern the progenitors that give rise to the digits[27], we also assessed the SHH protein distribution (Fig. 3b). In mouse limb

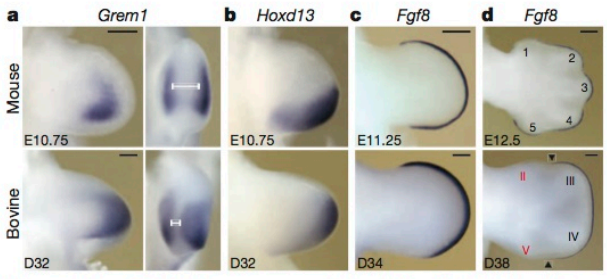

Figure 2 | Loss of molecular asymmetry in bovine forelimb buds. **a**, In contrast to the mouse, *Grem1* expression becomes more symmetrical (left, dorsal view) and distalized (right, apical view) in bovine forelimb buds by D32. The white line indicates the gap between the dorsal and ventral *Grem1* domains. **b**, Distal shift of *Hoxd13* expression in bovine forelimb buds. **c**, **d**, Analysis of *Fgf8* reveals the progressive distal shift of the AER in bovine limb buds, which becomes symmetrical at late stages (black arrowheads). Per gene and species, the transcript distribution was determined in at least $n = 3$ independent limb bud samples in independent experiments. Scale bars, 0.25 mm.

buds, the SHH protein is abundant in the posterior mesenchyme, whereas much lower levels are detected in the subapical mesenchyme (Fig. 3b, upper panels)[28]. In contrast, SHH proteins extend beyond the apex in bovine limb buds (Fig. 3b, lower panels). Not only SHH protein levels but also SHH signalling were extended in bovine limb buds, as revealed by the anteriorly expanded expression of the direct transcriptional target *Gli1* (Fig. 3c).

Ptch1 alteration in the bovine limb bud

Interaction of SHH with its receptors PTCH1 and PTCH2 enables signal transduction, whereas unbound PTCH receptors inhibit the pathway. *Ptch* genes are direct targets of SHH and their transcriptional upregulation is highest close to the SHH source. This regulatory feedback enhances PTCH-mediated sequestering of ligands and effectively restricts the range of SHH diffusion[29–31]. Therefore, the anterior expansion of the SHH protein and *Gli1* transcript domains could be a direct consequence of altered *Ptch* expression in bovine limb buds. In mouse limb buds, *Ptch1* is upregulated in the posterior mesenchyme and ectoderm[32], whereas in bovine limb buds *Ptch1* is only upregulated in the ectoderm (Fig. 3d, e). The initially low mesenchymal *Ptch1* expression (Extended Data Fig. 4a) becomes undetectable during bovine autopod development (Fig. 3e). As *Ptch1* expression is very similar in all other bovine and mouse embryonic tissues (see for example Extended Data Fig. 3c), the alterations in upregulating *Ptch1* expression seem to be restricted to the bovine limb-bud mesenchyme. This mesenchymal *Ptch1* deficiency cannot be compensated by *Ptch2*, as its expression remains largely restricted to the ectoderm (Extended Data Fig. 4b). However, bovine limb-bud mesenchymal cells are able to respond to SHH as the expression of targets such as *Grem1*, *Hoxd13* and in particular *Gli1* (ref. 17) is upregulated (Figs 2a, b and 3c). To gain an insight into this regulatory conundrum, we derived a minimal network of experimentally verified interactions for mathematical simulations (Extended Data Fig. 5 and Supplementary Note). Removing the GLI-dependent *cis*-regulatory inputs on *Ptch1* expression from the simulations and fixing the rate of *Ptch1* production at low levels is sufficient to reproduce the anterior expansion of *Gli1* that is observed in bovine limb buds (Extended Data Fig. 5a–c, compare to Fig. 3c). Alterations of other parameters such as increasing SHH diffusion did not reproduce the opposing changes in *Gli1* and *Ptch1* expression (Extended Data Fig. 5d, compare to Fig. 3c, d).

A *Ptch1* limb bud *cis*-regulatory module

Molecular analysis and mathematical simulations indicated that alterations in the *Ptch1 cis*-regulatory landscape could account for the failure to upregulate its mesenchymal expression in bovine limb buds. Previous analysis had pinpointed several *cis*-regulatory modules (CRMs) containing GLI binding sites around the transcriptional start site of the *Ptch1* locus[17,33]. These CRMs overlap with regions of active chromatin as revealed by DNase I hypersensitivity and histone H3K27 acetylation (H3K27ac)[34] marks (Fig. 4a). Lentivector constructs[35] encoding the mouse or bovine *Ptch1* 5′ proximal enhancer (PPE) direct expression of a *lacZ* reporter (with a β-globin minimal promoter; *βlacZ*) in a pattern similar to the endogenous gene with exception of limb buds (Fig. 4b)[33,36]. Both PPE-*βlacZ* transgenes are expressed in the posterior AER (white arrowheads in Fig. 4b) but not in the mesenchyme, which is reminiscent of *Ptch1* expression in bovine limb buds (Fig. 3e). As the other mouse 5′ CRMs identified by GLI1 chromatin immunoprecipitation (ChIP)[33] are not active in limb buds (K. A. Peterson and A. P. McMahon, unpublished), this indicated the possible existence of a mouse limb-bud mesenchymal CRM. Therefore, we used chromosome conformation capture in combination with deep sequencing (4C)[37,38] to identify genomic regions that loop to the *Ptch1* proximal promoter in mouse limb buds (Fig. 4c). The 4C contact map reveals the preferential interaction of the *Ptch1* proximal promoter (used as bait) with a region located ~37 kilobases (kb) downstream. As this interaction was most prominent in posterior limb buds, we named this candidate region limb *cis*-regulatory module (LRM, Fig. 4c).

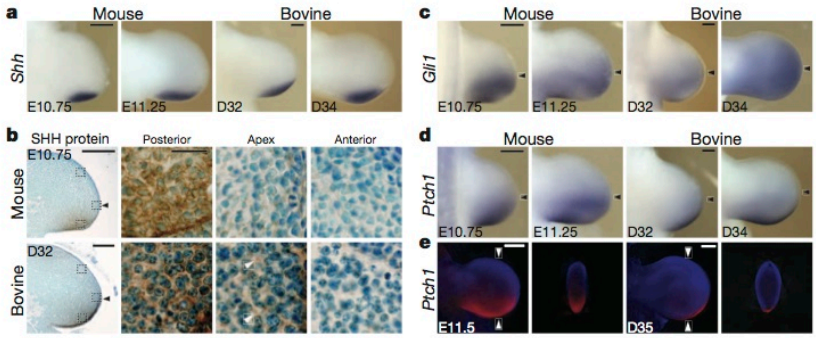

Figure 3 | Specific failure to upregulate mesenchymal *Ptch1* expression in bovine forelimb buds. **a**, *Shh* transcript distribution in mouse and bovine forelimb buds. **b**, SHH protein distribution (brown staining) on histological sections of forelimb buds. Nuclei are counterstained in blue. High-magnification insets are shown to the right (scale bar, 25 μm). White arrowheads point to extracellular SHH immunocomplexes. **c**, *Gli1* transcription senses the range of SHH signalling. **d**, **e**, Analysis of *Ptch1* expression by conventional (**d**) and optical projection tomography imaging (OPT, panel **e**). White arrowheads indicate the planes of OPT cross-sections shown to the right. Black arrowheads in **b**–**d** indicate the limb bud apex. Per gene and species, the transcript distribution was reproduced in at least $n = 3$ independent limb bud samples in independent experiments. Scale bars, 0.25 mm.

Inactivation of the bovine *Ptch1* LRM

The LRM is located in a genomic region between *Ptch1* coding exons 15–19 and includes several blocks of evolutionarily conserved intronic sequences that carry marks of active chromatin in mouse limb buds (Fig. 5a). As GLI proteins upregulate *Ptch1* expression in response to SHH signalling[33], their potential interactions with the LRM were studied by ChIP-seq analysis using a mouse strain with a 3×Flag epitope tag in the endogenous GLI3 protein. In mouse limb buds, GLI3 preferentially interacts with three of the evolutionarily conserved regions (Fig. 5a), and similar interactions were also detected for GLI2 and GLI1 proteins (data not shown). Together, these results indicated that at least two *cis*-regulatory regions could be present in the ~9-kb mouse LRM region (Fig. 5a). Comparison of LRM sequences from different mammalian species revealed two artiodactyl-specific insertions in these regions (red triangles, Fig. 5a). One of these is a microsatellite expansion, which varies considerably among different artiodactyls and is not present in non-artiodactyl mammals (Extended Data Fig. 6a). Therefore, the two conserved regions of the mouse and bovine LRM (regions A and B, Fig. 5a) were cloned in tandem and assayed for enhancer activity in transgenic mouse embryos. The analysis of several independent founders showed that both *ßlacZ* transgenes are only expressed in the limb-bud core mesenchyme; that is, do not reproduce *Ptch1* expression (Extended Data Fig. 6b–d). This indicated that the non-conserved regions might be required for full LRM activity. Indeed, a conventional transgene encompassing the entire mouse LRM results in robust *lacZ* expression in the posterior limb bud and autopod mesenchyme, markedly similar to *lacZ* driven by the *Ptch1* genomic landscape (Fig. 5b, c and Extended Data Fig. 7a). In particular, the mouse LRM is activated by ~E10.75 (Extended Data Fig. 7b); that is, around the developmental period when asymmetry is lost in bovine limb buds (Figs 2 and 3). Therefore, we assessed the transcriptional activity of the orthologous bovine LRM region. In contrast to the mouse, the bovine LRM-*ßlacZ* transgene remains restricted to the core mesenchyme (Fig. 5d and Extended Data Fig. 7c). As SHH signal transduction is intact in transgenic mouse limb buds, the bovine

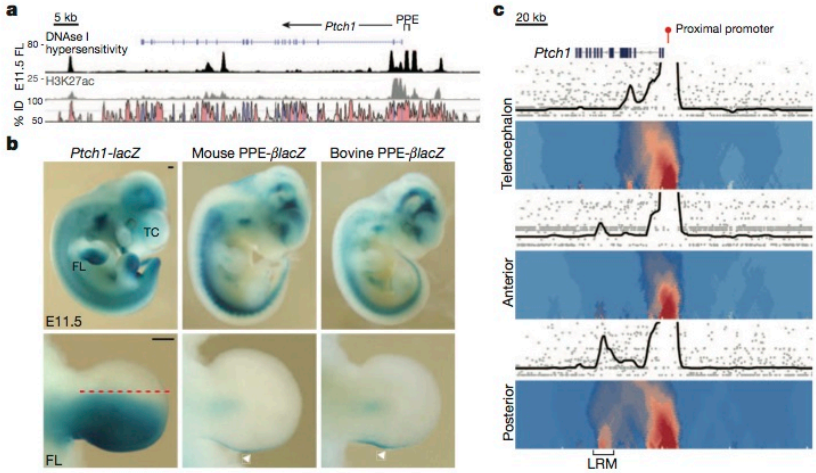

Figure 4 | Identification of a *Ptch1* limb *cis*-regulatory module (LRM). **a**, Scheme of the *Ptch1* locus with the profiles of DNase I hypersensitivity and H3K27ac marks[34] in mouse forelimb buds at E11.5. VISTA conservation plot comparison of the mouse and bovine *Ptch1* loci (mm9: chr13 63,592,959–63,682,958; see http://genome.ucsc.edu). **b**, Expression of a *lacZ* reporter inserted into the *Ptch1* locus compared with expression driven by the mouse and bovine 5′ proximal enhancer (PPE, mouse: $n = 19$ of 32; bovine: $n = 24$ of 46 embryos). White arrowheads point to AER expression. FL, forelimb bud. Scale bars, 0.25 mm. Broken red line in panel **b** indicates the dissection of limb buds into anterior and posterior halves as used for 4C analysis. **c**, 4C contact analysis (mm9: chr13 63,575,000–63,760,000) using the proximal promoter as viewpoint, which reveals its interaction with an intragenic region in posterior limb buds. This interaction was not detected in the telencephalon (TC), which served as a control for the 4C analysis.

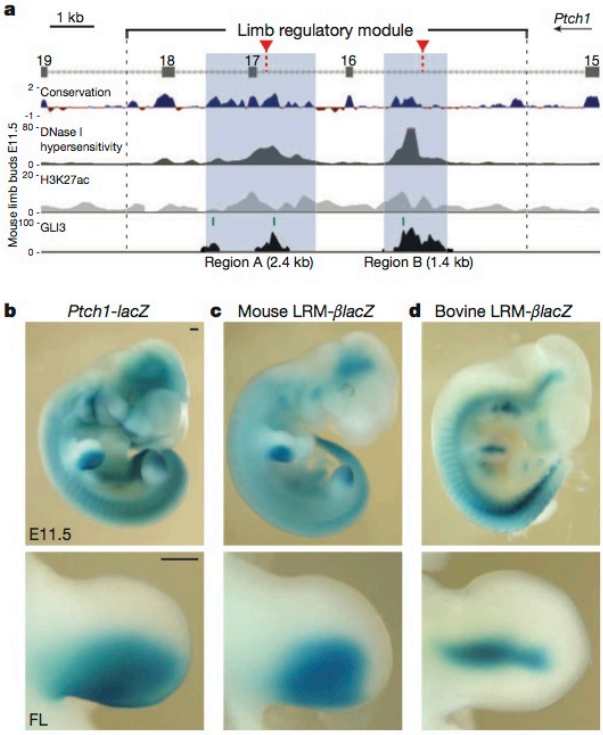

Figure 5 | Functional analysis of the mouse and bovine LRM in transgenic mouse embryos. **a**, Scheme depicting the mouse LRM in the *Ptch1* locus (mm9: chr13 63,621,577–63,634,154) with the placental mammal conservation plot (PhyloP; conserved regions in blue; fast-evolving regions in red), the distributions of DNase I hypersensitivity and H3K27ac marks, and the regions interacting with GLI3 proteins. Red triangles, artiodactyl-specific insertions. Green lines, conserved GLI binding motifs. Blue shaded areas indicate the conserved core regions A and B. **b**–**d**, Expression of a reporter *lacZ* transgene under control of the endogenous *Ptch1* locus (**b**), the mouse LRM (**c**) and the bovine LRM (**d**) in transgenic mouse embryos (mouse: $n = 4$ of 4; bovine: $n = 7$ of 12 embryos, others show no expression). FL, forelimb. Scale bars, 0.25 mm.

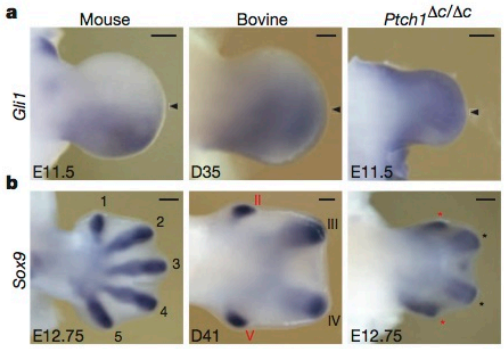

Figure 6 | Similarity of gene expression in bovine and mouse *Ptch1*$^{\Delta c/\Delta c}$ forelimb buds. **a**, **b**, *Gli1* and *Sox9* expression in forelimb buds of mouse, bovine and *Ptch1*$^{\Delta c/\Delta c}$ embryos. Vestigial digits are indicated in red. Asterisks indicate digits with uncertain identities. Arrowheads indicate limb bud apex. Per gene, species and mouse genotype, the transcript distribution was reproduced in at least $n = 3$ independent limb bud samples in independent experiments. Scale bars, 0.25 mm.

LRM is apparently unable to respond to graded SHH signalling (Fig. 5d, compare to Fig. 5b, c). Our transgenic analysis shows that (1) conserved and non-conserved regions are required for full activity of the mouse LRM, and (2) loss of its activity underlies the failure to upregulate *Ptch1* during bovine autopod development.

Prx1-Cre-mediated inactivation of *Ptch1* in the mouse limb-bud mesenchyme (*Ptch1*$^{\Delta c/\Delta c}$) causes loss of anterior–posterior asymmetry and predominant oligodactyly in forelimb buds[39], which resembles the alterations observed in bovine autopods. In *Ptch1*$^{\Delta c/\Delta c}$ autopod primordia, *Gli1* expression expands even farther anterior than in bovine limb buds (Fig. 6a), whereas *Hoxd13* expression is distalized to a similar extent (Extended Data Fig. 8a). Most strikingly, the *Sox9* transcript distribution reveals the similarities in the pattern of digit condensations in bovine and mouse *Ptch1*$^{\Delta c/\Delta c}$ autopods (Fig. 6b and Extended Data Fig. 8b; $n = 7$ of 18, others have only 3 condensations). In bovine and mouse *Ptch1*$^{\Delta c/\Delta c}$ forelimb buds, the two lateral condensations are much reduced, whereas the primordia of the two central digits appear symmetrical and of equal length. This shows that loss of *Ptch1* is sufficient to phenocopy molecular and morphological hallmarks of the bovine autopod.

Discussion

Our study reveals the molecular changes underlying the loss of anterior–posterior asymmetry in bovine limb autopods. The symmetrical *Hoxd13* expression in the mesenchyme and more restricted *Fgf8* expression in the AER underlie the preferential and isomorphic elongation of the middle digits in bovine limbs[18–20]. The distal restriction of AER *Fgf8* expression in bovine limb buds could be a consequence of differences in *Grem1* expression[9] and/or increased SHH signalling to the AER[32]. The loss of autopod asymmetry is a likely consequence of the loss of activity of the LRM enhancer that normally upregulates *Ptch1* expression in the limb-bud mesenchyme in response to SHH signalling. During evolution, such a tissue-specific *cis*-regulatory rather than a pleiotropic alteration was probably favoured[12], as *Ptch1* inactivation causes embryonic lethality[36]. Tissue-specific modifications in gene expression have previously been linked to the regulatory alterations underlying evolutionary diversification of embryonic structures[24,40–43]. All these studies epitomize the potential for rewiring robust developmental pathways during morphological evolution[44,45].

Analysis of the mouse LRM indicates that this *cis*-regulatory module senses graded SHH signalling in the limb-bud mesenchyme and that both conserved and non-conserved regions are required for its full functionality. In agreement, active chromatin marks cover the entire mouse LRM and sequence analysis predicts additional species-specific GLI binding sites scattered throughout the non-conserved regions. Rather than being completely inactivated or deleted[24,40], the bovine LRM could have been altered in a way similar to the evolutionary diversification of the *ovo*/*shavenbaby* (*svb*) locus that controls formation of dorsal cuticular hairs in *Drosophila*[42,46]. Alteration or loss of these structures in different *Drosophila* species requires multiple changes in the redundant and non-conserved *cis*-regulatory elements that control *svb* expression[46]. These and other studies[41] show how molecular alterations in several *cis*-regulatory elements with individually small phenotypic effects are able to change a robust trait and/or promote morphological convergence through parallel genetic changes under evolutionary constraints[47].

A similar mechanism might underlie the evolutionary diversification of artiodactyl autopods. The fossil records show that primitive artiodactyls were pentadactylous and reveal the progressive loss of anterior–posterior polarity in metacarpals and middle digits[2]. This shift towards an unguligrade posture is paralleled by digit reductions and/or loss that occurred independently in different artiodactyl lineages[48]. These findings support a progressive, and in part convergent, adaptation of the limb skeleton during artiodactyl evolution. Molecular analysis (this study and ref. 7) reveals the variability in limb bud development among different artiodactyl families, which is in agreement with progressive evolutionary adaptation. Similar to bovine, *Ptch1* expression is not upregulated in the mesenchyme of pig limb buds[7]. As Ruminantia (encompassing Bovidae) and Suina (encompassing Suidae) diverged early during artiodactyl

evolution[2,3], the mechanism that normally upregulates *Ptch1* in the autopod mesenchyme should have been disrupted by a common initiating alteration. However, *Ptch1* expression is upregulated in the limb-bud mesenchyme of camel embryos, which also diverged early during artiodactyl evolution. Another major difference is the elimination of lateral digit primordia by apoptosis in camel, but not bovine and pig limb buds (this study and refs 7,8). Our analysis provides evidence that the reduction and loss of digits in bovine limbs is secondary to the loss of autopod asymmetry caused by inactivation of the *Ptch1* LRM. One possible explanation for the differences in *Ptch1* expression[7] could be that the alterations in the LRM that preceded divergence were compensated by genetic robustness involving other elements in certain artiodactyls such as camelids. Alternatively, the initiating events only weakened the inherent robustness of the *Ptch1* LRM in basal artiodactyls and subsequent inactivating alterations only occurred in some but not all lineages, which would explain why *Ptch1* upregulation is not disrupted in limb buds of all clades. Together with adaptive changes in other genes/pathways, these alterations would have caused the gradual loss of digit asymmetry and facilitated the adoption of unguligrade postures as evidenced by morphological analysis of extinct and modern artiodactyls.

METHODS SUMMARY

All experimental procedures involving bovine and mouse embryos were conducted in accordance with national laws, taking into account the 3R and the Basel Declaration principles.

Online Content Any additional Methods, Extended Data display items and Source Data are available in the online version of the paper; references unique to these sections appear only in the online paper.

Received 16 December 2013; accepted 27 March 2014.
Published online 18 June 2014.

1. Polly, P. D. Limbs in mammalian evolution. In *Fins into Limbs* (Hall, B. K. ed.) 245–268 (Univ. Chicago Press, 2007).
2. Prothero, D. R. & Foss, S. E. (eds) *The Evolution of Artiodactyls* (Johns Hopkins Univ. Press, 2007).
3. Spaulding, M., O'Leary, M. A. & Gatesy, J. Relationships of Cetacea (Artiodactyla) among mammals: increased taxon sampling alters interpretations of key fossils and character evolution. *PLoS ONE* **4,** e7062 (2009).
4. Zeder, M. A. Domestication and early agriculture in the Mediterranean Basin: Origins, diffusion, and impact. *Proc. Natl Acad. Sci. USA* **105,** 11597–11604 (2008).
5. Budras, K. D. & Habel, R. E. (eds) *Bovine Anatomy* (Schlütersche, 2011).
6. de Bakker, M. A. *et al.* Digit loss in archosaur evolution and the interplay between selection and constraints. *Nature* **500,** 445–448 (2013).
7. Cooper, K. L. *et al.* Patterning and post-patterning modes of evolutionary digit loss in mammals. *Nature* (in the press).
8. Sears, K. E. *et al.* Developmental basis of mammalian digit reduction: a case study in pigs. *Evol. Dev.* **13,** 533–541 (2011).
9. Benazet, J. D. *et al.* A self-regulatory system of interlinked signaling feedback loops controls mouse limb patterning. *Science* **323,** 1050–1053 (2009).
10. Lopez-Rios, J. *et al.* GLI3 constrains digit number by controlling both progenitor proliferation and BMP-dependent exit to chondrogenesis. *Dev. Cell* **22,** 837–848 (2012).
11. Zeller, R., Lopez-Rios, J. & Zuniga, A. Vertebrate limb bud development: moving towards integrative analysis of organogenesis. *Nature Rev. Genet.* **10,** 845–858 (2009).
12. Carroll, S. B. Evo-devo and an expanding evolutionary synthesis: a genetic theory of morphological evolution. *Cell* **134,** 25–36 (2008).
13. Galli, A. *et al.* Distinct roles of Hand2 in initiating polarity and posterior Shh expression during the onset of mouse limb bud development. *PLoS Genet.* **6,** e1000901 (2010).
14. te Welscher, P., Fernandez-Teran, M., Ros, M. A. & Zeller, R. Mutual genetic antagonism involving GLI3 and dHAND prepatterns the vertebrate limb bud mesenchyme prior to SHH signaling. *Genes Dev.* **16,** 421–426 (2002).
15. Marigo, V., Johnson, R. L., Vortkamp, A. & Tabin, C. J. Sonic hedgehog differentially regulates expression of *GLI* and *GLI3* during limb development. *Dev. Biol.* **180,** 273–283 (1996).
16. Zhu, J. *et al.* Uncoupling Sonic hedgehog control of pattern and expansion of the developing limb bud. *Dev. Cell* **14,** 624–632 (2008).
17. Vokes, S. A., Ji, H., Wong, W. H. & McMahon, A. P. A genome-scale analysis of the cis-regulatory circuitry underlying sonic hedgehog-mediated patterning of the mammalian limb. *Genes Dev.* **22,** 2651–2663 (2008).
18. Woltering, J. M. & Duboule, D. The origin of digits: expression patterns versus regulatory mechanisms. *Dev. Cell* **18,** 526–532 (2010).
19. Lewandoski, M., Sun, X. & Martin, G. R. Fgf8 signalling from the AER is essential for normal limb development. *Nature Genet.* **26,** 460–463 (2000).
20. Mariani, F. V., Ahn, C. P. & Martin, G. R. Genetic evidence that FGFs have an instructive role in limb proximal-distal patterning. *Nature* **453,** 401–405 (2008).
21. Sanz-Ezquerro, J. J. & Tickle, C. Fgf signaling controls the number of phalanges and tip formation in developing digits. *Curr. Biol.* **13,** 1830–1836 (2003).
22. Chiang, C. *et al.* Manifestation of the limb prepattern: limb development in the absence of Sonic Hedgehog Function. *Dev. Biol.* **236,** 421–435 (2001).
23. Lettice, L. A. *et al.* A long-range Shh enhancer regulates expression in the developing limb and fin and is associated with preaxial polydactyly. *Hum. Mol. Genet.* **12,** 1725–1735 (2003).
24. Sagai, T. *et al.* Phylogenetic conservation of a limb-specific, cis-acting regulator of Sonic hedgehog (Shh). *Mamm. Genome* **15,** 23–34 (2004).
25. Sagai, T., Hosoya, M., Mizushina, Y., Tamura, M. & Shiroishi, T. Elimination of a long-range cis-regulatory module causes complete loss of limb-specific Shh expression and truncation of the mouse limb. *Development* **132,** 797–803 (2005).
26. Shapiro, M. D., Hanken, J. & Rosenthal, N. Developmental basis of evolutionary digit loss in the Australian lizard Hemiergis. *J. Exp. Zool. B* **297,** 48–56 (2003).
27. Harfe, B. D. *et al.* Evidence for an expansion-based temporal Shh gradient in specifying vertebrate digit identities. *Cell* **118,** 517–528 (2004).
28. Gritli-Linde, A., Lewis, P., McMahon, A. P. & Linde, A. The whereabouts of a morphogen: direct evidence for short- and graded long-range activity of hedgehog signaling peptides. *Dev. Biol.* **236,** 364–386 (2001).
29. Briscoe, J., Chen, Y., Jessell, T. M. & Struhl, G. A hedgehog-insensitive form of patched provides evidence for direct long-range morphogen activity of sonic hedgehog in the neural tube. *Mol. Cell* **7,** 1279–1291 (2001).
30. Chen, Y. & Struhl, G. Dual roles for patched in sequestering and transducing hedgehog. *Cell* **87,** 553–563 (1996).
31. Marigo, V., Davey, R. A., Zuo, Y., Cunningham, J. M. & Tabin, C. J. Biochemical evidence that patched is the Hedgehog receptor. *Nature* **384,** 176–179 (1996).
32. Bouldin, C. M., Gritli-Linde, A., Ahn, S. & Harfe, B. D. Shh pathway activation is present and required within the vertebrate limb bud apical ectodermal ridge for normal autopod patterning. *Proc. Natl Acad. Sci. USA* **107,** 5489–5494 (2010).
33. Vokes, S. A. *et al.* Genomic characterization of Gli-activator targets in sonic hedgehog-mediated neural patterning. *Development* **134,** 1977–1989 (2007).
34. Cotney, J. *et al.* Chromatin state signatures associated with tissue-specific gene expression and enhancer activity in the embryonic limb. *Genome Res.* **22,** 1069–1080 (2012).
35. Friedli, M. *et al.* A systematic enhancer screen using lentivector transgenesis identifies conserved and non-conserved functional elements at the Olig1 and Olig2 locus. *PLoS ONE* **5,** e15741 (2010).
36. Goodrich, L. V., Milenkovic, L., Higgins, K. M. & Scott, M. P. Altered neural cell fates and medulloblastoma in mouse patched mutants. *Science* **277,** 1109–1113 (1997).
37. van de Werken, H. J. *et al.* 4C Technology: Protocols and Data Analysis. *Methods Enzymol.* **513,** 89–112 (2012).
38. van de Werken, H. J. *et al.* Robust 4C-seq data analysis to screen for regulatory DNA interactions. *Nature Methods* **9,** 969–972 (2012).
39. Butterfield, N. C. *et al.* Patched 1 is a crucial determinant of asymmetry and digit number in the vertebrate limb. *Development* **136,** 3515–3524 (2009).
40. Chan, Y. F. *et al.* Adaptive evolution of pelvic reduction in sticklebacks by recurrent deletion of a Pitx1 enhancer. *Science* **327,** 302–305 (2010).
41. Gompel, N., Prud'homme, B., Wittkopp, P. J., Kassner, V. A. & Carroll, S. B. Chance caught on the wing: cis-regulatory evolution and the origin of pigment patterns in *Drosophila*. *Nature* **433,** 481–487 (2005).
42. McGregor, A. P. *et al.* Morphological evolution through multiple cis-regulatory mutations at a single gene. *Nature* **448,** 587–590 (2007).
43. Cretekos, C. J. *et al.* Regulatory divergence modifies limb length between mammals. *Genes Dev.* **22,** 141–151 (2008).
44. Davidson, E. H. & Erwin, D. H. Gene regulatory networks and the evolution of animal body plans. *Science* **311,** 796–800 (2006).
45. Peter, I. S. & Davidson, E. H. Evolution of gene regulatory networks controlling body plan development. *Cell* **144,** 970–985 (2011).
46. Stern, D. L. & Frankel, N. The structure and evolution of cis-regulatory regions: the shavenbaby story. *Phil. Trans. R. Soc. B* **368,** 1632 (2013).
47. Stern, D. L. The genetic causes of convergent evolution. *Nature Rev. Genet.* **14,** 751–764 (2013).
48. Clifford, A. B. The evolution of the unguligrade manus in artiodactyls. *J. Vertebr. Paleontol.* **30,** 1827–1839 (2010).

Supplementary Information is available in the online version of the paper.

Acknowledgements We thank K. Cooper and C. Tabin for sharing their results before publication and providing camel genomic DNA. Dolphin samples were received from C. Frere and D. Duffield. Pigmy hippopotamus mouth swabs for DNA extraction were provided by S. Furrer and B. Zimmerman from the Zoo of Zurich, whereas all other artiodactyl blood samples were donated from available frozen stocks by S. and M. Hoby from the Zoo of Basel. B. Wainwright provided the *Ptch1* conditional mouse line. We are grateful to E. Terszowska and A. Offinger for mouse care; V. Metis and M. Rondon for assistance in colony maintenance and collection of *Prx1*-Cre *Ptch1*$^{\Delta c/\Delta c}$ mouse embryos; and N. Dumesnil for assistance in collecting bovine embryos. All lentivector-mediated transgenic mouse embryos were produced by the EPFL transgenic platform, whereas conventional mouse transgenic embryos were produced commercially by Cyagen Biosciences Inc. We thank S. Beck-Cormier, A. Gritli-Linde, D. Haag-Wackernagel, Y. Lallemand, P. Zimmermann, G. Nusspaumer and A. Zuniga for technical advice and input and M. Bertaud, I. Ginez, D. Jardet and M. Moroldo for technical assistance. We are grateful to V. Taylor and members of our research groups for critical discussions and input on the manuscript. This research was supported by SNF grants 31003A_130803/146248 and the University of Basel (to R.Z.), EU

reintegration grant PERG-GA-2009-246576 (to J.L.-R.), SystemsX.ch iPhD Grant 20101078 (to D.I. and R.Z.), INRA (to A.D.), ANR grant No. 06-MRAR-027-01 (to B.R.), the EPFL and ERC grant Systems*Hox*.ch (to D.D.), NIH grant no. NS 033642 (to A.P.M.) and Australian National Health and Medical Research Council grant no. 569713 (to C.W.).

Author Contributions J.L.-R., A.D. and R.Z. conceived the project and wrote the manuscript; J.L.-R. and A.D. performed most of the mouse and bovine experimental studies. D.S. and E.U. performed mouse and bovine experiments under supervision of J.L.-R. and R.Z.; J.L-.R. and D.S. isolated, sequenced and analysed the ~9-kb LRM from different species. G.A. performed the lentivector studies under supervision of D.D. J.L. generated the *Gli3*$^{3Xt^{J}lag}$ mouse strain and K.A.P. performed the GLI3 ChIP-seq analysis under supervision of A.P.M. P.G. performed the *in silico* simulations under supervision of D.I. S.F. participated in the design of bovine ISH probes and together with A.D., S.B. and Y.G. produced and collected the bovine embryos for the study. M.M.-G. did the skeletal analysis of bovine foetuses using CT scanning. A.D.C. and C.W. provided all mouse embryos lacking *Ptch1* in the limb bud mesenchyme. C.B. performed all deep sequencing of the *Ptch1* loci from different species and as part of the 4C analysis. R.I. assisted in high-throughput data analysis. C.K. and S.R. participated in *in silico* assembly and analysis of the *Ptch1* loci from different species. B.R. was key to conceiving and initiating this project.

Author Information All 4C-seq data sets are deposited in the Gene Expression Omnibus repository under accession number GSE52988. The GLI3 ChIP-seq data relevant to this study are deposited in the Gene Expression Omnibus repository under accession number GSE52939. All the raw data for sequencing of the *Ptch1* locus are deposited in the European Nucleotide Archive (study accession number PRJEB5056). Reprints and permissions information is available at www.nature.com/reprints. The authors declare no competing financial interests. Readers are welcome to comment on the online version of the paper. Correspondence and requests for materials should be addressed to R.Z. (rolf.zeller@unibas.ch) or A.D. (amandine.duchesne@jouy.inra.fr, for bovine embryos and materials).

METHODS

Bovine embryos. All procedures to produce and harvest bovine embryos and fetuses were conducted in strict accordance with French laws and taking into account the 3R principles. All protocols were approved by the Ethics Committee C2EA-07 on Animal Experimentation in Rennes. Embryos were produced using cattle (*Bos taurus*) from the experimental dairy herd of INRA at Domaine du Pin that were destined to be killed for meat production (mostly crosses between Holstein and Normande breeds). Dams were hormonally synchronized and artificially inseminated or used for transfer of *in vitro* fertilized embryos (detailed protocols are available on request). Overall, 32% of all inseminations and transfers resulted in pregnancies (monitored by ultrasound) that yielded one embryo per dam. Pregnant cows were killed at defined gestational days and embryos isolated. After removing the chorionic membranes, embryos were rinsed in PBS and fixed overnight in 4% PFA/PBS (for RNA *in situ* hybridization) or in 95% ethanol/1% acetic acid (Sainte-Marie solution for detection of SHH proteins)[28] as required. For this study, a total of 60 bovine embryos were produced over 4 years and staged using both gestational days (day of fertilization is D0) and gross-morphological and molecular criteria (size, external morphological features of entire embryo and limb buds and gene expression) to account for variations in developmental timing. The approximately equivalent mouse and bovine limb-bud stages were refined during the study considering actual limb-bud shapes and the activation and temporal progression of gene expression to arrive at the comparative table included in Extended Data Fig. 1a (ref. 49). Mostly forelimb buds, but also some hindlimb buds, were used for analysis as the generation of bovine embryos is quite laborious and the distal fore- and hindlimb skeletons are identical (Extended Data Fig. 1b)[5]. In all cases, bovine fore- and hindlimb buds of equivalent developmental stages yielded identical results. For the RNA *in situ* hybridization and immunohistochemical analyses described in this study, the same result was obtained by analysing three or more independent bovine limb buds at developmentally equivalent or close stages and representative forelimb buds are shown in all figures.

Mouse embryos. All mouse studies were carried out in accordance with the national laws and regulations governing animal experimentation in Switzerland, Australia and the USA and approved by the responsible Ethics and Regulatory Boards. Wild-type NMRI or C57BL/6J mouse embryos were used for RNA *in situ* hybridization and immunohistochemistry. Age-matched (±1 somite) *Prx1*-Cre *Ptch1*$^{\Delta c/\Delta c}$ and wild-type control embryos were produced as previously described[50] in a mixed 129Sv]xC57BL/6J background, while the *Ptch1*^{LacZ} null allele[36] was maintained in a C57BL/6J background. In all *Prx1*-Cre *Ptch1*$^{\Delta c/\Delta c}$ embryos, the anterior–posterior forelimb bud asymmetry is lost ($n = 3$ per probe analysed), whereas the oligodactylous forelimb bud phenotype is variable ($n = 7$ of 18: four digit primordia; $n = 11$ of 18: three primordia with vestigial lateral digits).

Generation and analysis of transgenic mouse embryos. Lentivector-mediated transgenic founder embryos were generated as previously described[35]. Putative CRMs were amplified by PCR from mouse and bovine BAC DNA, cloned into the pRRL-LacZ vector upstream of the β-globin minimal promoter (*βlacZ*) and validated by sequencing. Vector particles were produced by co-transfecting HEK293T cells with PMD2G, R8.74 plasmids and the pRRL transfer vector (http://tronolab.epfl.ch/lentivectors). Lentivector particles secreted into the medium were concentrated by ultracentrifugation. Vector preparations with sufficient titre ($>5 \times 10^8$ infectious particles per ml) were injected in the perivitelline space of 1-cell mouse zygotes at the EPFL transgenic mouse core facility[51,52]. Between 50 and 150 injected zygotes were transferred into pseudo-pregnant foster mothers (16 eggs per foster). Pregnant mice were killed at E11.0–E11.5 to recover between 5 to 14 embryos per foster mother. Transgenic embryos were genotyped using a primer upstream of the β-globin minimal promoter (FW2: GTGAACGGATCTCGACGGTA) and a reverse primer specific for each region assayed. The sequences of the specific primers used for genotyping, genomic coordinates of the candidate CRMs assayed by lentivirus-mediated transgenesis and the fractions of *LacZ* expressing embryos are listed in Supplementary Table 1.

The LRM vectors for producing transgenic mouse embryos by pronuclear injection were constructed as follows: a fragment containing the mouse *Ptch1* LRM and flanking regions was excised as a 9,782-bp SfuI fragment from BAC RP23-477K20 (genomic coordinates mm9 chr13 63,623,323–63,633,104). The LRM region was defined according to the pattern of DNase I hypersensitivity and the conserved regions enriched in the GLI3 ChIP-seq limb data sets (Fig. 5a). The orthologous bovine genomic region was isolated as a 9,172-bp MfeI fragment from BAC CH240_37L23 (genomic coordinates bosTau7 chr8 86,642,592–86,651,763). Both fragments were cloned into the p1230 plasmid upstream of a β-globin minimal promoter/*lacZ* reporter cassette[23]. The linearized transgenic constructs were gel-purified, microinjected into the pronuclei of fertilized mouse eggs and transferred into pseudo-pregnant foster mothers by Cyagen Biosciences Inc. Transgenic embryos were collected between E10.0 and E11.5 and stained to detect *lacZ* expression. All embryos were genotyped using *lacZ*-specific oligonucleotides (Fw: TCGTTGCTGCATAAACCGACT; Rv: GACCATTTTCAATCCGCACCT). Transgene copy numbers were determined by qPCR using primers in the *lacZ* reporter (Fw: AACGATCGCCAGTTCTGTATG; Rv: ATTCGCTGGTCACTTCGATG) with iQ SYBR Green Supermix in a CFX96 Real-Time PCR System (Bio-Rad Laboratories). The oligonucleotides used for normalizing qPCR values detect the *Dbh* locus (Fw: AGGACATCAGCCACTCTG CT; Rv: AATTGTCTTGGTGGCCCTC). Normalized values were compared with those of genomic DNA of embryos with one or two copies of a *lacZ* reporter transgene inserted into an unrelated locus.

The expression of the *lacZ* reporter in transgenic embryos was detected according to standard procedures. For the mouse LRM construct, 6 of 7 transgenic embryos express the transgene in a similar pattern. All four transgenic embryos collected at E11.5 strongly express the *lacZ* reporter in the posterior limb-bud mesenchyme (Fig. 5c and Extended Data Fig. 7a, b). In contrast, only 7 of 12 embryos transgenic for bovine LRM construct express the *lacZ* reporter, weakly within the core limb-bud mesenchyme (Fig. 5d and Extended Data Fig. 7c). The copy numbers of integrated transgenes are similar for both constructs.

Skeletal preparations and computed tomography (CT) scans. Cartilage and bone of mouse and bovine embryos were detected by staining with Alcian blue and Alizarin red. The CT data set of a 5-month-old calf fetus was generated using a conventional CT scanner (SOMATOM 16, Siemens, 120 kV, 180 mAs, slice thickness 0.625 mm, axial slices) and processed using Slicer software (http://www.slicer.org). Images were edited by threshold selection and skeletal bones were false-coloured. Three-dimensional renderings of all structures were generated using surface rendering and the contour of the skin was made transparent using a transfer function.

Whole-mount RNA *in situ* hybridization. The transcript distributions in mouse embryos were analysed by whole-mount RNA *in situ* hybridization. A similar protocol with extended proteinase K treatment was used in bovine embryos to ensure complete probe penetration and hybridization within the tissue. The primers used to generate the riboprobe templates from limb bud cDNAs are listed in Supplementary Table 2. All fragments were cloned in pGEM-T vectors (Promega) and validated by sequencing. All bovine riboprobes were first tested on mouse embryos using low-stringency hybridization to establish that the overall pattern is identical to the orthologous mouse riboprobe. Two different riboprobes that detect *Ptch1* transcripts were used in both mouse and bovine embryos, and yielded identical results. This was important to confirm the limb-bud mesenchymal lack of *Ptch1* upregulation in bovine embryos. Mouse and bovine embryos were processed for OPT analysis as described[53]. All results shown are representative expression patterns obtained by analysing at least three independent bovine limb buds per probe.

Immunohistochemistry and detection of apoptotic cells by TUNEL. Immunodetection of SHH proteins in mouse and bovine limb buds ($n = 3$) was done using 6-μm-thick paraffin sections of samples fixed in Sainte-Marie solution using affinity-purified Ab80 antibodies (1:600)[28]. The Ab80 antibody was previously established to recognize SHH proteins in bovine tissues[54]. Simultaneous detection of SOX9 proteins (1:2000, Millipore; secondary antibody Alexa Fluor 594 goat anti-rabbit 1:500, Invitrogen) and apoptotic cells by TUNEL (*In situ* cell death detection kit, Roche) was done using 6-μm-thick paraffin sections of bovine embryonic limbs fixed in 4% PFA ($n = 3$). Nuclei were always counterstained with Hoechst-33258.

Microscopy. Bright-field images of tissue sections were acquired using a Zeiss Axioskop-2 microscope in combination with a Nikon DXM1200F camera. Fluorescent images were captured with a Leica TCS SP5 confocal laser-scanning microscope in combination with the LAS AF software. Raw data were imported sequentially into the Fiji[55] and Photoshop CS6 programs (Adobe). Photos of whole embryos and dissected limb buds after RNA *in situ* hybridization or *lacZ* detection were taken using a Leica MZ16 stereo-microscope equipped with a DFC300FX camera. Brightness and contrast were adjusted uniformly for all images of a particular set of experimental and control samples using the appropriate functions in Photoshop CS6.

Chromosome conformation capture in combination with deep sequencing (4C). Mouse forelimbs from 20 embryos at E11.5 (45–46 somites) were dissected into posterior (2/3) and anterior (1/3) parts (the approximate plane of dissection is indicated by the red dotted line in Fig. 4b). Dorsal telencephalic regions were used as a control tissue as they express only low levels of *Ptch1*. Tissue samples were pooled and processed for 4C analysis as described previously[37,38]. The first restriction digestion was done with NlaIII, whereas the second enzyme was DpnII (New England Biolabs). The selected viewpoint within the *Ptch1* proximal promoter corresponds to a 1,163-bp NlaIII fragment (mm9: chr13 63,667,995–63,669,157) located immediately upstream of the PPE used for lentivector-mediated transgenesis (Fig. 4a, b). A total of 1.6 μg of the 4C library from each sample was amplified using the following viewpoint-specific oligonucleotides that in addition encoded Illumina adapters for paired-end sequencing and indexing: *Ptch1_F1_TUA* (common oligo; TrueSeq Universal Adaptor) AATGATACGGCGACCACCGAGATCTAC ACTCTTTCCCTACACGACGCTCTTCCGATCTCTGGACCGAGAGGCCCAT;

Ptch1_R1b_AR4 (posterior limb 4C-seq library; Illumina index 4) CAAGCAGAAGACGGCATACGAGATTGGTCAGTGACTGGAGTTCAGACGTGTGCTCTTCCGATCTACAGGGTGTGTATCGAGCTTTATT; *Ptch1_R1b_AR5* (anterior limb 4C-seq library; Illumina index 5) CAAGCAGAAGACGGCATACGAGATCACTGTGTGACTGGAGTTCAGACGTGTGCTCTTCCGATCTACAGGGTGTGTATCGAGCTTTATT; *Ptch1_R1b_AR6* (telencephalon 4C-seq library; Illumina index 6) CAAGCAGAAGACGGCATACGAGATATTGGCGTGACTGGAGTTCAGACGTGTGCTCTTCCGATCTACAGGGTGTGTATCGAGCTTTATT.

Deep-sequencing analysis was done with multiplexed samples that in addition included two unrelated 4C libraries with compatible indexes and yielded 150-bp paired-end reads on the MiSeq Illumina system. 4C reads were trimmed to 50 nucleotides and analysed using the 4C analysis pipeline, which includes statistical verification and normalization to compute the significant enrichments (http://compgenomics.weizmann.ac.il/tanay/?page_id=367)[38]. Briefly, sequencing reads (posterior limb bud: $\sim 1.1 \times 10^6$; anterior limb bud: $\sim 0.5 \times 10^6$; brain: $\sim 0.6 \times 10^6$) were mapped onto a pre-built database of restriction fragment locations and fragment end sequences defined by the primary (NlaIII) and secondary (DpnII) restriction enzymes. Mapping takes into account fragment end uniqueness and mappability and uses base-calling qualities to partially apportion reads according to mismatch probabilities. Dense genomic profiles were created for the four distinct classes of fragment ends by linear interpolation of mapped reads. One interpolated profile was selected and the three other profiles were quantile-normalized to match its distribution. Resulting profiles were combined by direct summation, resulting in a coverage profile. Finally, medians of normalized coverage and the 20th and 80th percentiles were calculated for sliding windows ranging from 2 kb to 50 kb in size. To screen for candidate *cis*-regulatory regions interacting with the viewpoint at the *Ptch1* proximal promoter, semi-quantitative contact maps were generated for the 1-Mb region surrounding the viewpoint. All 4C-seq data sets are deposited in the Gene Expression Omnibus repository (accession number GSE52988).

GLI3 ChIP-seq and chromatin marker analysis. Chromatin immunoprecipitation (ChIP) was used to detect the N-terminal Flag epitope tag inserted into the endogenous GLI3 protein (J. Lui and A. P. McMahon, unpublished data; this *Gli3* allele will be described elsewhere). Briefly, individual forelimbs and hindlimbs were pooled from fourteen E11.5 embryos obtained from timed matings of homozygous $Gli3^{3XFlag}$ males with Swiss Webster females (Taconic). ChIP was performed using a mouse monoclonal anti-Flag M2 antibody (Sigma F1804)[17]. High-throughput single-end sequencing was done using the Hi-Seq platform (Illumina). The resulting 50-bp sequencing reads were mapped using BWA[56] and filtered for the region corresponding to 500 kb flanking the *Ptch1* locus (mm9: chr13 63,112,841–64,166,828). These results were independently verified as similar binding patterns were detected for GLI2 and GLI1 chromatin complexes (data not shown). The GLI3 ChIP-seq data relevant to this study are deposited in the Gene Expression Omnibus repository (accession number GSE52939). DNase I hypersensitivity and H3K27ac data sets are publicly available (http://genome.ucsc.edu and ref. 34). High-quality reads from the E11.5 forelimb H3K27ac[34] and DNase I hypersensitivity[57] data sets were mapped to the mouse genome (mm9) using the Bowtie (version 0.9.9.1) application tracking up to 100 best alignment positions per query and allowing at most two mismatches. Each alignment was weighted by the inverse of the number of hits, and all quantifications were based on weighted alignments. For the H3K27ac data set, the alignments were shifted by 110 bases using an estimated fragment length of 220 bp (Chip-Cor; http://ccg.vital-it.ch/chipseq).

Sequencing of the *Ptch1* locus and LRM from different artiodactyl species. From several artiodactyl species, the *Ptch1* locus and flanking regions was sequenced as available sequence data were incomplete or inconsistent (bovine, pig) or not available (goat, sheep). Genomic BAC libraries for bovine, sheep, goat and pig[58–61] were screened by PCR using primers that recognize highly conserved regions upstream and downstream of the *Ptch1* locus (Supplementary Table 3). BAC clones were amplified and pooled. Indexed-library construction used the Nextera Genomic DNA Sample Prep kit and paired-end sequencing was done on a HiSeq 2000 machine (Illumina). After quality control and curating the high-throughput sequence data sets, a subset of one million reads per species was processed through a multi-kmer de Bruijn graph-based assembly using Abyss (version 1.3.1)[62] followed by meta-assembly with Mira (version 3.4.0; http://www.chevreux.org/projects_mira.html). For each species, contigs were constructed and manually reordered along the *Bos taurus* UMD3 reference sequence. All the raw data are deposited in the European Nucleotide Archive (study accession number PRJEB5056). The assembled *Ptch1* locus for the goat genome is available through NCBI (http://www.ncbi.nlm.nih.gov/genome?term=capra%20hircus) whereas the others are available through the UCSC browser (http://genome.ucsc.edu).

The sequence of the entire *Ptch1* LRM region in bottlenosed dolphin (*Tursiops truncatus*; GenBank accession number KF932275), dromedary camel (*Camelus dromedarius*; GenBank accession number KF932276) and pygmy hippopotamus (*Hexaprotodon liberiensis*; GenBank accession number KF932277) was determined by Sanger sequencing of PCR fragments amplified from genomic DNA using Q5 high-fidelity DNA polymerase (New England Biolabs). This was done using oligonucleotides designed to match the highest conserved regions between exons 15–19 of the *Ptch1* locus (primer sequences available on request). The sequence containing the artiodactyl-specific microsatellite variation (Extended Data Fig. 6a) was determined using the same approach. Pigmy hippopotamus DNA was extracted from mouth swabs using the QIAamp DNA Investigator kit (Qiagen), while genomic DNA of all other artiodactyl species was extracted from frozen blood samples using the Wizard Genomic DNA purification kit (Promega). The sequence of the *Ptch1* LRM in other mammalian species was obtained via the UCSC Genome Browser, ENSEMBL or NCBI websites. Pair-wise or multiple alignments were performed using VISTA (http://genome.lbl.gov/vista) and ClustalW tools (http://www.ebi.ac.uk/Tools/msa/clustalw2).

49. Ross, D. G., Bowles, J., Hope, M., Lehnert, S. & Koopman, P. Profiles of gonadal gene expression in the developing bovine embryo. *Sex Dev.* **3,** 273–283 (2009).
50. Ellis, T. *et al.* Patched 1 conditional null allele in mice. *Genesis* **36,** 158–161 (2003).
51. Lois, C., Hong, E. J., Pease, S., Brown, E. J. & Baltimore, D. Germline transmission and tissue-specific expression of transgenes delivered by lentiviral vectors. *Science* **295,** 868–872 (2002).
52. van den Brandt, J., Wang, D., Kwon, S. H., Heinkelein, M. & Reichardt, H. M. Lentivirally generated eGFP-transgenic rats allow efficient cell tracking in vivo. *Genesis* **39,** 94–99 (2004).
53. Quintana, L. & Sharpe, J. Preparation of mouse embryos for optical projection tomography imaging. *CSH Protocols* **2011,** 664–669 (2011).
54. Koyama, E. *et al.* Development of stratum intermedium and its role as a Sonic hedgehog-signaling structure during odontogenesis. *Dev. Dyn.* **222,** 178–191 (2001).
55. Schindelin, J. *et al.* Fiji: an open-source platform for biological-image analysis. *Nature Methods* **9,** 676–682 (2012).
56. Li, H. & Durbin, R. Fast and accurate short read alignment with Burrows-Wheeler transform. *Bioinformatics* **25,** 1754–1760 (2009).
57. Rosenbloom, K. R. *et al.* ENCODE data in the UCSC Genome Browser: year 5 update. *Nucleic Acids Res.* **41,** D56–D63 (2013).
58. Eggen, A. *et al.* Construction and characterization of a bovine BAC library with four genome-equivalent coverage. *Genet. Sel. Evol.* **33,** 543–548 (2001).
59. Schibler, L. *et al.* Construction and extensive characterization of a goat bacterial artificial chromosome library with threefold genome coverage. *Mamm. Genome* **9,** 119–124 (1998).
60. Vaiman, D. *et al.* Construction and characterization of a sheep BAC library of three genome equivalents. *Mamm. Genome* **10,** 585–587 (1999).
61. Rogel-Gaillard, C., Bourgeaux, N., Billault, A., Vaiman, M. & Chardon, P. Construction of a swine BAC library: application to the characterization and mapping of porcine type C endoviral elements. *Cytogenet. Cell Genet.* **85,** 205–211 (1999).
62. Simpson, J. T. *et al.* ABySS: a parallel assembler for short read sequence data. *Genome Res.* **19,** 1117–1123 (2009).

a

Bovine			Mouse
FL	HL	CRL(mm)	
D25	-	-	E9.25-E9.5
D28	D30	-	E9.75
D30	D32	-	E10.0
D31	D33	11	E10.5
D32	D34	12	E10.75
D34	D36	14	E11.25
D35	-	16	E11.5
D38	-	18	E12.5
D41	-	23	E12.75
D52	-	-	E14.5

b

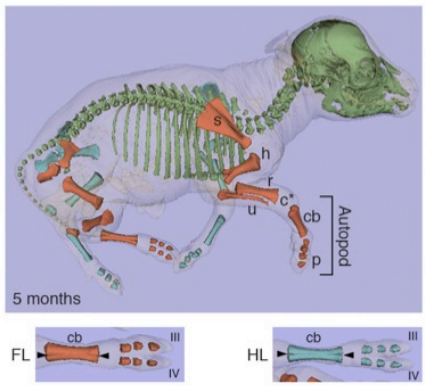

Extended Data Figure 1 | Equivalent stages of mouse and bovine fore- and hindlimb development. a, Table listing the developmentally equivalent bovine fore- and hindlimb bud stages in comparison to mouse forelimb buds. CRL, approximate crown-rump length as previously defined[49]. **b**, False-coloured CT scan of a bovine fetus (at 5 months of gestation) to detect the ossified skeletal bones. Left limbs were coloured blue and right limbs orange. Radius and ulna form as two distinct skeletal elements, while the metacarpals/metatarsals fuse during ossification to give rise to the cannon bone, a convergent trait in many artiodactyls[2]. Lower panels illustrate the similarities of the forelimb (FL) and hindlimb (HL) autopod skeletal bones. Arrowheads indicate the plane of fusion of the metacarpal/metatarsal bones. Two independent fetuses were analysed. s, scapula; h, humerus; r, radius; u, ulna; c*, region corresponding to the not yet ossified carpus; cb, cannon bone; p, phalanges. III, IV, digits.

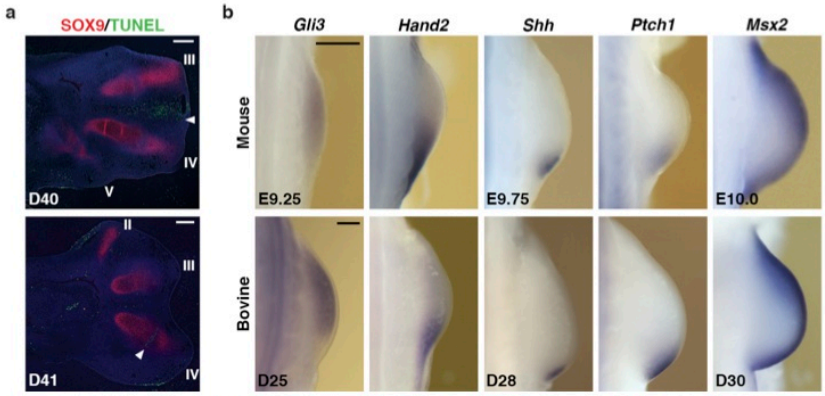

Extended Data Figure 2 | Apoptosis in bovine forelimb buds during digit formation and gene expression during the onset of limb bud development. **a**, The SOX9 transcriptional regulator (red immunofluorescence) marks all chondrogenic progenitors of the forming digit primordia in the bovine forelimb autopod. Apoptotic cells (TUNEL; green fluorescence) are only detected in the interdigit region that is being eliminated at these developmental stages (arrowhead in top panel). No apoptosis is detected in the digit-forming territories, except in the forming joints (arrowhead in bottom panel). Sections were counterstained with Hoechst-33258 to label cell nuclei. **b**, During initiation of limb bud outgrowth, the complementary expression of *Gli3* and *Hand2* marks the establishment of anterior–posterior asymmetry and is required to activate *Shh* expression. Mesenchymal cells responding to SHH signalling upregulate the expression of the SHH receptor *Ptch1*. *Msx2* is a transcriptional sensor of BMP activity and its distribution marks territories of active BMP signalling. The expression of these genes is comparable in early mouse and bovine forelimb buds. In all Extended Data figures, limb buds are oriented with anterior to the top. Per marker and species, the distribution was reproduced in at least $n = 3$ independent limb bud samples in independent experiments. Scale bar, 0.25 mm.

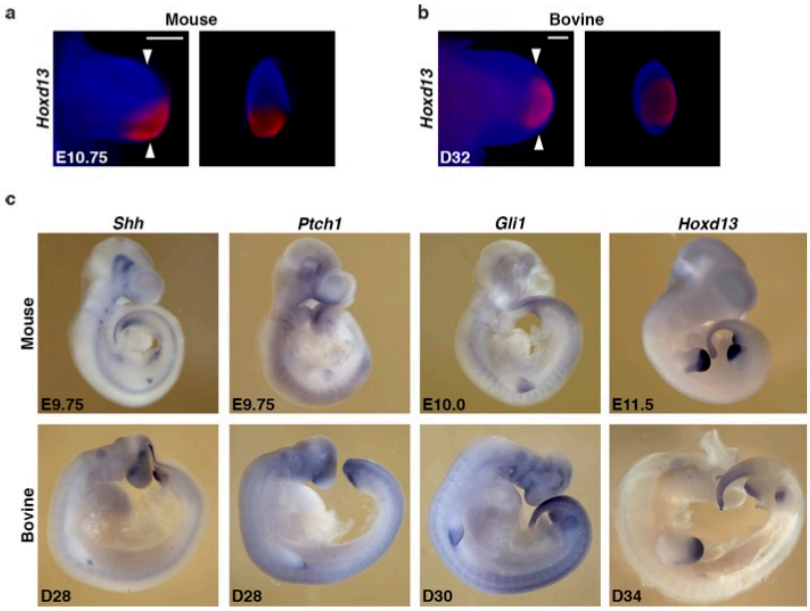

Extended Data Figure 3 | Validation of the whole-mount *in situ* hybridization probes and techniques in bovine embryos. **a**, **b**, OPT analysis of *Hoxd13* transcripts in the mesenchyme of mouse (**a**) and bovine (**b**) forelimbs. White arrowheads indicate the planes of the virtual OPT sections shown in the right panels. This analysis establishes that mesenchymal transcripts are equally well detected in mouse and bovine limb buds. Note the distal shift and more symmetric expression of *Hoxd13* transcripts in bovine limb buds. **c**, Bovine and mouse embryos hybridized with the riboprobes for *Shh*, *Ptch1*, *Gli1* and *Hoxd13*. No apparent changes in their expression in tissues other than limb buds were detected by comparing bovine and mouse embryos. Per gene and species, the transcript distribution was reproduced in at least $n = 3$ independent samples in independent experiments. Scale bar, 0.25 mm.

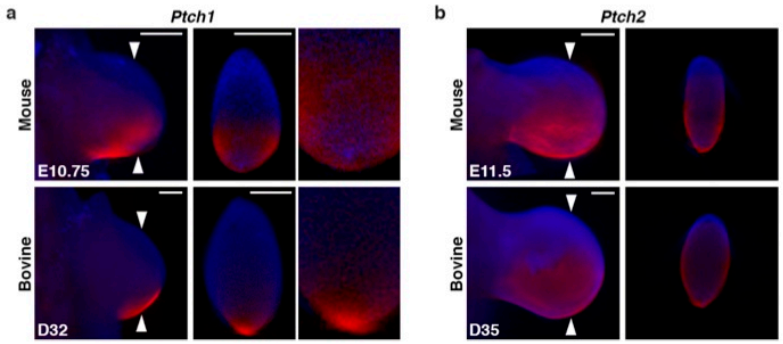

Extended Data Figure 4 | *Ptch1* and *Ptch2* expression in limb buds. **a**, OPT analysis of *Ptch1* expression in mouse and bovine limb buds. White arrowheads indicate the levels of optical sections shown in the middle panels. Right panels show enlargements of the posterior part. **b**, *Ptch2* expression in mouse and bovine limb buds. White arrowheads indicate the levels of optical sections shown in the right panels. Per gene and species, the transcript distribution was reproduced in at least $n = 3$ independent limb bud samples in independent experiments. Scale bars, 0.25 mm.

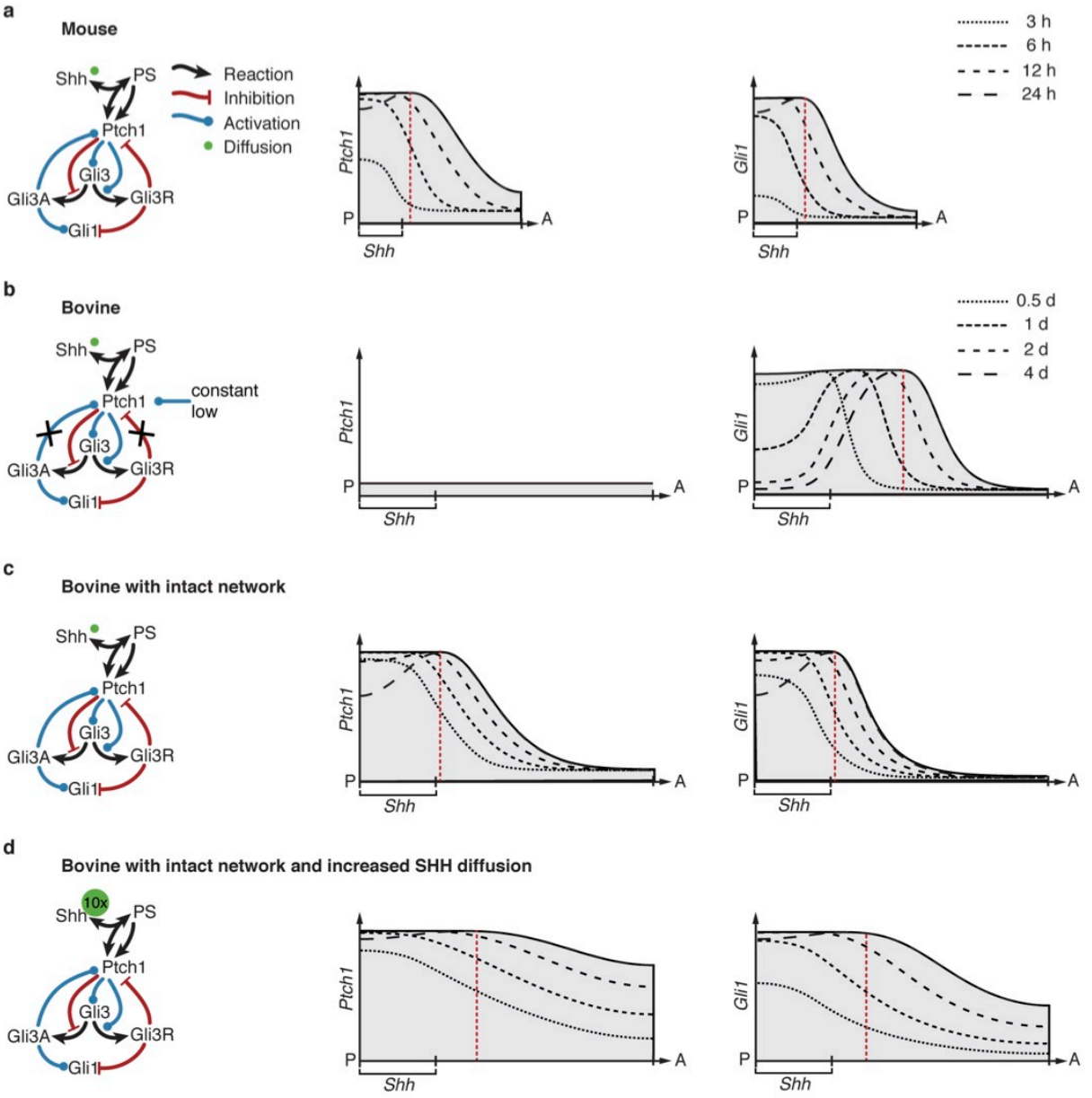

Extended Data Figure 5 | Mathematical simulation of the mesenchymal response to SHH signal transduction with intact (mouse) and absent (bovine) *Ptch1* upregulation in limb buds. **a**, Simulations in wild-type mouse limb buds using the following minimal regulatory network (P. Germann and D. Iber, unpublished data). In the absence of Shh, Ptch1 promotes the formation of Gli repressor (predominantly Gli3R, indicated in blue) and antagonizes (in red) the formation of Gli activators (Gli3A, but also representing contributions by Gli2). Ptch1 is also genetically required for *Gli3* expression in limb buds. Binding of Shh to Ptch1 (PS) relieves the tonic inhibition of Smo by Ptch1 (not shown), which promotes activator and inhibits repressor formation. Both Gli3A and Gli3R isoforms impact on *Ptch1* and *Gli1* expression, the expression kinetics of which were simulated (middle and right panels). For details of network construction and all references see Supplementary Note. In wild-type mouse limb buds, *Ptch1* and *Gli1* are upregulated in the posterior mesenchyme. **b**, Simulation of *Ptch1* and *Gli1* expression in bovine limb buds. The impact of Gli3A and Gli3R on *Ptch1* transcription was removed from the network and the rate of Ptch1 production fixed at constant low levels. Simulations using this altered network result in progressive anterior expansion of *Gli1* expression. **c**, Simulations of hypothetical bovine limb buds with an intact network results in posterior upregulation of both *Ptch1* and *Gli1* expression. **d**, Increasing Shh diffusion rates by tenfold (green dot in scheme) in an otherwise intact network leads to upregulation and anterior expansion of both *Ptch1* and *Gli1* expression, that is, fails to reproduce the real gene expression patterns. Broken lines in all panels indicate the simulated *Ptch1* and *Gli1* transcriptional activities at the indicated time points and the grey shaded area bordered by a solid line corresponds to the overall transcript levels. Red dotted line marks the position of peak expression. Gene symbols correspond to the computational variables used for simulations. A, anterior; P, posterior; h, hours; d, days. For detailed description of all simulations see Supplementary Note.

a

```
Mouse          ACCAGTGTGTTTACAGCAAACACACG----------GTTCCGCAGATGGCCCAGGAATTGGC
Human          ACTGGCGTGTTTATAACAAACACA----------GTTCTGCAGATGGCCCAGGAATTGGC
Rh. macaque    ATTGGCGTGTTTATAACAAACACA----------GTTCTGCAGATGGCCGAGGAATTGGC
Dog            ATCAGTGTGTTTCTAACACACACACA----------GTTCTGCAGATGGTCCAGGAATTGAC
Horse          ATCGGCGTGTTTATAACACACACACA----------GCTCTGCAGATGGCCCAGGAATCGAC
Alpaca         ATCAGCATGTTTATAACACACACACACGCGCGCGCGCACACACAGA----------GTCCTGCAGATGGCCCAGGAATTGAC
Camel          ATCAGCATGTTTATAACACACACACACACACACACACGCACGCACACACAGA----------GTCCTGCAGATGGCCCAGGAATTGAC
Pig            ACAGGCATGTTTATAACACACACACACACACACACACACACACACACACACACACACACACACACACACACACGCAGTTCTGCAGATGGCCCGGGAGTTGAC
Bovine         ATCGGCATGTTTATAACACACATACACACACACACACACA----------GTTCGGCAGATGGCCCAGGAATTGAC
Sheep          ATCGGCATGTTTATAACACACATACACACACACACACA----------GTTCGGCAGATGGCCCAGGAATTGAC
Goat           ATCGGCATGTTTATAACACACATACACACACACACACA----------GTTCGGCAGATGGCCCAGGAATTGAC
Hippo          ATCGGCATGTTTATAACACACACACACACACACAGA----------GTTCTGCAGATGGCCCAGGAATTGAC
Dolphin        ACCGGCATGTTTGTAACACACACACACA----------GTTCTGCAGACGGCCCAGGAATGGAC
Minke whale    ATCGGCATGTTTATAACACACACACA----------GTTCTGCAGACGGCCCAGGAATGGAC
               *   *  *****  * ** *** *                *  * ***** ** *  *** * * *
```

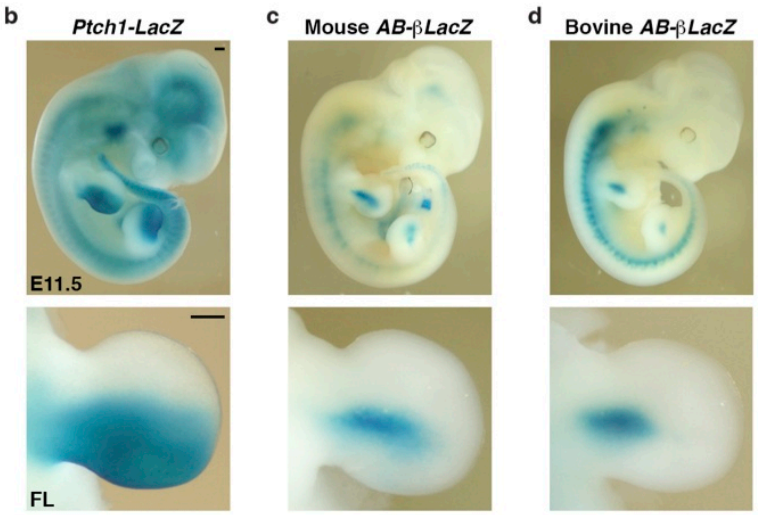

Extended Data Figure 6 | Functional analysis of the conserved mouse and bovine core regions A and B using lentiviral transgenesis. a, A variable and artiodactyl-specific microsatellite expansion (CA/CG_{2-27}, red shading) in region A is located just upstream of exon 17 (Fig. 5a). **b**, Expression of a *lacZ* reporter inserted into the *Ptch1* locus. **c**, **d**, Expression of lentivector *ßlacZ* reporter constructs controlled by the mouse and bovine conserved regions A and B (Fig. 5a) in transgenic mouse embryos (mouse: $n = 12$ of 41; bovine: $n = 12$ of 20 embryos). FL, forelimb. Scale bar, 0.25 mm.

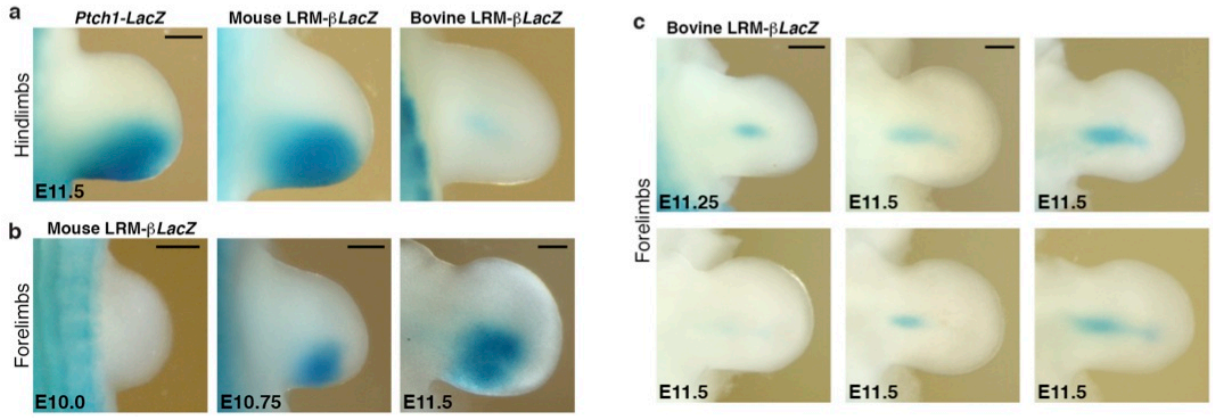

Extended Data Figure 7 | Functional analysis of the mouse and bovine LRM. **a**, Expression of the mouse and bovine LRM in mouse hindlimb buds (E11.5). **b**, Transgenic mouse embryos collected at different stages reveal the temporal kinetics of activation and upregulation of the mouse LRM-*ßlacZ* transgenic reporter in forelimb buds ($n = 3$ independent embryos per stage). **c**, Forelimb buds of $n = 6$ independent transgenic embryos expressing the *lacZ* reporter under control of the bovine LRM region. The variable expression is in all cases restricted to the core mesenchyme (compare to Fig. 5d). Scale bar, 0.25 mm.

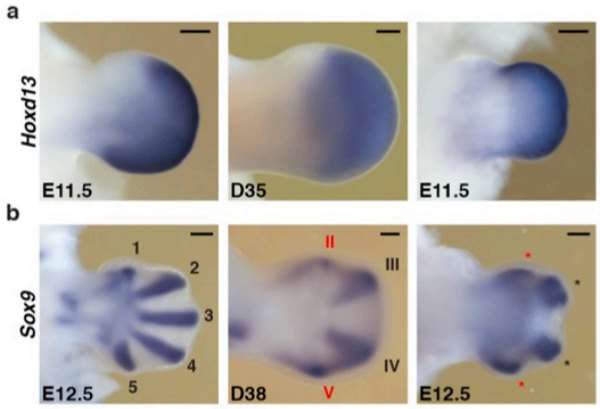

Extended Data Figure 8 | *Prx1*-Cre-mediated conditional inactivation of *Ptch1* in the mouse limb mesenchyme phenocopies the loss of asymmetry and alterations in digit primordia similar to bovine handplates.
a, **b**, Detection of *Hoxd13* (**a**) and *Sox9* (**b**) transcripts in mouse (left), bovine (middle) and $Ptch1^{\Delta c/\Delta c}$ (right panels) forelimb buds. Per gene, species and mouse genotype, the transcript distribution was reproduced in at least $n = 3$ independent limb bud samples in independent experiments. Vestigial digit primordia are indicated in red. Asterisks indicate digit primordia with uncertain identities. Scale bars, 0.25 mm.

Publication 3: An interplay between geometry and signaling enables robust lung branching morphogenesis

For this project, I produced embryos that harbor GFP signal in the lung epithelium by crossing the Shh-Cre-GFP and β-actin-GFP mice, and I did the mouse colony maintenance and animal crosses.

© 2014. Published by The Company of Biologists Ltd | Development (2014) 141, 4526-4536 doi:10.1242/dev.116202

RESEARCH ARTICLE

An interplay of geometry and signaling enables robust lung branching morphogenesis

Denis Menshykau[1,2], Pierre Blanc[3], Erkan Unal[1,2,4], Vincent Sapin[3] and Dagmar Iber[1,2,*]

ABSTRACT

Early branching events during lung development are stereotyped. Although key regulatory components have been defined, the branching mechanism remains elusive. We have now used a developmental series of 3D geometric datasets of mouse embryonic lungs as well as time-lapse movies of cultured lungs to obtain physiological geometries and displacement fields. We find that only a ligand-receptor-based Turing model in combination with a particular geometry effect that arises from the distinct expression domains of ligands and receptors successfully predicts the embryonic areas of outgrowth and supports robust branch outgrowth. The geometry effect alone does not support bifurcating outgrowth, while the Turing mechanism alone is not robust to noisy initial conditions. The negative feedback between the individual Turing modules formed by fibroblast growth factor 10 (FGF10) and sonic hedgehog (SHH) enlarges the parameter space for which the embryonic growth field is reproduced. We therefore propose that a signaling mechanism based on FGF10 and SHH directs outgrowth of the lung bud via a ligand-receptor-based Turing mechanism and a geometry effect.

KEY WORDS: Branching morphogenesis, Image-based modeling, Turing pattern, Computational biology

INTRODUCTION

To achieve a large area of gas exchange within a limited thorax volume, lung development must be tightly controlled (Weibel, 1991). Embryonic development of the lung is indeed stereotyped to an extent that random development is unlikely. The lung tree is built by the sequential use of mostly three branching modes, namely lateral branching, planar bifurcations and orthogonal bifurcations (Metzger et al., 2008), and by rare trifurcations (Blanc et al., 2012). The sequence of these branching events is fixed in embryos from the same genetic background, and few errors are observed in wild-type littermates (Metzger et al., 2008), although a certain level of variation in the position and direction of branch outgrowth has been documented (Blanc et al., 2012; Short et al., 2012).

A number of models have been proposed to explain the control of the branching events. The earliest models focused on physical forces (reviewed by Lubkin, 2008), and combinations of experimental and computational studies have since confirmed that mechanical stress and internal pressure influence branching morphogenesis (Gjorevski and Nelson, 2010, 2012; Kim et al., 2013; Nelson and Gleghorn, 2012; Unbekandt et al., 2008; Varner and Nelson, 2014). WNT signaling affects the epithelial shape of new lung buds, but WNT signaling is not essential for lung branching morphogenesis and is thus not part of the core regulatory network (Kadzik et al., 2014).

Other models focus on diffusion-based signaling effects because the secreted, diffusible proteins fibroblast growth factor 10 (FGF10) and sonic hedgehog (SHH) are necessary for lung branching morphogenesis (Abler et al., 2009; Bellusci et al., 1997a; Chiang et al., 1996; Peters et al., 1994; Weaver et al., 2000). As FGF10 signaling is necessary for the outgrowth of branches, it is generally assumed that FGF10 must vanish at the tip and concentrate on the sides adjacent to the lung bud tip to induce a splitting of the tip during bud outgrowth, thus resulting in bifurcating outgrowth. Lateral branching then requires the emergence of FGF10 signaling in multiple spots along the lung bud, while maintaining FGF10 signaling at the tip to support further outgrowth. It is a long-standing question how the expression and signaling patterns arise in the developing lung. A number of geometry-driven mechanisms have been proposed to explain how bifurcations may be directed. One such proposed mechanism is based on the distance between the FGF10-producing (i.e. the sub-mesothelial mesenchyme) and the FGF10-sensing (i.e. the epithelium) tissue (Bellusci et al., 1997b). It was noted that the closer the two tissues then the steeper the diffusional gradient should be, if the concentration were homogeneous in a given tissue layer (Clément et al., 2012a). If cells were responding to the FGF10 gradient rather than to the FGF10 concentration this mechanism would support bifurcations (Clément et al., 2012a,b). In an alternative model it was proposed that FGF10 accumulates at the sides and drives bifurcating outgrowth because the tip of the *Shh*-expressing lung bud epithelium grows closer to the mesothelium. FGF10 and SHH engage in a negative feedback in that FGF10 signaling induces *Shh* expression (Abler et al., 2009), while SHH signaling represses the expression of *Fgf10* (Bellusci et al., 1997b). The higher local SHH concentration would then inhibit *Fgf10* production in the *Fgf10*-expressing sub-mesothelial mesenchyme (Bellusci et al., 1997b). In a computational implementation of the model, the mesothelium had to act as a diffusion barrier and lower SHH concentrations had to induce rather than inhibit *Fgf10* expression (Hirashima and Iwasa, 2009), both of which remain to be demonstrated.

A further mechanism has been proposed based on the observation that the expression of key ligands is restricted to parts of the tissue, and certain patterns emerge when the soluble signaling proteins diffuse away from the producing tissue (Nelson et al., 2006). Using 3D shapes of lung bud epithelia extracted from early developing chicken lungs, visual inspection suggested that the areas where branching of secondary bronchi is inhibited coincide with where a steady-state diffusion model would predict high concentrations of diffusible inhibitory molecules when these are secreted from the epithelium into a large computational bounding box (Gleghorn et al., 2012).

[1]Department of Biosystems, Science and Engineering (D-BSSE), ETH Zurich, Mattenstraße 26, 4058 Basel, Switzerland. [2]Swiss Institute of Bioinformatics (SIB), Mattenstraße 26, 4058 Basel, Switzerland. [3]R2D2/Retinoids, Reproduction, Developmental Diseases, Faculté de Médecine, 28 Place Henri Dunant, BP 38, 63001 Clermont-Ferrand Cedex, France. [4]Developmental Genetics, Department Biomedicine, University of Basel, Mattenstraße 28, 4058 Basel, Switzerland.

*Author for correspondence (dagmar.iber@bsse.ethz.ch)

Received 3 August 2014; Accepted 10 September 2014

Development (2014) 141, 4526-4536 doi:10.1242/dev.116202

We have recently shown that a ligand-receptor-based Turing mechanism can result in FGF10 signaling patterns that correspond to either lateral branching or to bifurcations, and recapitulates even counterintuitive mutant phenotypes such as the abrupt increase in the spacing between buds in the *Fgf10* allelic sequence as the *Fgf10* expression levels fall below a threshold (Celliere et al., 2012; Menshykau et al., 2012). Using a simplified geometry, others have since shown that FGF10-dependent Turing mechanisms can, in principle, also support the outgrowth of branches (Guo et al., 2014a,b). Interestingly, although *Fgf10* expression is necessary for branching morphogenesis (Abler et al., 2009), it has recently been shown that branching is still observed when *Fgf10* is expressed homogenously, although the branching pattern is then different (Volckaert et al., 2013). Similarly, it is well established that lung epithelium will branch *in vitro* in the absence of mesenchyme if FGF is provided (Nogawa and Ito, 1995). Both experimental results contradict earlier models that were based on the distance of the *Fgf10*-expressing domain and the epithelium, while they are in agreement with a ligand-receptor-based Turing mechanism, because Turing mechanisms can yield patterns from a homogenous (noisy) distribution of the components without any need for a pre-pattern.

Turing mechanisms permit the self-organized emergence of a wide range of different patterns based on a diffusion-driven instability (Turing, 1952). They emerge for a particular network architecture (Gierer and Meinhardt, 1972; Prigogine, 1967; Prigogine and Lefever, 1968) and typically require at least two interacting factors that diffuse at substantially different rates, as is naturally the case for receptor-ligand systems. If ligands L and receptors R interact cooperatively and ligand-receptor binding results in an increased emergence of receptor on the membrane (by increased transcription, translation, recycling, less constitutive removal or similar) one obtains the standard Schnakenberg-type or activator-depleted substrate reaction kinetics for Turing patterns (Badugu et al., 2012; Gierer and Meinhardt, 1972; Kurics et al., 2014; Menshykau and Iber, 2013; Menshykau et al., 2012; Prigogine, 1967; Prigogine and Lefever, 1968; Schnakenberg, 1979; Tanaka and Iber, 2013), which take the form:

$$\frac{\partial L}{\partial t} = D\Delta L + \gamma(a - L - R^2L), \quad (1)$$

$$\frac{\partial R}{\partial t} = \Delta R + \gamma(b - R + R^2L). \quad (2)$$

Here, the terms on the left-hand side of Eqs 1 and 2 are the time derivatives. The first term on the right-hand is the diffusion term, with $D>1$, since the ligand diffuses faster than its receptor. Although the mode of transport for morphogens is still a matter of debate (Müller et al., 2013) and often only a small fraction of morphogens may diffuse freely in the extracellular matrix (Zhou et al., 2012), we note that diffusion-based transport in combination with a realistic description of the receptor dynamics and ligand turnover has previously been shown to faithfully recapitulate the observed patterning process in a number of different developmental systems (Fried and Iber, 2014; Lopez-Rios et al., 2014; Nahmad and Stathopoulos, 2009). The non-dimensionalized reaction kinetics have three parameters: γ, a and b. γ is a scaling factor that influences the number of spots that can emerge on a domain; a and b are the constitutive production rates of ligand and receptor, respectively. $-L$ and $-R$ describe the linear decay of ligand and receptor, while $-R^2L$ describes receptor-dependent decay of ligand. The term $+R^2L$ describes the combined effects of ligand-triggered receptor turnover and ligand-induced receptor expression. In deriving this formula, a quasi-steady-state approximation was made for the concentration of the ligand-receptor complex, and the signaling complex was approximated by R^2L (Badugu et al., 2012; Menshykau and Iber, 2013; Menshykau et al., 2012). We have previously shown that both the FGF10-receptor and SHH-receptor interactions are well described by Eqs 1 and 2 (Kurics et al., 2014; Menshykau et al., 2012).

A sequence of 3D lung geometries at different murine embryonic stages has recently been published (Blanc et al., 2012) and now permits for the first time the testing of the different proposed mechanisms with murine embryonic growth data. To that end we determined the displacement fields between four subsequent developmental stages. We then simulated the different models on the embryonic domains and checked whether the predicted signaling domains would coincide with where the lung bud actually grows out. We repeated the same procedure with time-lapse data for embryonic lung explants. In both cases, we show that only for a particular ligand-receptor Turing mechanism, but not for any of the alternative mechanisms studied, the signaling patterns coincide with the areas of growth. We further show in simulations that morphogen distributions that arise from the tissue-specific expression of morphogens (Nelson et al., 2006) are unstable under deforming outgrowth because the curvature would change as buds start to grow out at the sides. This mechanism thus creates split concentration profiles, but does not support the emergence of bifurcations of the bud tip as the bud is growing out. The Turing mechanism, by contrast, permits the emergence of such bifurcations in 3D simulations. The type of pattern that emerges via Turing mechanisms is typically very dependent on the (noisy) initial conditions. Importantly, the tissue-specific expression of ligand and receptor ensures patterning robustness of the ligand-receptor-based Turing mechanism and thus enables robust branching in 3D.

RESULTS

Model evaluation: comparison of predicted and real areas of growth on 3D lung bud shapes

We used a published sequence of 3D lung geometries at four different murine embryonic stages between E11.25 and E11.75 [stages 1 to 4 (S1-S4) in Fig. 1A-D] (Blanc et al., 2012) to evaluate how well alternative mechanisms would predict the regions of lung bud outgrowth; image segmentation as well as surface and volume mesh generation were performed using the commercial software package Amira (Iber et al., 2015). In a first step, we calculated the displacement fields (Fig. 1E-G) between subsequent stages of the published lung geometries, using the landmark-based Bookstein algorithm (Bookstein, 1989) as implemented in Amira. We found that the lung buds predominantly grow at the tips and shrink in other places (red and blue arrows, respectively, in Fig. 1E-G). We focus on the signaling-dependent control of the outward movement of the epithelium, and do not attempt to predict the extent of shrinkage in the neighborhood, which may occur because of cell migration, deformation and rearrangements during the budding process (Kim et al., 2013). Accordingly, we set the length of all inward-pointing displacement vectors to zero (Fig. 1H-J). In the following, we refer to the resulting displacement vector field as the embryonic growth field. For every mesh point in the epithelium we next calculated the minimal distance to the mesenchyme surface using Amira. The distance between the epithelium and the mesenchyme surface is lowest at the tips of the lung buds (Fig. 1K; supplementary material Fig. S1A,B), but the distances do not vary across the lung bud as much as the embryonic growth field (Fig. 1L; supplementary material Fig. S1C,D).

Development (2014) 141, 4526-4536 doi:10.1242/dev.116202

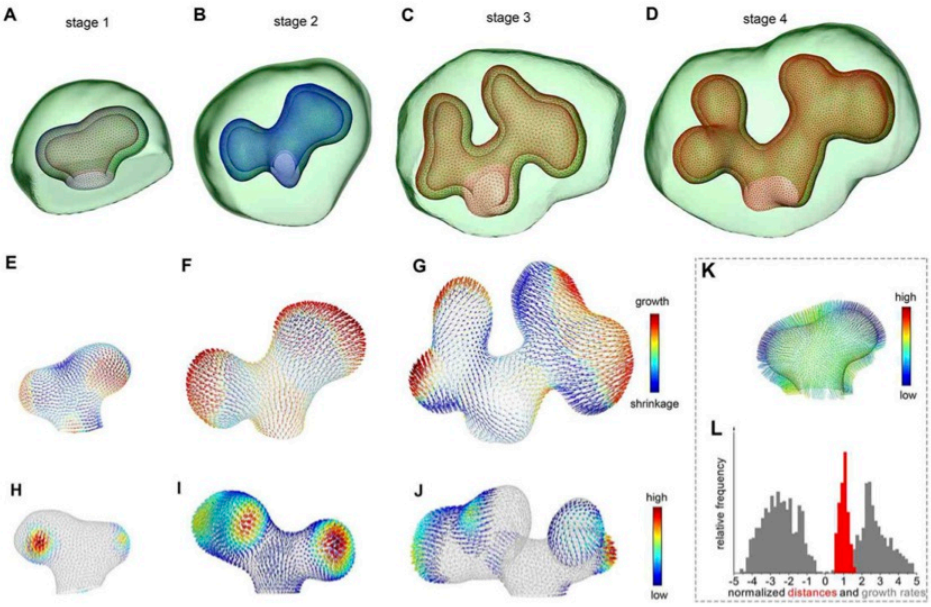

Fig. 1. Embryonic growth fields in lung branching morphogenesis. (A-D) A sequence of 3D embryonic lung buds between E11.25 and E11.75 with epithelium (wireframe) and mesenchyme (green). Stage (S) 1 is at 46 somites; S2 at 51 somites. (E-G) The calculated displacement fields of the epithelial layer between (E) S1 and S2, (F) S2 and S3 and (G) S3 and S4. Outward, red; inward, blue; the color bar indicates the strength of the displacement. (H-J) The calculated outward-pointing displacement fields of the epithelium layer between (H) S1 and S2, (I) S2 and S3 and (J) S3 and S4. (K) The distance field between epithelium and mesenchyme in S1 lung buds. (L) The distances between the epithelium and the mesenchyme (red) do not greatly vary across the S1 lung bud (mean distance=1, minimal distance=0.6, maximal distance=1.6, s.d.=0.25), whereas the relative growth rate (gray) has a much broader distribution.

To evaluate the alternative models that we discussed in the Introduction, and which are summarized in supplementary material Table S1, we determined the match between the embryonic growth fields and the predicted signaling domains on lung buds of the different stages over the likely physiological range of the parameter sets. At three different developmental stages (Fig. 1A-C) we subsequently calculated the deviation Δ (Eq. 4 in the Materials and Methods) of the normalized concentration of the ligand-receptor complex from the normalized length of the embryonic growth field shown in Fig. 1H-J. In other words, Δ quantifies the 'overall' deviation between the embryonic growth field and the predicted signaling patterns. We note that comparable results were obtained with different normalizations (supplementary material Text 1.1, Figs S2 and S3). The minimal Δ that corresponds to a good match between the predicted signaling field and the embryonic growth field varies between the stages: for the first transition from S1 (46 somites) to S2 (51 somites), the different models and parameter sets resulted in values of Δ of 0.62 and higher. Visual inspection showed that, for this stage, values of Δ up to 0.7 correspond to a good match between signaling pattern and growth field (supplementary material Fig. S4A). Note that the deviation of the embryonic displacement field to a signaling model with no signal would be equal to 1.

A ligand-receptor-based Turing mechanism correctly predicts the lung growth fields

An FGF10-based Turing mechanism

Both the FGF10 and SHH ligand-receptor systems can form independent Turing modules (Kurics et al., 2014). We will analyze the two Turing modules separately, starting with the FGF10-based Turing mechanism, without including the SHH module. In this case, the ligand FGF10 is represented by L, and its receptor FGFR2b is represented by R in Eqs 1 and 2. FGF10 signaling triggers outgrowth of the lung bud (Weaver et al., 2000), and the outgrowth of lung branches (but not of the main bud) is strictly dependent on FGF10 signaling (Peters et al., 1994). Accordingly, we expect branch outgrowth to occur in places where the concentration of the FGF10-FGFR2b signaling complex, R^2L, is highest. *Fgf10* is expressed only in the mesenchyme (blue areas in the cartoon in Fig. 2), while the FGF10 receptor *Fgfr2b* is expressed only in the epithelium (gray areas in the cartoon in Fig. 2) (Bellusci et al., 1997b). Accordingly, when we solved Eqs 1 and 2, the ligand expression rate, a, was non-zero only in the mesenchyme and the constitutive receptor expression rate, b, was non-zero only in the epithelium; receptor diffusion was also limited to the epithelium such that there are no FGFR2b receptors in the mesenchyme (see supplementary material Table S1, case T1 for details).

We next sampled the parameter values for a, b, d and γ and compared the simulated patterns with the measured embryonic displacement field. We obtained a wide range of patterns for the different parameter sets with a deviation (Δ, Eq. 4) between the predicted signaling levels and the embryonic growth field of 0.7 and above (Fig. 2A; supplementary material Fig. S4A). The best matching patterns could be further optimized with a local optimization algorithm to Δ=0.62 (Fig. 2A), and the predicted signaling domain (solid) overlays perfectly with the embryonic growth field (arrows). Differential growth and cellular responses can be expected only for a sufficient concentration difference within the domain. We therefore also analyzed the quality of the pattern as the maximal concentration difference within the domain, and we note that those parameters that yield the best match between the model and the embryonic growth field also result in the largest concentration difference inside and outside the signaling spots (Fig. 2, black spots).

Development (2014) 141, 4526-4536 doi:10.1242/dev.116202

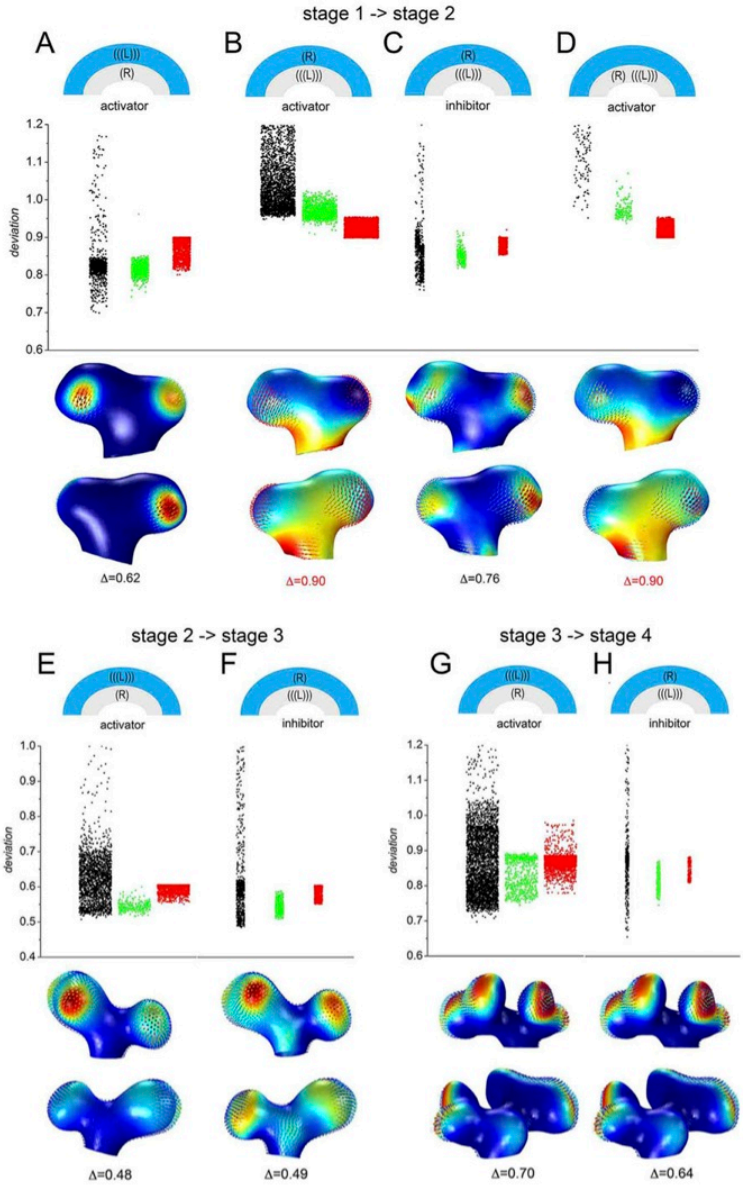

Fig. 2. Comparison of 3D lung embryonic growth fields and predicted ligand-receptor-based signaling strengths. The deviation, Δ (Eq. 4), of the spatial distribution of signaling strength S_n for the ligand-receptor-based signaling mechanism (Eqs 1 and 2) from the embryonic growth fields (Fig. 1H-J) at different stages: (A-D) S1 to S2, (E,F) S2 to S3 and (G,H) S3 to S4. The mathematical models are summarized in supplementary material Table S1, cases T1-T4. Receptors and ligands are expressed either in the epithelium (gray layer) or in the mesenchyme (blue layer), as indicated in the cartoon in the top row. The different colors indicate parameter sets for which the ratio of the maximal and minimal concentrations of the receptor-ligand complex at the epithelial-mesenchyme border is at least 5-fold (black, likely Turing space; for details see supplementary material Text 1.2 and 3), less than 2-fold (red, likely outside Turing space) or in between (green). The width of the columns reflects the number of parameter sets that have been screened (1000-10,000). The lower panels show the best matches of computed areas of signaling (solid) and the embryonic displacement fields (vector field) for each case for two different orientations of the lung buds. Red, high; blue, low.

Given the domain-dependent expression pattern of receptors and ligands, we could not carry out a linear stability analysis to define the parameter sets that give rise to a Turing instability, i.e. that are part of the Turing space. However, we note that such large concentration differences are typical for Turing patterns, and the parameter sets that yield such large concentration differences also exhibit other properties that are characteristic of Turing patterns (see supplementary material Text 1.2 and Fig. S4B-D).

The best (and the worst) matches between the signaling model and the physiological displacement field were thus all obtained for parameter sets that lay within this (inferred) Turing space (Fig. 2A, black dots). The best fit for a parameter set outside this (inferred) Turing space is considerably worse (Δ=0.8, supplementary material Fig. S4E) than the best fit obtained with parameters within the (inferred) Turing space (Δ=0.62, Fig. 2A).

An SHH-based Turing mechanism

Shh is essential for the development of the respiratory system and *Shh*-deficient lungs do not form branches (Pepicelli et al., 1998). We therefore examined whether an SHH-based mechanism could also predict the embryonic growth patterns. We have shown previously that the interaction of the ligand SHH (*L* in Eqs 1 and 2) with its receptor PTCH1 (*R* in Eqs 1 and 2) results in the ligand-receptor-based Turing model given in Eqs 1 and 2 (Menshykau et al., 2012) (see supplementary material Table S1, case T2 for details). The expression pattern of *Shh/Ptch1* is the inverse of that of *Fgf10/Fgfr2b* in that the ligand *Shh* is expressed in the epithelium, whereas the receptor *Ptch1* is expressed in the mesenchyme (Bellusci et al., 1997a). We therefore switched the position of the ligand and receptor expression domains such that the ligand would be produced in the epithelium (Fig. 2B, gray in the cartoon) and the receptor

Development (2014) 141, 4526-4536 doi:10.1242/dev.116202

would be expressed in the mesenchyme (Fig. 2B, blue in the cartoon). The smallest deviation (Δ=0.9) is now obtained with a non-Turing pattern, but the overall match is poor (Fig. 2B, lower panel). Further local optimization barely improved the patterns. However, we note that, unlike in the case of FGF10, SHH signaling inhibits lung bud outgrowth as it represses the expression of *Fgf10* (Bellusci et al., 1997b). Outgrowth should therefore be strongest where the concentration of the SHH-PTCH1 complex, R^2L, is lowest, i.e. where the level of $1/R^2L$ is highest. When we compared the level of $1/R^2L$ with the embryonic growth field we obtained a match that was almost as good as for the FGF10-based Turing model as long as the parameters were within the (inferred) Turing space (Fig. 2C, black dots, $\Delta \geq 0.76$). To judge the relevance of the two distinct tissue layers we carried out a further parameter screen in which we expressed both the receptor and the ligand in the epithelium (supplementary material Table S1, case T3). In this scenario, the best match of the Turing patterns is worse than that of the non-Turing patterns (Fig. 2D) and the overall best match is rather poor ($\Delta \geq 0.9$, supplementary material Fig. S4F).

We repeated the analysis of FGF10 and SHH signaling models for the next two stages of lung development and obtained similar results (Fig. 2E-H), even though the lung geometry is more complicated at these later stages (Fig. 2E-H, lower panels). Finally, we acquired several movies of branching lung buds over 36 h of culture (Fig. 3A; supplementary material Fig. S5A), segmented the images and calculated the growth fields (see Materials and Methods for details). Again, we find that ligand-receptor-based Turing models, both for FGF10 (Fig. 3B-D; supplementary material Fig. S5B-D) and for SHH (Fig. 3E-G; supplementary material Fig. S5E-G) best predict the growth fields over time, even though the 2D branching patterns differ substantially from those observed in 3D in the embryo. This confirms the robustness of the proposed patterning mechanism. We conclude that both the FGF10-based Turing signaling model and the SHH-based Turing signaling model present excellent candidate mechanisms to control growth in the developing lung bud as long as the genes are expressed in their physiological domains.

Negative feedbacks enlarge the Turing space for the control of lung outgrowth

Although the ligand-receptor-based Turing mechanism predicts the embryonic growth fields very well, the Turing spaces (i.e. the part of the parameter space where Turing patterns can be observed) for the core ligand-receptor mechanisms (FGF10 and SHH) are tiny (Fig. 4A). We have recently shown that negative feedbacks and the coupling of two Turing systems, as is the case for FGF10 and SHH, can massively increase the size of the Turing space (Kurics et al., 2014). We now examined whether this would also apply in

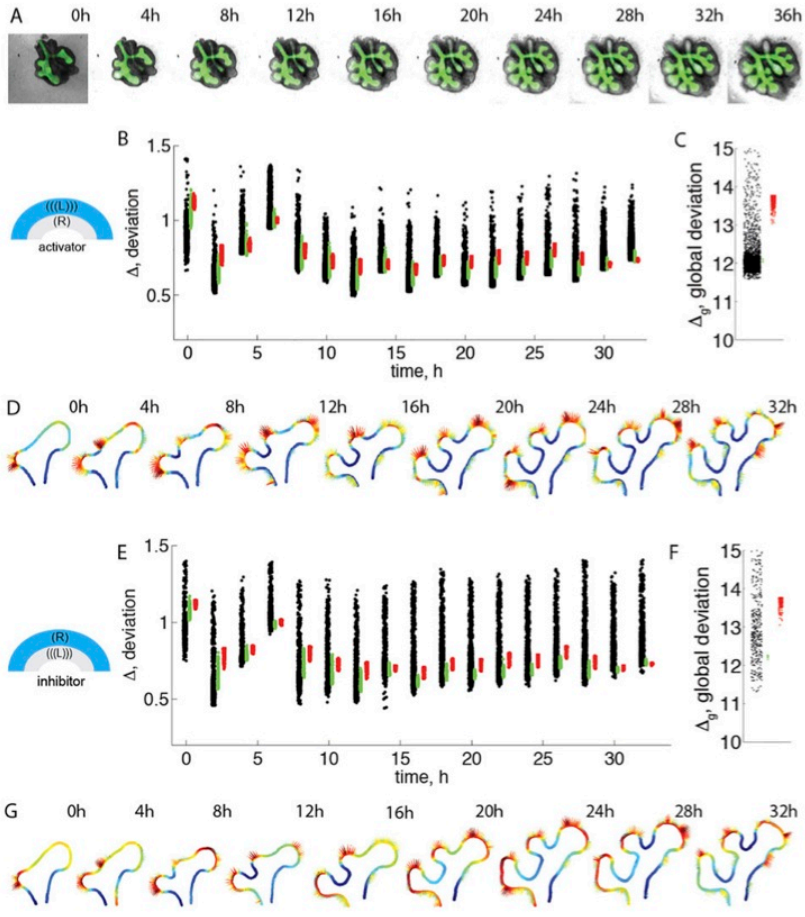

Fig. 3. Comparison of 2D lung displacement fields as obtained from lung cultures with those predicted by a ligand-receptor-based signaling mechanism. (A) A 2D time-lapse movie (2 h frames) of a cultured lung bud (starting at E11.5) undergoing branching morphogenesis, showing the EGFP-expressing epithelium (green) and the mesenchyme (gray). (B-G) Deviation, Δ (Eq. 4), of the predicted spatial distribution of signaling strengths from the experimentally determined growth fields (B,E) in each frame and (C,F) over all frames, as well as (D,G) the best match of the predicted signaling strengths (solid color) and the experimentally observed growth fields (vector field), if (B-D) ligand is expressed in the mesenchyme and receptor is expressed in the epithelium, as is the case for FGF10, or if (E-G) ligand is expressed in the epithelium and receptor is expressed in the mesenchyme, as is the case for SHH. The different colors indicate parameter sets for which there is an at least 5-fold concentration difference (black, likely Turing space; for details see supplementary material Text 1.2), an at least 2-fold concentration difference (green), or a concentration difference that is less than 2-fold (red, likely outside Turing space) at the border of epithelium and mesenchyme; for details see supplementary material Text 1.2.

Development (2014) 141, 4526-4536 doi:10.1242/dev.116202

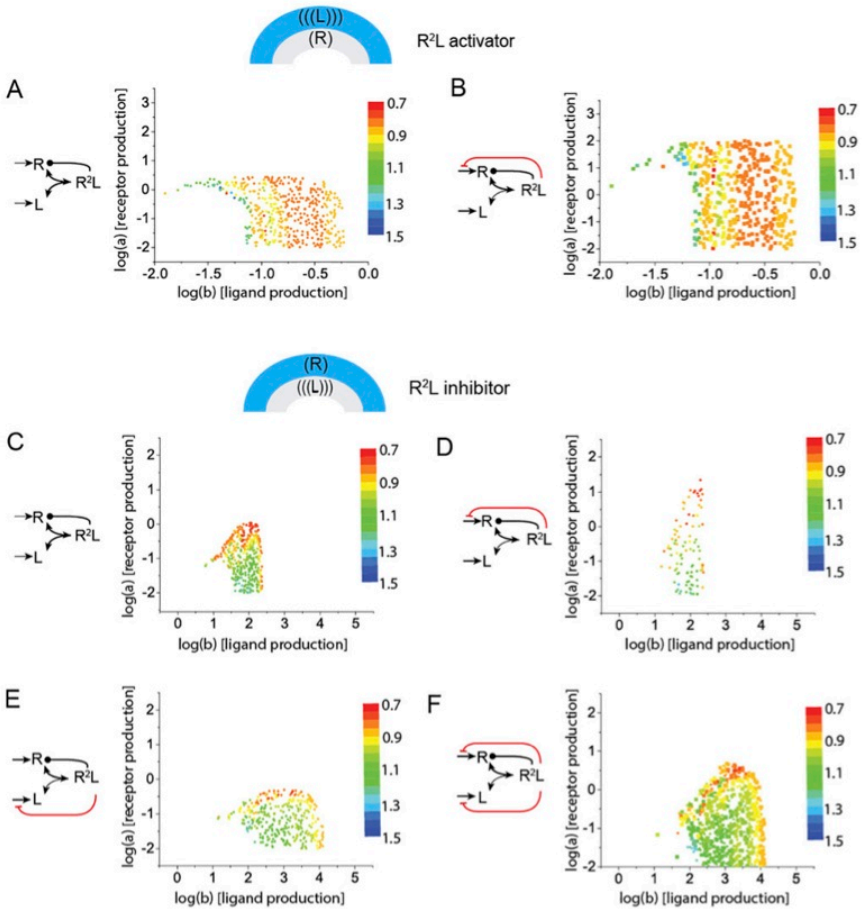

Fig. 4. Negative feedbacks increase the size of the Turing space and the parameter range for which the embryonic growth field is reproduced. To the left the regulatory networks are illustrated, with receptor represented by *R* and ligand represented by *L*. The core Turing system is depicted in black, with additional feedbacks in red. Graphs show the deviation Δ (Eq. 4, encoded by the color bar) between the signaling model (Eqs 1 and 2) and the embryonic displacement field for S1-S2 embryonic lungs (as shown in Fig. 1H) for the (*a*,*b*) parameter sets that lie within the inferred Turing space (for details see the supplementary material Text 1.2). The simulations were carried out on an embryonic 3D domain with an infinitely thin epithelium. (A,B) Receptor is expressed in the epithelium (blue), while ligand is expressed in the mesenchyme (gray), as is the case for FGF10, and signaling strength was assumed to be proportional to the concentration of the ligand-receptor complex, R^2L, as FGF10 induces outgrowth of branches. (C-F) Receptor is expressed in the mesenchyme (blue), while ligand is expressed in the epithelium (gray), as is the case for SHH, and signaling strength was assumed to be proportional to the inverse of the concentration of the ligand-receptor complex, R^2L, as SHH inhibits branching morphogenesis. 1000-4000 parameter sets have been screened for the different models, with P=0.1, D=100, γ=0.01.

case of the physiological model, in which ligands and receptors are expressed in different tissue layers. We note that the presence of subdomains in itself does not lead to a substantial change in the size of the Turing space (supplementary material Fig. S6) (Fujita and Kawaguchi, 2013). Owing to computational limitations when solving the models on the embryonic 3D domains, we could not explore the combined Turing space of the FGF10/SHH network, and we had to restrict our study to the effects of negative feedbacks within the FGF10 or SHH module that arise because of the SHH-FGF10 regulatory interaction. Accordingly, we studied one set of models with the receptor expressed in the epithelium, as characteristic for FGF10 (Fig. 4A,B; supplementary material Table S1, cases T1, TF1), and one set of models with the receptor expressed in the mesenchyme, as characteristic for SHH (Fig. 4C-F; supplementary material Table S1, cases T2, TF2-4).

In the first case (FGF10), the ligand-receptor complex triggers branch outgrowth, whereas in the second case (SHH) the complex prevents outgrowth. Since we only consider a single Turing system, we could implement a negative feedback only in the layer that expresses the receptor, and we therefore cannot include a negative feedback on the ligand production rate when the receptor is expressed in the epithelium. When the receptor is expressed in the mesenchyme, such negative feedback can be included though, because we approximate the thin epithelium by an infinitely thin layer (Menshykau and Iber, 2012). In both cases, we confirm the increase in the size of Turing space in the presence of additional negative feedbacks. Thus, the additional negative feedback on the receptor expression rate, a, results in an approximately 10-fold larger maximal receptor expression rate [compare the size of the inferred Turing space along the log(a)-axis in B and D with those in A and C, respectively, in Fig. 4]; the minimal receptor expression rate is zero. Similarly, the negative feedback on the ligand expression rate permits Turing patterns to emerge for a 10-fold larger range of the ligand expression rate, b [compare the size of the inferred Turing space along the log(b)-axis in C and E in Fig. 4]. A negative feedback on both the ligand and receptor expression rates results in a Turing space that is enlarged in the direction of both the ligand and receptor expression rates (compare the size of the inferred Turing space in C and F in Fig. 4). Based on our previous results (Kurics et al., 2014), we expect that substantially larger Turing spaces could still be obtained by coupling the FGF10 and SHH regulatory modules. Importantly, the Turing space not only widens, as observed previously (Kurics et al., 2014), but the physiological growth field can now be reproduced over a wider parameter range (i.e. the size of the red/yellow areas increases when negative feedbacks are introduced, Fig. 4). The quality of the fit changes more or less continuously as the parameter values are varied such that mutation and selection processes could have gradually improved the pattern by evolving the system into an optimal part of the parameter space from a first patterning solution.

Development (2014) 141, 4526-4536 doi:10.1242/dev.116202

Alternative mechanisms for the control of branching morphogenesis

A number of alternative mechanisms have been proposed, as recently reviewed (Iber and Menshykau, 2013) (supplementary material Table S1, cases A1-A5). One of the earliest proposed mechanisms suggested that the distance between the *Fgf10*-expressing distal mesenchyme and the *Shh*-expressing epithelium would induce a pattern that could control branch point selection, because the repressive effect of SHH on *Fgf10* expression would be stronger at a shorter distance (Bellusci et al., 1997b; Hirashima and Iwasa, 2009). More recently, the tissue-specific expression of ligands in either mesenchyme or epithelium has been shown to result in patterns, and this has been suggested to control the selection of branch points (Gleghorn et al., 2012; Nelson et al., 2006). In the following, we will test both mechanisms with the embryonic dataset. In both cases, we can represent the models by a single non-dimensional equation for the ligand concentration L:

$$\frac{\partial L}{\partial t} = D\Delta L - L + b \text{ with } b = 1 \text{ in } \Omega_L \text{ and } b = 0 \text{ in } \Omega_0, \quad (3)$$

where the ligand production rate b is non-zero only in part of the domain, Ω_L. When testing the suitability of the models, we varied the single parameter value, i.e. the non-dimensional diffusion coefficient D, over four orders of magnitude; the parameter range was adjusted such that at the low end the diffusion length scale is much smaller than the domain, whereas at the high end it is much larger.

Distance-based mechanisms

To test the distance-based mechanism we need to restrict the expression of the ligand L to the outer boundary of the mesenchyme (by setting b in Eq. 3 accordingly; supplementary material Table S1, case A1). The ligand can, in principle, either trigger or inhibit branch outgrowth. If the ligand L triggers lung bud outgrowth the highest ligand concentration should coincide with the strongest displacement. For this case we obtain a deviation of $\Delta \geq 0.81$ between the signaling model and the embryonic growth field as we screen the physiological range of D; visual inspection reveals a bad fit (Fig. 5A, lower panel). In particular, we always just observed two signaling spots in the simulations, whereas in the embryonic data there are three areas of outgrowth. If L were to act as an inhibitor, then we need to evaluate the match of $1/L$ and the displacement field, and this match is even worse (Fig. 5B, $\Delta \geq 0.9$). It has been proposed that lung buds might respond to the local gradient rather than to the local concentration (Clément et al., 2012a). A gradient-based readout mechanism (supplementary material Table S1, case A2) does not improve the best match between model and embryonic growth field if the ligand is activating (Fig. 5C) and worsens the match when the ligand is inhibiting (Fig. 5D) lung bud outgrowth. We note that, in the case of a gradient-based readout, the quality of the match is independent of the parameter value (Fig. 5C,D). Based on the available data we can therefore rule out this mechanism.

Pattern emergence because of tissue-specific expression domains

We next tested the potential of tissue-specific protein expression to generate ligand patterns that would match the embryonic growth field. To this end we solved the model given by Eq. 3 with ligand production in the epithelium (b=1), but not in the mesenchyme (b=0) (supplementary material Table S1, case A3); ligand could diffuse everywhere. If the ligand L triggered lung bud outgrowth, the highest ligand concentration should coincide with the strongest displacement. However, we did not obtain a good match ($\Delta \geq 0.9$) between signaling model and embryonic growth field as we screened the physiological range of D. Visual inspection of the best fit confirmed the bad match in that the strength of the growth field (colored arrows) and the intensity of the signaling field (solid colors) do not coincide (Fig. 5E, lower panel). If we assume that the ligand L acts as an inhibitor of growth and we evaluate the match of $1/L$ and the displacement field we get a slightly better match (Fig. 5F), but the deviation is still very high ($\Delta \geq 0.86$) and visual inspection confirms a bad fit (Fig. 5F, lower panel). Including a positive feedback (Fig. 5G; supplementary material Table S1, case A4) or a negative feedback (Fig. 5H; supplementary material Table S1, case A5) of L on its own production does not improve the fit, even though we have a further parameter.

Tissue-specific protein expression is also incorporated in the previously analyzed ligand-receptor-based Turing mechanisms (Eqs 1 and 2). Outside the Turing space, the two models are thus very similar, except that in the Turing model a receptor is included. The deviations in the two models are indeed very similar outside the inferred Turing space, i.e. $\Delta \geq 0.9$ with receptor (Eqs 1 and 2) and $\Delta \geq 0.9$ without receptor (Eq. 3) if the ligand acts as activator, and $\Delta \geq 0.85$ with receptor and $\Delta \geq 0.86$ without receptor if the ligand acts as inhibitor, even though four parameter values rather than one parameter value were optimized in the Turing model. The higher number of parameters thus does not improve the fit.

Similarly, when we analyzed the alternative models with the 2D time-lapse data, we found that the global deviation Δ_γ for the alternative mechanisms (Fig. 5A′-F′) is always higher than that for the ligand-receptor-based Turing-type mechanisms (Fig. 3A,C).

Branch outgrowth

The comparison of the predicted signaling domains and the embryonic growth fields supports a ligand-receptor-based Turing model (Eqs 1 and 2) to define the points of bud outgrowth. We next considered whether any of the proposed mechanisms would also support the outgrowth of a bud. We simulated a single tissue layer that is embedded in a 3D environment and that grows at the sites of strongest signaling in the direction perpendicular to its surface (for details see Materials and Methods). We started with the patterning mechanism that is based on the tissue-specific expression of ligand. As a result of the tissue-specific expression, the diffusible ligand will be lost at the edges and the highest concentration will therefore accumulate in the center of the domain (supplementary material Text 2 and Fig. S7A-C). A positive feedback can further enhance, whereas a negative feedback diminishes, this effect (supplementary material Fig. S7D,E). If this factor drives outgrowth of the domain, then a bud will emerge. More ligand is lost as the curvature of a domain increases (supplementary material Fig. S7F). As the length of the stalk increases, relatively more ligand will be lost at the curved tip, and the highest ligand concentration will therefore be found at the sides, resulting in a split localization of the diffusible ligand (supplementary material Fig. S7G,H). We tested a range of different growth functions to see whether the bifurcating ligand profile would support bifurcating outgrowth. However, none of these led to bifurcating outgrowth (Fig. 6A). The likely reason is that, as the curvature increases, more ligand is lost by diffusion (supplementary material Fig. S7F). As the bud would start to bifurcate, the curvature would increase locally and the concentration would diminish. As a result, outgrowth would come to an immediate halt. Furthermore, as shown in supplementary material Fig. S7B,G,H and Fig. 6A, the ligand distribution on a surface embedded into a 3D domain has rotational symmetry. Thus, tissue-specific ligand expression does not provide a mechanism to break radial symmetry, which is

Development (2014) 141, 4526-4536 doi:10.1242/dev.116202

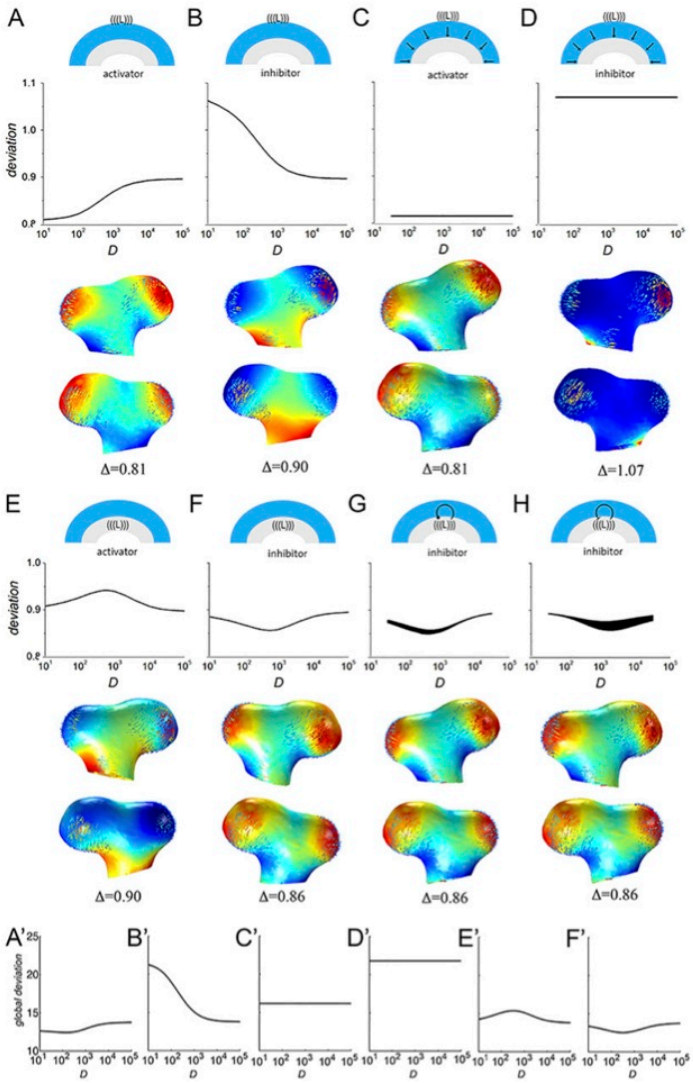

Fig. 5. Comparison of measured lung displacement fields with those predicted by alternative mechanisms. Deviation, Δ (Eq. 4), of the spatial distribution of ligand-receptor-based signaling S_n for different signaling models from the growth field obtained from the embryonic measurements between S1 and S2 (Fig. 1A,H). The results of different models are shown (supplementary material Table S1, cases A1-A5). (A) Ligand is expressed under the mesothelium and activates bud outgrowth. (B) Ligand is expressed under the mesothelium and inhibits bud outgrowth. (C,D) Ligand is expressed under the mesothelium and is rapidly consumed in the tissue. The spatial gradient of the ligand concentration at the epithelium is used as a readout for signaling. (E) Ligand is expressed in the epithelium and stimulates lung bud outgrowth. (F) Ligand is expressed in the epithelium and inhibits bud outgrowth. (G) Ligand is expressed in the epithelium, activates its own production and inhibits bud outgrowth. (H) Ligand is expressed in the epithelium, inhibits its own production and inhibits bud outgrowth. The lower panels show the best matches of computed areas of signaling (solid) and the embryonic displacement fields (vector field) for two different orientations of the lung buds. Red, high; blue, low. (A′-F′) Results for the analysis of the 2D time-lapse data with the alternative models as described in A-F.

necessary for branching to occur. We conclude that tissue-specific ligand expression alone cannot drive the branching of a domain.

We next explored whether the Turing-type signaling mechanisms would support bifurcating outgrowth of the domain. To that end, we solved the ligand-receptor-based Turing model (Eqs 1 and 2) on a domain in the shape of a thin 2D disk, which was allowed to deform and grow within a 3D domain (see Materials and Methods for details). The Turing mechanism can indeed control the branching of a domain, and yields both bifurcating (Fig. 6B) and trifurcating (Fig. 6C) branch points. Bifurcating outgrowth can be observed on a closed domain (where ligand cannot diffuse away from the ligand-producing tissue layer), but the patterning mechanism is robust only on an open domain (where the ligand can diffuse away). On a closed domain, different patterns can emerge with the same parameter set depending on the noisy initial conditions, and only some of these patterns will support bud formation (Fig. 6D). The reason for the robust patterning on the open domain is the impact of the geometry, which concentrates the ligand in the center of the domain initially and thus strongly biases the Turing mechanism to this particular pattern.

We tested this observation on the embryonic lung geometry. When we remove the mesenchyme and express ligand and receptor both in the epithelium, the solution depends on the initial conditions, and for the same parameter values a wide range of different patterns is observed (Fig. 6E; supplementary material Table S1, case T4). The presence of the mesenchyme is thus important to stabilize the pattern. Interestingly, when lung epithelium is cultured in the absence of mesenchyme, random budding is indeed observed (Ohtsuka et al., 2001), whereas normal branching patterns are observed when both lung epithelium and mesenchyme are maintained in culture (Carraro et al., 2010). The Matrigel that surrounds the epithelium in the mesenchyme-free culture (Ohtsuka et al., 2001) is unlikely to stabilize the budding process because of the higher diffusion constant (Ciocan and Ciocan, 2009), which our analysis shows to reduce the geometry effect (supplementary material Fig. S7C).

Development (2014) 141, 4526-4536 doi:10.1242/dev.116202

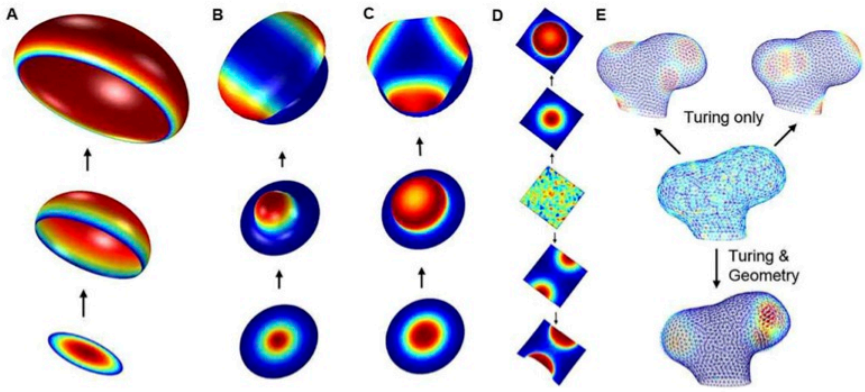

Fig. 6. Branch outgrowth. (A) Gradients based only on tissue-restricted ligand expression fail to support deforming outgrowth of branches. (B,C) Signaling-based Turing mechanisms permit (B) bifurcating and (C) trifurcating outgrowth. (D) On closed domains noisy initial conditions can result in various patterns. (E) Ligand-receptor-based Turing mechanisms result in a wide range of different patterns for the same parameter set if solved only on the lung epithelium (top). Inclusion of the lung mesenchyme together with tissue-specific expression of ligand and receptor gives rise to a diffusion-based geometry effect that biases the Turing mechanism to a single pattern (bottom) in spite of noisy initial conditions (middle).

DISCUSSION

It is a long-standing question how branching is controlled during development. Given the remarkably stereotyped nature of branching in the developing lung of wild-type littermates (Metzger et al., 2008), the branching mechanism must yield robust patterning in the same genetic background while allowing for differences in animals from a different genetic background without resulting in the failure of the entire branching program. Moreover, given the differences in the branching programs of different organs, such mechanism should be sufficiently flexible to permit organ-specific differences in branching programs. Finally, given the differences in the signaling networks that control branching in the different organs (Iber and Menshykau, 2013), it must be possible to implement such branching mechanisms with different signaling proteins and networks.

We have shown here that (unlike other proposed mechanisms) a ligand-receptor-based Turing mechanism in combination with tissue-restricted gene expression allows us to predict the growth fields of developing lungs buds. FGF10 or SHH or the combined FGF10/SHH network can each constitute the core Turing patterning mechanism in the developing lung. Given that the negative feedback between these two Turing systems greatly increases the parameter range for which Turing patterns are observed (the Turing space), as well as the range for which we can reproduce the embryonic growth pattern, it is, however, likely that the core mechanism is based on both signaling proteins, FGF10 and SHH. We note that the restriction of receptors to single cells as well as cooperative binding also increase the size of the Turing space (Kurics et al., 2014). The expression of ligand and receptors in different tissue layers is important to obtain the geometry effect that ensures robust pattern formation in spite of molecular noise. We therefore propose that the combination of geometry and signaling enables robust pattern selection and morphogenesis.

We note that a Turing mechanism alone can control the different branching modes (domain branching, planar and orthogonal bifurcations, trifurcations) and sequences (Iber and Menshykau, 2013), such that no 'hierarchical and modular program that combines a small number of basic operations', as previously conjectured by Krasnow and colleagues (Metzger et al., 2008), would be required. Given that many ligand-receptor pairs can give rise to a Turing system (Kurics et al., 2014), we propose that ligand-receptor-based Turing mechanisms together with tissue-restricted gene expression constitute a general mechanism to robustly control stereotyped branching as well as other patterning processes during morphogenesis (Badugu et al., 2012).

MATERIALS AND METHODS

Mouse strains and ethics statement

Shh-GFP-Cre (Harfe et al., 2004) was used to conditionally activate EGFP expression [β-actin-EGFP (Jagle et al., 2007)] in the lung epithelium. The mouse experiments were approved by the legally required regional commission in strict accordance with Swiss law. All studies were classified as grade zero implying minimal suffering of animals.

Two-dimensional time-lapse imaging

To follow lung branching morphogenesis in culture, E11.5 mouse embryonic lung rudiments were dissected and imaged as previously described; the culture media was additionally supplemented with bovine fetal serum (Carraro et al., 2010). Lung buds were imaged every 60 min using a Nikon Ti-E epifluorescence inverted microscope with a 4× lens.

Analysis of 2D lung movie data

We segmented the lung epithelium (GFP) and the mesenchyme (wide field) of the left lobe of the embryonic lung using standard MATLAB functions (see supplementary material Text 1.3 for details). The displacement fields between consecutive movie frames (separated by 2 h) were calculated as the set of vectors that are normal to the epithelium boundary in the current movie frame and that intersect the boundary in the next movie frame (Schwaninger et al., 2014). The growth fields were obtained by setting all vectors pointing inward (shrinkage) to zero.

Numerical computations

The partial differential equations (PDEs) were solved on the imported 2D geometries and 3D computational meshes using COMSOL Multiphysics 4.3× as previously described (Menshykau and Iber, 2012; Vollmer et al., 2013). Several independent studies confirm that COMSOL provides accurate solutions to reaction-diffusion equations both on constant (Cutress et al., 2010; Kurics et al., 2014) and growing (Carin, 2006; Thummler and Weddemann, 2007; Weddemann and Thummler, 2008) domains.

Deviation of predicted signaling patterns and measured displacement fields

The PDE models were solved for a wide range of parameter values. To evaluate the quality of the model predictions the L^2 distance (Euclidean

distance), Δ, between the computed signaling field and the registered displacement fields (areas of growth) was calculated using the formula:

$$\Delta = \sqrt{\sum_{EM} \left(|\vec{v}_n| - S_n\right)^2}. \quad (4)$$

Here, EM refers to all mesh points in the interface between epithelium and mesenchyme. $\vec{v}_n$ refers to all outward-pointing, normalized vectors of the measured lung displacement field. $|\vec{v}_n|$ denotes the length of the vector. The displacement field vectors were normalized by the average vector length, such that the average length of all vectors $\vec{v}_n$ is 1. S_n refers to the normalized computational signal; the signal was normalized by the average signal, such that the average of S_n is 1. In the case of an activating signal:

$$S_n = \frac{R^2L}{\overline{R^2L}}, \quad (5)$$

while in case of an inhibiting signal:

$$S_n = \frac{\frac{1}{R^2L}}{\overline{\frac{1}{R^2L}}}. \quad (6)$$

Here, the bar indicates the average value in the domain.

Typically, 1000-10,000 parameter sets were first randomly sampled from a log-uniform distribution in the ranges: $\log_{10}(a)$: [−1 … 1], $\log_{10}(b)$: [−1 … 2], $\log_{10}(\gamma)$: [−4 … −1], $\log_{10}(D)$: [1 … 3], or similar. For the cases depicted in Fig. 3, between 10^3 to 10^4 parameter values were sampled. Sampled parameter sets with a minimal value of Δ were used as a starting point for the local minimization with the gradient-free coordinate search algorithm (Conn et al., 2009) as implemented in COMSOL Multiphysics 4.3a (Menshykau et al., 2013). We run this algorithm on the best 10-20 parameter sets obtained with random sampling. In all cases the coordinate search algorithm minimized Δ only by 0.02 or less, except for the case depicted in Fig. 3A, where Δ was reduced from 0.70 to 0.62.

Deforming outgrowth of branches

We solved the PDE models on a deforming domain, where the deformation was normal to the surface and proportional to the local concentration, such that the velocity field was given by $\vec{v} = \vec{n} v_g c^m$. Here, $\vec{v}_n$ is the normal surface vector, v_g is the growth speed, and m accounts for any possible non-linear dependence on the signal concentration, c. In the case of geometry-based mechanisms c refers to the ligand concentration L, whereas in the case of the Turing mechanism c refers to the concentration of the receptor-ligand complex R^2L. To incorporate noisy initial conditions we set the initial conditions to L=1+ξ(x,y,z,θ), where ξ(x,y,z,θ) is a normally distributed random function with a mean value of zero and half width θ.

Acknowledgements

We thank Rolf Zeller for access to lab space, mouse strains, consumables and support; Erica Montani and Thomas Horn for assistance with live imaging; Xin Sun for discussion; and Markus Affolter for critical reading of the manuscript.

Competing interests

The authors declare no competing financial interests.

Author contributions

D.I. and D.M. conceived the study; D.M. carried out all computational analysis as well as 2D lung culturing and imaging; P.B. and V.S. provided the 3D embryonic data; E.U. performed all mouse work related to lung culturing. All authors approved the final version of the manuscript.

Funding

The authors acknowledge funding from a SystemsX and Sinergia SNF grant and an ETH Fellowship to D.M.

Supplementary material

Supplementary material available online at
http://dev.biologists.org/lookup/suppl/doi:10.1242/dev.116202/-/DC1

References

Abler, L. L., Mansour, S. L. and Sun, X. (2009). Conditional gene inactivation reveals roles for Fgf10 and Fgfr2 in establishing a normal pattern of epithelial branching in the mouse lung. *Dev. Dyn.* **238**, 1999-2013.

Badugu, A., Kraemer, C., Germann, P., Menshykau, D. and Iber, D. (2012). Digit patterning during limb development as a result of the BMP-receptor interaction. *Sci. Rep.* **2**, 991.

Bellusci, S., Furuta, Y., Rush, M. G., Henderson, R., Winnier, G. and Hogan, B. L. (1997a). Involvement of Sonic hedgehog (Shh) in mouse embryonic lung growth and morphogenesis. *Development* **124**, 53-63.

Bellusci, S., Grindley, J., Emoto, H., Itoh, N. and Hogan, B. L. (1997b). Fibroblast growth factor 10 (FGF10) and branching morphogenesis in the embryonic mouse lung. *Development* **124**, 4867-4878.

Blanc, P., Coste, K., Pouchin, P., Azaïs, J.-M., Blanchon, L., Gallot, D. and Sapin, V. (2012). A role for mesenchyme dynamics in mouse lung branching morphogenesis. *PLoS ONE* **7**, e41643.

Bookstein, F. L. (1989). Principal warps: thin-plate splines and the decomposition of deformations. *Pattern Anal. Mach. Intell.* **11**, 567-585.

Carin, M. (2006). Numerical Simulation of moving boundary problems with the ALE method: validation in the case of a free surface and a moving solidification front. In *Proceedings of COMSOL Conference 2006*. Paris.

Carraro, G., del Moral, P.-M. and Warburton, D. (2010). Mouse embryonic lung culture, a system to evaluate the molecular mechanisms of branching. *J. Vis. Exp.* **40**, ii: 2035.

Celliere, G., Menshykau, D. and Iber, D. (2012). Simulations demonstrate a simple network to be sufficient to control branch point selection, smooth muscle and vasculature formation during lung branching morphogenesis. *Biol. Open* **1**, 775-788.

Chiang, C., Litingtung, Y., Lee, E., Young, K. E., Corden, J. L., Westphal, H. and Beachy, P. A. (1996). Cyclopia and defective axial patterning in mice lacking Sonic hedgehog gene function. *Nature* **383**, 407-413.

Ciocan, E. and Ciocan, R. (2009). Optimized numerical pharmacokinetics model for optical molecular probes based on diffusion coefficients in matrigel measured using fluorescence imaging. In *Conf. Proc. IEEE Eng. Med. Biol. Soc. 2009*, 4925-4928.

Clément, R., Blanc, P., Mauroy, B., Sapin, V. and Douady, S. (2012a). Shape self-regulation in early lung morphogenesis. *PLoS ONE* **7**, e36925.

Clément, R., Douady, S. and Mauroy, B. (2012b). Branching geometry induced by lung self-regulated growth. *Phys. Biol.* **9**, 066006.

Conn, A. R., Scheinberg, K. and Vicente, L. N. (2009). *Introduction to Derivative-Free Optimization*. Philadelphia: Society for Industrial and Applied Mathematics.

Cutress, I. J., Dickinson, E. J. F. and Compton, R. G. (2010). Analysis of commercial general engineering finite element software in electrochemical simulations. *J. Electroanal. Chem.* **638**, 76-83.

Fried, P. and Iber, D. (2014). Dynamic scaling of morphogen gradients on growing domains. *Nat. Commun.* **5**, 5077.

Fujita, H. and Kawaguchi, M. (2013). Pattern formation by two-layer Turing system with complementary synthesis. *J. Theor. Biol.* **322**, 33-45.

Gierer, A. and Meinhardt, H. (1972). A theory of biological pattern formation. *Kybernetik* **12**, 30-39.

Gjorevski, N. and Nelson, C. M. (2010). Endogenous patterns of mechanical stress are required for branching morphogenesis. *Integr. Biol.* **2**, 424-434.

Gjorevski, N. and Nelson, C. M. (2012). Mapping of mechanical strains and stresses around quiescent engineered three-dimensional epithelial tissues. *Biophys. J.* **103**, 152-162.

Gleghorn, J. P., Kwak, J., Pavlovich, A. L. and Nelson, C. M. (2012). Inhibitory morphogens and monopodial branching of the embryonic chicken lung. *Dev. Dyn.* 241, 852-862.

Guo, Y., Chen, T.-H., Zeng, X., Warburton, D., Bostrom, K. I., Ho, C.-M., Zhao, X. and Garfinkel, A. (2014a). Branching patterns emerge in a mathematical model of the dynamics of lung development. *J. Physiol.* **592**, 313-324.

Guo, Y., Sun, M., Garfinkel, A. and Zhao, X. (2014b). Mechanisms of side branching and tip splitting in a model of branching morphogenesis. *PLoS ONE* **9**, e102718.

Harfe, B. D., Scherz, P. J., Nissim, S., Tian, H., McMahon, A. P. and Tabin, C. J. (2004). Evidence for an expansion-based temporal Shh gradient in specifying vertebrate digit identities. *Cell* **118**, 517-528.

Hirashima, T. and Iwasa, Y. (2009). Mechanisms for split localization of Fgf10 expression in early lung development. *Dev. Dyn.* 238, 2813-2822.

Iber, D. and Menshykau, D. (2013). The control of branching morphogenesis. *Open Biol.* **3**, 130088.

Iber, D., Tanaka, S., Fried, P., Germann, P. and Menshykau, D. (2015). Simulating tissue morphogenesis and signaling. *Methods Mol. Biol.* **1189**, 323-338.

Jagle, U., Gasser, J. A., Müller, M. and Kinzel, B. (2007). Conditional transgene expression mediated by the mouse beta-actin locus. *Genesis* **45**, 659-666.

Kadzik, R. S., Cohen, E. D., Morley, M. P., Stewart, K. M., Lu, M. M. and Morrisey, E. E. (2014). Wnt ligand/Frizzled 2 receptor signaling regulates tube shape and branch-point formation in the lung through control of epithelial cell shape. *Proc. Natl. Acad. Sci. USA* **111**, 12444-12449.

Kim, H. Y., Varner, V. D. and Nelson, C. M. (2013). Apical constriction initiates new bud formation during monopodial branching of the embryonic chicken lung. *Development* **140**, 3146-3155.
Kurics, T., Menshykau, D. and Iber, D. (2014). Feedbacks, receptor clustering, and receptor restriction to single cells yield large Turing spaces for ligand-receptor based Turing models. *Phys. Rev. E Stat. Nonlin. Soft Matter Phys.* **90**, 022716.
Lopez-Rios, J., Duchesne, A., Speziale, D., Andrey, G., Peterson, K. A., Germann, P., Unal, E., Liu, J., Floriot, S., Barbey, S. et al. (2014). Attenuated sensing of SHH by Ptch1 underlies evolution of bovine limbs. *Nature* **511**, 46-51.
Lubkin, S. R. (2008). Branched organs: mechanics of morphogenesis by multiple mechanisms. *Curr. Top. Dev. Biol.* **81**, 249-268.
Menshykau, D. and Iber, D. (2012). Simulating organogenesis with COMSOL: interacting and deforming domains. In *Proceedings of COMSOL Conference 2012*. Milan.
Menshykau, D. and Iber, D. (2013). Kidney branching morphogenesis under the control of a ligand-receptor-based Turing mechanism. *Phys. Biol.* **10**, 046003.
Menshykau, D., Kraemer, C. and Iber, D. (2012). Branch mode selection during early lung development. *PLoS Comput. Biol.* **8**, e1002377.
Menshykau, D., Shrivastsan, A., Germann, P., Lemereux, L. and Iber, D. (2013). Simulating organogenesis in COMSOL: parameter optimization for PDE-based models. In *Proceedings of COMSOL Conference 2013*. Rotterdam.
Metzger, R. J., Klein, O. D., Martin, G. R. and Krasnow, M. A. (2008). The branching programme of mouse lung development. *Nature* **453**, 745-750.
Müller, P., Rogers, K. W., Yu, S. R., Brand, M. and Schier, A. F. (2013). Morphogen transport. *Development* **140**, 1621-1638.
Nahmad, M. and Stathopoulos, A. (2009). Dynamic interpretation of hedgehog signaling in the Drosophila wing disc. *PLoS Biol.* **7**, e1000202.
Nelson, C. M. and Gleghorn, J. P. (2012). Sculpting organs: mechanical regulation of tissue development. *Annu. Rev. Biomed. Eng.* **14**, 129-154.
Nelson, C. M., VanDuijn, M. M., Inman, J. L., Fletcher, D. A. and Bissell, M. J. (2006). Tissue geometry determines sites of mammary branching morphogenesis in organotypic cultures. *Science* **314**, 298-300.
Nogawa, H. and Ito, T. (1995). Branching morphogenesis of embryonic mouse lung epithelium in mesenchyme-free culture. *Development* **121**, 1015-1022.
Ohtsuka, N., Urase, K., Momoi, T. and Nogawa, H. (2001). Induction of bud formation of embryonic mouse tracheal epithelium by fibroblast growth factor plus transferrin in mesenchyme-free culture. *Dev. Dyn.* **222**, 263-272.
Pepicelli, C. V., Lewis, P. M. and McMahon, A. P. (1998). Sonic hedgehog regulates branching morphogenesis in the mammalian lung. *Curr. Biol.* **8**, 1083-1086.
Peters, K., Werner, S., Liao, X., Wert, S., Whitsett, J. and Williams, L. (1994). Targeted expression of a dominant negative FGF receptor blocks branching morphogenesis and epithelial differentiation of the mouse lung. *EMBO J.* **13**, 3296-3301.
Prigogine, I. (1967). On symmetry-breaking instabilities in dissipative systems. *J. Chem. Phys.* **46**, 3542-3550.
Prigogine, I. and Lefever, R. (1968). Scitation: symmetry breaking instabilities in dissipative systems. II. *J. Chem. Phys.* **48**, 1965.
Schnakenberg, J. (1979). Simple chemical reaction systems with limit cycle behaviour. *J. Theor. Biol.* **81**, 389-400.
Short, K., Hodson, M. and Smyth, I. (2012). Spatial mapping and quantification of developmental branching morphogenesis. *Development* **140**, 471-478.
Schwaninger, C. A., Menshykau, D. and Iber, D. (2014). Simulating organogenesis: algorithms for the image-based determination of growth fields. *ACM Transactions on Modeling and Computer Simulation (TOMACS)* (in press).
Tanaka, S. and Iber, D. (2013). Inter-dependent tissue growth and Turing patterning in a model for long bone development. *Phys. Biol.* **10**, 056009.
Thummler, V. and Weddemann, A. (2007). Computation of space-time patterns via ALE methods. In *Proceedings of COMSOL Conference 2007*. Grenoble.
Turing, A. M. (1952). The chemical basis of morphogenesis. *Phil. Trans. R. Soc. Lond. B* **237**, 37-72.
Unbekandt, M., del Moral, P.-M., Sala, F. G., Bellusci, S., Warburton, D. and Fleury, V. (2008). Tracheal occlusion increases the rate of epithelial branching of embryonic mouse lung via the FGF10-FGFR2b-Sprouty2 pathway. *Mech. Dev.* **125**, 314-324.
Varner, V. D. and Nelson, C. M. (2014). Cellular and physical mechanisms of branching morphogenesis. *Development* **141**, 2750-2759.
Volckaert, T., Campbell, A., Dill, E., Li, C., Minoo, P. and De Langhe, S. (2013). Localized Fgf10 expression is not required for lung branching morphogenesis but prevents differentiation of epithelial progenitors. *Development* **140**, 3731-3742.
Vollmer, J., Menshykau, D. and Iber, D. (2013). Simulating organogenesis in COMSOL: cell-based signaling models. In *Proceedings of COMSOL Conference 2013*. Rotterdam.
Weaver, M., Dunn, N. R. and Hogan, B. L. (2000). Bmp4 and Fgf10 play opposing roles during lung bud morphogenesis. *Development* **127**, 2695-2704.
Weddemann, A. and Thummler, V. (2008). Stability analysis of ALE-methods for advection-diffusion problems. In *Proceedings of COMSOL Conference 2008*. Hannover.
Weibel, E. (1991). Fractal geometry: a design principle for living organisms. *Am. J. Physiol.* **261**, L361-L369.
Zhou, S., Lo, W.-C., Suhalim, J. L., Digman, M. A., Gratton, E., Nie, Q. and Lander, A. D. (2012). Free extracellular diffusion creates the Dpp morphogen gradient of the Drosophila wing disc. *Curr. Biol.* **22**, 668-675.

Publication 4: Simulating Organogenesis in COMSOL: Image-based modeling

I was involved in concept development and limb bud geometry production for this project.

Simulating Organogenesis in COMSOL: Image-based Modeling

Z. Karimaddini[1,2], E. Unal[1,2,3], D. Menshykau[1,2] and D. Iber*[1,2]
[1]Departement for Biosystems Science and Engineering, ETH Zurich, Switzerland
[2]Swiss Institute of Bioinformatics (SIB), Switzerland
[3]Developmental Genetics, Department Biomedicine, University of Basel, Switzerland
*Corresponding author: Mattenstrasse 26, CH-4058 Basel, dagmar.iber@bsse.ethz.ch

Abstract: Mathematical Modelling has a long history in developmental biology. Advances in experimental techniques and computational algorithms now permit the development of increasingly more realistic models of organogenesis. In particular, 3D geometries of developing organs have recently become available. In this paper, we show how to use image-based data for simulations of organogenesis in COMSOL Multiphysics. As an example, we use limb bud development, a classical model system in mouse developmental biology. We discuss how embryonic geometries with several subdomains can be read into COMSOL using the Matlab LiveLink, and how these can be used to simulate models on growing embryonic domains. The ALE method is used to solve signaling models even on strongly deforming domains.

Keywords: *in silico* organogenesis, image-based modeling, limb development, computational biology, numerical simulation, COMSOL

1. Introduction Organogenesis is a highly dynamic process that is tightly regulated during embryogenesis. Many of the individual regulatory components, e.g. signaling molecules and their receptors, as well as their regulatory interactions have been identified in experiments. However, an integrative mechanistic understanding of the regulatory network is missing **[1]**. Mathematical modeling has a long history in developmental biology **[2,3]**. Limb development, in particular, has attracted much attention from modellers **[4]**. Early models were rather simplistic, and to this date most models are still solved on idealized domains that at most qualitatively resemble the physiological domains. However, the geometry can greatly impact the patterning process **[5]**, and it is therefore important to solve these models on physiological domains.

COMSOL Multiphysics is a versatile package that provides finite element method (FEM)-based solvers to solve a wide range of partial differential equation (PDE)-based problems on complex domains. We have used COMSOL to solve models of limb development **[5,6]**, bone development **[7]**, ovarian follicle development **[8]**, and branching morphogenesis **[9,10,11]**. In a series of papers on simulating organogenesis in COMSOL **[12,13,14,15]**, we have discussed methods to efficiently solve models for organogenesis on complex static and growing domains as well as models, which consider cells explicitly. Initially, these models were formulated on idealized geometries. Recently, we have started to take advantage of advancements in imaging techniques, which now provide us with detailed imaging data of organogenesis **[15]**. This now allows us to simulate our models on realistically growing embryonic domains in COMSOL Multiphysics **[16]**.

In this paper, we show how to use image-based data for simulations of organogenesis in COMSOL Multiphysics. As an example, we use limb bud development, a classical model system in mouse developmental biology. In the first step, computer readable geometries must be extracted from the 3D images and must then be imported into COMSOL. Many tissues contain clearly defined subdomains with different properties. These can be identified with suitable staining protocols for marker proteins or marker protein expression. We show how complex domains with subdomains can be imported. In a second step, the displacement fields between two consecutive image frames must be calculated and imported into COMSOL. Finally, the imported displacement fields can be used to simulate the domain shape evolution in COMSOL. Given the large number of stages that we use, we implement our models using Matlab LiveLink. We use the ALE method to solve our PDE-based

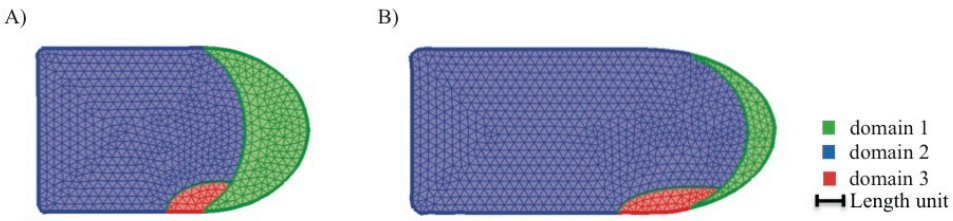

Figure 1. An idealized 2D limb bud domain at two different time points. The entire domain is divided into three subdomains ($domain_1$ – green, $domain_2$ - blue, $domain_3$ - red). The domains and subdomains deform during development. (**A**) Domain at time t, and (**B**) at $t+1$.

signaling models even on strongly deforming domains. The simulation results can be compared to experimental data, and parameter values can be optimized to obtain an optimal match of model predictions and experimental results [14]. We conclude that the image-based modeling approach allows us to build realistic models of highly dynamic developmental processes, and allows us to study the combined impacts of patterning and growth.

2. Method

2.1 Model Formulation

Our models are defined as a set of n reaction-diffusion equations in the form of:

$$\frac{\partial C_i}{\partial t} + \underbrace{u\nabla C_i}_{advection} + \underbrace{C_i \nabla u}_{dilution} = \underbrace{D_i \Delta C_i}_{diffusion} + \underbrace{R_i(C_1,\ldots,C_n)}_{reaction}$$

where C_i denotes the concentration of component i (n total components), D_i its diffusion constant, and Δ refers to the Laplace operator such that $D_i \Delta C_i$ describes the diffusion flux of C_i. In case of growing domains, advection and dilution terms have to be added to the reaction-diffusion equations; u represents the velocity field of the domain, for more details refer to [15]. The reaction term, $R_i(C_1,\ldots,C_n)$, is very often non-linear and describes all reactions of component i, i.e. its production, degradation, and complex formation. For more details refer to [12]. The presence of species can be restricted to parts of the domain, and in that case also some reactions can become spatially restricted.

2.2 Regulatory Network

To illustrate our approach, we consider a concrete example. Consider a domain with 3 subdomains as shown in Figure 1, and a regulatory network that involves three components, A, B and C (Figure 2). All components are assumed to diffuse in the entire domains and to be degraded everywhere. Moreover, we assume that the components A and C are produced only in $domain_1$ and $domain_3$, respectively, whereas component B is produced in all domains. We formulate the sub domains using the unit function,

$$\mathrm{I}_j = \begin{cases} 1 & if\,(x,y) \in domain_j \\ 0 & otherwise. \end{cases}$$

The spatio-temporal dynamics of the aforesaid network can be described by the following reaction terms:

$$R_A(A,B,C) = \rho_A \frac{K_{BA}^2}{K_{BA}^2 + B^2} \mathrm{I}_{domain_1} - d_A A$$

$$R_B(A,B,C) = \rho_B \left(\frac{A^2}{K_{AB}^2 + A^2} \frac{K_{CB}^2}{K_{CB}^2 + C^2}\right) - d_B B$$

$$R_C(A,B,C) = \rho_C \frac{A^2}{K_{AC}^2 + A^2} \mathrm{I}_{domain_3} - d_C C,$$

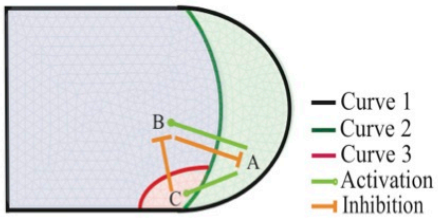

Figure 2. Regulatory Network. The network consists of three components, A, B and C. These components are produced and regulated in specific subdomains: A is produced and is inhibited only in $domain_1$ (green), C is activated only in $domain_3$ (red), and B is activated and repressed in the entire domain. All components diffuse in all domains.

where $\frac{C_j^2}{K_{C_jC_i}^2 + C_j^2}$ and $\frac{K_{C_jC_i}^2}{K_{C_jC_i}^2 + C_j^2}$ describe the activating and inhibitory actions of C_j, respectively.

Initial and Boundary Conditions: The initial condition of A is $1.\mathrm{I}_{domain_3}$; the initial values of B and C are set to zero. Zero flux boundary conditions, $\vec{n}.\nabla C_i$, are used for all components on the outer boundary, as the outer layer, the ectoderm, can be considered impermeable.

2.3 Boundaries and Displacement Fields

Using standard techniques for image segmentation, external and internal boundaries can be extracted [16]. This process can be repeated at different developmental time points to obtain a developmental sequence of shapes [15]. In this study, we consider the two geometries in Figure 1 as our extracted 2D geometries at two subsequent developmental time steps, t and $t+1$. As can be seen, the entire domain as well as the subdomains deform from t to $t+1$.

To describe the growing domains, we need to calculate the displacement fields between the two shapes at t and $t+1$. A range of algorithms can be employed, which have their advantages and disadvantages dependent on the details of the geometries and their deformations (Schwaninger et al., submitted). Here, we use the uniform displacement field algorithm proposed by (Schwaninger et al., submitted): consider a curve at time t, γ^t, that is deformed to γ^{t+1} within the next time step. This algorithm interpolates N points on both curves:

$$\gamma^t = \left\{(x_1^t, y_1^t), \ldots, (x_N^t, y_N^t)\right\}$$

$$\gamma^{t+1} = \left\{(x_1^{t+1}, y_1^{t+1}), \ldots, (x_N^{t+1}, y_N^{t+1})\right\}$$

such that $\left\|(x_i^T, y_i^T), (x_j^T, y_j^T)\right\|_2$ is equal for all i, j and $T \in \{t, t+1\}$. The displacement filed matrix, D, is defined as $D_i = \left[x_i^t, y_i^t, (x_i^{t+1} - x_i^t), (y_i^{t+1} - y_i^t)\right]$. For inner boundaries, it is important to use the COMSOL built-in surface-boundary parameter, S: every point (x_i^t, y_i^t) on the curve γ^t maps to S_i and the displacement matrix is defined as $D = \left[S, (X^{t+1} - X^t), (Y^{t+1} - Y^t)\right]$. Figure 3 shows the displacement fields between two curves at two subsequent time steps t and $t+1$. The displacement fields are imported into COMSOL as *Interpolation* function and are later employed in the *Moving Mesh (ale)* module to describe the domain deformation due to the growth.

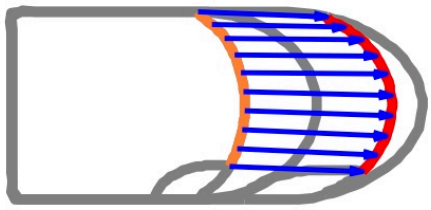

Figure 3. Displacement fields. Blue arrows show the displacement fields between two curves at two time steps, t (orange) and $t+1$ (red).

2.4 Displacement of intersecting Curves

The introduction of subdomains results in intersecting boundary curves (Figure 1). The function *Interpolation Curve*, that we used to generate the boundaries, does not discriminate between intersection points and other points on the curve. All points are interpolated in the same way. Given the interpolation, there is no guarantee that the intersection point of two curves at time t will be accurately displaced to their prescribed intersection point at time $t+1$. This issue can cause distorted meshes, inverted meshes, and numerical problems close to the intersection points. In case of spatially restricted variables, this inaccuracy can result in leakage of variables out of their restricted domains. From here on we will refer to the model with these problems as $Model_1$.

To deal with this problem, we propose the following algorithm. Assume curve$_1$ at time t, γ_1^t, intersects with γ_2^t at point $P=(X,Y)$ (Figure 4A) such that

$$\gamma_1^t = \left\{(x_1^t, y_1^t), \ldots, (X, Y), \ldots, (x_n^t, y_n^t)\right\}$$

$$\gamma_2^t = \left\{(X, Y), \ldots, (x_m^t, y_m^t)\right\}.$$

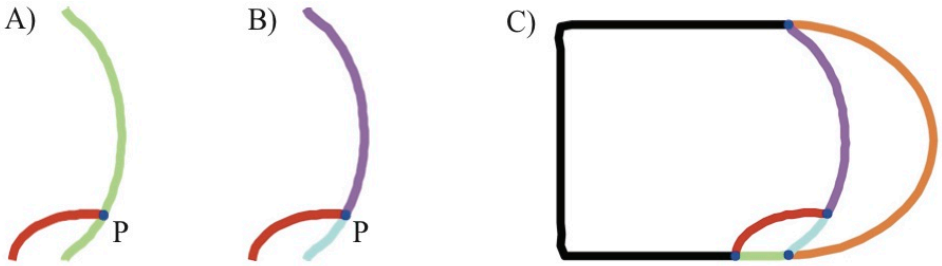

Figure 4. Framework to deal with intersecting boundary curves. **(A)** $Curve_1$ (green) and $curve_2$ (red) of Figure 2 intersect at point *P*. **(B)** To map the intersection point (blue point) at time *t* to the intersection point at *t*+1, the curves are divided into segments, such that the point *P* becomes the start/end point of the intersecting curves. **(C)** This algorithm is applied to all curves of Figure 2. $Curve_1$ is divided into two segments; $Curve_3$ is divided into three segments, whereas $Curve_2$ has only one segment.

Since we want to preserve the intersection point, the curves γ_1^t and γ_2^t have to be divided into segments such that point *P* is the start/end point of segments. We divide γ_1^t into two segments (Figure 4B) such that:

$$\gamma^t_{1_{segment_1}} = \left\{(x_1^t, y_1^t), \ldots, (X, Y)\right\}$$

$$\gamma^t_{1_{segment\,2}} = \left\{(X, Y), \ldots, (x_n^t, y_n^t)\right\}$$

We implemented this algorithm for all intersecting curves (Figure 4C) and determined the displacement fields for each segment individually. The coordinates of each segment and their corresponding displacement fields were then imported into COMSOL separately. Using the above algorithm, we obtain an accurate mapping of all domains and intersection points. From here on, we will refer to this model as $Model_2$.

3. Results

$Model_1$ and *$Model_2$* were implemented in COMSOL with the parameter values as given in

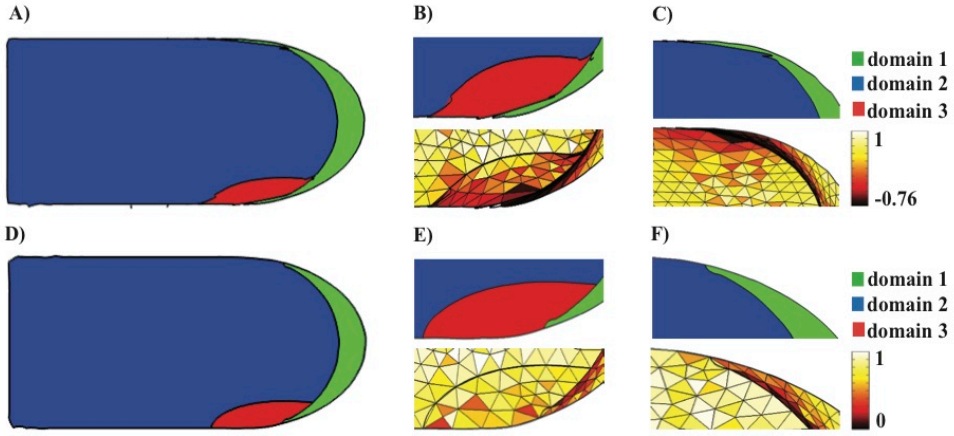

Figure 5. The deformed domain at the final time point. All boundary points at time *t* are mapped to their corresponding points at time *t+1* using the displacement field matrix D. **(A-C)** Final deformed domain at time *t+1* using *$Model_1$*. In this case, not only the intersection points are not displaced correctly, but also their adjacent points are displaced improperly. **(D-F)** Final deformed domain at time *t+1* using *$Model_2$*. In this case, all intersecting curves are divided into segments at their intersection points (Figure 4C). The intersection points and their neighbours are displaced perfectly. **(B,E-top)** Focus on the intersection of $Curve_1$, $Curve_2$ and $Curve_3$. **(C,F-top)** Focus on the intersection of $Curve_1$ and $Curve_2$. **(B,C-bottom)** Inaccuracies in the mapping of the intersection points result in inverted meshes close to these points in *$Model_1$*. **(E,F-bottom)** High quality meshes close to the intersection points in *$Model_2$*. The color bar indicates the quality of mesh elements; negative values indicate inverted meshes.

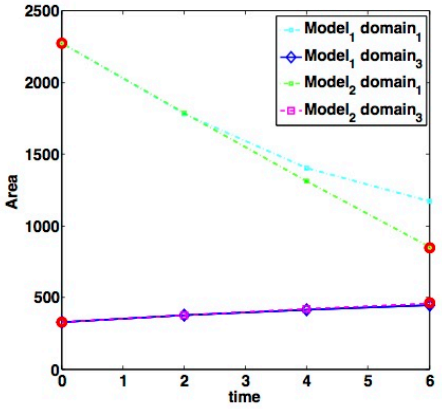

Figure 6. The domain areas over simulation time in $Model_1$ and $Model_2$. The real areas (red circles) of the domains at time t and $t+1$ are provided for comparison.

Table 1 in the Appendix. Figure 5A-C shows that in $Model_1$ the intersection points are not displaced correctly. This problem leads to the inverted meshes close to the intersection points (Figure 5B,C bottom panels), and the subdomains are distorted (Figure 5B,C top panels) as compared to Figure 1B. Segmenting the curves at the intersection points before deformation ($Model_2$) leads to a higher quality of mesh elements and therefore accurate numerical solution and correct domain deformation (Figure 5D-F). The inverted meshes that result from inaccuracies in the mappings also lead to differences in the domain areas. Thus, Figure 6 reports the area of $domain_1$ and $domain_2$ at different time steps. As can be seen, the final area in $Model_1$ differs from the real size of the domain at $t+1$. The inverted meshes also lead to numerical problems and consequently inaccurate solutions. Thus, Figure 7 shows that the expression patterns, i.e. the effective spatial production rates, of A and C in $Model_1$ and $Model_2$ differ at time $t+1$. The components A and C have lower expression in $Model_1$ than in $Model_2$.

4. Conclusion

In this paper, a framework is presented to simulate PDE models on growing, embryonic domains with subdomains, using COMSOL Multiphysics. Intersecting boundaries are not mapped accurately using the standard COMSOL Interpolation function. We addressed this problem by introducing segmented boundaries.

Using this algorithm and COMSOL's Matlab LiveLink interface, one can implement also complicated domains and large sets of PDEs. This permits the simulation of large, complex regulatory networks on physiological domains. We expect that this will further increase the predictive value of the models, and will allow to better test, improve, and validate the models with experimental data.

5. References

1. Iber, D., Zeller, R., Making sense - data-based simulations of vertebrate limb development, *Current Opinion in Genetics & Development*, **22**, 570-577 (2012)

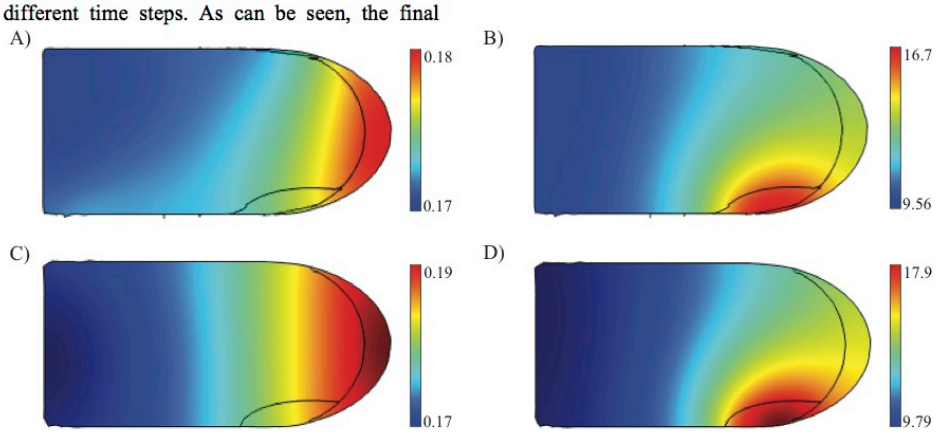

Figure 7. Expression patterns. Effective production rate as predicted by **(A,B)** $Model_1$ for (A) species A, and (B) species C, and by **(C,D)** $Model_2$ for (C) species A, and (D) species C.

2. Wolpert, L.,Positional information and the spatial pattern of cellular differentiation, *Journal of theoretical biology,* **25**, 1-47 (1969)
3. Turing, A. M., The chemical basis of morphogenesis. *Philosophical Transactions of the Royal Society of London. Series B, Biological Sciences*, **273**, 37-72 (1952)
4. Iber, D., Germann, P., How do digits emerge? - Mathematical Models of Limb Development, *Embryo Today, Special Issue on Musculoskeletal Development*, **102**, 1-12 (2014)
5. Badugu, A., Conradin, K., Germann, P., Menshykau, D., Iber, D., Digit patterning during limb development as a result of the BMP-receptor interaction, *Scientific Reports,* **2**, 99 (2012)
6. Lopez-Rios, J., Duchesne, A., Speziale, D., Andrey, G., Peterson, K., Germann, P., Unal, E., Liu, J., Floriot, S., Barbey, S., et al., Attenuated sensing of SHH by Ptch1 underlies evolution of bovine limbs, *Nature,* **511**, 46-51 (2014)
7. Tanaka, S., Iber, D., Inter-dependent tissue growth and Turing patterning in a model for long bone development, *Physical Biology*, **10**, 056009 (2013)
8. Bächler, M., Menshykau, D., De Geyter, C., Iber, D., Species-specific differences in follicular antral sizes result from diffusion-based limitations on the thickness of the granulosa cell layer, *Molecular Human Reproduction*, **20**, 208-22 (2014)
9. Menshykau, D., Iber, D., Kidney branching morphogenesis under the control of a ligand--receptor-based Turing mechanism, *Physical biology*, **10**, 046003 (2013)
10. Menshykau, D., Kraemer, C., Iber, D., Branch mode selection during early lung development, *PLoS computational biology,* **8**, e1002377 (2012)
11. Cellière, G., Menshykau, D., Iber, D., Simulations demonstrate a simple network to be sufficient to control branch point selection, smooth muscle and vasculature formation during lung branching morphogenesis, *Biology open*, **1**, 775-788 (2012)
12. Germann, P., Menshykau, D., Tanaka, S., Iber, D., Simulating Organogenesis in COMSOL, *Proceedings of COMSOL Conference* (2012)
13. Menshykau, D., Iber, D., Simulation Organogenesis in COMSOL: Deforming and Interacting Domains, *Proceedings of COMSOL Conference* (2012)
14. Menshykau, D., Adivarahan, S., Germann, P., Lermuzeaux, L., Iber, D., Simulating Organogenesis in COMSOL: Parameter Optimization for PDE-based models, *Proceedings of COMSOL Conference* (2013)
15. Iber, D., Tanaka, S., Fried, P., Germann, P., Menshykau, D.: Simulating Tissue Morphogenesis and Signaling. In Nelson, C., ed., *Tissue Morphogenesis: Methods and Protocols*, Springer Book Series: Methods in Molecular Biology (2013)
16. Adivarahan, S., Menshykau, D., Michos, O., Iber, D., Dynamic Image-Based Modelling of Kidney Branching Morphogenesis. In Henzinger, A., ed. , *Computational Methods in Systems Biology (CMSB)*, **8130**, 106-119 (2013)

6. Acknowledgements

We thank the COMSOL support team, specially Sven Friedel for their support and insightful discussions. The authors acknowledge funding from the SystemsX RTD NeurostemX, a SystemsX iPhD, and a SNF Sinergia grant.

7. Appendix

Table 1: Non-dimensionalized Model Parameters with characteristic time T = 3600 sec and characteristic length L = 150 µm

Parameter	Value	Description
D	1*T	Diffusion constant
ρ_A	1E-4*T	Production rate
ρ_B	50* ρ_A	Production rate
ρ_C	200* ρ_A	Production rate
d_A, d_B, d_C	1E-6*T	Degradation rate
K_{BA}	0.2	Hill constant
K_{AB}	0.125	Hill constant
K_{CB}	0.5	Hill constant
K_{AC}	0.025	Hill constant

Publication 5: Image-based parameter inference for spatio-temporal models of organogenesis

I provided the real limb bud geometries and was involved for the gene expression pattern comparison analysis for this work.

Image-based Parameter Inference for Spatio-temporal models of Organogenesis

Britta Velten, Erkan Uenal and Dagmar Iber

Department for Biosystems Science and Engineering, ETH Zurich, Mattenstrasse 26, 4058 Basel, Switzerland;
Swiss Institute of Bioinformatics (SIB), Switzerland
Email: britta.velten@arcor.de, dagmar.iber@bsse.ethz.ch

Abstract—Advances in imaging technology now provide us with detailed 3D data on gene expression patterns in developing embryos. This information can be used to build predictive mathematical models of embryogenesis. Current modelling approaches are, however, limited by lack of methods to automatically infer the regulatory networks and the parameter values from the image-based information. Here we make a first step to the development of such methods. We use limb bud development as a model system. For a given regulatory network we developed a decision tree based algorithm to automatically determine parameter values for which the model reproduces the expression patterns. Starting from this parameter set, local optimization was performed to further reduce the chosen goodness-of-fit measure. This approach allowed us to recover the target expression patterns, as judged by eye, and thus provides a first step towards the automated inference of parameter values for a given regulatory network.

1. Introduction

Developmental processes are controlled by complex regulatory networks. Decades of genetic experiments have defined the core regulatory proteins for most developmental processes and many regulatory links. The resulting regulatory networks are complex and the regulatory interactions change dynamically as the embryo is developing. As a consequence, our understanding of the regulatory logic that controls patterning in time and space remains limited. Mathematical modelling offers the opportunity to integrate the experimental information into a consistent framework and to define the underlying regulatory mechanisms [1].

To obtain a mathematical model with predictive value the model must be firmly rooted in experimental data. Available experimental data mainly consists of images that show the spatial distribution of mRNAs as a measure of gene expression at the different stages of development. This information is not quantitative, but provides a qualitative indication of expression patterns. Current models of the spatio-temporal processes in the embryo are largely hand-tuned to reproduce the experimental data both in wild type and mutants [2]. Computational methods are largely missing for the image-based inference of the the biological network architecture and the parameter values, even though

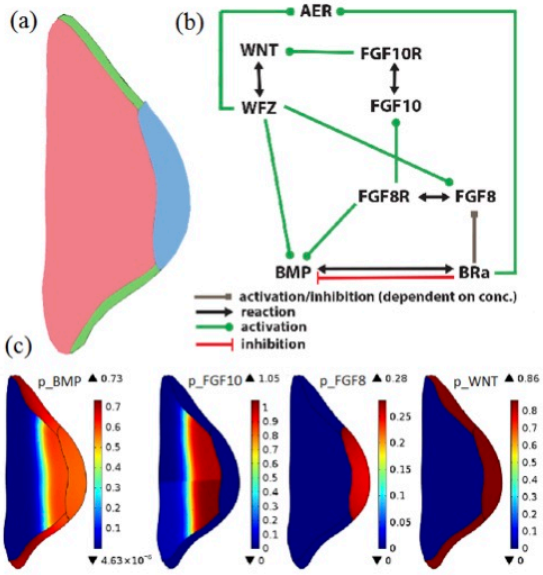

Figure 1: The Limb Bud Model System. (a) Subdomains of the limb bud: mesenchyme (red), apical ectodermal ridge AER (blue) and additional ectoderm (green). (b) The core network of regulatory interactions. (c) *In silico* generated expression patterns using parameter values in table 1, representing the experimentally observed patterns.

methods for the estimation of parameter values for partial differential equation (PDE) models have been established. An important limitation are the higher computational costs for the simulations, which renders many approaches computationally infeasible for models of organogenesis. Here, we will focus on a model for mouse limb bud development to illustrate the challenges in inferring parameter values from the available data.

Limb buds grow out of the flank at about day 9 of mouse embryonic development [3]. Importantly, the limb bud consists of different tissue domains, and the expression of some of the proteins is restricted to particular subdomains, i.e. to either the mesenchyme (Fig.1a, red part), the apical ectodermal ridge (AER) (Fig.1a, blue part) or the ectoderm (Fig.1a, green and blue part). We will focus on the

early regulatory interactions, and we will thus restrict ourselves to the core regulatory interactions between fibroblastic growth factor (FGF) 10, WNT3, FGF8 and BMP. Decades of experiments have defined the core regulatory interactions (Fig.1b). Thus, WNT2B from the flank induces the expression of *Fgf10* in the mesenchyme. FGF10 signalling induces the expression of *Wnt3* in the ectoderm. WNT signalling is necessary for the development of the AER, which expresses *Fgf8* and other *Fgfs*. FGF8 diffuses into the mesenchyme and maintains the expression of *Fgf10*. FGF8 together with WNT3 also induce the expression of *Bmp*s and BMPs supports the development of the AER.

In the following, we will build a mathematical model that represents these regulatory interactions. The focus will then be on the inference of the parameter values. To test the approach we will use simulated *in silico* data rather than experimental gene expression data as obtained from *in situ* hybridisation.

2. Results & Discussion

2.1. The Model

To keep the computational costs to a minimum we will limit ourselves to a 2D limb bud domain (Fig.1a). To simulate the regulatory network (Fig.1b) with n components on a limb bud domain we use a set of coupled partial differential equations of reaction-diffusion type, i.e.

$$\frac{\partial c_i}{\partial t} = D_i \Delta c_i + R(c_1, \ldots, c_n) \tag{1}$$

where c_i denotes the concentration of species i, with diffusion constant D_i and reaction term $R(c_1, \ldots, c_n)$. As network components we include the morphogens FGF10 (F10), FGF8 (F8), BMP, WNT and the structure AER with diffusion constant D as well as the respective receptor-ligand-complexes with FGF10, denoted F10R, with FGF8, denoted F8R, with BMP, denoted BRa, and with WNT, denoted WFZ with diffusion constant DR. The reaction terms are set to

$$\begin{aligned}
R(F10) &= \rho_{F10} p_{FGF10} - d\,F10 \\
&\quad + (1 - \mathbb{1}_{Mes})(k_{off} F10R - k_{onR} F10(RT_{F10} - F10R)) \\
R(F8) &= \rho_{F8} p_{FGF8} - d\,F8 \\
&\quad - \mathbb{1}_{Mes} k_{onR} F8(RT_{F8} - F8R) + \mathbb{1}_{Mes} k_{off} F8R \\
R(WNT) &= \rho_{WNT} p_{WNT} - d\,WNT \\
&\quad - k_{onR} WNT(RT - WFZ) + k_{off} WFZ \\
R(BMP) &= \rho_{BMP} p_{BMP} - d\,BMP \\
&\quad - k_{onR} BMP(RT_{BRa} - BRa) + k_{off} BRa \\
R(F10R) &= k_{onR} F10(RT_{F10} - F10R) - (k_{off} + d_{F10R}) F10R \\
R(F8R) &= k_{onR} F8(RT_{F8} - F8R) - (k_{off} + d_{F8R}) F8R \\
R(WFZ) &= k_{onR} WNT(RT - WFZ) - (k_{off} + d_{BR}) WFZ \\
R(BRa) &= k_{onR} BMP(RT_{BRa} - BRa) - (k_{off} + d_{BR}) BRa \\
R(AER) &= \rho_{AER} \left(\mathbb{1}_{AER} \frac{WFZ^2}{WFZ^2 + K^2_{WNT}} \frac{BRa^2}{BRa^2 + K^2_{BRa_AER}} \right) \\
&\quad - d_{AER} \frac{K^2_{WNT1}}{WFZ^2 + K^2_{WNT1}} \frac{K^2_{BRa_AER1}}{BRa^2 + K^2_{BRa_AER1}} AER
\end{aligned} \tag{2}$$

with production terms

$$\begin{aligned}
p_{FGF10} &= \tfrac{1}{20} \mathbb{1}_{lowMes} + \frac{F8R^2}{F8R^2 + K^2_{F8R_F10}} \mathbb{1}_{Mes} \\
p_{FGF8} &= \mathbb{1}_{AER} AER \frac{WFZ^2}{WFZ^2 + K^2_{WNT_FGF}} \frac{BRa^2}{BRa^2 + K^2_{BRa_FGF}} \frac{K^2_{BRi}}{BRa^2 + K^2_{BRi}} \\
p_{WNT} &= \frac{F10R^2}{F10R^2 + K^2_{F10R}} (\mathbb{1}_{Ect} + AER \mathbb{1}_{AER}) \\
p_{BMP} &= \left(\mathbb{1}_{Mes} \frac{F8R^2}{F8R^2 + K^2_{F8R}} + (1 - \mathbb{1}_{Mes}) \frac{WFZ^2}{WFZ^2 + K^2_{WNT}} \right) \frac{K^2_{BRi_Bmp}}{BRa^2 + K^2_{BRi_Bmp}}.
\end{aligned} \tag{3}$$

The indicator function $\mathbb{1}_X$ denotes that the corresponding reaction only take place in domain X, as the expression of the morphogens and receptors is restricted to different parts of the limb bud domain. Here, 'lowMes' denotes the lower half of the Mesenchyme, 'Mes' the Mesenchyme, 'Ect' the Ectoderm, and 'AER' the AER. To account for the inhibitory and activating effects on gene expression as displayed in the regulatory network (Fig.1b) the model uses Hill kinetics with maximum production rates ρ_c and Hill constants K_{xx}.

2.2. Parameter Inference

To prepare for the inference of the parameter values, θ, we first generate *in silico* data with the parameter set, θ_0, in Table 1. These result in the expression patterns in Fig. 1c. As starting values for parameter inference we then use diffusion constants (in $[\mu m^2 h^{-1}]$) in Table 1, as their physiological range is typically rather well known. For the other parameters we set all maximal production rate to 2, all Hill constants and maximum receptor capacities to 1, and all binding and degradation rates to 0.01. These initial parameter values result in the expressions patterns shown in Fig. 2. Starting from those, we aim at finding a set of parameter values, with which we can reproduce the expression patterns in Fig. 1c.

Quantitative, spatial expression data is currently not available in the limb bud. Therefore, the model only needs to match the observed patterns qualitatively. To quantify the goodness-of-fit of the simulated expression patterns, we used a mathematical formulation for the constraints that describe the desired patterns. Thus, based on the image data we require p_{FGF10} to be present in the mesenchyme with a gradient, p_{FGF8} to be uniformly present in AER, p_{BMP} to be uniformly present in the ectoderm and AER as well as in the mesenchyme with a gradient and p_{WNT} to be uniformly present in the ectoderm. The absence of WNT and F8 production in the mesenchyme and (in case of F8) in the ectoderm is already hard-coded by the indicator-functions in the PDEs. As the production rates range from 0 to 1 we choose by eye 0.3 as a threshold for presence, and a penalty term enforces presence of substance c in domain X, i.e.

$$\int_X \max(0.3 - c, 0)^2 d\mu. \tag{4}$$

For uniform production, we added the penalty term

$$\int_X (c - \max_X(c))^2 d\mu. \tag{5}$$

Table 1: Parameter set θ_0 to generate *in silico* data

Name	Value	Description
D	3600	Diffusion constant of proteins
DR	36	Diffusion constant of receptors
ρ_{F8}	0.9	max. production rate of FGF8
ρ_{F10}	7.2	max. production rate of FGF10
ρ_{BMP}	1.8	max. production rate of BMP
ρ_{WNT}	1.8	max. production rate of WNT
ρ_{AER}	0.36	max. production rate of AER
$init_{F10}$	0	initial concentration of FGF10
d	0.0036	degradation rate of morphogenes
d_{AER}	3.6	degradation rate of AER
d_{BR}	1.8	degradation rate of WFZ, BRa
d_{F10R}	0.36	degradation rate of F10R
d_{F8R}	0.288	degradation rate of F8R
k_{onR}	3.6	on-binding rate to receptors
k_{off}	0.0036	off-binding rate from receptors
RT	10	max. capacity of WNT receptor
RT_{F8}	2.5	max. capacity of FGF8 receptor
RT_{F10}	2.5	max. capacity of FGF10 receptor
RT_{BRa}	0.6	max. capacity of BMP receptor
K_{F8R}	0.1	Hill constant
K_{F8R_F10}	0.025	Hill constant
K_{F10R}	1	Hill constant
K_{BRa}	0.3	Hill constant
K_{BRa_FGF}	0.01	Hill constant
K_{BRa_AER}	0.01	Hill constant
K_{BRa_AER1}	0.001	Hill constant
K_{BRi}	0.25	Hill constant
K_{BRi_Bmp}	0.5	Hill constant
K_{WNT}	0.1	Hill constant
K_{WNT_FGF}	0.1	Hill constant
K_{WNT1}	0.001	Hill constant
K_{WNT_Bmp}	0.01	Hill constant

The constraint given by a gradient was approximated using a smoothed step function $\varphi_c(x)$ in x-direction, i.e.

$$\int_X (0.3 - c)_+^2 \varphi_c(x) + (c - 0.1)_+^2 (1 - \varphi_c(x)) d\mu. \quad (6)$$

Adding all these constraints provides us with a fitness function $f(\theta)$ as a measure for the goodness-of-fit. For the *in silico* generated expression pattern (Table 1) its value is $f(\theta_0) = 3852$, whereas for the initial parameter values in our optimisation we obtain $f(\theta_{start}) = 13989$. Only the relative, but not the absolute value of $f(\theta)$ matters.

A sensitivity analysis revealed that the expression patterns are sensitive to all parameters except for K_BRa_AER and K_BRa_AER1. The parameters in the model are highly correlated and the vast dimension of the parameter space as well as the non-smooth fitness function render standard optimization methods such as Coordinate Search, gradient-based methods like SNOPT adjoint method, or random algorithms such as the Particle Swarm Optimization unable

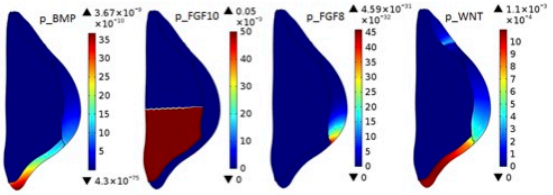

Figure 2: Predicted expression patterns with the initial parameter values.

to improve the value of the fitness function and to arrive at a parameter set for which the model reproduces the patterns in Fig. 1c. We note that the repeated simulation of the PDEs is computationally very expensive.

2.3. A decision tree approach for the sequential inference of parameter values

To overcome the difficulties described above, we developed a decision tree that also uses prior knowledge and that optimises parameter values sequentially given that most parameter values affect the patterning process only at certain time intervals. To determine the sequence, in which parameters are identified, we start with the initial conditions and the constitutive production rates and check which production rates are controlled by those factors that are initially present, here FGF10 production in the lower part of the mesenchyme. All production rates except for the direct downstream targets are set to zero. For each of these steps only a subset of the original parameters has a direct influence. This subset is tuned with help of a decision tree that checks whether the currently considered components are present in the correct domains. If all important features are reproduced, the algorithm goes on to check the next component activated downstream; if not, the parameters which have direct influence on the considered feature are doubled or halved depending on the sign of their influence and then the procedure of the decision tree in the current step is repeated until the constraint is fulfilled or a maximum number of calls is reached. For the model considered here this approach results in the steps

1. F10 production → check F10, F10R
2. F10 and WNT production → check WNT, WFZ in Ectoderm (Ecto)
3. F10, WNT, BMP, AER production → check BMP, BRa in Ecto, check AER, check WNT, WFZ in Ecto
4. F10, WNT, BMP, AER, F8 production→ check F8, F8R, check BMP in Mesenchyme, check F10 in Mesenchyme

The decision tree for the second step of the algorithm is illustrated in Fig. 3. Starting with the parameter values θ_{start} results in a set of parameters θ_{dec}, for which the model yields expression patterns (Fig. 4) close to the original patterns (Fig. 1c), and the fitness function f reduces from $f(\theta_{start}) = 13989$ to $f(\theta_{dec}) = 5598$.

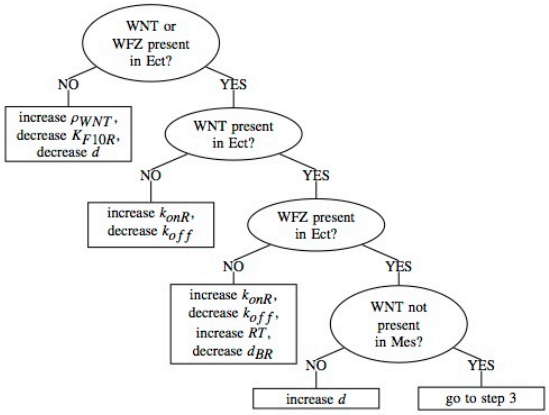

Figure 3: The decision tree performed by the parameter inference algorithm in step 2.

2.4. Local optimization with SNOPT

The parameter values recovered from the decision tree approach are used as initial values to perform local optimization using the SNOPT algorithm implemented in COMSOL 4.4, a gradient-based algorithm that uses sequential quadratic programming (SQP) methods and which requires the least computation time for this problem among the COMSOL methods. To calculate the gradient, the adjoint method was used, as it is most efficient in case of many parameters. At this step of our approach we compare the optimised patterns (Fig. 5) to the *in silico* generated patterns (Fig. 1c) directly, i.e. as objective function $J(\theta)$ we integrate the difference between the *in silico* generated expression values and the model output, while adding scaling factors λ_i as additional parameters as we aim at reproducing the patterns and no absolute values, i.e. $J(\theta) =$

$$\int_{AER} (p_{FGF8} - \lambda_1 \hat{p}_{FGF8})^2 \, d\mu + \int_{AER,Ect} (p_{WNT} - \lambda_2 \hat{p}_{WNT})^2 \, d\mu$$
$$+ \int_{all} (p_{BMP} - \lambda_3 \hat{p}_{BMP})^2 \, d\mu + \int_{all} (p_{FGF10} - \lambda_4 \hat{p}_{FGF10})^2 \, d\mu$$

This formulation allows us to evaluate the recovered parameter values with statistical measures, i.e. calculate the profile likelihood. To reduce computational costs we exclude the Hill constants, which are correlated in particular with expression and decay rates, from the optimization, and we reduce the accuracy of the simulation. Thereby, we can reduce the computation time from 24 hours to approx. 2 hours for one optimization. Within 100 iterations the algorithm halves the value of the objective function and recovers parameter values θ_{opt} with a fitness function value $f(\theta_{opt}) = 4526$ (Fig. 5), reasonably close to the fitness function value of the target pattern, $f(\theta_0) = 3852$ (Fig. 1c).

3. Methods

The model was solved with COMSOL Multiphysics using the Optimization Toolbox (version 4.4) and the MATLAB Livelink (version 4.3b) as described before [4, 5].

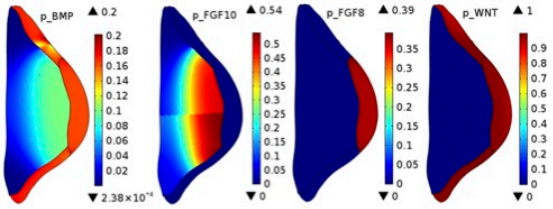

Figure 4: Expression patterns after the decision-tree based parameter inference.

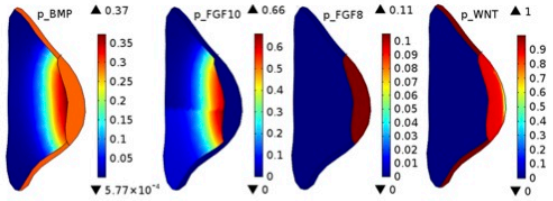

Figure 5: Expression patterns after the optimization with SNOPT, using the parameters recovered by the decision tree algorithm as initial values.

4. Acknowledgements

We thank Z. Karimaddini, and R. Zeller for discussions. The work was in part funded by the SNF Sinergia and NeuroStemX grants.

References

[1] D. Iber and R. Zeller, "Making sense-data-based simulations of vertebrate limb development.," *Curr Opin Genet Dev*, vol. 22, pp. 570–577, 12 2012.

[2] S. Probst, C. Kraemer, P. Demougin, R. Sheth, G. R. Martin, H. Shiratori, H. Hamada, D. Iber, R. Zeller, and A. Zuniga, "Shh propagates distal limb bud development by enhancing cyp26b1-mediated retinoic acid clearance via aer-fgf signalling.," *Development*, vol. 138, pp. 1913–1923, 5 2011.

[3] R. Zeller, J. Lopez-Rios, and A. Zuniga, "Vertebrate limb bud development: moving towards integrative analysis of organogenesis.," *Nat Rev Genet*, vol. 10, pp. 845–858, 12 2009.

[4] P. Germann, D. Menshykau, S. Tanaka, and D. Iber, "Simulating organogensis in comsol," in *Proceedings of COMSOL Conference 2011*, 9 2011.

[5] D. Menshykau, A. Shrivastsan, P. Germann, L. Lemereux, and D. Iber, "Simulating organogenesis in comsol: Parameter optimization for pde-based models.," in *Proceedings of COMSOL Conference 2013, Rotterdam*, 10 2013.